Probing cosmic monsters: confronting hydrodynamic simulations with new observations of high-density environments

Ahad, S.L.

Probing Cosmic Monsters

Confronting Hydrodynamic Simulations with New Observations of High-density Environments

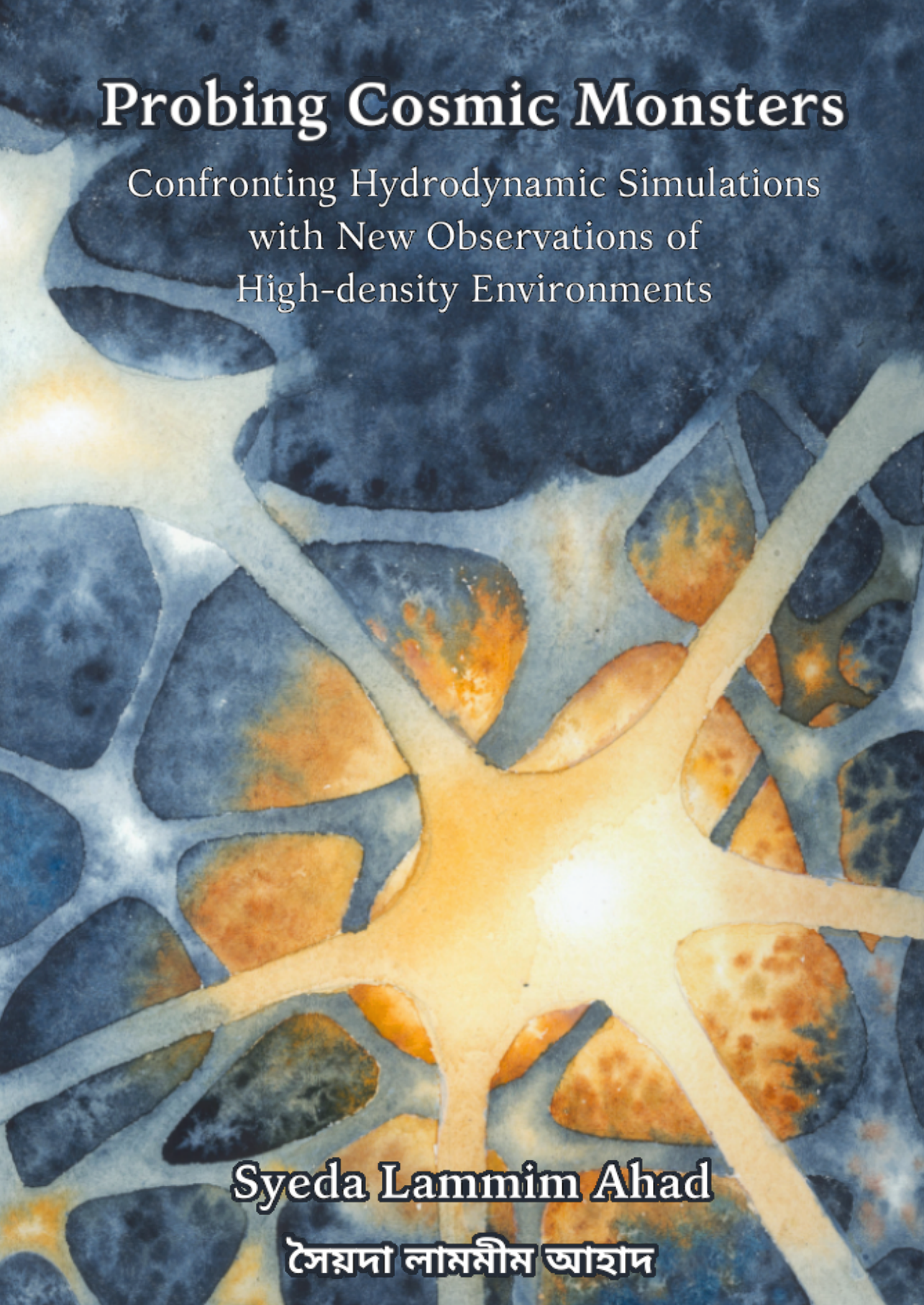

Syeda Lammim Ahad

সৈয়দা লামমীম আহাদ

Probing Cosmic Monsters

Confronting Hydrodynamic Simulations with New Observations of High-density Environments

Proefschrift

ter verkrijging van
de graad van doctor aan de Universiteit Leiden,
op gezag van rector magnificus prof.dr.ir. H. Bijl,
volgens besluit van het college voor promoties
te verdedigen op dinsdag 21 november 2023
klokke 11:15 uur

door

Syeda Lammim Ahad

geboren te Madaripur, Bangladesh
in 1992

Promotores:

Prof. dr. H. Hoekstra	
Dr. Y.M. Bahé	(École Polytechnique Fédérale de Lausanne)

Promotiecommissie:

Prof. dr. I.A.G. Snellen	
Prof. dr. K. Kuijken	
Prof. dr. M. Kriek	
Dr. N. Hatch	(University of Nottingham)
Dr. A. Muzzin	(York University)

ISBN: 978-94-93330-40-5

Cover art: The habitat of cosmic monsters, watercolour painting by the author. Digitally modified to add the text by R. Brilenkov.

"The sky is full of the sun and stars
The universe is full of life,
Among all these, I have found a place,
At the wonder, my heart sings."
— Rabindranath Tagore

"আকাশ ভরা সূর্য-তারা বিশ্বভরা প্রাণ,
তাহারি মাঝখানে আমি পেয়েছি মোর স্থান,
বিস্ময়ে তাই জাগে আমার গান।"
--- রবীন্দ্রনাথ ঠাকুর

Contents

1

Introduction

1.1 Our understanding of the Universe: A brief history

Similar to the development of human civilization, our progress in understanding the Universe and our place in it, has made the biggest leaps in the last few centuries compared to the last few millennia and in the last few decades compared to the last few centuries. Not surprisingly, our understanding of the Universe improved in tandem with the advent and availability of new technology. Only a few hundred years ago, the first use of a refractive telescope to look at the skies showed that Jupiter and Saturn also have moons orbiting them, challenging the long-standing Earth-centric model of the Universe before that. A few centuries later, less than a hundred years ago, Edwin Hubble used the 100-inch telescope at Mount Wilson Observatory to measure distances of variable stars in M31 and M33 by using the period-luminosity relations of Cepheid variable stars. He demonstrated that the fuzzy cloud-like 'nebulae' in the night sky were indeed very large systems that were very far away. This was the first proof that our Milky Way is not the only 'island' of stars or 'galaxy' in the Universe, but rather one of many. In Western culture, the name 'galaxy' comes from the Greek word $\gamma\acute{\alpha}\lambda\alpha$, which means milk, referring to the fuzzy and milky appearance of the Milky Way[1]. From naming our Galaxy after some spilt milk in the sky to understanding that these stars are not the only objects in the Universe, rather we are in a galaxy like many others, took us thousands of years. However, from realizing that there are other galaxies to finding hundreds of other galaxies and classifying them into types took only a few. Based on how the galaxies appear in optical images, or what we call galaxy morphology, Hubble proposed a classification of galaxies following a progression from simple (Spherical/Elliptical) to more complex (spirals/barred spirals) forms, which

[1]The name Milky Way is derived from its classical Latin term 'via lactea', which is translated from the Hellenistic Greek term $\gamma\alpha\lambda\alpha\xi\acute{\iota}\alpha\varsigma\ \kappa\acute{\upsilon}\kappa\lambda\varsigma$ (galaxías kýklos), meaning 'milky circle'.

was possible through the use of the biggest telescope at that time. Soon after, in 1927-1929, based on the measured distances from Hubble and redshifts from Slipher (1917), Hubble and Lemaître linked that all these galaxies are moving away from us, and their receding velocities are proportional to their distances from us[2]. Detailed discussions of pre-1929 observations leading to this conclusion can be found in Trimble (2012) and Trimble (2013). This discovery drastically changed yet another idea about our Universe: it is expanding over time instead of being static as previously thought of because of the apparent static location of stars in the sky. This discovery brought humankind's long-held question of 'where did everything come from' from a pure theoretical practice into the realm of data-driven science, providing a crucial clue to guide the theory of modern Cosmology as we know it today.

1.2 The Standard Model of Cosmology

The current Standard Model of Cosmology, also called the 'Concordance Cosmological Model' or the 'Lambda Cold Dark Matter (ΛCDM) Model', is one of the best achievements of modern science, both theoretically and observationally, albeit with several loose ends including the reliance on untested theories about inflation, dark matter, and dark energy. The primary assumption of this model is the 'cosmological principle', which states that the Universe is homogeneous and isotropic on sufficiently large scales. Based on the framework of Einstein's general theory of relativity (GTR) and the cosmological principle, the metric describing space-time and determining the distances separating nearby points (e.g., stars, galaxies) is the Friedmann-Lemaître-Robertson-Walker metric (FLRW metric). Friedman (1922) solved the field equations of GTR by assuming the cosmological principle. A similar result was obtained by Lemaître (1927). Most of the solutions of the Friedmann field equations predict an expanding or contracting universe, depending upon initial parameters such as the mass-energy of the universe.

Discovery of the Hubble-Lemaître law (Hubble, 1929) implied that (i) only the expanding solutions of the Friedmann equations are allowed as solutions for the Universe and (ii) the universe must have had a very dense and hot beginning, motivating the Big Bang model, an important element in our current understanding of the Universe.

According to the ΛCDM cosmology model, the mass-energy budget of the Universe is distributed mainly between the invisible but gravitationally interacting 'dark'

[2]Previously known as the Hubble Law. In 2018, the International Astronomical Union resolved it to be referred to as the Hubble-Lemaître law

matter ($\approx$ 25%) and an even more mysterious 'dark energy' ($\approx$ 70%), leaving only $\approx$ 5% to ordinary matter that includes all the elements in the periodic table (Planck Collaboration XVI, 2014; Planck Collaboration et al., 2020).

So far, we have only found indirect evidence of the presence of dark matter and dark energy. Oort (1932) inferred missing matter in the Solar neighbourhood from the velocity of stars. However, the first indirect observation of dark matter is usually attributed to Fritz Zwicky in 1933 (e.g. Trimble 1987; Einasto 2013). By studying the motion of galaxies in the Coma cluster of galaxies, Zwicky (1933) found that these galaxies move faster than the expected velocities their total visible mass could gravitationally hold, and inferred that there must be more (10 to 100 times) mass in that system than the amount we can estimate from the visible light. Several decades later, through a study of the rotation velocity of stars in spiral galaxies, Rubin and Ford (1970) and Rubin et al. (1980) also reported that most of the gravitational matter in galaxies could not be observed, providing a sign of dark matter on the galaxy scale.

The first observational evidence of dark energy came from another surprising discovery. Through the study of distant type Ia supernovae, Riess et al. (1998) and Perlmutter et al. (1999) found that the expansion of the Universe is accelerated. We use the term 'dark energy' to refer to the cause of this acceleration, and the 'Λ' term was added in the ΛCDM model to represent it.

The ΛCDM model is supported by several other empirical pillars, including (i) the primordial nucleosynthesis (Alpher et al., 1948), i.e. the formation theory of the light elements (Hydrogen, Helium, Lithium) very soon following the Big Bang and the fact that the quantitative predictions from this theory agree extremely well with observations, (ii) the discovery of the cosmic microwave background radiation (CMBR) by Penzias and Wilson (1965). The CMB is predicted by the hot Big Bang hypothesis (Dicke et al., 1965), being the afterglow with very small temperature fluctuation ($dT/T \approx 10^{-5}$) approximately 380,000 years after the Big Bang. (iii) the development of the inflationary model that explains the homogeneity of the CMB with a brief period of exponential size growth of the very early Universe (Guth, 1981). Since its discovery in 1965, the CMB, in particular, has been studied with continuously improved measurements from multiple observational programs (COBE - Bennett et al. 1996, WMAP - Bennett et al. 2003, Planck - Planck Collaboration et al. 2020) and has been the most constraining probe of the standard cosmology model.

The ΛCDM model of cosmology has been, so far, the most evidence-supported model of the Universe. However, there are still several missing elements, especially our lack of understanding about the nature of the dominant components of the Uni-

verse, dark energy and dark matter. While many current and upcoming efforts are ongoing to understand the nature of these components, there is also room for alternative theories, such as a different type of dark matter other than the 'cold dark matter' or an alternative theory to explain gravity other than the GTR.

1.3 Hierarchical structure formation

According to the Big Bang theory in the ΛCDM paradigm, the extrapolation of the expansion of the Universe backwards in time yields an approximation of the time when it all started, about 13.8 billion years ago. Just after the Big Bang, all the matter in the Universe was hot, dense, ionised, and remarkably homogeneously distributed. We see an imprint of this matter density distribution of the early Universe in the nearly isotropic temperature of the CMB. However, the density distribution also had very small inhomogeneities, which we see in the small-scale temperature fluctuations of the CMB. From that (nearly) smooth distribution, the transition into the current distribution of galaxies in the Universe as we observe (e.g. Colless et al. 2001) started with these very small initial density perturbations in the early Universe.

While the thermal photons interacted with the baryonic matter and kept them in a fluid-like form with complex oscillatory behaviour (Peebles and Yu, 1970), the non-interacting dark matter could clump together due to gravity, increasing the amplitude of the primordial density fluctuations. These small density fluctuations then grew larger under the influence of gravity over time, eventually initiating gravitational collapse and forming dark matter haloes (e.g. Peacock 1999; Delos and White 2023). The hot, ionized baryons remained tightly coupled to the radiation field and could not collapse further until the Universe cooled sufficiently. At this point, about 100 million years after the Big Bang, the baryons were able to collapse into the early dark matter haloes and formed the first stars that subsequently created the first galaxies (Press and Schechter, 1974; White and Rees, 1978; Mo et al., 2010).

At present, galaxies in the Universe are not distributed randomly, but in a complex web-like structure with voids, filaments, and at the junction of the latter – nodes, which is known as the Cosmic Web structure. This large-scale structure of the Universe is observed in large galaxy surveys like the 2DF survey (Colless et al., 2001) and the Sloan Digital Sky Survey (SDSS; York et al. 2000). As the Universe is, to first order, governed by gravity (especially when dark matter dominates), we can evolve the primordial dark

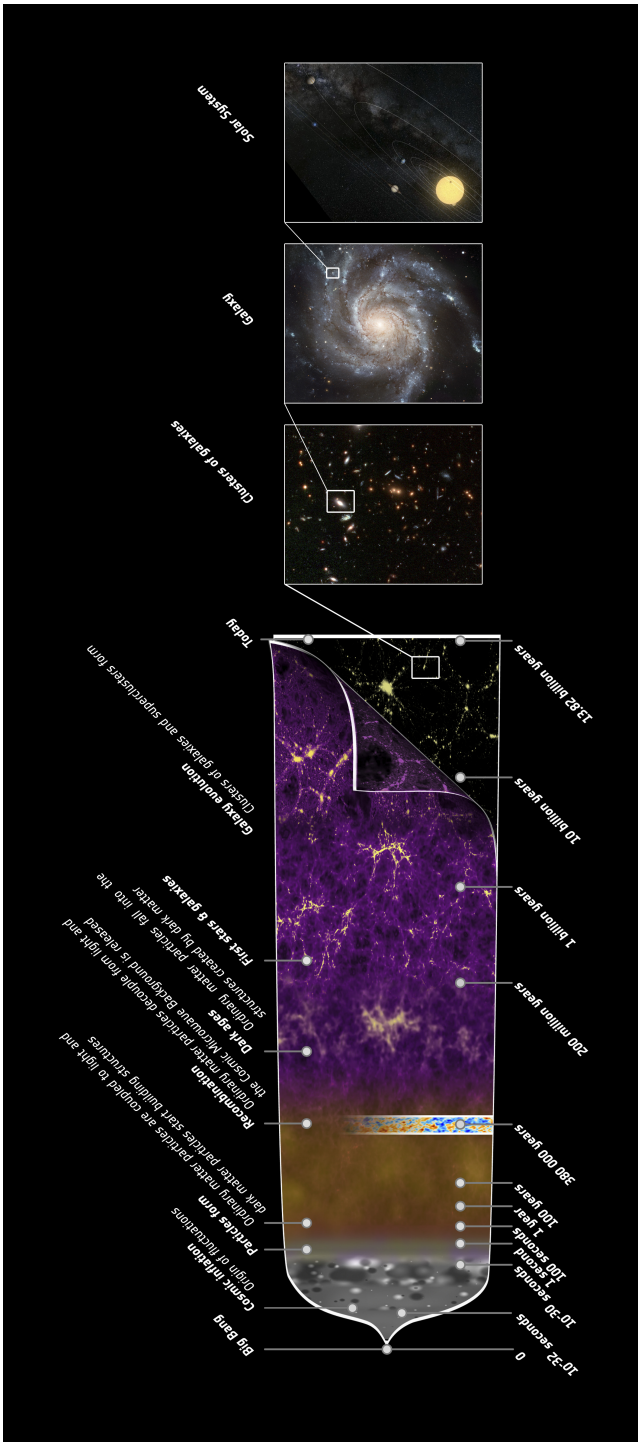

Figure 1.1: Timeline of the Universe from the beginning through the 13.8 billion-year history. It shows the main events that occurred between the initial small density fluctuations and the rich variety of galaxies that we observe today. The panels on the right side zoom into the large-scale structures to reveal a cluster of galaxies, a spiral galaxy, and the Solar System, respectively. Figure from ESA/Planck.

matter fluctuations to present days under the influence of gravitational force using numerical N-body simulations, which reproduce similar cosmic web-like structures to the observations (e.g., Springel et al. 2005). The formation of stars and evolution of galaxies in the dark matter haloes of these galaxies, however, follows complex baryonic physics. A central question of modern extragalactic astronomy is to understand a complete picture of the complex processes that transform the hot ionized gas in dark matter haloes into the diverse types of galaxies that populate our Universe now.

From the first stars to the Cosmic Web, the growth of the large-scale structure of the Universe can be explained in a hierarchical formation scenario (an illustration of the timeline of the Universe is provided in Fig. 1.1). In the early Universe, the typical masses of the dark matter haloes were small, but they grew hierarchically with cosmic time through merging with other haloes and accretion of diffuse dark matter. This is also observed in the aforementioned N-body simulations. Galaxies formed within these dark matter haloes and aggregated along the already existing interconnected cosmic filaments of dark matter, eventually leading to the formation of massive galaxy clusters at the intersections of filaments, making them the largest gravitationally bound structures in the Universe. Being the last-formed structures in the hierarchical formation model, their abundance and mass distributions are excellent tools to test the theory of structure formation over cosmic time. Moreover, the matter density and the expansion of the Universe regulate when such massive structures like galaxy clusters can form and how far apart they can be at different cosmic epochs. Therefore, the number density of clusters and their formation epochs can provide significant constraints on the nature of dark matter and dark energy. These parameters can be studied on a linear scale from the large-scale structure of the Universe. However, to constrain these measurements further, a detailed understanding of the formation and evolution of galaxy clusters and the galaxies within them is necessary. For more discussion on the formation of galaxy clusters and their role as cosmological probes, see e.g., Allen et al. (2011) and Kravtsov and Borgani (2012).

1.4 Galaxy evolution in high-density environments

Galaxy groups and clusters contain hundreds to thousands of galaxies in a small volume (1-2Mpc radius) compared to how galaxies are distributed in other areas along the large-scale structure. From small groups with halo mass $\sim 10^{12.5}\mathrm{M}_{\odot}$, to large clusters like the Coma cluster with $> 10^{15}\mathrm{M}_{\odot}$, these systems cover a wide mass range. Because of their dense distribution of galaxies, galaxy groups and clusters are unique cosmic

laboratories to study the impact of galaxy interactions and environment on galaxy formation. Many observational studies have been conducted on galaxy groups and clusters over the last 50+ years, and it is well-established that galaxy properties differ significantly between these dense systems and the average sparse galaxy distribution or the "field" environment. For example, at a fixed stellar mass, galaxies in denser environments are more likely to be elliptical in morphology (Dressler, 1980), have low levels of or no recent or ongoing star formation (Dressler, 1980; Balogh et al., 1999; Kauffmann et al., 2004; Weinmann et al., 2006; Blanton et al., 2005; Peng et al., 2010; Wetzel et al., 2012; Woo et al., 2012), and have a much lower amount of atomic hydrogen (e.g. Giovanelli and Haynes, 1985; Fabello et al., 2012; Hess and Wilcots, 2013; Odekon et al., 2016; Brown et al., 2017) in comparison with galaxies in the field.

Over the last decades, different physical mechanisms have been identified as potential causes of such differences in galaxy properties in groups and clusters compared to the field. A review of these can be found in Boselli and Gavazzi (2006) and Boselli et al. (2022). The hot halo of gas or the intracluster medium (ICM) can exert ram pressure on galaxies moving through it (Gunn and Gott, 1972; Larson et al., 1980; McCarthy et al., 2008). The ram pressure from the ICM can be strong enough to strip cold gas from a group/cluster galaxy and prevent further star formation (Gunn and Gott, 1972). Ram pressure may also trigger temporary star formation bursts in the galaxy (Tonnesen and Bryan, 2012) and consequently deplete it of available gas resources. If ram pressure is not efficient enough to strip the cold gas directly, it may still be able to remove the hot gas haloes in the circumgalactic medium (CGM). The hot CGM is expected to act as a reservoir that gradually replenishes the more centrally concentrated cold gas disc as it is used up by star formation (White and Rees, 1978; White and Frenk, 1991). Once the central cold gas is used up for star formation, losing the hot CGM will eventually quench the star formation. This process is referred to as 'strangulation' or 'starvation' (Larson et al. 1980, see also Balogh et al. 2000; McCarthy et al. 2008). Tidal forces due to the halo potential can temporarily increase the star formation activity of cluster galaxies by causing disc gas clouds to collide and collapse (Byrd and Valtonen, 1990). Such tidal forces can strip the haloes of gas, stars, and dark matter (e.g. Willman et al. 2004; Weinmann et al. 2010.

Besides the above-mentioned processes, frequent encounters between galaxies can also contribute to the observed diversity of galaxy morphology in dense environments (e.g. Merritt 1983). 'Galaxy harassment' or repeated rapid encounters in galaxy clusters can particularly impact the morphology of low surface brightness galaxies (Moore et al., 1996; Moore et al., 1998). Galaxy mergers and repetitive slow encounters be-

tween group members can form an elliptical galaxy from two spirals and also trigger temporary starbursts (e.g., Bekki and Couch 2011).

While our understanding of the processes that dominate galaxy evolution in dense environments has grown over the last decades, many open questions remain in our picture of how the interplay of these processes shapes the galaxy population in such environments. A few of such issues that are relevant to this thesis are discussed in the following section.

1.4.1 Some recent highlights of the field

In the local Universe, we can reproduce the assembly of galaxies in such a system with simplified galaxy evolution models (e.g., Peng et al., 2010, 2012; Wetzel et al., 2012), although a clear understanding of the processes is yet to be uncovered. Moreover, at higher redshifts ($z > 1$), these theories fail to explain some more recent observations. For example, from studying a set of 11 massive clusters at $1 < z < 1.5$ from the Gemini Observations of Galaxies in Rich Early Environments (GOGREEN) project (Balogh et al., 2017, 2021), van der Burg et al. (2020) found that the stellar mass function (SMF) of quenched galaxies has almost the same shape as in the average field environment at the same redshift. The existing galaxy quenching models based on the observations of the local Universe, such as the model from Peng et al. (2010) would predict them to look different. This is because the SMF of quenched galaxies in clusters is shaped by both self- (independent from the environment) and environment-dependent quenching processes, whereas field galaxies are only self-quenched. As long as there is any excess environment-induced quenching—such as in the GOGREEN clusters—the shapes of quenched SMFs of cluster and field galaxies should not look the same. In a different study, Webb et al. (2020) found that the mean stellar ages of these quenched massive galaxies from the GOGREEN clusters are about $0.31^{+0.51}_{-0.33}$ Gyr older than field galaxies at the same redshift at the stellar mass range 10^{10} – $10^{11.8}\mathrm{M}_{\odot}$, with an inferred quenching epoch at $z > 3$. If environmental quenching were significant for these massive cluster galaxies, one would instead expect them to have been quenched later than the field, and therefore have younger stellar populations, contrary to what is observed. Also, this happened in the proto-cluster era, when the ICM was still forming and unlikely to induce efficient ram-pressure stripping. Although some studies found evidence of ram-pressure stripping out to $z = 2$, whether it was strong enough to induce environmental quenching is still not resolved (for more discussion on this, see e.g. Boselli et al., 2022). These recent findings posed a new question: were galaxies

in field and dense environments fundamentally different in some of their aspects when clusters formed, or are they similar objects in different distributions as it seems based on observations in the local Universe? Galaxy evolution in high-redshift clusters and protoclusters, as well as cluster formation and growth in the protocluster era, are areas where we have many unanswered questions, and many future programs are being designed to investigate these.

Another recent area of focus in galaxy cluster study is the diffuse stellar halo around the central galaxies in groups and clusters, also known as the intragroup or intracluster light (IGL/ICL, for recent reviews, see e.g. Mihos, 2015; Montes, 2022)[3]. The ICL is essentially a fossil record of the galaxy interactions during the assembly of large-scale structures. Besides the galaxies in groups and clusters, ICL is generally considered as a separate stellar component of the host systems because it extends out to several hundreds of kilo-parsecs from the host centres and can envelop multiple galaxies in the host system. The radial extent of ICL around central galaxies in groups and clusters and the contribution of the ICL in the total light from these systems can provide important constraints for cosmic structure formation and assembly of giant elliptical galaxies. Due to its diffuse nature, the study of ICL falls into the low-surface brightness ($\mu \geq 27$ mag/arcsec^2) regime, which is one of the last remaining frontiers of observational optical astronomy. With the availability of deep multi-band photometry, there have been increasing efforts to study the ICL in individual clusters (e.g. Mihos et al., 2005; Montes and Trujillo, 2014, 2018; Jiménez-Teja et al., 2018; DeMaio et al., 2018, 2020; Montes et al., 2021; Martínez-Lombilla et al., 2023; Ragusa et al., 2023). Another way to account for the low signal-to-noise ratio in ICL analysis is to stack a large sample of groups/clusters from large surveys (e.g. Zibetti et al., 2005; Zhang et al., 2019).

The origin and growth of the ICL have been connected to multiple formation scenarios, including galaxy mergers (Murante et al., 2007), tidal stripping (Gallagher and Ostriker, 1972), galaxy disruption (Guo et al., 2011), and in-situ star formation in the ICM (Puchwein et al., 2010; Tonnesen and Bryan, 2012). A detailed discussion on the origin and growth of the ICL can be found in, e.g., Mihos et al. 2017 and Contini 2021. Moreover, the mass distribution of ICL has been observed to follow the global DM distribution, both in observations (e.g. Montes and Trujillo, 2019) and simulations (e.g. Alonso Asensio et al., 2020), making ICL a potential luminous tracer of the host DM halo mass distribution. To improve our understanding of the

[3]For ease of referring, I will use ICL to generally refer to this component in both groups and clusters.

growth of ICL, group-mass haloes provide an excellent link between galaxy and cluster haloes. Another interesting question is the formation timescale of ICL. Some recent studies have found ICL at $z > 1$ clusters and protoclusters, providing new insights about structure formation at such early epochs (e.g. Joo and Jee, 2023; Werner et al., 2023). One common finding from these works is that preprocessed free-floating stars from accreted haloes contributed more to the ICL than gradually stripped stars from orbiting satellite galaxies at $z > 1$, supporting the scenario that the dominant ICL production occurs concurrently with the growth of the central galaxies in high-redshift clusters. Despite the recent advancements in the study of ICL, there is much to be discovered about what we can learn from ICL about galaxy assembly and hierarchical structure formation, including the contribution of the stars in IGL/ICL to the total baryonic mass of the host systems, whether they can actually be used as a luminous tracer of the cluster halo, which processes are the dominant contributor to the ICL at different redshifts, and what can these processes imply about the formation history of galaxy clusters and their central galaxies.

State-of-the-art telescopes (e.g., JWST) and future surveys (e.g., *Euclid*, LSST of the Rubin Observatory) are going to provide deeper photometric and spectroscopic data from large areas in the sky, which will enable us to push boundaries in high-redshift and low-surface-brightness observations of galaxy groups and clusters. One major contribution from these next-generation wide surveys will be increasing the sample size of available galaxy groups and clusters by many times compared to currently available data. A larger sample size will improve the precision of our measurements and, therefore, enable more confident conclusions from the studies. Wide surveys in the infrared bands will help us study the high-redshift Universe in greater detail, enabling the development of a more informed timeline of cosmic events. Deeper photometric data will improve the LSB measurements, including IGL/ICL, and a large sample with deep data will enable us to perform statistical analysis of these components. All of these will provide better empirical constraints on galaxy and large-scale structure formation. However, to maximise the utility of these improved observations, it is crucial to develop improved tools to test galaxy formation theories against the observations, one of which is cosmological hydrodynamic simulations.

1.5 Cosmological Hydrodynamic simulations

Explaining the rich diversity of the galaxy population and characteristics from modern astronomical surveys across different environments over cosmic time with a compre-

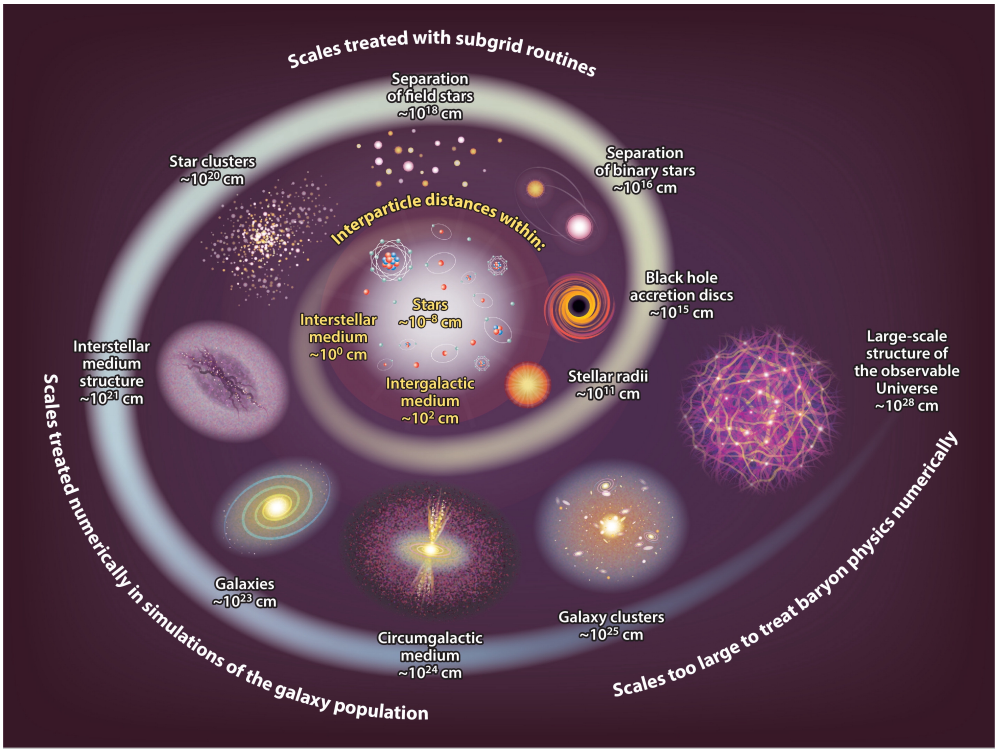

Figure 1.2: An illustration of the large dynamic range of length scales of processes that are relevant to galaxy formation and how they are modelled in hydrodynamic simulations. Figure from Crain and van de Voort (2023).

hensive theory of galaxy formation is a complex challenge due to its intrinsic multi-scale and multi-physics nature. However, the growth of DM haloes from cosmological initial conditions and the formation of galaxies within them is possible to model using numerical simulations. In particular, hydrodynamic simulations of representative cosmological volumes have been the most successful tool so far to involve DM and ordinary (or baryonic) matter that comprises gas, dust, and stars in the context of galaxy formation. For recent reviews on cosmological simulations and galaxy formation models, see e.g., Vogelsberger et al. (2020) and Crain and van de Voort (2023). Here, I am providing a short introduction on what are the building blocks of such simulations, what kinds of data products we obtain from these, and the performance of such simulations in explaining observed galaxy properties.

The framework of galaxy formation models is based on the cosmological model of the Universe (an overview of the building blocks of cosmological simulation is provided in Fig 1.3). In the ΛCDM cosmology, the DM distribution provides the skeleton of the large-scale structure formation. To capture structure formation in a cosmological volume—at least of the order of $(100\ \mathrm{Mpc})^3$—to star formation within galaxies from cold molecular gas, such simulations need to cover a very wide range of dynamic scales. However, it is computationally impossible to build these models entirely from first principles for the extremely large range of scale that needs to be covered. The only solution for this problem is to use subgrid physics models for processes that originate on smaller scales, including gas cooling, star formation, and the energy and momentum injection caused by supermassive black holes and massive stars. Figure 1.2 (Crain and van de Voort, 2023) illustrates the scale ranges of different physical processes and how they are tackled in such simulations.

Stars form due to the radiative cooling and gravity-induced condensation of gas. therefore, hydrodynamic simulation codes must allow for such a transformation from gas into stars. The cooling of gas particles is usually modelled by utilising pre-calculated and tabulated heating and cooling rates as a function of the redshift, temperature, density, and metallicity of the gas distribution (e.g. Wiersma et al., 2009; Ploeckinger and Schaye, 2020). The conversion of cold and dense gas into stars is applied as a stochastic process when the gas density exceeds a critical value (e.g. Schaye, 2004; Schaye and Dalla Vecchia, 2008). As the stellar population evolves, the associated stellar feedback to the galaxies and their CGM is modelled to replicate stellar winds and supernovae (e.g. Wiersma et al., 2009). In general, galaxy-scale stellar feedback is modelled by heating up the stellar surrounding either thermally or kinetically, therefore dispersing and ionizing the star-forming gas around stars. Additionally, stellar feedback enriches the chemical composition of the interstellar medium (ISM) by mixing-in metals that were synthesized in the stars. In the low-mass ($\leq 10^{10}\mathrm{M}_\odot$) galaxy population, stellar feedback is observed to regulate the star formation (by preventing extreme starburst at high redshift), and therefore, getting the stellar feedback right is necessary to reproduce the low-mass end of the observed galaxy stellar mass function (e.g. Puchwein and Springel, 2013).

Almost all galaxies with stellar mass $\geq 10^{10}\mathrm{M}_\odot$ are observed to have a central supermassive black hole (SMBH). In hydrodynamic simulations, the seeds of such black

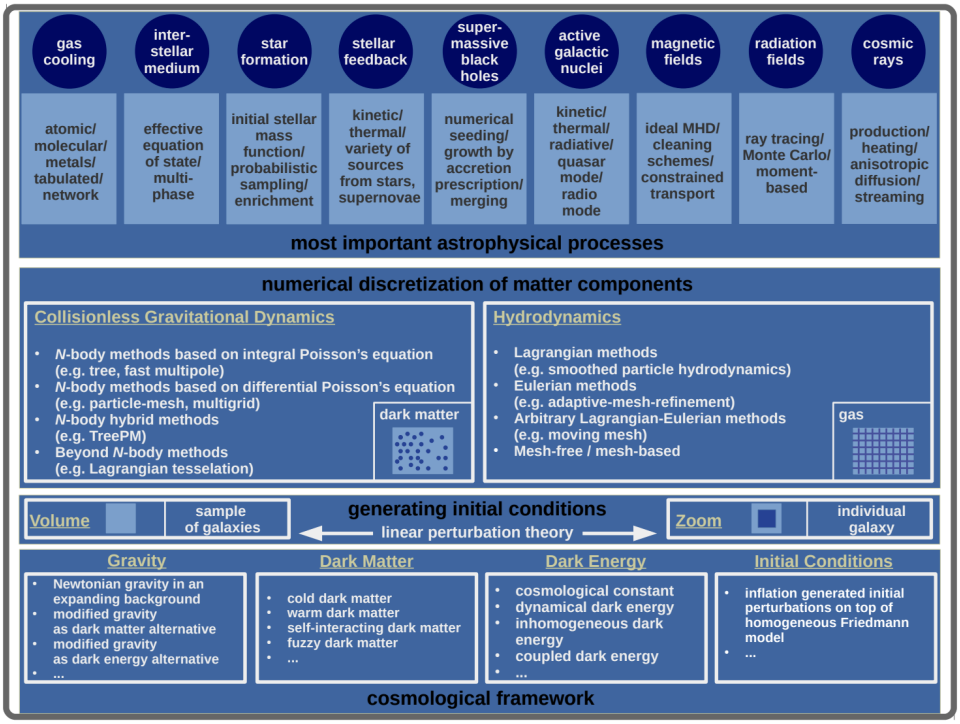

Figure 1.3: An overview of the primary ingredients of cosmological simulations. The ingredients are shown in a logical order from the bottom to the top of the figure, such that, the process starts from a given cosmological framework and follows from generating initial conditions to including the subgrid physics models. This is figure 2 from Vogelsberger et al. (2020).

holes are added following some empirical prescription because the formation mechanism of these SMBHs is still poorly understood. These black holes then grow via gas accretion and merging with other black holes (e.g. Bahé et al., 2022). During this accretion, the active galactic nucleus generates electromagnetic radiation, relativistic jets, and non-relativistic outflows, which are collectively referred to as the AGN feedback. Although only a fraction (likely small and unconstrained) of the AGN feedback couples with the surrounding gas, it regulates the black hole growth and star formation in massive haloes ($M_h \geq 10^{12}\mathrm{M}_\odot$, e.g., Booth and Schaye 2009). The AGN feedback plays an important role in reproducing the high-mass end of the observed galaxy stellar mass function (e.g. Puchwein and Springel, 2013). However, all the existing AGN feedback models are still quite over-simplified and have different issues in the entropy profiles of the ICM gas (see e.g. Oppenheimer et al., 2021; Altamura et al., 2023).

Along with these fundamental processes for galaxy formation, the physics of interstellar medium and dust, cosmic rays, magnetic field, and radiative transfer are also implemented in some recent simulations or are in the process of being implemented to achieve a more detailed evolution of galaxies in the cosmological context. The subgrid parameters whose values are unknown are now usually calibrated to match some reference observed quantity in the local Universe, such as the stellar mass function or the stellar-to-halo-mass. However, the highly non-linear relations between the subgrid model parameters and the simulated galaxy characteristics imply that calibration on one matched observable does not necessarily translate to reproducing any non-calibrated observable. Therefore, the validity of simulations to predict realistic observables should be subjected to multi-level and carefully designed checks.

Due to the required compromise between the spatial resolution and size of the simulation region, standard high-resolution cosmological simulation box sizes are around $(100\ \mathrm{Mpc})^3$. This size is too small for a statistical sample of massive galaxy clusters, whereas large simulation boxes in the order of Gpc^3 volumes have a poor spatial resolution compared to what is necessary to study galaxy evolution within group and cluster mass haloes. A solution to this problem is the use of 'zoom-in simulation', where targets of interest (galaxies or clusters) are selected from a large-volume low-resolution simulation box. Then these smaller volumes are re-run with much higher resolution while the boundary conditions are taken from the large low-resolution box.

After running such simulations, the primary outputs from the simulations are usually multi-level particle data at a set of redshift stamps or 'snapshots'. Then the particle data goes through different post-processing to be ready to use for validity checks and comparison with observation. One fundamental step of such post-processing is

using a halo-finder code, e.g. SUBFIND (Springel et al., 2001; Dolag et al., 2009) or VELOCIraptor (Elahi, 2013; Elahi et al., 2019) to identify gravitationally bound haloes and self-bound subhaloes within them. Usually, some information is directly recoverable from simulation output, including particle ID, mass, and instantaneous velocities of the star, gas, DM, and black hole particles at each redshift stamp. Using this information and outputs from the halo-finder, high-level catalogues of galaxies and systems of galaxies (groups and clusters) can be produced, which include different properties such as their stellar and halo mass at different apertures, stellar age, star-formation rate, half mass radius, metallicity. Producing even higher-level data, such as multi-band photometry and spectra, requires forward modelling and is not always a part of a standard simulation data release. The key takeaway from understanding the data produced from simulations is that any property of an object in a simulation output catalogue can have many definitions, e.g., the stellar mass of a galaxy can be measured in different apertures. Also, as the SNR in simulation output is practically infinite, this is not directly comparable to any observational data without testing the effect of different types of noises and uncertainties that affect both simulated and observational data.

1.5.1 Current state of the field

Over the last decade, the capacity of hydrodynamic simulations to reproduce different properties of observed galaxy populations has significantly improved. A successful galaxy formation model should be ideally able to reproduce the fundamental properties of galaxies, such as their intrinsic luminosities, stellar and halo masses, sizes (half-mass or half-light radii), morphologies, metal abundances, stellar age, star formation rate, and gas content. While there is still scope for improvement, multiple flagship-scale simulations have been studied in detail and have been successful to various degrees in reproducing several observables of the galaxy population. These simulations include Illustris (Genel et al., 2014; Vogelsberger et al., 2014), Magneticum (Hirschmann et al., 2014), EAGLE (Schaye et al., 2015; McAlpine et al., 2016), Romulus (Tremmel et al., 2017), Horizon-AGN (Dubois et al., 2014; Kaviraj et al., 2017), IllustrisTNG (Nelson et al., 2018; Pillepich et al., 2018), and SIMBA (Davé et al., 2019). Figure 1.4 provides a visual representation of some of these recent simulations. The properties of the observed galaxy population that these simulations have been broadly successful in reproducing include the global stellar mass functions at $0 < z < 7$ (Furlong et al.,

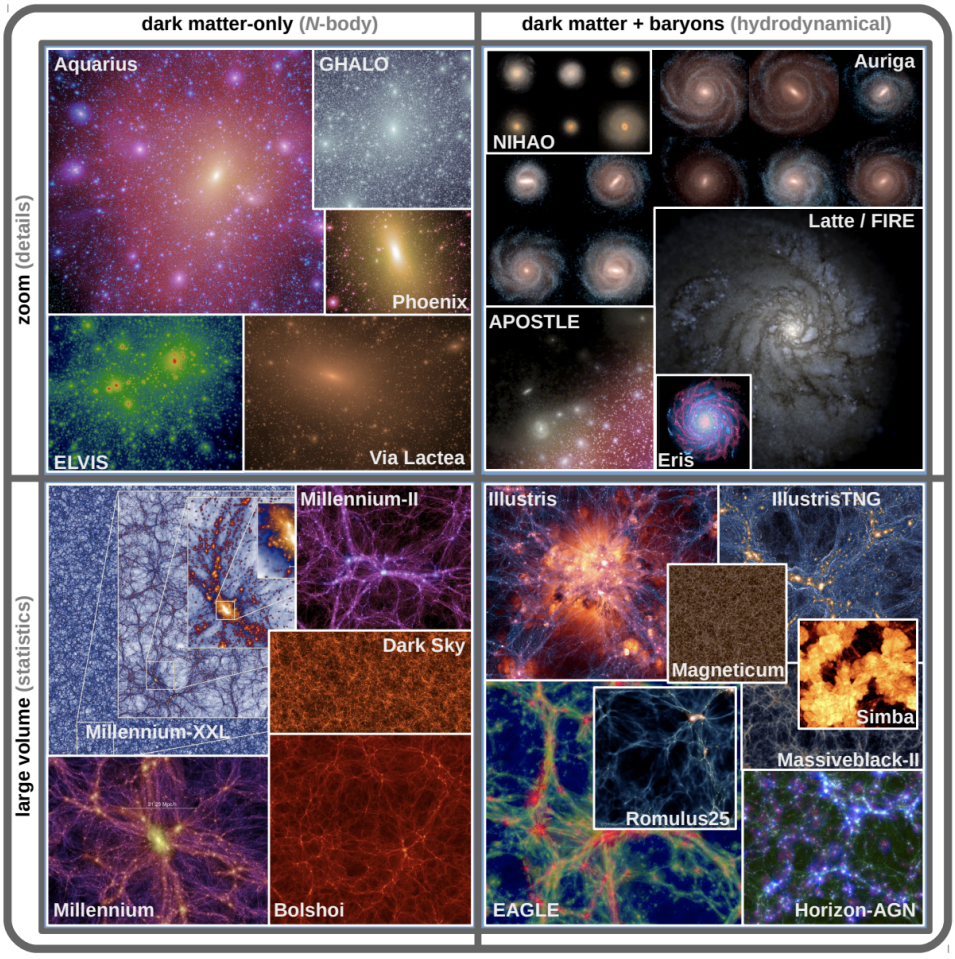

Figure 1.4: Visual representations from some recent simulations to illustrate their performance. The figure is divided in terms of their inclusion of dark matter only (N-body) and dark + baryonic matter from left to right; and between large volume and zoom simulations from bottom to top. Figure 1 from Vogelsberger et al. (2020).

2015; Pillepich et al., 2018; Davé et al., 2019), galaxy clustering (Artale et al., 2017; Crain et al., 2017; Springel et al., 2018), galaxy colours (Trayford et al., 2015, 2017; Nelson et al., 2018), and different scaling relations including the mass-metallicity relation (e.g., Lagos et al. 2016; Davé et al. 2019; Torrey et al. 2019, the Tully-Fisher relation (e.g., Vogelsberger et al. 2014; Ferrero et al. 2017; Sales et al. 2017, and the star-forming main sequence. For a detailed comparison of these simulations in reproducing different observables, see recent reviews by Vogelsberger et al. (2020) and Crain and van de Voort (2023).

While a lot of these aforementioned properties are broadly reproduced in the simulations, on a quantitative level, there is ample room for improvement. One general limitation in all the current simulations is that the subgrid models for supernovae and AGN feedback strongly affect their prediction of different galaxy properties. Given the complexity and our incomplete understanding of these feedback processes, these are usually modelled with simplified subgrid prescriptions, and their performance in different state-of-the-art simulations has degeneracy. These simulations also have a limited capacity to reproduce the internal and vertical structures of galaxies. Moreover, certain physical processes that can affect galaxy evolution significantly in different regimes are yet to be implemented, including the effects of magnetic fields (only implemented in IllustrisTNG so far), cosmic rays, thermal conduction, UVB radiation field (especially affecting galaxy evolution at the epoch of re-ionization), multi-phase CGM (cool gas and interface between cool and hot CGM), and local variation of radiation fields. For the next-generation simulations, a lot of effort is focused on incorporating these missing physics models with finer details, pushing the resolution limits, employing machine learning and AI to calibrate the subgrid models more efficiently, and probing larger volumes to be applicable to compare with high-redshift data from JWST and large-volume galaxy surveys like Euclid and LSST.

In this thesis, I have used the $(50\ \mathrm{Mpc})^3$ volume run of the EAGLE simulation and the Hydrangea simulations (Bahé et al., 2017), a suite of 24 high-resolution zoom-in simulations of massive (up to $> 10^{15}\mathrm{M}_\odot$ at $z = 0$) galaxy clusters and their large-scale surroundings. The Hydrangea simulations were run using the same variation of the EAGLE code that was used for the EAGLE volume used here. So far, the Hydrangea simulations, which are also part of the 30 cluster-EAGLE simulations, are the largest sample of massive galaxy clusters with comparable high resolution, and they have been broadly successful in reproducing observed properties of galaxies in dense environments (Bahé et al., 2017; Barnes et al., 2017). Although the above-mentioned limitations of current simulations are present in both EAGLE and Hydrangea, these

are the best simulation pairs to study the impact of different environments on galaxy evolution. However, one point of concern is that the availability of simulation data does not necessarily imply their utility or validity to compare to observations and draw useful insights from this. Especially because these simulations, like all state-of-the-art simulations, were calibrated with certain observables at $z = 0$, their performance in reproducing higher-redshift observations must be tested carefully before drawing any conclusions. Also, due to the coarse treatment of the subgrid physics models, just because the simulations reproduce an observable, it does not imply that it could replicate the physical processes leading to the observable as it occurs in the real Universe. That is why careful comparison of the simulated data to observational data is crucial along with the development of such sophisticated simulations.

1.6 Detailed comparison between simulations and observations

In recent years, multiple works (e.g. Bahé et al., 2021; Font et al., 2022) have shown that while comparing simulations to observations, subtle details in the analysis methods can strongly influence the conclusion of the analysis. A more reliable methodology requires an understanding of the nature of the data from both simulations and observations, and of the biases that may be included from either side of the data processing pipeline. A carefully designed comparison serves two major purposes: firstly, it enables us to test and improve the credibility of the simulations and their physics models. Secondly, it enables us to explain the physical processes that result in the observed properties of galaxies.

To illustrate the need for detail-oriented comparison, an example could be the comparison of mass and light between simulations and observations. In observations of galaxies, our primary data is the photons we get from these systems. To estimate the mass of a galaxy from the light, we need to make many assumptions about which environments those photons passed through, how much of that light was absorbed in cold gas clouds inside and outside of the Milky Way galaxy, what is the typical luminosity of different types of stars, what are the initial mass function and star-formation rate in the galaxy, and which distribution of age, metallicity, and type of stars can contribute to the combined spectral energy distribution and multi-band luminosity of the observed galaxy. All of these assumptions are physically motivated from detailed studies of each of these phenomena. However, even physically motivated

assumptions are subjected to the limitation of available information from the data and limitations in our understanding of these processes. On the other hand, in simulations, getting the mass is fairly straightforward because we have information about the mass of each type of particle that are gravitationally bound in a system. However, whether the mass inferred from observations is the same definition of mass we calculate by adding the particle masses does not have a simple answer due to the difference in the processes they are measured from and the potential biases and uncertainties they have. One may wonder, then, why we do not convert the mass from simulations to the light we may obtain from them at a comparable distance and environment to the observations. It is possible and is being done in multiple recent works. However, this process is again subject to all the above-mentioned assumptions in the physical processes that we have in converting light to mass. Explaining this complex process is not to discourage such attempts but, on the contrary, to demonstrate that we must take as detailed steps as possible to make sure that the data from simulations and observations are as similar as possible to make any conclusion and insight derived from such comparisons useful.

Another important point of concern is that the simulations are calibrated to match properties in the local Universe. It is quite possible that the good performance of all of the current state-of-the-art simulations in reproducing different properties at $z = 0$ is somewhat influenced by the calibration, and their data at higher redshifts are only numerical relics and unsuitable to be used to test galaxy formation theories at relevant epochs. Already existing tests of some properties at higher redshifts from some simulations show promising performance. However, we need to test their validity in much more detail at higher redshifts to confirm their credibility or lack thereof at such redshifts.

To summarise, state-of-the-art cosmological simulations can now reproduce fundamental properties of observed galaxies (e.g., the total stellar mass, stellar mass function) with unprecedented accuracy both in the local Universe and over more than half of the age of the Universe. Moreover, the next generation of simulations with improved physics models, better resolution, and larger cosmological volumes are underway. At the same time, state-of-the-art observational facilities (and next-generation survey instruments) are now (and getting ready for) producing deeper and higher-resolution data. This tremendous progress in both theory and observational sides implies that the measurement error will be low enough that systematics in the methodology will be the limiting factor in the conclusions we draw from comparing them. Therefore, now is the perfect time to build systems that improve the quality of insights we can

obtain from such comparisons.

1.7 Thesis outline

In this thesis, we compare different properties of galaxies in groups and clusters from the Hydrangea and EAGLE simulations to recent observations across $0 < z < 3.5$. We design these comparisons such that we start with broad properties, like the total stellar mass in groups and clusters, before we move on to more detailed properties, such as the spatial distribution of mass in galaxies within the clusters, the intragroup and intracluster light, and processes that quench massive galaxies at high redshifts ($z > 1$). We also prepare mock observations from simulations that are matched with deep imaging surveys such as the Kilo-Degree Survey (KiDS, De Jong et al., 2013; Kuijken et al., 2019) before we compare observables between them. By comparing a wide range of galaxy and host system properties from cosmological hydrodynamic simulations to recent high-quality observations of galaxy groups and clusters, we test the validity of the simulations at higher redshifts, and demonstrate how such comparisons can motivate new tests and provide novel insights about galaxy evolution in dense environments.

In **Chapter 2**, we compared different properties of massive galaxy clusters ($M \geq 10^{14}\mathrm{M}_{\odot}$ at z=0) from the Hydrangea simulation suite to recently observed data from different galaxy cluster studies out to z=2. We first confirmed that the total stellar mass in the Hydrangea clusters at a fixed halo mass and redshift is comparable to observed clusters in our tested redshift range. In a following test, we produced synthetic observations of galaxy clusters from Hydrangea and confirmed that the galaxy stellar mass from simulations within 30 kiloparsecs is a reasonable estimate of their observable stellar mass. Checking the dependency of the galaxy stellar mass function (SMF) on cluster halo mass showed that, at a fixed redshift, the normalization of cluster SMF strongly correlates with the cluster halo mass. Consequently, with a matched halo mass distribution to an observed cluster sample, the simulations predicted the observed SMF well out to z=1.5, which was not evident before matching the halo masses. We then studied the density profiles of clusters at $0 < z < 2$, for both the DM and stellar masses. By comparing the concentration parameters from the fitted Navarro-Frenk-White (NFW) profiles to previous observation-based works, this work verified that the opposite evolution of the DM and stellar concentration in clusters over cosmic time is not in tension with the ΛCDM cosmology. These findings illustrate how paying attention to detail changes our conclusions in such comparisons.

In **Chapter 3**, we studied a subtle but significant observable property of clusters, the intragroup or intracluster light (IGL or ICL). There has been an increasing effort in recent years to understand the origin and distribution of this diffuse light in systems of different halo masses. However, there was a gap between the simulation-based works (tracing mass distribution), and observation-based works (tracing light distribution). To bridge this gap, we created multi-band synthetic observations of ∼500 galaxy groups and clusters from the Hydrangea simulations, and matched the systematics to the Kilo Degree Survey (KiDS) and Galaxy and Mass Assembly (GAMA) survey data to which we compared the analysis from the work in the following chapter. This work resolved one crucial problem in the stacking analysis of IGL - selecting the best centre of the group on which that stacking will be performed. We found that selecting the galaxy with the highest associated halo mass as the central group galaxy, instead of the brightest galaxy, gives the best estimation. Also, instead of stacking groups from a large halo mass range, binning them by central galaxy luminosity provided a better understanding of the IGL growth. Finally, studying the colour, mass, and metallicity profiles of the diffuse light in groups and clusters from Hydrangea indicated that in low-mass groups, the IGL is predominantly accumulated by major mergers, whereas in more massive clusters, the main channel of ICL growth is via accretion of stripped stars from satellites.

The foundations of **Chapter 4** were based on the insights from **Chapter 3**, where we measured the IGL fraction in galaxy groups from KiDS+GAMA survey data and compared these results to the findings from **Chapter 3**. The standard data-processing pipeline for large cosmological imaging surveys, such as KiDS, is optimised to detect small, faint galaxies and measure their positions, fluxes, and shapes but not to retain the diffuse light in IGL/ICL at extended radii. We developed a special pipeline to re-process the KiDS survey images to optimise their use for diffuse light analysis and obtained the first robust measurement of IGL from a large group sample (850×5 exposures) down to 31-32 mag/arcsec^2. We found that systematics in the imaging data can affect IGL measurements even with our special-purpose pipeline. However, with a large sample and carefully optimised analysis, we can place well-constrained upper and lower limits on the IGL fraction for our group ensemble across redshifts $0.09 \leq z \leq 0.27$ and halo-masses $12.5 \leq \log_{10}[M_{200}/\mathrm{M}_{\odot}] \leq 14.0$. Our measurements are compatible with existing measurements of IGL in individual systems at similar redshift and halo mass ranges, however, with better constraints in the range of IGL fraction for the advantage of stacking. This work shed light on the potential performance of statistical analysis of diffuse light in large samples of groups and clusters from next-generation

observational programs like *Euclid* (Troja et al., 2023) and LSST (Ivezić et al., 2019). Moreover, the developed pipeline can be applied to the data from these surveys with minimum modification when that data is available.

In **Chapter 5**, we explored the potential of an environment-dependent halo mass function as a driver for the early quenching of $z \geq 1.5$ cluster galaxies. Recent works have found that a fraction of the intermediate-mass galaxies ($10^{10}\mathrm{M}_{\odot} \leq M_{*} \leq 10^{11}\mathrm{M}_{\odot}$) in galaxy clusters are already quenched by $z \sim 1.5$. This is very puzzling as the clusters were not yet completely formed by that time and therefore, the known quenching mechanisms that work in clusters could not be strong enough. Moreover, these massive quenched galaxies have stellar populations of similar age in both clusters and the field. This suggests that the dominant quenching mechanism for massive galaxies is similar in both environments. In this work, we used data from the Hydrangea and EAGLE simulations to test whether this early quenching of massive galaxies in $z \geq 1.5$ clusters results from fundamental differences in their halo properties compared to the field. We found that at $10^{10} \leq M_{\star}/\,\mathrm{M}_{\odot} \leq 10^{11}$, quenched fractions in the redshift range $1.5 < z < 3.5$ are consistently higher for galaxies with higher peak maximum circular velocity of the dark matter halo ($v_{\mathrm{max,peak}}$). We also found that the distribution of $v_{\mathrm{max,peak}}$ is strongly biased towards higher values for cluster satellites than the field centrals. Due to this difference in the halo properties of cluster and field galaxies, secular processes alone may account for (most of) the environmental excess of massive quenched galaxies in high-redshift (proto) clusters. Taken at face value, our results challenge a fundamental assumption of popular quenching models, namely that clusters are assembled from an unbiased subset of infalling field galaxies. If confirmed, this would imply that such models must necessarily fail at high redshift, as indicated by recent observations. This work identifies a new way to examine the effects of environment and internal processes in quenching massive galaxies at high redshift.

Along with the above chapters, I have worked as a part of the low-surface-brightness working group of the Legacy Survey of Space and Time (LSST) collaboration of the Vera Rubin Telescope, where we predicted the fraction and other measurements of the ICL in galaxy clusters (halo mass$\sim 10^{14}\mathrm{M}_{\odot}$) by applying different observational methods in LSST-like mock observations. These mock observations were created from multiple cosmological hydrodynamic simulations - Hydrangea, IllustrisTNG, Horizon-AGN, and Magneticum. These predictions from matched synthetic observations will be crucial to optimize the utility of the large volume of exceptional data from the upcoming LSST survey. This collective effort also shed light on whether simulators

and observers measure the same component while studying ICL and possible reasons behind any match or lack thereof in these approaches. The manuscript from this work is currently under review in the journal 'Monthly Notices of the Royal Astronomical Society'.

References

Allen, S. W., Evrard, A. E., and Mantz, A. B., 2011, ARA&A, 49, 409
Alonso Asensio, I., Dalla Vecchia, C., Bahé, Y. M., et al., 2020, MNRAS, 494, 1859
Alpher, R. A., Bethe, H., and Gamow, G., 1948, Physical Review, 73, 803
Altamura, E., Kay, S. T., Bower, R. G., et al., 2023, MNRAS, 520, 3164
Artale, M. C., Pedrosa, S. E., Trayford, J. W., et al., 2017, MNRAS, 470, 1771
Bahé, Y. M., Schaye, J., Schaller, M., et al., 2021, arXiv e-prints, arXiv:2109.01489
Bahé, Y. M., Schaye, J., Schaller, M., et al., 2022, MNRAS, 516, 167
Bahé, Y. M. et al., 2017, MNRAS, 470, 4186
Balogh, M. L., Gilbank, D. G., Muzzin, A., et al., 2017, MNRAS, 470, 4168
Balogh, M. L., Navarro, J. F., and Morris, S. L., 2000, ApJ, 540, 113
Balogh, M. L., van der Burg, R. F. J., Muzzin, A., et al., 2021, MNRAS, 500, 358
Balogh, M., Morris, S., and Yee, H., 1999, ApJ, 527, 54,
Barnes, D. J., Kay, S. T., Bahé, Y. M., et al., 2017, MNRAS, 471, 1088
Bekki, K. and Couch, W. J., 2011, MNRAS, 415, 1783
Bennett, C. L., Banday, A. J., Gorski, K. M., et al., 1996, ApJL, 464, L1
Bennett, C. L., Halpern, M., Hinshaw, G., et al., 2003, ApJS, 148, 1
Blanton, M. R., Eisenstein, D., Hogg, D. W., et al., 2005, ApJ, 629, 143
Boselli, A., Fossati, M., and Sun, M., 2022, A&AR, 30, 3
Boselli, A. and Gavazzi, G., 2006, Publications of the Astronomical Society of the Pacific, 118, 517
Brown, T., Catinella, B., Cortese, L., et al., 2017, MNRAS, 466, 1275
Byrd, G. and Valtonen, M., 1990, ApJ, 350, 89
Colless, M., Dalton, G., Maddox, S., et al., 2001, MNRAS, 328, 1039
Contini, E., 2021, Galaxies, 9, 60
Crain, R. A., Bahé, Y. M., Lagos, C. d. P., et al., 2017, MNRAS, 464, 4204
Crain, R. A. and van de Voort, F., 2023, Annual Review of Astronomy and Astrophysics, 61, 473
Davé, R., Anglés-Alcázar, D., Narayanan, D., et al., 2019, MNRAS, 486, 2827
Delos, M. S. and White, S. D. M., 2023, MNRAS, 518, 3509
DeMaio, T., Gonzalez, A. H., Zabludoff, A., et al., 2018, MNRAS, 474, 3009
DeMaio, T., Gonzalez, A. H., Zabludoff, A., et al., 2020, MNRAS, 491, 3751
Dicke, R. H., Peebles, P. J. E., Roll, P. G., et al., 1965, ApJ, 142, 414
Dolag, K., Borgani, S., Murante, G., et al., 2009, MNRAS, 399, 497
Dressler, A., 1980, ApJ, 236, 351
Dubois, Y., Pichon, C., Welker, C., et al., 2014, MNRAS, 444, 1453
Einasto, J., 2013, Brazilian Journal of Physics, 43, 369
Elahi, P. J. (June 2013). *STF: Structure Finder*. Astrophysics Source Code Library, record ascl:1306.009. ascl: 1306.009.
Elahi, P. J., Poulton, R., and Canas, R. (Nov. 2019). *VELOCIraptor-STF: Six-dimensional Friends-of-Friends phase space halo finder*. Astrophysics Source Code Library, record ascl:1911.020. ascl: 1911.020.
Fabello, S., Kauffmann, G., Catinella, B., et al., 2012, MNRAS, 427, 2841
Ferrero, I., Navarro, J. F., Abadi, M. G., et al., 2017, MNRAS, 464, 4736
Font, A. S., McCarthy, I. G., Belokurov, V., et al., 2022, MNRAS, 511, 1544
Friedman, A., 1922, Zeitschrift für Physik, 10, 377
Furlong, M., Bower, R. G., Theuns, T., et al., 2015, MNRAS, 450, 4486

1.7. REFERENCES

Gallagher John S., I. and Ostriker, J. P., 1972, Astronomical Journal, 77, 288
Genel, S., Vogelsberger, M., Springel, V., et al., 2014, MNRAS, 445, 175
Giovanelli, R and Haynes, M., 1985, ApJ, 292, 404
Gunn, J. E. and Gott J. Richard, I., 1972, ApJ, 176, 1
Guo, Q., White, S., Boylan-Kolchin, M., et al., 2011, MNRAS, 413, 101
Guth, A. H., 1981, Physical Review D, 23, 347
Hess, K. M. and Wilcots, E. M., 2013, Astronomical Journal, 146, 124
Hirschmann, M., Dolag, K., Saro, A., et al., 2014, MNRAS, 442, 2304
Hubble, E., 1929, Proceedings of the National Academy of Science, 15, 168
Ivezić, Ž., Kahn, S. M., Tyson, J. A., et al., 2019, ApJ, 873, 111
Jiménez-Teja, Y., Dupke, R., Benítez, N., et al., 2018, ApJ, 857, 79
De Jong, J. T. A., Kuijken, K., Applegate, D., et al., 2013, The Messenger, 154, 44
Joo, H. and Jee, M. J., 2023, Nat., 613, 37
Kauffmann, G., White, S. D. M., Heckman, T. M., et al., 2004, MNRAS, 353, 713
Kaviraj, S., Laigle, C., Kimm, T., et al., 2017, MNRAS, 467, 4739
Kravtsov, A. V. and Borgani, S., 2012, ARA&A, 50, 353
Kuijken, K., Heymans, C., Dvornik, A., et al., 2019, A&A, 625, A2
Lagos, C. d. P., Theuns, T., Schaye, J., et al., 2016, MNRAS, 459, 2632
Larson, R. B., Tinsley, B. M., and Caldwell, C. N., 1980, ApJ, 237, 692
Lemaître, G. H. (Jan. 1927). "The Gravitational Field in a Fluid Sphere of Uniform Invariant Density, According to the Theory of Relativity." PhD thesis. Massachusetts Institute of Technology.
Martínez-Lombilla, C., Brough, S., Montes, M., et al., 2023, MNRAS, 518, 1195
McAlpine, S., Helly, J. C., Schaller, M., et al., 2016, Astronomy and Computing, 15, 72
McCarthy, I. G., Frenk, C. S., Font, A. S., et al., 2008, MNRAS, 383, 593
Merritt, D., 1983, ApJ, 264, 24
Mihos, C. (Aug. 2015). "Intragroup and Intracluster Light". *IAU General Assembly*. Vol. 29, 2247903, 2247903.
Mihos, J. C., Harding, P., Feldmeier, J., et al., 2005, ApJL, 631, L41
Mihos, J. C., Harding, P., Feldmeier, J. J., et al., 2017, ApJ, 834, 16
Mo, H., van den Bosch, F. C., and White, S. (2010). *Galaxy Formation and Evolution*.
Montes, M., 2022, Nature Astronomy, 6, 308
Montes, M., Brough, S., Owers, M. S., et al., 2021, ApJ, 910, 45
Montes, M. and Trujillo, I., 2014, ApJ, 794, 137
Montes, M. and Trujillo, I., 2018, MNRAS, 474, 917
Montes, M. and Trujillo, I., 2019, MNRAS, 482, 2838
Moore, B., Katz, N., Lake, G., et al., 1996, Nat., 379, 613
Moore, B., Lake, G., and Katz, N., 1998, ApJ, 495, 139
Murante, G., Giovalli, M., Gerhard, O., et al., 2007, MNRAS, 377, 2
Nelson, D., Pillepich, A., Springel, V., et al., 2018, MNRAS, 475, 624
Odekon, M. C., Koopmann, R. A., Haynes, M. P., et al., 2016, ApJ, 824, 110
Oort, J. H., 1932, Bulletin Astronomical Institute of the Netherlands, 6, 249
Oppenheimer, B. D., Babul, A., Bahé, Y., et al., 2021, Universe, 7, 209
Peacock, J. A. (1999). *Cosmological Physics*.
Peebles, P. J. E. and Yu, J. T., 1970, ApJ, 162, 815
Peng, Y.-j., Lilly, S. J., Kovač, K., et al., 2010, ApJ, 721, 193
Peng, Y.-j., Lilly, S. J., Renzini, A., et al., 2012, ApJ, 757, 4
Peng, Y., Lilly, S. J., Kovač, K., et al., 2010, ApJ, 721, 193
Penzias, A. A. and Wilson, R. W., 1965, ApJ, 142, 419
Perlmutter, S., Aldering, G., Goldhaber, G., et al., 1999, ApJ, 517, 565
Pillepich, A., Nelson, D., Hernquist, L., et al., 2018, MNRAS, 475, 648
Planck Collaboration, Aghanim, N., Akrami, Y., et al., 2020, A&A, 641, A6
Planck Collaboration XVI, 2014, A&A, 571, A16
Ploeckinger, S. and Schaye, J., 2020, MNRAS, 497, 4857
Press, W. H. and Schechter, P., 1974, ApJ, 187, 425

Puchwein, E. and Springel, V., 2013, MNRAS, 428, 2966
Puchwein, E., Springel, V., Sijacki, D., et al., 2010, MNRAS, 406, 936
Ragusa, R., Iodice, E., Spavone, M., et al., 2023, A&A, 670, L20
Riess, A. G., Filippenko, A. V., Challis, P., et al., 1998, Astronomical Journal, 116, 1009
Rubin, V. C., Ford W. K., J., and Thonnard, N., 1980, ApJ, 238, 471
Rubin, V. C. and Ford W. Kent, J., 1970, ApJ, 159, 379
Sales, L. V., Navarro, J. F., Oman, K., et al., 2017, MNRAS, 464, 2419
Schaye, J., 2004, ApJ, 609, 667
Schaye, J., Crain, R. A., Bower, R. G., et al., 2015, MNRAS, 446, 521
Schaye, J. and Dalla Vecchia, C., 2008, MNRAS, 383, 1210
Slipher, V. M., 1917, The Observatory, 40, 304
Springel, V., Pakmor, R., Pillepich, A., et al., 2018, MNRAS, 475, 676
Springel, V., White, S. D. M., Jenkins, A., et al., 2005, Nat., 435, 629
Springel, V., White, S. D. M., Tormen, G., et al., 2001, MNRAS, 328, 726
Tonnesen, S. and Bryan, G. L., 2012, MNRAS, 422, 1609
Torrey, P., Vogelsberger, M., Marinacci, F., et al., 2019, MNRAS, 484, 5587
Trayford, J. W., Camps, P., Theuns, T., et al., 2017, MNRAS, 470, 771
Trayford, J. W., Theuns, T., Bower, R. G., et al., 2015, MNRAS, 452, 2879
Tremmel, M., Karcher, M., Governato, F., et al., 2017, MNRAS, 470, 1121
Trimble, V., 2012, The Observatory, 132, 33
Trimble, V., 1987, ARA&A, 25, 425
Trimble, V., 2013, arXiv e-prints, arXiv:1307.2289
Troja, A., Tutusaus, I., Sorce, J., et al. (June 2023). "Euclid in a nutshell". *41st International Conference on High Energy physics*, 94, 94. DOI: 10.48550/arXiv.2211.09668. arXiv: 2211.09668 [astro-ph.IM].
van der Burg, R. F. J., Rudnick, G., Balogh, M. L., et al., 2020, A&A, 638, A112
Vogelsberger, M., Genel, S., Springel, V., et al., 2014, MNRAS, 444, 1518
Vogelsberger, M., Marinacci, F., Torrey, P., et al., 2020, Nature Reviews Physics, 2, 42
Webb, K., Balogh, M. L., Leja, J., et al., 2020, MNRAS, 498, 5317
Weinmann, S. M., Kauffmann, G., von der Linden, A., et al., 2010, MNRAS, 406, 2249
Weinmann, S. M., Van Den Bosch, F. C., Yang, X., et al., 2006, MNRAS, 372, 1161
Werner, S. V., Hatch, N. A., Matharu, J., et al., 2023, MNRAS, 523, 91
Wetzel, A. R., Tinker, J. L., and Conroy, C., 2012, MNRAS, 424, 232
White, S. D. M. and Rees, M. J., 1978, MNRAS, 183, 341
White, S. D. M. and Frenk, C. S., 1991, ApJ, 379, 52
Wiersma, R. P. C., Schaye, J., Theuns, T., et al., 2009, MNRAS, 399, 574
Wiersma, R. P., Schaye, J., and Smith, B. D., 2009, MNRAS, 393, 99
Willman, B., Governato, F., Wadsley, J., et al., 2004, MNRAS, 355, 159
Woo, J., Dekel, A., Faber, S. M., et al., 2012, MNRAS, 428, 3306
York, D. G., Adelman, J., Anderson John E., J., et al., 2000, Astronomical Journal, 120, 1579
Zhang, Y., Yanny, B., Palmese, A., et al., 2019, ApJ, 874, 165
Zibetti, S., White, S. D. M., Schneider, D. P., et al., 2005, MNRAS, 358, 949
Zwicky, F., 1933, Helvetica Physica Acta, 6, 110

2

The stellar mass function and evolution of the density profile of galaxy clusters from the Hydrangea simulations at $0 < z < 1.5$

Abstract

Galaxy clusters are excellent probes to study the effect of environment on galaxy formation and evolution. Along with high-quality observational data, accurate cosmological simulations are required to improve our understanding of galaxy evolution in these systems. In this work, we compare state-of-the-art observational data of massive galaxy clusters ($> 10^{14}\,\mathrm{M}_\odot$) at different redshifts ($0 < z < 1.5$) with predictions from the Hydrangea suite of cosmological hydrodynamic simulations of 24 massive galaxy clusters ($> 10^{14}\,\mathrm{M}_\odot$ at $z = 0$). We compare three fundamental observables of galaxy clusters: the total stellar mass to halo mass ratio, the stellar mass function (SMF), and the radial mass density profile of the cluster galaxies. In the first two of these, the simulations agree well with the observations, albeit with a slightly too high abundance of $M_\star \lesssim 10^{10}\,\mathrm{M}_\odot$ galaxies at $z \gtrsim 1$. The NFW concentrations of cluster galaxies increase with redshift, in contrast to the decreasing dark matter halo concentrations. This previously observed behaviour is therefore due to a qualitatively different assembly of the smooth DM halo compared to the satellite population. Quantitatively, we however find a discrepancy in that the simulations predict higher stellar concentrations than observed at lower redshifts ($z < 0.3$), by a factor of $\approx$2. This may be due to selection bias in the simulations, or stem from shortcomings in the build-up and stripping of their inner satellite halo.

Ahad, S. L., Bahé, Y. M., Hoekstra, H., van der Burg, R. F. J., Muzzin, A., 2021, MNRAS, 504, 1999

2.1 Introduction

During the last few decades, our understanding of the formation and evolution of galaxies and the large scale structures they are part of has increased significantly. The Λ cold dark matter (ΛCDM) model has been extremely successful in describing the gravity-driven growth of structures from dwarf galaxies to super-clusters, based on a Universe dominated by dark matter (DM) and, at low redshift, dark energy. One of the most important questions, however, still remains: how exactly did baryonic structures such as galaxies form and grow in this Universe? A particularly useful setting to explore this question is in clusters of galaxies – the largest gravitationally bound structures in the Universe. Harbouring thousands of galaxies in a relatively small volume, they are akin to cosmic laboratories to study the impact of galaxy interactions and environment on galaxy formation. For example, many observational studies have concluded that at a fixed stellar mass, galaxies in denser environments (especially in groups or clusters) are more likely to be elliptical in morphology (Dressler, 1980), lack or have low levels of recent or ongoing star formation (Dressler, 1980; Balogh et al., 1999; Kauffmann et al., 2004; Weinmann et al., 2006; Blanton et al., 2005; Peng et al., 2010; Wetzel et al., 2012; Woo et al., 2012), and are devoid of atomic hydrogen (e.g. Giovanelli and Haynes, 1985; Fabello et al., 2012; Hess and Wilcots, 2013; Odekon et al., 2016; Brown et al., 2017) in comparison with galaxies in more isolated, "field", environments.

The arguably most fundamental observable property of galaxies and clusters is their total stellar mass and the way in which this is distributed over differently massive galaxies – i.e. the stellar mass function (SMF) – and galaxies at different cluster-centric radii. The SMF is the product of star formation, galaxy mergers, and stripping, so that its shape and temporal evolution provide an observationally accessible tracer of galaxy evolution, and of the role of environment in this process. In simulations, model adjustments typically manifest themselves as pronounced differences in the predicted field SMF (e.g. Crain et al., 2015), which has therefore emerged as a prime calibration diagnostic for cosmological hydrodynamic simulations of representative volumes such as EAGLE (Schaye et al., 2015) or IllustrisTNG (Pillepich et al., 2017). Furthermore, several observational studies have reported differences between the satellite and field stellar mass functions (e.g. Yang et al., 2009; Wang and White, 2012; Vulcani et al., 2014), so that the cluster SMF also provides a valuable test for the validity of theoretical models.

Another important indicator of the growth of cluster haloes and the formation

and evolution of galaxies within them are the radial density profiles of total matter and galaxies in the clusters. Simulations robustly predict that the density profile of the dominant CDM component is well described by the Navarro-Frenk-White (NFW) profile (Navarro et al., 1996; Navarro et al., 1997; Schaller et al., 2015b), which can be parameterised in terms of the halo concentration and mass. A clear prediction from these simulations is that the concentration of cluster haloes increases with cosmic time (e.g. Duffy et al., 2008; Muñoz-Cuartas et al., 2011) – in other words, the dark matter in clusters with fixed halo mass (and also of individual evolving clusters) was less concentrated at high redshift than it is now.

Measuring these profiles observationally is challenging, however, because indirect detection methods such as gravitational lensing have to be used (e.g. Williams et al., 2018; Mahler et al., 2019; Gonzalez et al., 2020). The (projected) satellite stellar mass density profile, on the other hand, can be measured quite clearly and robustly from observations[1]. Since both dark matter and stars are, essentially, collisionless fluids on cluster scales, one might expect to observe a similar concentration evolution for these stellar profiles as what is predicted for DM. Surprisingly, recent observational studies have revealed a rather different picture: stellar concentrations were much higher than DM predictions at redshift $z \approx 1$ (Muzzin et al., 2007), but then became less concentrated over cosmic time, and at $z \approx 0$ the stellar concentration is a factor of $\approx$2 lower (Budzynski et al., 2012; Burg et al., 2015) than what simulations predict for DM.

While it may be tempting to interpret this discrepancy as a failure of ΛCDM, a more straightforward solution is that the DM and stellar components of galaxy clusters are built up differently over time. It is therefore important to test this interpretation by analysing the evolution of stellar density profiles in cosmological hydrodynamic simulations, which self-consistently model the formation and evolution of stellar mass. Comparing the predicted stellar density profiles to both observations and the simulated DM density profiles can then reveal whether the observed decrease in stellar concentration over time is indeed explained by astrophysical effects, or hints at a need to modify the ΛCDM paradigm.

For a simulation to be of use in this experiment, it must as a minimum requirement reproduce the observed field SMF and its evolution ; the simulation resolution must also be high enough that cluster-specific processes such as star formation quenching

[1]Most observational work has focused on the profile of the stellar mass in satellites, i.e. the stellar-mass-weighted satellite halo profile. The diffuse stellar halo of the cluster itself, the intra-cluster light (ICL) has only recently become accessible observationally beyond the very nearby Universe (e.g. Mihos et al. 2005; Montes and Trujillo 2018; Zhang et al. 2019). We do not consider the ICL in this paper, but refer the interested reader to Alonso Asensio et al. (2020) and Deason et al. (2020) for recent analyses of its low-redshift properties and radial profiles in Hydrangea.

and stellar stripping can be modelled reliably. The EAGLE simulations satisfy both of these needs: the field SMF is reproduced both at $z \approx 0$, where it was used as a calibration diagnostic (Crain et al., 2015; Schaye et al., 2015) and at higher redshift (Furlong et al., 2015), and at a baryon mass resolution of $\approx 2 \times 10^6\,\mathrm{M}_\odot$, Milky Way like galaxies are resolved by $\gtrsim 10^4$ star particles each. Comparably successful projects include IllustrisTNG (Pillepich et al., 2018), Horizon-AGN (Dubois et al., 2014), and Simba (Davé et al., 2019).

However, galaxy clusters inhabit only a small volume fraction of the Universe, so that they are not generally represented (at least not in statistically significant numbers) in simulations comparable to the resolution of EAGLE, which are typically limited to volumes of $\leq (100\ \mathrm{cMpc})^3$. Larger-volume simulations, such as IllustrisTNG-300 (Pillepich et al., 2018) or BAHAMAS (McCarthy et al., 2017) – which contain galaxy clusters in sufficient numbers – in turn still lack the resolution to model individual cluster galaxies in detail. This motivates the use of zoom-in cluster simulations, where only a carefully chosen region within a large volume (such as the site of a massive galaxy cluster) is simulated at high resolution.

In this work, we perform a detailed analysis of one set of such zoom-in simulations, the Hydrangea cluster suite (Bahé et al., 2017; Barnes et al., 2017), to gain insight into the evolution of the stellar component of galaxy clusters over cosmic time. Various predictions from these simulations in the local Universe have previously been compared to observations and found to be broadly realistic, including the stellar mass function, quenched fractions (Bahé et al., 2017), total gas and stellar content (Barnes et al., 2017). It is far from guaranteed, however, that these agreements will also hold at higher redshift, especially considering that the simulation model was calibrated at $z \approx 0$ (albeit on the field, not clusters). We therefore perform careful tests of simulation predictions at higher redshift, up to $z \approx 1.4$, by comparing them with state-of-the-art observational data. Specifically, we analyse the total stellar content, the satellite stellar mass function, and the radial distribution of stellar mass within the cluster; we then use the latter as a basis to interpret the difference between the observed evolution of stellar concentration and that predicted for DM from N-body simulations over cosmic time.

The remainder of this paper is structured as follows. In Section 2.2, we describe the key aspects of the Hydrangea simulations, and test their predicted evolution of the total stellar content. In Section 2.3, we outline the observational data sets that we have used to test the simulations. The predicted SMF is compared to observations at various redshifts in Section 2.4, followed by a comparison of the predicted and

observed stellar density profiles in Section 2.5. Finally, in Section 2.6, we summarize our findings and present our conclusions.

2.2 Simulated Data

2.2.1 The Hydrangea Simulation Suite

The Hydrangea simulations (Bahé et al., 2017; Barnes et al., 2017) are a suite of high-resolution cosmological hydrodynamic zoom-in simulation of 24 massive galaxy clusters. They are part of the 30 clusters of the 'C-EAGLE' project, and were chosen from a low-resolution N-body (DM only) parent simulation (Barnes et al., 2017) of a $(3200\ \mathrm{cMpc})^3$ volume[2]. Each of the high-resolution simulation regions is centred on a massive cluster with M_{200c} in the range $10^{14.0}$–$10^{15.4}\,\mathrm{M}_\odot$ at $z = 0$[3]. The particle mass resolution is $m_{\mathrm{baryon}} = 1.81 \times 10^6\,\mathrm{M}_\odot$ for baryons and $m_{\mathrm{DM}} = 9.7 \times 10^6\,\mathrm{M}_\odot$ for dark matter, respectively[4]; the gravitational softening length is $\epsilon = 0.7$ physical kpc (pkpc) at $z < 2.8$. The high-resolution simulation regions include the large scale surroundings of the clusters to ≥ 10 virial radii (r_{200c}), making them also suitable to study the large scale environmental influence on galaxy evolution in and around clusters. To ensure that these clusters are centred at the peak of the local density field, there was an additional selection criteria of having no more massive halo within 30 pMpc or $20 \times r'_{200c}$ (whichever value is larger, r'_{200c} is the virial radius of the neighbouring more massive halo).

The AGNdT9 variant of the EAGLE simulation code (Schaye et al. 2015, see also Crain et al. 2015) was used to run the Hydrangea simulations. A significantly modified version of the smooth particle hydrodynamic (SPH) simulation code GADGET-3 (Springel, 2005), this code uses an updated hydrodynamics scheme (Schaye et al., 2015; Schaller et al., 2015a) and a range of subgrid physics models to simulate astrophysical processes that originate below the resolution scale of the simulation. These astrophysical processes include star formation (based on the Kennicutt-Schmidt relation as in Schaye and Dalla Vecchia 2008, with the metallicity-dependent star for-

[2]Throughout this paper, we use the prefixes 'c' and 'p' to refer to comoving and proper quantities, respectively: 'cMpc', for example, denotes 'co-moving Mpc'.

[3]M_{200c} refers to the mass enclosed within a sphere centred at the potential minimum of the cluster radius r_{200c}, within which the average density of matter equals 200 times the critical density.

[4]Ludlow et al. (2019) have recently shown that this (common practice) use of lower resolution for the DM component leads to an artificial transfer of energy from DM to stars, which can puff up the central regions of galaxies. We do not expect this to have an effect on our study, since the concentrations we measure in Section 2.5 are derived from the (unaffected) radii of galaxies within the cluster, rather than the distribution of stars within them.

mation threshold from Schaye 2004), energy feedback from star formation in thermal, stochastic form to limit numerical cooling losses (Dalla Vecchia and Schaye, 2012), radiative cooling, photo-heating and re-ionization (Wiersma et al., 2009), and metal enrichment from stellar evolution (Wiersma et al., 2009). Models based on Springel (2005), Rosas-Guevara et al. (2015), and Schaye et al. (2015) are used to simulate the seeding, growth of, and feedback from supermassive black holes at galactic centres. The efficiency scaling of star formation feedback was calibrated against low-redshift observations of the field stellar mass function (SMF) and stellar mass–size relation (Crain et al., 2015).

A flat ΛCDM cosmology is assumed in the Hydrangea suite (and EAGLE), with parameters taken from the *Planck* 2013 results, combined with baryonic acoustic oscillations, polarization data from WMAP, and high multipole moment experiments (Planck Collaboration XVI, 2014): Hubble parameter $H_0 = 67.77$ kms^{-1}Mpc^{-1}, dark energy density parameter $\Omega_\Lambda = 0.693$, matter density parameter $\Omega_M = 0.307$, and baryon density parameter $\Omega_b = 0.04825$.

The primary output from each simulation are 30 snapshots spaced (mostly) equally between $0 < z < 14.0$, with a time step of $\Delta t = 500$ Myr. In each of these snapshots, structures were identified through two consecutive steps with the SUBFIND code (Dolag et al. 2009, see also Springel et al. 2001), which determines the gravitationally bound stellar, dark matter, and gas content of each identified object. In the first step, a friends-of-friends (FoF) algorithm with linking length equal to 0.2 times the mean inter-particle separation is used to identify spatially disjoint groups of DM particles. Baryon particles are attached to the FoF group (if any) of their nearest DM particle (Dolag et al., 2009) and FoF groups with fewer than 32 DM particles are discarded. In the second step, gravitationally bound candidate 'subhaloes' within each FoF group are identified as locally over-dense regions. Particles that are not gravitationally bound to each of the subhalo candidate are then iteratively removed, and particles in the FoF group that are not part of any subhalo, but still gravitationally bound to the group, are considered as the 'background' or 'central' subhalo (see Bahé et al. 2017 and Bahé et al. 2019 for more details). In this paper, we refer to all the subhaloes other than the central subhaloes as the 'satellites'. We use the terms 'subhaloes' and 'galaxies' interchangeably (i.e. both the terms refer to the baryonic and DM contents within the structure together). The most massive FoF group in each simulation is identified as the galaxy cluster whose properties we study in this work. Its (dominant) background subhalo is identified as the central, brightest cluster galaxy (BCG), all others are referred to as satellite galaxies.

Figure 2.1 shows the mass evolution of the 24 simulated clusters over the redshift range $0 \leq z \leq 2$. To construct the growth curves shown by the black lines in Fig. 2.1, we select at each redshift the most massive cluster halo from each of the 24 Hydrangea simulations. At the redshifts we consider ($z \leq 2$), these are mostly the actual main progenitors of the most massive $z = 0$ clusters: even at $z = 2$, only five of the most massive clusters in their simulation at this time are not going to remain the most massive one[5] until $z = 0$. Selecting the actual main progenitors instead would decrease the median halo mass by only 25 per cent at $z = 2$, and 6 per cent at $z = 1$; our results are therefore insensitive to this choice.

As expected (e.g. Burg et al., 2015), the distribution of Hydrangea cluster masses decreases steadily towards higher redshift, but maintains its roughly one order of magnitude spread. At $z = 1$ (2), the median mass is lower by a factor of $\approx$3 (10) than at $z = 0$. This broadly mimics the distribution of the observed cluster masses from our comparison samples (coloured symbols in Fig. 2.1), as we discuss in Section 2.3.

2.2.2 Verifying the consistency between satellite stellar masses from Subfind and observations

Previous works have shown that during the subhalo identification step, SUBFIND can assign particles incorrectly to the central rather than to a satellite subhalo (e.g. Muldrew et al., 2011). This can artificially suppress the mass of subhaloes near the centre of a galaxy cluster or, in extreme cases, even lead to them being missed completely. Bahé et al. (2019) found that, in Hydrangea, only $\leq$ 5 per cent of cluster galaxies with $M_{\rm tot}^{\rm peak} > 10^{10}{\rm M}_{\odot}$ are missed completely by SUBFIND (where $M_{\rm tot}^{\rm peak}$ is the peak total mass of the DM, stars, and black hole particles over the entire life of the galaxy). However, the masses assigned to identified satellite subhaloes may still be significantly underestimated (e.g. Behroozi et al., 2013; Cañas et al., 2019). Before studying the stellar mass in the Hydrangea clusters in detail, we therefore test whether the estimated stellar masses of the satellite subhaloes are comparable with what would be inferred from the observations.

For this purpose, we produce synthetic images from the simulated cluster snapshot data at $z = 0$. We take the three dimensional (3D) stellar particle positions and calculate the 2D surface mass density distribution, projected along each principal axis

[5]In addition, two of them are subdominant progenitors of their $z = 0$ cluster.

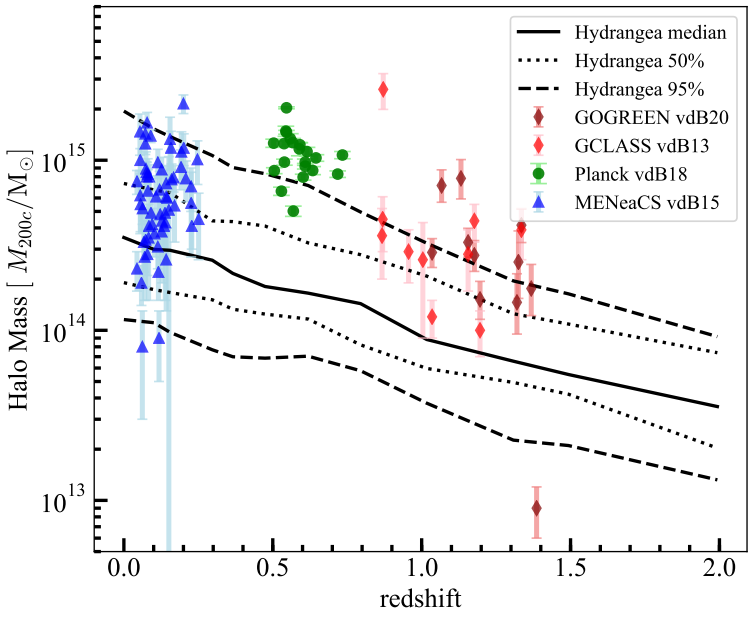

Figure 2.1: The time evolution of the cluster halo mass M_{200c} (growth curves) of the Hydrangea sample along with the observational data samples used in this paper. The solid black line shows the median cluster halo mass of the Hydrangea sample in the redshift range $0 \leq z \leq 2$. The dotted and dashed black lines include 50% and 95% of clusters from the Hydrangea sample, respectively. Brown diamonds represent the GOGREEN cluster sample (Old et al., 2020), red diamonds the GCLASS clusters (Burg et al., 2013; Burg et al., 2014), green squares the Planck-SZ sample (Burg et al., 2018), and blue triangles the MENeaCS cluster samples from Burg et al. (2015). While the MENeaCS, GCLASS, and GOGREEN samples are mostly overlapping the Hydrangea clusters in mass at their respective redshifts, some outliers are significantly more massive, as is the majority of the Planck-SZ clusters. In Section 2.4.1, we develop an extrapolation scheme to take these mass differences into account.

of the simulation, for the central region of each of the 24 simulated clusters (see Fig. 2.2 for an example). Each image has a size of 1000×1000 pixels of side length 2 Mpc and is centred at the position of the potential minimum of the central cluster[6]. The image value at each pixel, in units of $M_\odot$, represents the stellar mass surface density, which would be equivalent to the luminosity under the assumption of a fixed mass-to-light ratio.

As the output from the simulation is noise-free (except for Poisson noise from the finite number of particles), these raw images cannot be directly fit with observational techniques. We therefore add artificial noise at an RMS level of 1.5×10^6 $M_\odot$ per pixel to mimic the depth of the cluster images from the Multi-Epoch Nearby Cluster Survey (MENeaCS, see Section 2.3.1) at $z < 0.25$. The RMS noise level is determined by converting the noise level of light from the observations to stellar mass to be used for the simulated image. We then use Source Extractor (SExtractor, Bertin and Arnouts 1996, 2010) to detect the objects (in our case, galaxies) in the image. The detection criterion is set such that at least 3 adjacent pixels have a flux density that is greater than 4σ in comparison to the local background. Here, the threshold value of 4σ corresponds to $\sim 10^7$ $M_\odot$, which makes sure that we are not selecting spurious line-of-sight collections of star particles as galaxies, and that the threshold is small enough to not exclude any galaxies above a stellar mass of $10^9\,M_\odot$. The output flags for nearby bright neighbours and de-blending are taken into account to avoid overestimating the mass from the integrated flux of a faint object in case it is close to a very bright galaxy, especially in case of the smaller satellites near the BCG.

Using the position of sources detected in this way, we matched them to the subhaloes identified by Subfind. We consider a SExtractor source and subhalo to be matched if their projected distance is less than 1.5 pixels (= 3 pkpc). We take the 3D subhalo stellar mass within 30 pkpc from the subhalo center of potential for each of the matched subhaloes as the mass from Subfind. For field galaxies, this 3D aperture has previously been shown to mimick the 2D Petrosian aperture that is frequently used in observations (Schaye et al., 2015, see their sec. 5.1.1. and fig. 6). From the synthetic images, we estimate the mass from the integrated `FLUX_AUTO` output for each object from SExtractor. Then, we compare the stellar mass function from the Subfind stellar mass and the mass retrieved by SExtractor from the images. To account for any projection bias that may occur from taking the 2D projected data in this test, we project each cluster separately along the x, y, and z axes, and repeat the above procedure for each projection.

[6]The images therefore stretch to $\sim 0.5 \times r_{200c}$ from the cluster centre.

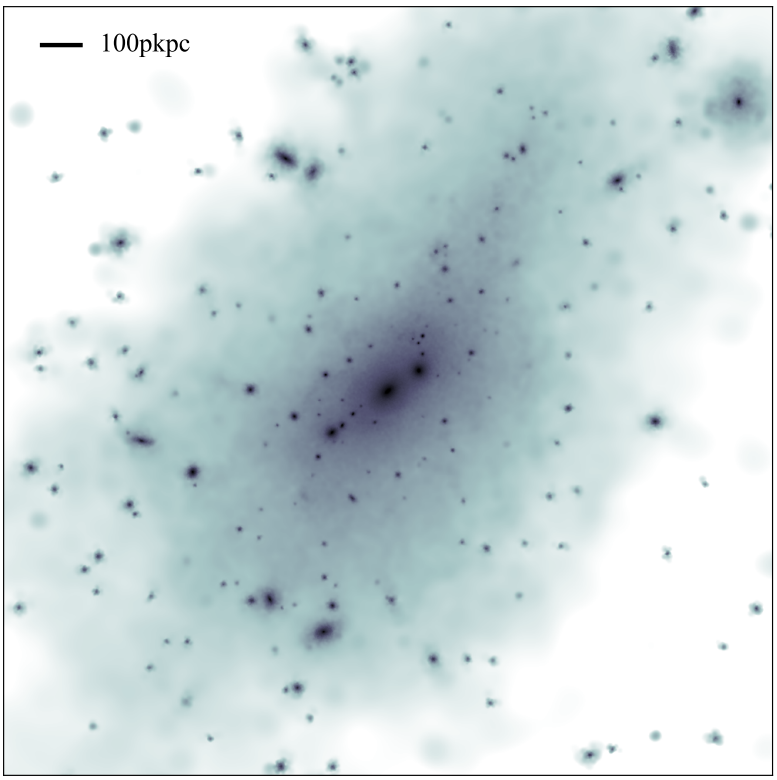

Figure 2.2: An example of a synthetic image of the surface mass density distribution of the stellar component of cluster CE-0 from the Hydrangea simulations. It is centered on the cluster potential minimum and extends to 1 pMpc on each side from the center along both axes. The image is obtained by projecting the star particles along the y-z axis of the simulation frame. There is no noise added in this figure, and the pixel values range from $\sim$10 to $\sim 10^9\,\mathrm{M}_\odot\,\mathrm{kpc}^{-2}$.

Figure 2.3 shows the galaxy SMFs obtained from the SUBFIND output (blue) and the synthetic images (magenta). The error bars here represent the Poisson errors obtained from 100 bootstrap re-samplings of the stack of galaxies in each sample. For all three projections, the stellar mass functions using galaxy masses from SUBFIND and those from the synthetic images agree within their uncertainties. The best-fit Schechter functions (Schechter, 1976) for the SMFs (solid lines, see Section 2.4.1 for details) in Fig. 2.3 indicate that the SUBFIND and SEXTRACTOR outputs agree well within the error bars. To test for different depths from observations at different redshifts, we repeated the procedure for RMS noise levels of 7.5×10^5, 3.0×10^6, and $6.0 \times 10^6\,\mathrm{M}_\odot\,\mathrm{pixel}^{-1}$. The SMFs resulting from these SExtractor outputs agree similarly well with the SUBFIND SMF as the one shown in Fig. 2.3, albeit with a mild dependence of the best-fit SMF parameters on the noise level (see Appendix 2.6). We therefore conclude that the subhalo stellar mass within 30 pkpc as measured by the SUBFIND code can be reliably used for the following analysis.

2.2.3 Total stellar mass fractions predicted at different redshifts

As mentioned above, the Hydrangea simulations successfully reproduce the observed SMF of galaxy clusters in the local Universe, at $z \approx 0.1$ (Bahé et al., 2017). As a first test, we explore how well the Hydrangea suite reproduces the observed total stellar mass content at higher redshifts, up to $z = 1.4$. In recent studies, the stellar content of galaxy clusters (and also their total baryon content) has been observed to depend strongly on cluster halo mass, but at best weakly with redshift up to $z \approx 1.3$ (Chiu et al., 2016a,b, 2018). Chiu et al. (2018) explored the mass scaling relations of the stellar content, as well as the intracluster medium, and total baryon mass in their sample of 91 Sunayev-Zel'dovich effect (SZE) selected galaxy clusters from the South Pole Telescope (SPT-SZ) survey in the redshift range $0.2 < z < 1.25$. They compared their scaling relations with other observational data, and showed that despite the residual systematic uncertainties among different datasets, the qualitative trend of the scaling relations does not vary significantly (see e.g. their fig. 6). As a first test, we compare the Hydrangea clusters with the scaling relation presented in Chiu et al. (2018) to investigate whether the simulations can reproduce these fundamental and robustly measured observational features.

Figure 2.4 shows the scaling relation of the total stellar mass fraction within the (projected) radius R_{500c} of the Hydrangea clusters at redshifts $0.1 < z < 1.5$ with

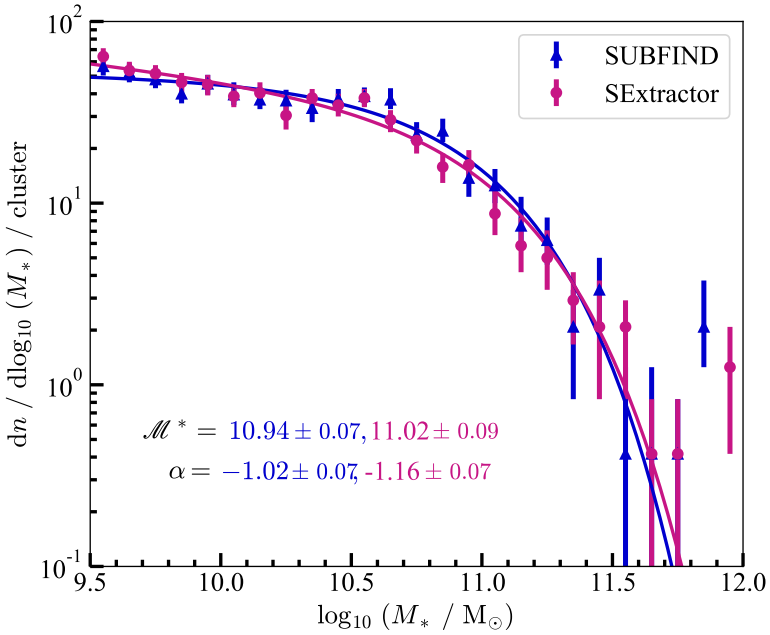

Figure 2.3: The galaxy stellar mass function (GSMF) of the simulated clusters (coloured symbols) and their best-fit Schechter functions (solid lines). The blue points are obtained from the subhalo stellar mass measured by SUBFIND within 30 pkpc from the centre of potential of each subhalo; magenta points are obtained from the estimated stellar mass of each galaxy by running SEXTRACTOR on synthetic images (see text for details). The error bars are obtained by bootstrap re-samplings of the stack of galaxies in each sample. Both the non-parametric mass functions and their Schechter fits agree within statistical uncertainties, indicating that the SUBFIND mass measurement is consistent with the observational approach.

respect to their total halo mass (M_{500c}, to match what is used by Chiu et al. 2018), along with the Chiu et al. (2018) scaling relation within its 1σ confidence interval. To compare with these results, we compute the stellar mass fraction in the simulations from the summed stellar masses of all galaxies (as computed by SUBFIND, within a 30 pkpc radial aperture) with $M_{\rm star} > 10^{10}\,{\rm M}_\odot$ that lie within a 2D projected radius of R_{500c} from the centre of potential of each cluster.

As in Chiu et al. (2018), we fit the stellar mass fractions with a relation of the form

$$\frac{f_\star}{\left(\frac{1+z}{1+z_{\rm piv}}\right)^{C_\star}} = A \times \frac{10^{12}\,{\rm M}_\odot}{M_{500c}} \times \left(\frac{M_{500c}}{M_{\rm piv}}\right)^{B}, \tag{2.1}$$

where $f_\star$ is the stellar mass fraction, $z_{\rm piv}$ the pivot redshift, and $M_{\rm piv}$ the pivot halo mass, and A, B, and $C_\star$ are free parameters; we follow Chiu et al. (2018) and use $z_{\rm piv} = 0.6$ and $M_{\rm piv} = 4.8 \times 10^{14}\,{\rm M}_\odot$, respectively[7]. We fit the Hydrangea data with Eqn. 2.1 for parameters A and B by maximizing the log likelihood value. The redshift scaling index $C_\star$ is kept fixed at 0.05, the best-fit value of Chiu et al. (2018).

The best-fit parameters, represented by the green dash-dotted line in Fig. 2.4, and their 1σ confidence intervals, are $A = 4.5 \pm 0.8$, and $B = 0.79 \pm 0.1$. In comparison, the observational best-fit parameters (Chiu et al., 2018) are $A = 4.0 \pm 0.28$, and $B = 0.8 \pm 0.12$, respectively, as indicated by the dotted black line and gray band in Fig. 2.4. The deviation, $\Delta A = 0.5$ and $\Delta B = 0.01$, is within the 1σ uncertainty in both cases. The slightly higher-than-observed normalization for the Hydrangea clusters is in fact not too surprising, given that Bahé et al. (2017) showed that the simulated BCGs at $z = 0$ are a factor of $\sim$3 too massive. We also note that the cluster-to-cluster scatter in Fig. 2.4 is similar to what is shown in fig. 6 of Chiu et al. (2018), where they show their cluster sample along with other observed cluster samples at a range of redshifts.

From the comparison presented in Fig. 2.4, we therefore conclude that the Hydrangea simulations predict a total stellar content within galaxy clusters that is quantitatively consistent with observations out to $z \approx 1.5$. Based on this fundamental success, we explore in the subsequent sections whether the Hydrangea suite can reproduce the distribution of the total stellar mass in individual galaxies, i.e., the stellar mass function (SMF) at redshifts in the range $0 < z < 1.4$.

[7]Following Chiu et al. (2018), we divide $f_\star$ by the factor $\left((1+z)/(1+z_{\rm piv})\right)^{C_\star}$ to account for the (slight) redshift dependence of the stellar mass fractions.

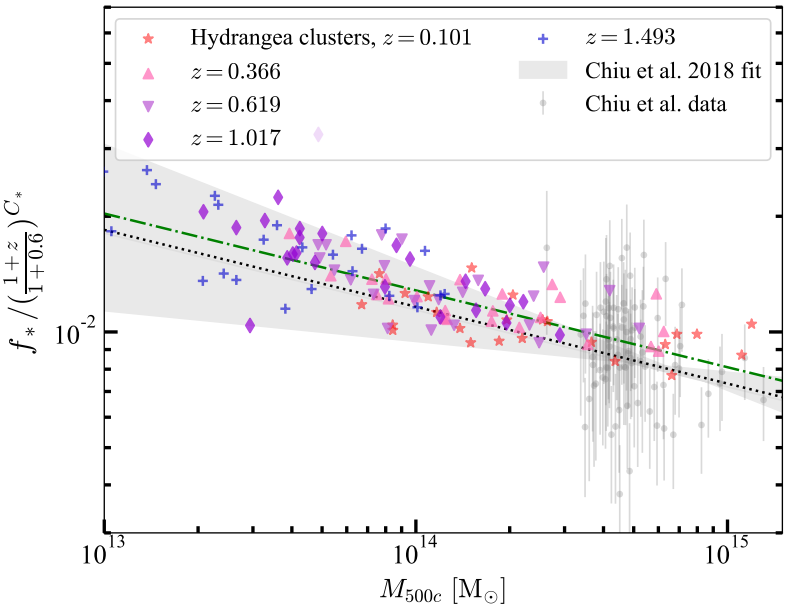

Figure 2.4: The scaling relation of the total stellar mass fraction with respect to the cluster halo mass. Different colored symbols (except for the grey ones) represent individual Hydrangea clusters at five different redshifts, as specified in the legend. The green dash-dotted line shows the best-fit scaling relation to all these points (see text for details). The grey data points and corresponding error bars are the SPT clusters from Chiu et al., 2018. The dotted black line and grey shaded region give the corresponding best-fit relation from Chiu et al., 2018 and its 1σ confidence interval, respectively. The simulations and observations agree well within uncertainties, confirming that the Hydrangea clusters contain realistic amounts of stellar mass over the majority of cosmic history.

2.3 Observational Data

To test the accuracy of the GSMF and the radial distribution of stellar mass predicted by Hydrangea, we compare the simulations with several recent observational data sets at a range of redshifts. These include the MENeaCS and CCCP cluster samples at $z \approx 0.15$ as analysed by Burg et al. (2014) and Burg et al. (2015), the Planck-SZ clusters at $z \approx 0.6$ (Burg et al., 2018), GCLASS clusters at $z \approx 1.0$ as presented by Burg et al. (2013), and from the GOGREEN survey at $z \approx 1.3$ (van der Burg et al., 2020). In this section, we summarize the aspects of these different data sets and how their relevant characteristics are reproduced in our simulation analysis. To illustrate their halo mass range and its relation to Hydrangea at the respective redshifts, all observed clusters used for comparison in Sections 2.4 and 2.5 are shown as symbols in Fig. 2.1; we comment on the mass distribution of each sample in the respective sub-sections below.

2.3.1 MENeaCS and CCCP

The sample from the the Multi-Epoch Nearby Cluster Survey (MENeaCS) and the Canadian Cluster Comparison Project (CCCP) consists of 60 massive clusters in the local Universe ($z < 0.25$, Burg et al., 2015). For this sample, deep *ugri*-band photometry (with a median limiting g-band magnitude of 24.8) is used together with spectroscopic observations to determine cluster membership and to estimate the dynamical mass of the clusters. The cluster halo masses, defined as M_{200c}, range from $8 \times 10^{13}\,\mathrm{M}_\odot$ to $2.15 \times 10^{15}\,\mathrm{M}_\odot$, with a mean of $6.8 \times 10^{14}\,\mathrm{M}_\odot$. In comparison, the average halo mass of the Hydrangea clusters at similar redshift is $\approx 5 \times 10^{14}\,\mathrm{M}_\odot$; as can be seen from Fig. 2.1 (blue triangles), the range of simulated clusters masses overlaps well with these observed samples despite the slightly different averages.

From these clusters, we use the radial stellar mass density distribution of their satellite galaxies presented in Burg et al. (2015). These authors construct an ensemble cluster by stacking the satellites around individual clusters, with their (2D) radial distances normalised by their respective R_{200c}, and determine the 2D density profile in this stack over the (projected) radial range from 0.1 to $2 \times R_{200c}$. We apply the same stacking procedure and radial range in our simulation analysis.

2.3.2 *Planck*-SZ

The observed clusters at $z \approx 0.6$ from Burg et al. (2018) were primarily detected with *Planck* via the Sunayev-Zeldovich (SZ) effect and later confirmed with follow-up observations. The Planck-SZ selected clusters are part of the most massive cluster samples from that epoch. Burg et al. (2018) present the GSMF of 21 *Planck*–SZ selected galaxy clusters. The cluster halo masses are obtained by applying the $M - Y_{\rm X}$ relation to deep X-ray maps, and range between $M_{\rm 500c} = 3.17 \times 10^{14}\,{\rm M}_\odot$ and $1.28 \times 10^{15}\,{\rm M}_\odot$ with a mean of $6.9 \times 10^{14}\,{\rm M}_\odot$. This is significantly higher than the average of the Hydrangea clusters at similar redshift ($1.6 \times 10^{14}\,{\rm M}_\odot$); as Fig. 2.1 shows, all but two of their clusters (green circles) lie above the 95 per cent halo mass interval of the simulations. We overcome this mismatch through a mass extrapolation scheme that we apply to the simulations, as described in Section 2.4.1.

We use the GSMF of the Planck-SZ clusters as published by Burg et al. (2018) for comparison with our simulations. The brightest cluster galaxy (BCG), selected in the K_s band within a $1'$ location limit from the X-ray peak for each cluster, is excluded and the GSMF is constructed by stacking all other galaxies located within $2 \times R_{\rm 500c}$, with a stellar mass limit of $10^{9.5}\,{\rm M}_\odot$ for the total galaxy population. For statistical background subtraction and comparison with the field environment, they use data from the COSMOS/Ultra VISTA field at similar redshift range (Muzzin et al., 2013).

2.3.3 GCLASS and GOGREEN

The GCLASS cluster sample reported in Burg et al. (2013) consists of 10 red-sequence selected rich galaxy clusters at $0.86 < z < 1.34$ in the Gemini Cluster Astrophysics Spectroscopic Survey (GCLASS). The cluster halo masses, defined as $M_{\rm 200c}$, are estimated from the line-of-sight velocity dispersion of the spectroscopic targets and range from $1.0 \times 10^{14}\,{\rm M}_\odot$ to $2.61 \times 10^{15}\,{\rm M}_\odot$ with a mean of $5.3 \times 10^{14}\,{\rm M}_\odot$. As with the *Planck*-SZ clusters, this is a factor of ≈5 higher than the equivalent Hydrangea average ($9.4 \times 10^{13}\,{\rm M}_\odot$). However, the wide range in GCLASS halo masses means that more than half of the sample nevertheless overlaps with the Hydrangea clusters in mass (see the red diamonds in Fig. 2.1). We apply the same extrapolation scheme as for the Planck-SZ clusters to account for this mass mismatch in our comparison of the GSMF. Burg et al. (2013) construct the GSMF by stacking the satellite galaxies located within a projected radius of 1 pMpc from the cluster centre with a lower stellar mass limit of $10^{10}\,{\rm M}_\odot$.

At a similar redshift range, ($1.0 < z < 1.4$) van der Burg et al. (2020) present the

GSMF of 11 galaxy clusters from the Gemini Observations of Galaxies in Rich Early Environments (GOGREEN) survey. The cluster halo masses range from $M_{200c} = 1.0 \times 10^{13}$ to $7.8 \times 10^{14}\,\mathrm{M}_\odot$, with a mean of $3.2 \times 10^{14}\,\mathrm{M}_\odot$. This is similar to the GCLASS sample (also in terms of cluster-to-cluster scatter, see the brown diamonds in Fig. 2.1), so that again only a small extrapolation correction is required in our comparison below. van der Burg et al. (2020) construct the GSMF by stacking all the cluster galaxies (including the BCGs) with $M_\star \geq 10^{9.75}\,\mathrm{M}_\odot$ that are located within a projected radius of 1 pMpc from the cluster centre.

2.4 Galaxy Stellar Mass Function

As we have shown in Section 2.2.3, the Hydrangea simulations predict a total stellar mass fraction in clusters that is consistent with observations out to $z \approx 1.5$. We now perform the more stringent test of how realistically this mass is distributed over satellites of different masses, i.e. the accuracy of the predicted satellite GSMF. We first describe our approach for dealing with the (moderate) offsets between the masses of simulated and observed clusters as discussed above (Section 2.4.1), and then confront simulations and observations in Section 2.4.2.

2.4.1 Accounting for differences in cluster halo mass

As shown in Fig. 2.1, the mass range of the Hydrangea clusters is not exactly matched to the observational comparison samples, with many of the more massive observed clusters not having any similarly massive analogue in the simulations. Although the offsets are not huge (factors of $\lesssim 5$, see Section 2.3), the tight correlation between cluster richness and mass (e.g. Yee and Ellingson, 2003; Budzynski et al., 2012; Pearson et al., 2015) means that they nevertheless have to be accounted for to enable a meaningful test of the GSMF. We do this by means of an extrapolation model based on the Schechter (1976) fitting formula:

$$\Phi(M) = \ln(10)\,\Phi^*\,(M/\mathscr{M}^*)^{(1+\alpha)}\,\mathrm{e}^{-M/\mathscr{M}^*}, \tag{2.2}$$

with normalization Φ^*, characteristic mass $\mathscr{M}^*$, and α setting the (logarithmic) slope at the low-mass end.

In Fig. 2.3, we had already seen that the $z = 0$ GSMF predicted by Hydrangea is well-fit with a Schechter function. Similarly good fits are achieved at higher redshift: as an example, we show in Fig. 2.5 the predicted GSMF at $z = 0.6$, splitting our

cluster sample into a low- and high-mass subset at the mean $\overline{M}_{500c} = 1.6 \times 10^{14}\,M_\odot$. The satellite GSMF for the low (high) mass clusters is shown with magenta squares (blue circles). Error bars indicate 1σ confidence intervals from 100 bootstrap resamplings; for each of these, we draw from all galaxies with $M_\star \geq 10^{9.5}\,M_\odot$ in the cluster ensemble a Poisson-distributed number with mean equal to the total number of galaxies in the ensemble (with replacement). We use the Monte-Carlo Markov Chain (MCMC) package EMCEE (Foreman-Mackey et al., 2013) to find the best-fit Schechter function parameters (Φ^*, $\mathscr{M}^*$, α) and their uncertainties.

These best-fit Schechter functions are plotted in Fig. 2.5 as dashed lines in the same colour as the corresponding binned GSMF (see Table 2.B.1 for the corresponding values). Two key features are evident: the GSMF of the lower-mass clusters (magenta) is indeed significantly lower than for the more massive cluster set (blue), and each is well-described by its best-fit Schechter function (with the possible exception of the very high mass end, where the best fit for both sets falls slightly below their respective binned data points). As expected, the GSMF normalisations Φ^* of the high- and low-mass cluster stacks differ significantly (by a factor greater than 2), but the characteristic mass $\mathscr{M}^*$ and low-mass slope parameter α are similar in both stacks (to within 39 and 13 percent, respectively). Similarly good Schechter fits are obtained for the cluster ensembles at other redshifts (not shown).

Having established that the Schechter function is indeed a good representation for the satellite GSMF in Hydrangea, we then proceed to model its mass dependence for comparison to the observations. First, we compute and fit satellite mass functions over a range of cluster masses at each of the three required redshifts ($z = 0.619$, 1.017, and 1.308), in analogy what is shown in Fig. 2.5. At the high-mass end, we use the seven most massive clusters at each redshift individually, which yield good Schechter fits (reduced $\chi^2 \leq 2.0$ in most cases). For less massive clusters, however, we have found that their individual satellite counts are not high enough to derive robust Schechter fits. We therefore stack the lower mass clusters in sets of four at successively higher mass, and derive (and fit) composite mass functions from these stacks.

The result for $z \approx 0.6$ is shown in the three panels of Fig. 2.6, where the turquoise, blue, and purple symbols indicate the best-fit Schechter parameters Φ^*, $\mathscr{M}^*$, and α, respectively, as a function of cluster mass M_{500c}. For the seven massive clusters that are fit individually, we show the best-fit parameters as circles, whereas stars represent the best-fit parameters for the ensemble stacks of lower-mass clusters, plotted at their mean M_{500c}.

The left-hand panel shows the expected tight correlation between Φ^* and M_{500c}.

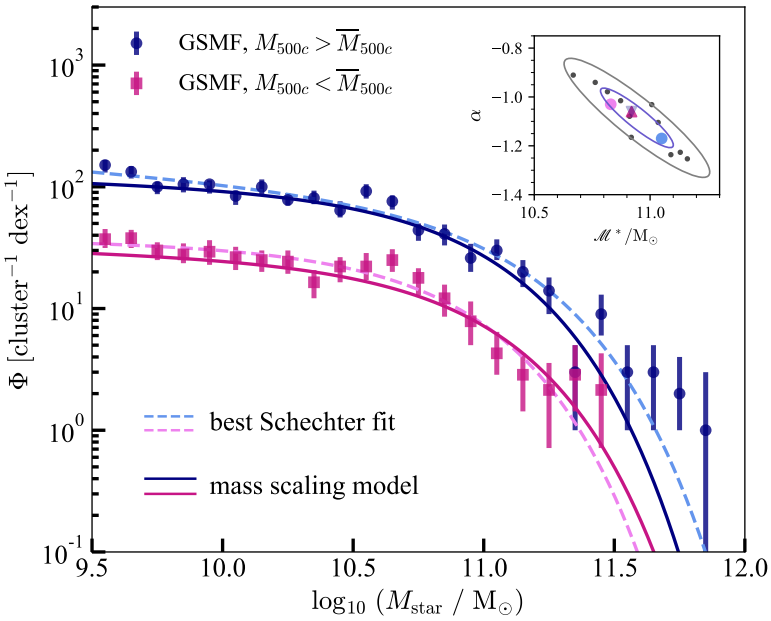

Figure 2.5: The stellar mass function (SMF) of the Hydrangea clusters in 2 mass bins at $z \approx 0.6$. The dark blue circles (magenta squares) show the stacked SMF of clusters with M_{500c} above (below) the mean $\overline{M}_{500c} = 1.6 \times 10^{14}\,\mathrm{M}_\odot$ of all the clusters; error bars represent 1σ uncertainties from bootstrapping (see text for details). Dashed lines show the best-fit Schechter functions for each set of points, while solid lines represent the output from our mass scaling model (details in Section 2.4.1) at the mean M_{500c} of each stack. The inset in the upper-right corner shows the correlation between the Schechter parameters α and $\mathscr{M}^*$ for the two stacks (light blue/magenta circles), the mass scaling model (dark magenta upward/dark blue downward triangles), and the 11 individual fits described in Section 2.4.1 (black circles). The blue and gray ellipses in the inset represent the 1σ and 2σ uncertainties for the fitted parameters. The simulated SMF is well-described by the mass-scaled Schechter function, but with some degeneracy between its parameters α and $\mathscr{M}^*$.

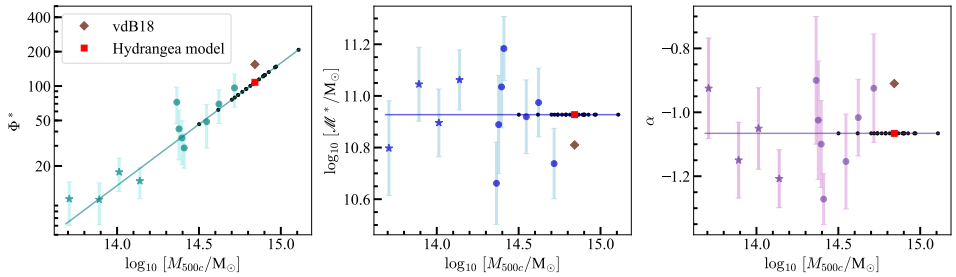

Figure 2.6: The best-fit Schechter function parameters of individual $z = 0.6$ simulated clusters (coloured circles), or stacks of four clusters with similar mass (coloured stars), as a function of cluster mass M_{500c}. From left to right, the panels show the variation in normalisation (Φ^*), characteristic mass ($\mathscr{M}^*$), and low-mass slope (α), respectively. The best-fit power law model to the Φ^*–M_{500c} relation, and the best-fit constant $\mathscr{M}^*$ and α, are shown with solid lines. Black dots represent the corresponding parameters predicted by these fits at the mass of observed clusters from Burg et al. (2018); the red square gives their weighted average (see text). The actual ensemble SMF parameters from the observations are shown as brown diamonds. These agree with the simulation predictions within the cluster-to-cluster scatter.

We fit it with a power-law in mass,

$$\Phi^* = a \cdot \left(\frac{M_{\mathrm{cluster}}}{M_{\mathrm{piv}}} \right)^b , \tag{2.3}$$

where M_{cluster} denotes the cluster mass (here M_{500c}, motivated by the use of that value by Burg et al. 2018), while a and b are the fitted parameters. The pivot mass M_{piv} is fixed to the mean M_{cluster} of all the objects included in the fit. The best-fit power law is shown as a turquoise solid line in Fig. 2.6; its index b is 1.07, i.e. a close-to-linear relation between Φ^* and M_{500c}. We note that the parameter Φ^* is closely related to the cluster richness; observationally, the cluster mass–richness relation follows a power-law with index b in the range 0.61–1.3 at $z \approx 0.6$ (Yee and Ellingson, 2003; Budzynski et al., 2012; Andreon and Congdon, 2014; Hurier, 2019). Encouragingly, the value we find from the simulations ($b = 1.07$) is well within this range.

The other two Schechter parameters, $\mathscr{M}^*$ and α, show no clear dependence on M_{500c} (middle and right-hand panels of Fig. 2.6). As shown in the top-right inset of Fig. 2.5, there is however a noticeable correlation (i.e. degeneracy) between these two parameters: higher $\mathscr{M}^*$ correlates with lower α. Since the majority of the individual best-fit parameters are consistent with a constant value of $\mathscr{M}^* = 10^{10.92}\,\mathrm{M}_\odot$ and

Table 2.1: Hydrangea model parameters for the Schechter function parameters of the simulated clusters at $z \approx 0.6$, $z \approx 1.0$, and $z \approx 1.3$.

Parameters →	$M_{\rm piv}$	Φ^*		$\log_{10} \mathscr{M}^*$	α
Redshift (z) ↓	$[10^{14}\ {\rm M}_\odot]$	a	b	$[{\rm M}_\odot]$	
0.6	1.59	22.10	1.07	10.92	−1.06
1.0	0.94	16.40	0.77	10.91	−0.99
1.3	0.89	13.91	1.05	10.83	−0.91

$\alpha = -1.06$, respectively, we therefore keep these values fixed in our mass dependence model.

In Fig. 2.5, we show the prediction from this mass-scaling model at the mean mass of the two cluster sets as solid lines. Although they do not trace the actual best-fit Schechter function (dashed lines) exactly – especially at the low-$M_\star$ end, they are biased low by ≈10–20 per cent – they clearly provide a comparably good description of the actual (binned) stellar mass functions.

We have repeated this procedure for $z = 1.0$ and $z = 1.3$, to enable GSMF comparisons to the *Planck*-SZ, GCLASS, and GOGREEN observations. In Table 2.1, we list the best-fit parameters a and b and the corresponding pivot masses $M_{\rm piv}$ for the power-law scaling of $\Phi^*(M_{\rm cluster})$, as well as the best-fit constant Schechter parameters $\mathscr{M}^*$ and α, for each of these three redshifts. We note that, for compatibility with the respective observational data, the $z = 0.6$ parameters use $M_{\rm 500c}$ as cluster mass, whereas those for $z = 1.0$ and $z = 1.3$ are based on $M_{\rm 200c}$.

The characteristic mass $\mathscr{M}^*$ and the low-mass slope α show only a slight variation between these three redshifts. The low-mass slope α increases by ≈14 per cent from $z = 0.6$ to $z = 1.3$, while $\mathscr{M}^*$ decreases by a similar amount, as expected from their anti-correlation at $z = 0.6$ (see the inset in Fig. 2.5). If real, the slight decrease in $\mathscr{M}^*$ could be interpreted as the most massive galaxies in the clusters ($M_\star > 10^{11}\,{\rm M}_\odot$) still growing at higher redshift. The power-law index for the scaling of Φ^* with cluster mass remains close to one (i.e. linear), although the pivot mass $M_{\rm piv}$ is (unsurprisingly) lower at higher redshift.

2.4.2 Confronting simulations and observations

Having constructed a model to scale the GSMF from Hydrangea to different cluster masses (Eqn. 2.3, Tab. 2.1), we now compare the simulation predictions to observations. To begin, we use the data of *Planck*-SZ selected clusters at $z \approx 0.6$ presented in Burg et al. (2018). We calculate the Schechter parameters predicted by our scaling

model for each of the observed clusters, based on their halo mass, and show these as small black circles[8] in each of the three panels of Fig. 2.6.

The ensemble average of each of these parameters is shown by the red squares in each panel. For $\mathscr{M}^*$ and α this is trivial, but for the normalization Φ^*, care must be taken to weight the individual clusters in a similar way as in the observations. Since more massive clusters will contain more galaxies and hence contribute more to the ensemble average, we weight the individual predictions (black circles) by the normalization Φ^* before estimating the ensemble average. The corresponding best-fit parameters for the observed clusters from Burg et al. (2018) are shown as brown diamonds. In all three cases, they lie close to the Hydrangea prediction, with an offset that is within the cluster-to-cluster scatter in the simulations.

In Fig. 2.7, we present our main result of the GSMF test by directly comparing the Schechter function predicted from the simulations (through our mass scaling model) to the observations. In the left-hand, central, and right-hand panels, respectively, we show as a red line the simulation predictions at $z = 0.6$ (with parameters as shown by the red squares in Fig. 2.6), $z = 1.0$, and $z = 1.3$. This is compared to the observationally measured GSMFs (black circles) from *Planck*-SZ (Burg et al., 2018), GCLASS (Burg et al., 2013), and GOGREEN (van der Burg et al., 2020) (black circles) and their best-fit Schechter functions (grey line), respectively.

For $z = 0.6$ (left-hand panel of Fig. 2.7), the predicted Schechter function agrees extremely well with its observational counterpart over the full stellar mass range we probe. At the highest masses ($M_\star > 10^{11.2}\,\mathrm{M}_\odot$), the Hydrangea prediction is marginally higher than the observational best-fit Schechter function from Burg et al. (2018). However, it is still fully consistent with the actual observational data points (black circles) within their (1σ) error bars.

The analogous comparison to GCLASS at $z \approx 1.0$ (Burg et al., 2013, middle panel of Fig. 2.7) and GOGREEN at $z \approx 1.3$ (van der Burg et al., 2020, right-hand panel) reveals similarly good agreement at $M_\star \gtrsim 10^{10.5}\,\mathrm{M}_\odot$. With respect to GCLASS, the high mass end of the predicted GSMF is slightly too high, although still consistent with the observed relation within its 1σ error (grey shaded band). The agreement with GOGREEN at the high-mass end is essentially perfect.

At the low-mass end ($M_\star \lesssim 10^{10.5}\,\mathrm{M}_\odot$), there is a significant discrepancy between the simulation and observations, in that the predicted GSMF is too high by a factor of up to ≈2 compared to both GCLASS and GOGREEN. Furthermore, there is *a clear qualitative difference between the shape of the simulated and observed Schechter*

[8] By construction, these all lie exactly along the best-fit line for each parameter.

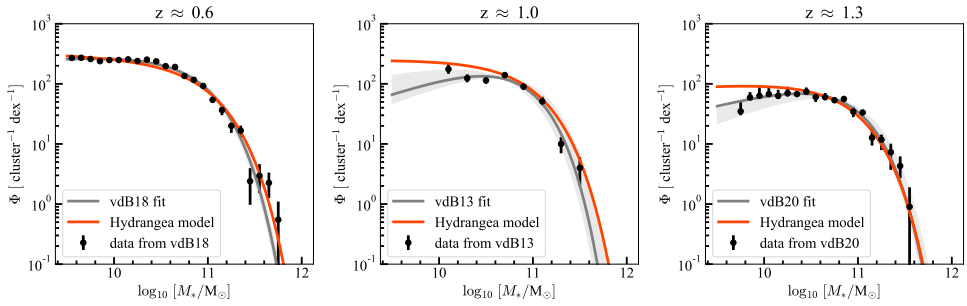

Figure 2.7: The stellar mass functions of the *Planck*-SZ clusters at $z \approx 0.6$ (Burg et al., 2018, left), the GCLASS clusters at $z \approx 1.0$ (Burg et al., 2013, middle), and the GOGREEN clusters at $z \approx 1.3$ (van der Burg et al., 2020, right) are shown as black circles with 1σ error bars, along with the best-fit Schechter functions from these papers (grey line, with 1σ uncertainty given by the light grey shaded region). Red lines represent the Schechter functions predicted from the Hydrangea simulations at the respective redshift and mean cluster mass. The simulations mostly agree with the observations, but predict too many low-mass galaxies ($M_\star \lesssim 10^{10.5}\,\mathrm{M}_\odot$) at $z \geq 1$, by up to a factor of ≈2.

functions at increasingly higher redshift: whereas the observed one shows a strong transition towards a down-turn at low masses (positive slope, i.e. $\alpha > -1$), the low-mass end of the Schechter function predicted by Hydrangea is closer to a flat profile with slow evolution at $0.6 \leq z \leq 1.3$. As noted above, the low-mass slope parameter α predicted by Hydrangea also increases towards higher redshift, corresponding to a (relative) decrease of the GSMF (reflected by a 14 per cent increase in α from $z = 0.6$ to $z = 1.3$) at the low-mass end. However, the redshift evolution is evidently much stronger in the real Universe, where α increases by 35 per cent from $z \approx 0.6$ to $z \approx 1.3$. This may hint at a failure in the simulation at disrupting low-mass satellites at $z \sim 1$ (see Bahé et al., 2019) or overly efficient star formation in low-mass galaxies (e.g. Furlong et al. 2015 also find a slightly too high field SMF at $M_\star < 10^{10}\,\mathrm{M}_\odot$ at these redshifts in EAGLE, see their fig. 2).

In principle, the discrepancy could also point to unaccounted systematic biases in the observations. While we note that multiple other studies have found a similar downturn (and flat slope) of the SMF at the low mass end (e.g., Annunziatella et al., 2014; Nantais et al., 2016; Papovich et al., 2018), these studies may conceivably all be biased in a similar way; below, we therefore discuss in detail why we are confident that this is not the case before proceeding.

A first concern may be incompleteness: although the GCLASS and GOGREEN analyses of Burg et al. (2013) and van der Burg et al. (2020) took particular care to ac-

count for this effect, the image simulations they used relied on assumptions about the properties of galaxies that were injected in these tests. Conceivably, a sub-population of very extended galaxies might therefore be missed in the data, since their low surface brightness makes them particularly difficult to observe. This would, however, require cluster galaxies to be biased to substantially larger sizes compared to the field, in contrast with current observational evidence (see e.g. Matharu et al. 2019 and references therein). Secondly, observational biases may arise from the membership correction, i.e. the separation of galaxies into true cluster members and fore- / background objects. However, the GCLASS and GOGREEN analyses correct for this via spectroscopic data sets (see van der Burg et al. 2020) and conclude from extensive tests that their results are robust. A third source of bias might be the stellar masses measurement of individual galaxies from SED fits, which require assumptions on the star formation history and the initial mass function (IMF). Differences in the assumed IMF in particular can affect the inferred stellar mass by a factor of $\approx$2 (Marchesini et al., 2009). However, since the simulations broadly match the observed field SMF at these redshifts (Furlong et al., 2015), invoking this explanation would require a very strong dependence of the IMF on environment, an assumption for which there is currently neither observational nor theoretical support. In short, none of these options is likely to yield a bias in the observations at the level of the discrepancy evident from Fig. 2.7.

Coming back to the simulations, the low-mass slope of the the field SMF at similar redshift, as reported by Furlong et al. (2015), is significantly steeper than what we find in the Hydrangea clusters: at $z = 0.5$ (2.0), Furlong et al. (2015) found a best-fit Schechter parameter $\alpha = -1.45$ (-1.57), compared to $\alpha = -1.06$ (-0.99) in the Hydrangea clusters. In addition, we note that the field SMF evolves towards a slightly steeper low-mass slope (more negative α) with increasing redshift (see table A1 of Furlong et al. 2015), whereas the cluster environment (and interestingly also the field observations of Muzzin et al. 2013) evolve towards a flatter or even inverted slope (less negative α). Both differences indicate that, at the intermediate redshifts we probe, the cluster environment has a substantial impact on the SMF and hence allows an additional, and almost independent, test of the simulation model.

2.5 Radial satellite density profiles within the clusters

In the previous sections, we have demonstrated that the Hydrangea clusters successfully reproduce the scaling between the observed total stellar mass fractions and cluster mass (Sec. 2.2.3), as well as the GSMF down to $\approx 3 \times 10^{10}\,\mathrm{M}_{\odot}$ up to $z \approx 1.5$, and down to at least $\approx 6 \times 10^{9}\,\mathrm{M}_{\odot}$ at $z \approx 0.6$ (Sec. 2.4). Therefore, we now investigate the radial distribution of cluster satellites over time, comparing it to both observations and to the corresponding evolution of the dark matter (DM) distribution. As well as testing the simulations in an additional way that is orthogonal to the GSMF, we also aim to shed light on the previously reported difference between the observed increase in satellite concentration with redshift and the predicted decrease of the DM halo concentration (Burg et al., 2015, see the Introduction).

The density profile of relaxed DM haloes in N-body simulations, as well as the DM component of haloes in hydrodynamical simulations (Schaller et al., 2015b) are robustly described by the NFW profile (Navarro et al. 1997, see also Dubinski and Carlberg 1991), which has the form

$$\frac{\rho(r)}{\rho_{cr}} = \frac{\delta_c}{\frac{r}{r_s}\left(1+\frac{r}{r_s}\right)^2}. \tag{2.4}$$

Here, ρ_{cr} is the critical density of the Universe, while δ_c and r_s are the characteristic amplitude parameter and scale length of the profile, respectively, that can alternatively be expressed in terms of the halo radius $r_{200\mathrm{c}}$ and concentration parameter $c = r_{200\mathrm{c}}/r_s$. In the following analysis, we use the NFW profile in Eqn. 2.4 to model the density profiles of both the DM and of the stars contained in the Hydrangea cluster satellites[9], and carefully compare them with the observational results of Burg et al. (2015). For simplicity, we will generally refer to the NFW concentration parameter c as "the concentration" for the remainder of this Section.

2.5.1 Evolution of the DM halo concentration

As an initial check, we derive the evolution of the DM halo concentration from the 3D distribution of individual DM particles. For this, we calculate the density of DM

[9]Recall that we are measuring the profile of satellites around the cluster, weighted by their stellar mass, rather than the distribution of stars within individual satellites.

particles in 20 consecutive shells, logarithmically spaced between 0.01 and 1.0 r_{200c} and centred on the cluster potential minimum[10]. We include all DM particles within a given shell, irrespective of their subhalo membership. The resulting (3D) density profiles are fit with the NFW functional form (eq. 2.4) to obtain the characteristic radius r_s and hence the concentration c, following e.g. Neto et al. (2007) and Schaller et al. (2015b). We repeat this process for each of the 24 Hydrangea clusters at 15 snapshots in the range $0 \leq z < 2$, and from these calculate the average concentration of the cluster ensemble and its confidence interval at each redshift.

The result is shown by the black line and grey shaded region in Fig. 2.8. In comparison with previous works (e.g. Springel, 2005; Neto et al., 2007; Duffy et al., 2008; Dutton and Macciò, 2014), we find a qualitatively similar evolution of the DM halo concentration, decreasing by ≈20 per cent from $z = 0$ to $z = 2$. At a given redshift, the concentrations we measure are slightly higher than reported in some earlier studies, as expected from the difference in cosmological parameters (Dutton and Macciò, 2014).

2.5.2 Concentration of stellar density profile

We now analyze the corresponding galaxy density profile and its evolution. For consistency with observations, we use 2D profiles here, which we obtain by projecting the galaxy coordinates (relative to the cluster centre) along each of the three principal coordinate axes of the simulation; each galaxy is weighted by its stellar mass (which we measure within 30 pkpc, see Sec. 2.2.2) to yield a 2D galaxy density profile. With the exception of the cluster BCG, we include all galaxies with stellar mass $M_\star > 10^9\,\mathrm{M}_\odot$ [11]within a cylinder of radius $2 \times R_{200c}$ and (total) length along the projection axis equal to $4 \times R_{200c}$ (we have verified that our results are insensitive to the choice of cylinder length[12] and minimum M_* in range 10^8 – $10^9\mathrm{M}_\odot$). We then calculate the surface density within concentric annuli whose edge radii are spread linearly between 0.01 and $0.1 \times R_{200c}$ ($\Delta R/R_{200c} = 0.03$), and logarithmically between 0.1 and $2 \times R_{200c}$ ($\Delta \log R = 0.19$).

An important subtlety in this procedure is the way in which fore- and background

[10]This radial range extends closer to the cluster centre than in e.g. Neto et al. 2007, which is possible due to the higher resolution of our simulations. Gao et al. (2008) have shown that this leads to a $\lesssim$10 per cent higher best-fit concentration, which is of no significance to our results.

[11]This stellar mass limit is chosen to match that of Burg et al. (2015). At higher redshift, the data from Burg et al. (2014) have a stellar mass limit of $M_\star \geq 10^{10.2}\,\mathrm{M}_\odot$, but we have verified that this difference affects the best-fit NFW concentration only at a level $\ll 1\sigma$.

[12]In the central region ($R_{2D} \leq 0.5 \times R_{200c}$), the density increases by <1 per cent if the cylinder length is increased further, from 4 to $6 \times R_{200c}$.

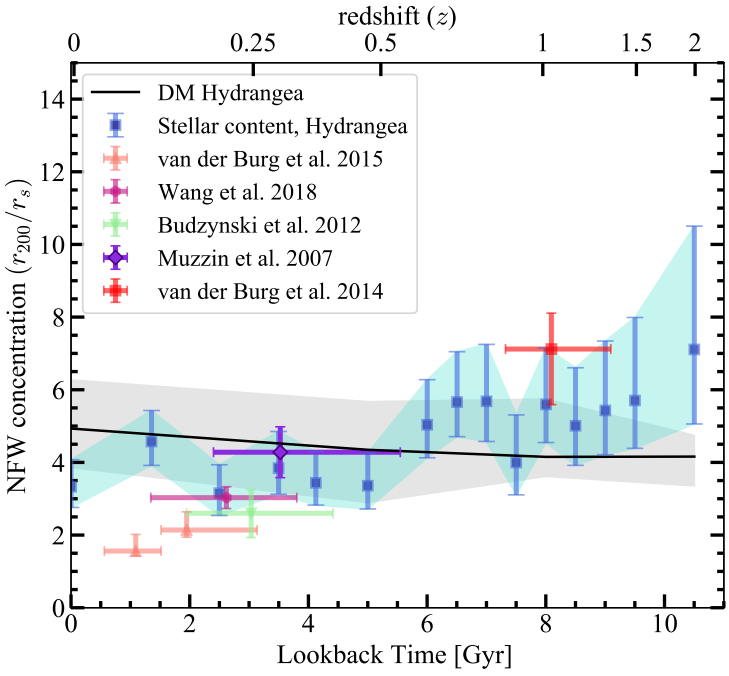

Figure 2.8: The redshift evolution of the NFW concentration of the dark matter (DM) halo and satellite galaxies for the Hydrangea clusters (black line and blue squares, respectively, with the shaded band and error bars enclosing regions with fitting $\chi^2 \leq 1$).The light-orange, light-green, magenta, purple, and red symbols represent corresponding observational measurements of the satellite galaxy concentrations from Muzzin et al. (2007), Budzynski et al. (2012), Burg et al. (2014), Burg et al. (2015), and Wang et al. (2018), respectively. At $z \geq 0.25$, the simulations predict the same increase in galaxy concentrations with redshift as observed, while the DM halo concentration decreases. At low z, however, the simulated galaxy distribution is more strongly concentrated, by a factor of $\approx$2.

galaxies are accounted for. Owing to the zoom-in nature of the Hydrangea simulations, our projected profiles cannot contain a contribution from galaxies at very large line-of-sight distances from the cluster, but correlated line-of-sight structures are still captured by the large Hydrangea zoom-in regions. For approximate consistency with the observational approach, we estimate and subtract the contribution of these nearby fore-/background galaxies to the projected galaxy density, rather than e.g. applying a cut in 3D radius or FoF membership. For this, we calculate the expected field galaxy density in each bin based on the galaxy volume density of the EAGLE S15_AGNdT9-L0050N0752 simulation (Schaye et al., 2015), and subtract this from the surface density we measure for the Hydrangea clusters. This correction does not make any significant difference to the surface densities ($< 0.17\%$ at all radii up to R_{200c}, and $< 1\%$ at $R_{200c} < R < 2 \times R_{200c}$), and does not affect the shapes of the density profiles.

We use EAGLE S15_AGNdT9-L0050N0752 to derive the field galaxy density, rather than a volume near the edge of the Hydrangea simulations, because we have found that even near the edge of the zoom-in regions, the GSMF still has a slightly higher normalization (see Appendix 2.6). This is not unexpected: clusters sit at the centre of large-scale overdensities in the cosmic web, with many galaxies merging into smaller groups before falling into the cluster halo instead of falling into the cluster halo individually from the field (e.g. McGee et al., 2009).

To reduce statistical noise, we stack the individual density profiles (in units of R/R_{200c}) from the 24 clusters at each redshift to obtain the average density profile for the simulation suite. As an example, Fig. 2.9 shows the density profile at $z = 0.101$ as dark-blue circles. 1σ uncertainties on the surface density in each bin, shown by dark-blue error bars, are obtained from 100 bootstrap re-samplings of galaxies (from the full stack) with replacement, with the total number drawn in each instance equal to the total number of galaxies in the stack. To reduce the dynamic range, we show the profile multiplied by R/R_{200c}. In this form, it shows – as expected for an NFW profile – a marked downturn at $R \gtrsim 0.2R_{200c}$, and a similar, but weaker, drop towards lower R.

We fit each stacked density profile with the 2D projected NFW profile (Bartelmann, 1996),

$$\Sigma(x) = \frac{2\rho_s r_s}{x^2 - 1} f(x) \tag{2.5}$$

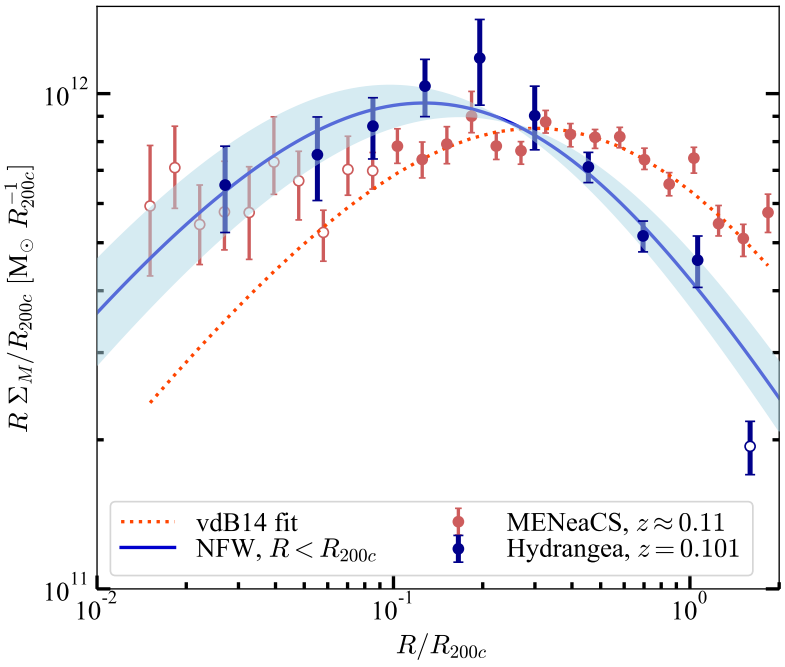

Figure 2.9: The stellar mass density distribution of the Hydrangea cluster ensemble at $z = 0.101$. The dark-blue circles are the average surface densities at corresponding radial bins of the ensemble of 24 clusters. The dark-blue error bars are obtained from 100 bootstrap re-samplings with replacement from the full stack of galaxies. The blue solid line is the best-fit 2D projected NFW profile within R_{200c} and the shaded light-blue region shows the $\Delta\chi^2 = 1$ region for the fitted concentration parameter. Dark-orange circles represent the MENeaCS GSMF from Burg et al. (2015) with their best-fit NFW profile shown as the dotted red line; both have been renormalized by the ratio of mean cluster masses in MENeaCS and Hydrangea (= 1.4) to enable an unbiased comparison. Filled circles represent bins included in the fit (for both the simulated and observed data), while open ones were excluded.

where $x \equiv r/r_s$ and

$$f(x) = \begin{cases} 1 - \frac{2}{\sqrt{x^2-1}} \arctan\sqrt{\frac{x-1}{x+1}}, & (x \geq 1) \\ 1 - \frac{2}{\sqrt{1-x^2}} \operatorname{arctanh}\sqrt{\frac{1-x}{1+x}}, & (x \leq 1) \\ 0, & (x = 1), \end{cases}$$

to obtain the concentration parameter, minimizing the χ^2 value between the functional form and the densities in each bin. For the $z \approx 0.1$ example shown in Fig. 2.9, the best-fit NFW profile is shown as a solid blue line, with the light blue shaded band marking the region that is covered by $\Delta\chi^2 \leq 1$ values of the fit. Within the uncertainties, this fit provides a good description of the density profile.

A point worth mentioning here is that the NFW profile is fitted only within a (projected) radius of 1, rather than $2 \times R_{200c}$, from the cluster centre of potential as in most of the observational studies that we compare to. As can be seen in Fig. 2.9, the rightmost dark-blue point (open circle) at $R > R_{200c}$ lies far below the best-fit NFW profile. Including this point in the fitting procedure would drive up the best-fit concentration and force a shift of the blue line towards the right side of the figure, resulting in an overall much worse fit (both visually and in terms of the best-fit χ^2 value). This behaviour is present in all the snapshots within the redshift range $0 < z < 2$. Therefore, we conclude that the stellar surface density profile of the Hydrangea clusters is well represented by the NFW profile only up to a distance of R_{200c} from the cluster centre, and use this radial distance limit in our fitting procedure for all the redshifts. This changed radial limit compared to the observations may lead to a slight difference in the estimated value of the concentration. However, as the concentration of the density profile is mainly dependant on the characteristic radius r_s in terms of including the radial range, having extended profiles beyond r_{200} does not make any significant difference to the estimation for the concentration range we are concerned about in this work ($r_s \leq 0.7 \times r_{200}$ for $c \geq 1.5$).

At each redshift, we calculate the best-fit satellite concentration for three orthogonal projections as described above. Figure 2.8 shows the evolution of the mean satellite concentration (averaged over all three projections) over redshift as blue points, with error bars representing the standard deviation between projections. The area within the error bars is shaded light blue for clarity. The light-orange, light-green, magenta, purple, and red symbols show observationally measured satellite concentrations over different redshift ranges, as indicated by the horizontal error bar (Muzzin et al., 2007; Budzynski et al., 2012; Burg et al., 2014; Burg et al., 2015; Wang et al., 2018).

Compared to the DM concentration (black line and gray shaded region), the satellite concentration clearly shows a different trend with redshift, especially at $z \geq 0.5$ where they are higher by up to a factor of 2. The predicted satellite concentrations agree well with what is observed at both $z \approx 1$ (Burg et al., 2014, red circle) and $z \approx 0.3$ (Muzzin et al., 2007, purple diamond), strongly suggesting that this is difference is not an artefact of the simulation. At lower redshift, $z < 0.5$, the satellite concentration in Hydrangea closely traces that of the DM halo. This is in marked contrast to the MENeaCS data of Burg et al. (2015), which indicate a continued decrease in satellite concentration with time, down to $c \lesssim 2$ at $z = 0$: at the present day, the Hydrangea concentrations are more than a factor of two higher than what is observed.

2.5.3 Interpreting the concentration evolution of DM and satellites

Burg et al. (2015) interpreted their finding of decreasing satellite concentration with time as evidence for an inside-out growth of the satellite halo of massive clusters: at high redshift, satellites are strongly concentrated towards the cluster centre, but over time new satellites are preferentially added to the cluster outskirts while tidal stripping reduces the mass (or even number) of satellites at small cluster-centric radii (see also Bahé et al. 2019). The excellent match between the satellite concentrations predicted by Hydrangea and inferred from observations at redshifts $z \gtrsim 0.25$ supports this picture: high-redshift satellite haloes are indeed more concentrated than the diffuse DM haloes built up at the same time. *The observational finding that the satellite concentrations are higher than DM haloes from N-body simulations is therefore a consistent prediction of* Λ*CDM*, rather than an indicator for incompleteness in the high-redshift observations or tensions with the cosmological model.

At lower redshift, however, the Hydrangea simulations are clearly in disagreement with observations on the satellite halo profile: the predicted concentrations are too high by more than a factor of two. The seemingly unchanged concentration at $z \lesssim 0.5$ in the simulations suggests almost self-similar galaxy cluster growth at all radial distances, in contrast to the inside-out scenario indicated by the observations. This tension is somewhat surprising: given that the EAGLE simulation model was calibrated against observations of the local, rather than high-redshift, Universe, one might instead have expected the simulation to match the observed satellite concentrations better at lower redshifts.

To investigate this discrepancy further, we plot the observed satellite density profile

from the MENeaCS clusters (Burg et al., 2015) in Fig. 2.9 as dark-orange points, with the dotted red line giving the best-fit projected NFW profile as found by these authors. To account for the slightly mass offset between MENeaCS and Hydrangea, these observed densities have been scaled by a factor of 1.4, the ratio of the mean cluster masses in MENeaCS and Hydrangea at $z = 0.1$ (see Sec. 2.3.1). Burg et al. (2015) reported an over-dense central region within $0.1 \times R_{200c}$ that can not be fitted with an NFW profile (shown with dark-orange open circles), and therefore restricted their fit to the range $0.1 < R/R_{200c} < 2.0$ where their profile is well described by an NFW profile with concentration parameter $c = 2.03 \pm 0.2$ (data points shown by filled grey circles in Fig. 2.9). The corresponding best-fit Hydrangea profile (blue line in Fig. 2.9, with a concentration parameter of $c = 4.5 \pm 1.01$) likewise provides a good fit to the simulated satellite profile.

Comparing the individual bin densities, the simulations predict an approximately realistic satellite density within $\approx$0.1 R_{200c} of the cluster centre (the simulated densities are $\approx$15 per cent higher, but this is still within the uncertainties). A more significant excess ($\approx$30 per cent) is predicted around $\approx$0.2 R_{200c}, followed by a similarly large shortfall at R_{200c}. To see whether the Hydrangea and MENeaCS satellite density profiles are compatible in terms of their total stellar mass, we have integrated them over the range $0.1 < R/R_{200c} < 1.0$. With the normalization correction as described above, the two profiles are within 10 per cent of each other in terms of total mass (slightly higher for MENeaCS). Consistent with our earlier results (Section 2.2.3), this confirms that the total stellar mass of the low-z Hydrangea satellite haloes is realistic, while its radial distribution is not.

While the low concentration of cluster satellite haloes in the local Universe is observationally well-established (Lin et al., 2004; Budzynski et al., 2012; Burg et al., 2015), the picture is less clear on the theoretical side. In a semi-analytic model of galaxy formation, Wang et al. (2014) have found that the distribution of satellites around massive isolated galaxies traces almost exactly that of the DM halo, as is the case in Hydrangea. These authors speculate that poor modelling of tidal disruption in their model may be the reason for the overly steep satellite halo profile, but this process is accounted for self-consistently in hydrodynamical simulations such as Hydrangea. In the BAHAMAS simulation[13], McCarthy et al. (2017) obtain a best-fit concentration of $c \approx 1.8$, in close agreement with the observations of Burg et al. (2015). In detail, however, their (3D) profile also shows a slight ($\approx$10 per cent) excess compared to the

[13]Like Hydrangea, this is a cosmological hydrodynamic simulation, but it models a large volume at much lower resolution.

observations at $r/r_{200c} \approx 0.3$, and follows a DM-like profile with $c = 4$ at larger radii (their fig. 9).

It is therefore unclear at present whether the tension in the low-redshift satellite halo concentrations is a particular shortcoming of Hydrangea, or may be a more generic deficiency of cosmological simulations; further work analysing the predictions from other recent theoretical models is necessary to establish a clearer picture. Two factors that might bias the satellite halo concentration high in Hydrangea are the selection of the clusters to be relatively isolated at low redshift – which might, conceivably, increase the fraction of clusters that have undergone significant merging shortly before $z = 0$, and have not yet reached an equilibrium state – and their overly massive BCGs (Bahé et al., 2017). The latter shortcoming, which is similarly affecting other simulations (e.g. Pillepich et al., 2018), may influence the dynamics, and hence density, of the central satellite halo, although we found in Fig. 2.9 that the differences between Hydrangea and the MENeaCS data of Burg et al. (2015) primarily originate in the cluster outskirts. More work is necessary to establish whether either of these aspects is related to the overly concentrated profile of satellite haloes in Hydrangea clusters.

2.6 Summary and Conclusions

Observations have shown that the high-redshift satellite galaxy haloes of massive clusters were significantly more concentrated than in the present Universe, while DM halo concentrations are predicted to evolve in the opposite direction. To gain insight into the nature of this evolution, we have analyzed the stellar content, galaxy stellar mass function, and satellite halo concentration in the Hydrangea suite of 24 massive galaxy clusters ($M_{200c} > 10^{14}\,\mathrm{M}_\odot$ at $z = 0$) over the redshift range $0 < z < 2$. From this analysis, including comparison to observational data up to $z \approx 1.3$, we draw the following conclusions:

- Stellar masses of simulated galaxies, as measured with the SUBFIND halo finder and within an aperture of 30 pkpc, agree well with masses recovered from synthetic images with SEXTRACTOR; they can therefore be compared meaningfully to stellar masses obtained from observational data (Fig. 2.3).

- The scaling relation of the cluster stellar mass fraction with respect to the cluster mass predicted by the Hydrangea simulations at $0.1 < z < 1.4$ agrees well with the equivalent relation reported from observational data (Chiu et al., 2018): the offsets in the best-fit power law index (1 per cent) and normalization (12.5 per

cent) are (well) within 1σ uncertainties. The total stellar content of Hydrangea clusters is therefore realistic out to at least $z = 1.4$ (Fig. 2.4).

- The galaxy stellar mass functions of Hydrangea clusters are well described by Schechter functions, whose best-fit normalization Φ^* depends approximately linearly on cluster mass, whereas the characteristic mass $\mathscr{M}^*$ and low-mass slope α show no significant trend with mass (Fig. 2.6). From this Φ^*–$M_{\rm cluster}$ relation, we have constructed a scaled Schechter function to compare the Hydrangea predictions to observations of clusters with moderately different masses (Table 2.1).

- Accounting for differences in the cluster mass distribution, the satellite GSMF predicted by Hydrangea shows an excellent match to observations up to $z = 1.3$, at $M_\star > 10^{10.5}\,{\rm M}_\odot$. At $M_\star < 10^{10.5}\,{\rm M}_\odot$, the predicted GSMF from Hydrangea is higher than observed by up to a factor of $\approx$2 and the simulations do not reproduce the qualitative shift from a negative to positive low-mass slope that is seen in observations. The best-fit α parameter also increases in the simulations, but only by 14 per cent, as opposed to a 35 per cent increase in the observations (Fig. 2.7).

- The concentration of the satellite halo profile (weighted by stellar mass) in Hydrangea clusters is up to a factor of 2 higher than that of the DM halo at redshift $z \gtrsim 0.5$, in agreement with observations. This discrepancy therefore stems from differences in the assembly of the satellite and DM halo; the high satellite concentrations are fully consistent with expectations from ΛCDM (Fig. 2.8).

- At low redshift ($z \lesssim 0.3$), the satellite halo concentration in Hydrangea clusters closely matches that of the DM halo and is too high by a factor of $\approx$2 at $z = 0$ compared to observations (Fig. 2.8). From a direct comparison of the full satellite halo profile to observations at $z = 0.1$, the simulations predict a satellite halo density that is too high in the inner part ($\approx 0.2\ R_{\rm 200c}$) and too low at larger radii ($\gtrsim 0.3\ R_{\rm 200c}$), both by factors of $\approx$30 per cent (Fig. 2.9). The physical origin of this inaccuracy, which has also been reported from a semi-analytic galaxy formation model (Wang et al., 2014), remains unclear.

Our analysis confirms that the Hydrangea simulations, and the underlying EAGLE simulation model, predict broadly realistic stellar properties of galaxy clusters, not just at low redshift (Bahé et al., 2017), but also across more than half the history of the Universe. They can therefore be used to make meaningful predictions about

the transformation of cluster galaxies, and the environmental mechanisms that cause them. At the same time, there are clear deviations from the real Universe in detail: at high redshift the simulations contain too many low-mass galaxies, and at low redshift the satellite halo is too concentrated. Both deficiencies may be related to overly efficient star formation in the simulations, or alternatively due to stellar stripping being suppressed by the limited resolution or as a consequence of too high stellar concentration within satellites. Future simulations can use these diagnostics to improve the fidelity of galaxy formation modelling.

Acknowledgements

The authors acknowledge support from the Netherlands Organization for Scientific Research (NWO) under Vici grant number 639.043.512 (SLA, HH), and Veni grant number 639.041.751 (YMB). YMB also acknowledges funding from the EU Horizon 2020 research and innovation programme under Marie Skłodowska-Curie grant agreement 747645 (ClusterGal). The Hydrangea simulations were in part performed on the German federal maximum performance computer "HazelHen" at the maximum performance computing centre Stuttgart (HLRS), under project GCS-HYDA / ID 44067 financed through the large-scale project "Hydrangea" of the Gauss Center for Supercomputing. Further simulations were performed at the Max Planck Computing and Data Facility in Garching, Germany. This work used the DiRAC@Durham facility managed by the Institute for Computational Cosmology on behalf of the STFC DiRAC HPC Facility (www.dirac.ac.uk). The equipment was funded by BEIS capital funding via STFC capital grants ST/K00042X/1, ST/P002293/1, ST/R002371/1 and ST/S002502/1, Durham University and STFC operations grant ST/R000832/1. DiRAC is part of the National e-Infrastructure.

This work has made use of Python (http://www.python.org), including the packages **numpy** (Harris et al., 2020) and **scipy** (http://www.scipy.org). Plots have been produced with **matplotlib** (Hunter, 2007).

Data Availability

The data presented in the figures are available upon request from the corresponding author. The raw simulation data can be requested from the C-EAGLE team (Bahé et al., 2017; Barnes et al., 2017).

References

Alonso Asensio, I., Dalla Vecchia, C., Bahé, Y. M., et al., 2020, MNRAS, 494, 1859
Andreon, S. and Congdon, P., 2014, A&A, 568, A23
Annunziatella, M., Biviano, A., Mercurio, A., et al., 2014, A&A, 571, A80
Bahé, Y. M., Schaye, J., Barnes, D. J., et al., 2019, MNRAS, 485, 2287
Bahé, Y. M. et al., 2017, MNRAS, 470, 4186
Balogh, M., Morris, S., and Yee, H., 1999, ApJ, 527, 54,
Barnes, D. J., Kay, S. T., Bahé, Y. M., et al., 2017, MNRAS, 471, 1088
Barnes, D. J., Kay, S. T., Henson, M. A., et al., 2017, MNRAS, 465, 213
Bartelmann, M., 1996, A&A, 313, 697
Behroozi, P. S., Wechsler, R. H., and Wu, H.-Y., 2013, ApJ, 762, 109
Bertin, E. and Arnouts, S., 1996, Astron. Astrophys. Suppl. Ser., 117, 393
Bertin, E. and Arnouts, S. (Oct. 2010). *SExtractor: Source Extractor*. ascl: 1010.064.
Blanton, M. R., Eisenstein, D., Hogg, D. W., et al., 2005, ApJ, 629, 143
Brown, T., Catinella, B., Cortese, L., et al., 2017, MNRAS, 466, 1275
Budzynski, J. M., Koposov, S. E., McCarthy, I. G., et al., 2012, MNRAS, 423, 104
Burg, R. F. van der, Muzzin, A, Hoekstra, H, et al., 2014, A&A, 561, A79
Burg, R. F. van der, Hoekstra, H., Muzzin, A., et al., 2015, A&A, 577, A19
Burg, R. F. van der et al., 2013, A&A, 557, A15
Burg, R. F. van der et al., 2018, A&A, 618, A140
Cañas, R., Elahi, P. J., Welker, C., et al., 2019, MNRAS, 482, 2039
Chiu, I., Mohr, J., McDonald, M., et al., 2016, MNRAS, 455, 258
Chiu, I., Mohr, J. J., McDonald, M., et al., 2018, MNRAS, 478, 3072
Chiu, I., Saro, A., Mohr, J., et al., 2016, MNRAS, 458, 379
Crain, R. A., Schaye, J., Bower, R. G., et al., 2015, MNRAS, 450, 1937
Dalla Vecchia, C. and Schaye, J., 2012, MNRAS, 426, 140
Davé, R., Anglés-Alcázar, D., Narayanan, D., et al., 2019, MNRAS, 486, 2827
Deason, A. J., Oman, K. A., Fattahi, A., et al., 2020, arXiv e-prints, arXiv:2010.02937
Dolag, K., Borgani, S., Murante, G., et al., 2009, MNRAS, 399, 497
Dressler, A., 1980, ApJ, 236, 351
Dubinski, J. and Carlberg, R. G., 1991, ApJ, 378, 496
Dubois, Y., Pichon, C., Welker, C., et al., 2014, MNRAS, 444, 1453
Duffy, A. R., Schaye, J., Kay, S. T., et al., 2008, MNRAS, 390, L64
Dutton, A. A. and Macciò, A. V., 2014, MNRAS, 441, 3359
Fabello, S., Kauffmann, G., Catinella, B., et al., 2012, MNRAS, 427, 2841
Foreman-Mackey, D., Hogg, D. W., Lang, D., et al., 2013, Publications of the Astronomical Society of the Pacific, 125, 306
Furlong, M., Bower, R. G., Theuns, T., et al., 2015, MNRAS, 450, 4486
Gao, L., Navarro, J. F., Cole, S., et al., 2008, MNRAS, 387, 536
Giovanelli, R and Haynes, M., 1985, ApJ, 292, 404
Gonzalez, E. J., Chalela, M., Jauzac, M., et al., 2020, MNRAS, 494, 349
Harris, C. R., Jarrod Millman, K., van der Walt, S. J., et al., 2020, arXiv e-prints, arXiv:2006.10256
Hess, K. M. and Wilcots, E. M., 2013, Astronomical Journal, 146, 124
Hunter, J. D., 2007, Computing in science & engineering, 9, 90
Hurier, G., 2019, arXiv e-prints, arXiv:1904.07610
Kauffmann, G., White, S. D. M., Heckman, T. M., et al., 2004, MNRAS, 353, 713
Lin, Y.-T., Mohr, J. J., and Stanford, S. A., 2004, ApJ, 610, 745
Ludlow, A. D., Schaye, J., Schaller, M., et al., 2019, MNRAS, 488, L123
Mahler, G., Sharon, K., Fox, C., et al., 2019, ApJ, 873, 96
Marchesini, D., van Dokkum, P. G., Förster Schreiber, N. M., et al., 2009, ApJ, 701, 1765
Matharu, J., Muzzin, A., Brammer, G. B., et al., 2019, MNRAS, 484, 595
McCarthy, I. G., Schaye, J., Bird, S., et al., 2017, MNRAS, 465, 2936

McGee, S. L., Balogh, M. L., Bower, R. G., et al., 2009, MNRAS, 400, 937
Mihos, J. C., Harding, P., Feldmeier, J., et al., 2005, ApJL, 631, L41
Montes, M. and Trujillo, I., 2018, MNRAS, 474, 917
Muñoz-Cuartas, J. C., Macciò, A. V., Gottlöber, S., et al., 2011, MNRAS, 411, 584
Muldrew, S. I., Pearce, F. R., and Power, C., 2011, MNRAS, 410, 2617
Muzzin, A., Marchesini, D., Stefanon, M., et al., 2013, ApJS, 206, 8
Muzzin, A., Marchesini, D., Stefanon, M., et al., 2013, ApJ, 777, 18
Muzzin, A., Yee, H. K. C., Hall, P. B., et al., 2007, ApJ, 659, 1106
Nantais, J. B., van der Burg, R. F. J., Lidman, C., et al., 2016, A&A, 592, A161
Navarro, J. F., Frenk, C. S., and White, S. D. M., 1996, ApJ, 462, 563
Navarro, J. F., Frenk, C. S., and White, S. D., 1997, ApJ, 490, 493
Neto, A. F., Gao, L., Bett, P., et al., 2007, MNRAS, 381, 1450
Odekon, M. C., Koopmann, R. A., Haynes, M. P., et al., 2016, ApJ, 824, 110
Old, L. J., Balogh, M. L., van der Burg, R. F. J., et al., 2020, MNRAS, 493, 5987
Papovich, C., Kawinwanichakij, L., Quadri, R. F., et al., 2018, ApJ, 854, 30
Pearson, R. J., Ponman, T. J., Norberg, P., et al., 2015, MNRAS, 449, 3082
Peng, Y., Lilly, S. J., Kovač, K., et al., 2010, ApJ, 721, 193
Pillepich, A., Nelson, D., Hernquist, L., et al., 2018, MNRAS, 475, 648
Pillepich, A., Springel, V., Nelson, D., et al., 2017, MNRAS, 473, 4077
Planck Collaboration XVI, 2014, A&A, 571, A16
Rosas-Guevara, Y., Bower, R., Schaye, J, et al., 2015, MNRAS, 454, 1038
Schaller, M., Dalla Vecchia, C., Schaye, J., et al., 2015, MNRAS, 454, 2277
Schaller, M., Frenk, C. S., Bower, R. G., et al., 2015, MNRAS, 452, 343
Schaye, J., 2004, ApJ, 609, 667
Schaye, J., Crain, R. A., Bower, R. G., et al., 2015, MNRAS, 446, 521
Schaye, J. and Dalla Vecchia, C., 2008, MNRAS, 383, 1210
Schechter, P., 1976, ApJ, 203, 297
Springel, V., 2005, MNRAS, 364, 1105
Springel, V., White, S. D. M., Tormen, G., et al., 2001, MNRAS, 328, 726
van der Burg, R. F. J., Rudnick, G., Balogh, M. L., et al., 2020, A&A, 638, A112
Vulcani, B., De Lucia, G., Poggianti, B. M., et al., 2014, ApJ, 788, 57
Wang, C., Li, R., Gao, L., et al., 2018, Monthly Notices of the Royal Astronomical Society, 475, 4020
Wang, W. and White, S. D. M., 2012, MNRAS, 424, 2574
Wang, W., Sales, L. V., Henriques, B. M. B., et al., 2014, MNRAS, 442, 1363
Weinmann, S. M., Van Den Bosch, F. C., Yang, X., et al., 2006, MNRAS, 372, 1161
Wetzel, A. R., Tinker, J. L., and Conroy, C., 2012, MNRAS, 424, 232
Wiersma, R. P. C., Schaye, J., Theuns, T., et al., 2009, MNRAS, 399, 574
Wiersma, R. P., Schaye, J., and Smith, B. D., 2009, MNRAS, 393, 99
Williams, L. L. R., Sebesta, K., and Liesenborgs, J., 2018, MNRAS, 480, 3140
Woo, J., Dekel, A., Faber, S. M., et al., 2012, MNRAS, 428, 3306
Yang, X., Mo, H. J., and van den Bosch, F. C., 2009, ApJ, 695, 900
Yee, H. K. C. and Ellingson, E., 2003, ApJ, 585, 215
Zhang, Y., Yanny, B., Palmese, A., et al., 2019, ApJ, 874, 165

Appendix A

Testing different noise levels for SMF recovery from synthetic images

In Sec. 2.2.2, we verified that the SUBFIND subhalo catalogues from the simulation output yield satellite stellar masses that are compatible with those derived by SEXTRACTOR from synthetic images. In Fig. 2.3, we showed the comparison of the SMF obtained from SUBFIND and SEXTRACTOR run on synthetic images that include noise at an RMS level of 1.5×10^6 $M_\odot$ per pixel. In Fig. 2.A.1, we show the analogous comparison to the SMF derived from SUBFIND (blue) and synthetic images (magenta) with three different RMS noise levels: 7.5×10^5 (left), 3.0×10^6 (middle), and $6.0 \times 10^6\,M_\odot\,\mathrm{pixel}^{-1}$ (right); except for the different noise levels, these are produced in exactly the same way as described in Sec. 2.2.2. Error bars represent the Poisson errors obtained from 100 bootstrap re-samplings of the stack of galaxies in each sample. In each case, the stellar mass functions from SUBFIND and those from the synthetic images agree within their uncertainties. Likewise, the best-fit Schechter functions to the SMFs (solid lines) all agree well within the error bars with the one from SUBFIND.

On closer inspection, however, two subtle trends of the best-fit Schechter functions with respect to the injected noise level become detectable. Firstly, the best-fit low-mass slope parameter α from the SEXTRACTOR catalogues (magenta text) is systematically lower than its SUBFIND equivalent (blue text), at all noise levels, even though the discrepancy is only at the $\approx 1\sigma$ level. This shift in α is mainly caused by projections at the lower mass end. As the SEXTRACTOR output gives the stellar masses of all the diffuse line-of-sight star particles from the simulation region along the direction of the projection, it increases the total stellar mass of each source by a small value even if there is only one source along the line of sight. This increase in the stellar mass is more significant for galaxies with a stellar mass lower than 10^9 $M_\odot$. We have verified that this is indeed the explanation by comparing the stellar masses of the detected and matched sources between SUBFIND and SEXTRACTOR outputs for all the stellar masses (not shown here).

Secondly, the best-fit characteristic mass $\mathscr{M}^*$ from SEXTRACTOR decreases systematically with increasing noise levels, while it is (unsurprisingly) constant for SUBFIND. Conceivably, this is because in noisier images, SEXTRACTOR recovers less stellar

mass for the individual sources. This loss is more prominent at the high-mass end, where galaxies have more extended and diffuse stellar haloes that become lost in the noise. Because of this, galaxies with true stellar mass above 10^{10} $M_\odot$ are assigned a lower stellar mass by SExtractor, lowering $\mathscr{M}^*$. To confirm and quantify the trend of lower $\mathscr{M}^*$ with noise levels, and resolve the apparent paradox that the best match to Subfind is seen for the highest noise level, we have fitted the SExtractor SMFs with Schechter functions again, but with α fixed to the Subfind average of -1.02 (not shown here). In this case, the lowest noise level yields a best-fit value of $\mathscr{M}^* = 10^{10.92}\,M_\odot$, very close to the Subfind value of $10^{10.94}$ $M_\odot$); the value then decreases with increasing noise (by $\approx$0.1 dex at the highest noise level), consistent with the trends in Fig. 2.A.1.

The slight difference in the fitted α value of the SMF from the Subfind outputs is caused by the matching of detected sources with the SExtractor output. The change is $<< 1\sigma$ value of the fitted α parameter, and therefore, considered negligible in this case.

From the close agreement between the simulations and the synthetic images for all the four different noise levels we have tested for, we conclude that the subhalo stellar mass within 30 pkpc as measured by the Subfind code can be reliably used for the analysis presented in the main text. However, the slight variation of the SMF shape with noise level may indicate that at higher redshifts, where the noise levels in the observed data are higher, our use of Subfind masses may cause a very small positive bias in the massive end of the GSMF.

Appendix B

Fitted Schechter function parameters

In Table 2.B.1, we list the best-fit Schechter parameters for the individual Hydrangea clusters, or stacks thereof, at $z \approx 0.6$. These data correspond to what is plotted in Fig. 2.6 in the main paper.

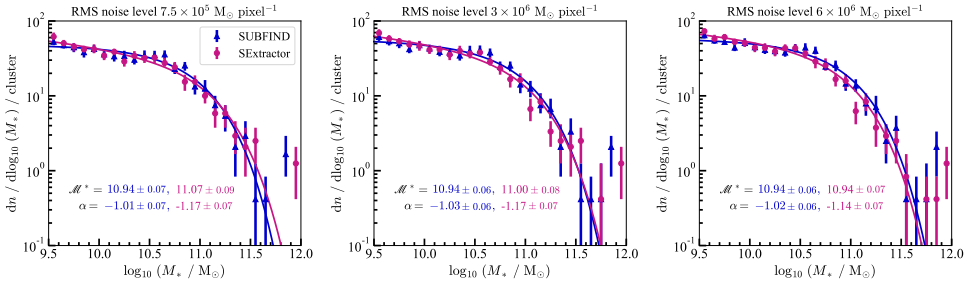

Figure 2.A.1: The galaxy stellar mass function (GSMF) of the simulated clusters (coloured symbols) and their best-fit Schechter functions (solid lines) for RMS noise levels of 7.5×10^5 (left), 3.0×10^6 (middle), and 6.0×10^6 $M_\odot$ pixel^{-1} (right). For all the panels, the blue points are obtained from the subhalo stellar mass measured by SUBFIND within 30 pkpc from the centre of potential of each subhalo; magenta points are obtained from the estimated stellar mass of each galaxy by running SEXTRACTOR on synthetic images (see Sec. 2.2.2 for details). The error bars indicate 1σ uncertainties obtained from bootstrap re-samplings of the stack of galaxies in each sample. Both the mass functions and their Schechter fits agree within statistical uncertainties, indicating that the SUBFIND mass measurement is consistent with the observational approach.

Table 2.B.1: Fitted parameters for the Schechter function of the simulated clusters at $z = 0.6$. The left column indicates the cluster number from the Hydrangea suite. M_{500c} indicates the corresponding cluster halo mass at that redshift. Φ^* is the overall normalization, M^* is the characteristic mass, and α is the low-mass slope. The first four results are from groups of four low-mass clusters each with $M_h \leq 1.75 \times 10^{14} M_\odot$. The group ID in the first column is given with increasing average halo mass of the cluster groups, and the average halo mass is given in the second column with the individual cluster halo mass.

Cluster ID	M_{500c} $[10^{14} M_\odot]$	Φ^*	$\log_{10}[M^*/M_\odot]$	α
Cgr-1	0.51	10.29 ± 4.24	10.79 ± 0.18	-0.93 ± 0.16
Cgr-2	0.78	10.16 ± 4.07	11.05 ± 0.14	-1.15 ± 0.12
Cgr-3	1.02	17.68 ± 5.75	10.89 ± 0.13	-1.05 ± 0.13
Cgr-4	1.38	14.78 ± 4.46	11.06 ± 0.11	-1.21 ± 0.09
CE-12	2.39	42.20 ± 19.54	10.89 ± 0.19	-1.02 ± 0.19
CE-18	2.49	35.15 ± 14.59	11.03 ± 0.16	-1.10 ± 0.14
CE-22	4.19	69.62 ± 22.71	10.97 ± 0.13	-1.02 ± 0.12
CE-24	3.52	48.75 ± 20.10	10.92 ± 0.14	-1.15 ± 0.15
CE-25	2.32	72.26 ± 25.41	10.66 ± 0.16	-0.90 ± 0.20
CE-28	2.57	28.75 ± 9.62	11.18 ± 0.12	-1.27 ± 0.08
CE-29	5.21	96.38 ± 31.04	10.74 ± 0.14	-0.92 ± 0.17

Appendix C

Comparison to the field environment

The outer regions of galaxy clusters are observed to have higher number density of galaxies compared to the average field environment. Therefore, before estimating the radial density profile of the clusters in Sec. 2.5.1, we subtract the average field density from the stellar density profile obtained from the Hydrangea clusters. To approximate the field environment, we test with the cluster SMF at different 2D projected annuli at increasing distances from the center of potential of the clusters ($3R_{200c} < R < 5R_{200c}$ to $8R_{200c} < R < 10R_{200c}$) and compare with field SMF from observational data at $z \approx 0.6$ from Burg et al. (2018). We observe a steady trend of the SMF having lower normalization at higher radial distance from the cluster center. However, even at the projected annulus between $8R_{200c} < R < 10R_{200c}$, the cluster SMF has a higher normalisation factor compared to the observed field SMF as shown by the open blue diamonds (Hydrangea and $8R_{200c} < R < 10R_{200c}$) and black circles (COSMOS/UltraVISTA field SMF from Burg et al. (2018)) in Fig. 2.A.1. The field SMF matched within errorbars with the observations after re-normalizing the matter density in the simulated clusters with the average density of the universe (green squares in Fig. 2.A.1). To recheck, we compare the SMF with the field SMF from the EAGLE run S15_AGNdT9-L0050N0752 (Schaye et al., 2015) at $z \approx 0.6$ and it matched with the observations (red stars in Fig. 2.A.1). This indicates that even at a large distance from the cluster center, the outskirts of the simulated clusters are over-dense compared to the average field environment.

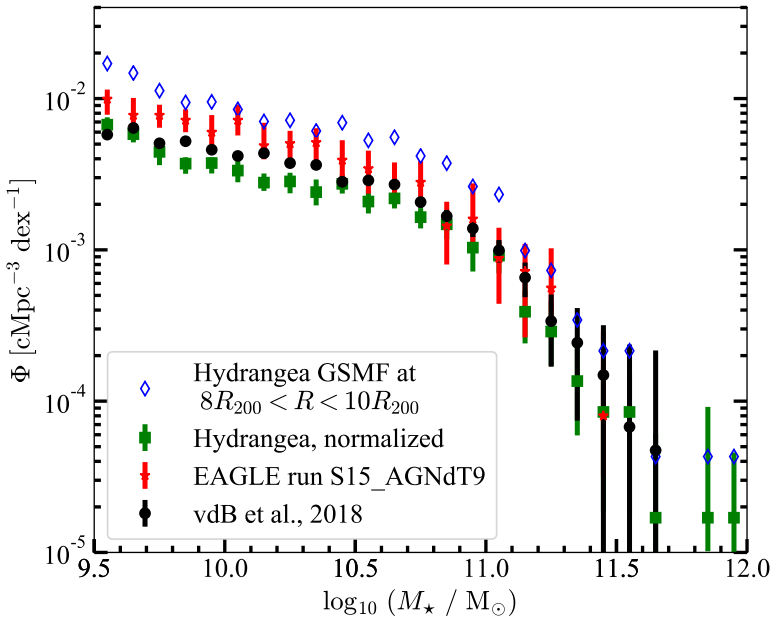

Figure 2.A.1: The galaxy stellar mass function (SMF) from simulations and observation at $z \approx 0.6$. The black circles show the SMF of the field environment from the observational data from COSMOS/UltraVISTA survey (Burg et al., 2018). The open blue diamonds are the SMF from the Hydrangea simulations at a projected distance range $8 \times R_{200c} < R < 10 \times R_{200c}$ from the centre of potential of each central galaxy clusters. The green squares are the same SMF shown in the blue open diamonds, re-normalized with the average density of the Universe at this redshift. The red stars are SMF from the EAGLE run S15_AGNdT9-L0050N0752 (Schaye et al., 2015).

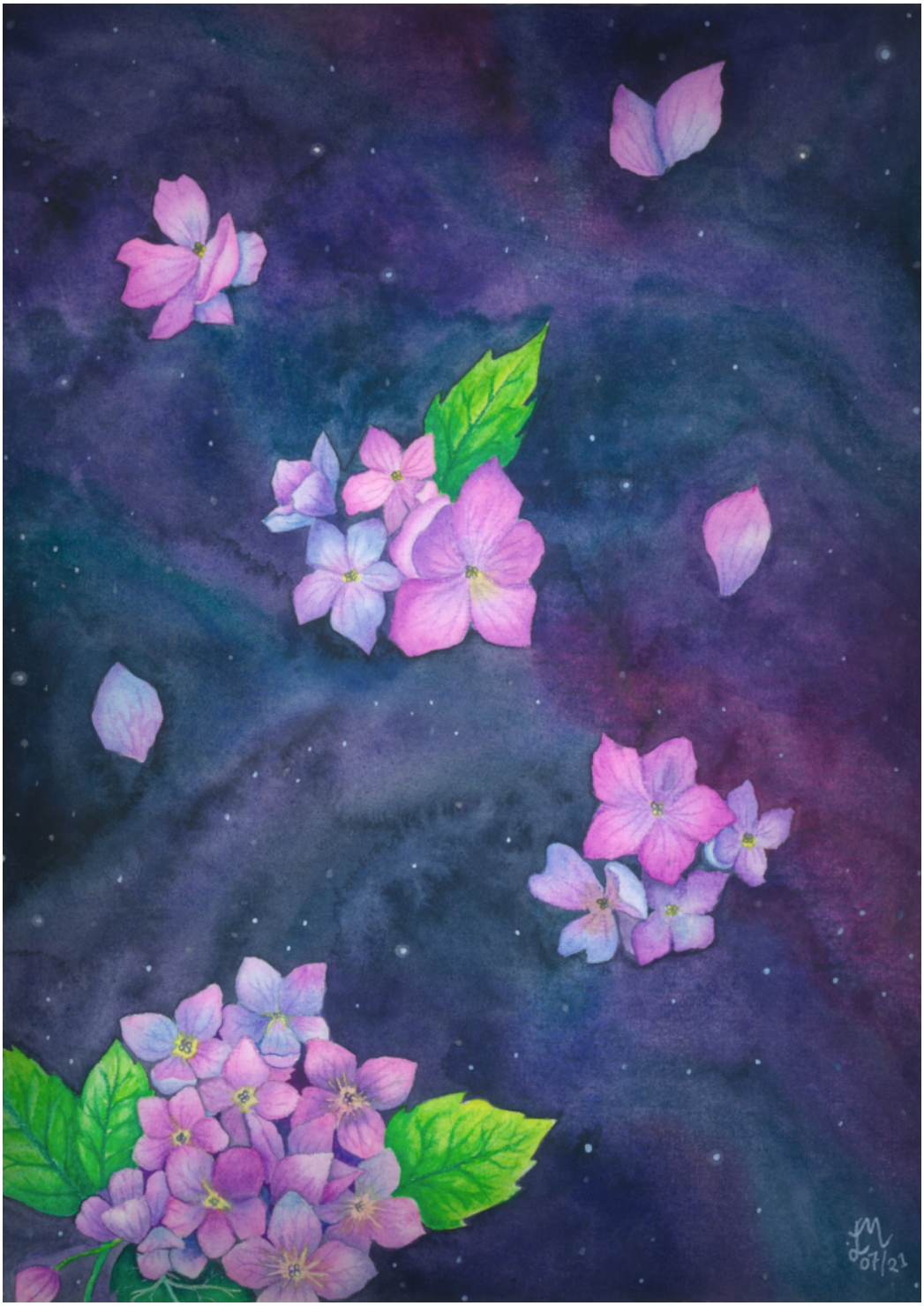
07/21

3

How to Interpret Measurements of Diffuse Light in Stacked Observations of Groups and Clusters of Galaxies

Abstract

The diffuse light within galaxy groups and clusters provides valuable insight into the growth of massive cosmic structures. Groups are particularly interesting in this context, because they represent the link between galactic haloes and massive clusters. However, low surface brightness makes their diffuse light extremely challenging to detect individually. Stacking many groups is a promising alternative, but its physical interpretation is complicated by possible systematic variations of diffuse light profiles with other group properties. Another issue is the often ambiguous choice of group centre. We explore these challenges using mock observations for 497 galaxy groups and clusters with halo masses from $\sim 10^{12}\mathrm{M}_\odot$ to $1.5\times10^{15}\mathrm{M}_\odot$ at redshift 0.1 from the Hydrangea cosmological hydrodynamic simulations. In 18 per cent of groups with at least five galaxies above $10^9\mathrm{M}_\odot$ in stellar mass, the r-band brightest galaxy is not the one at the centre of the gravitational potential; line-of-sight projections account for half of these cases. Miscentring does not significantly affect the ensemble average mass density profile or the surface brightness profile for our sample: even within ambiguously centred haloes, different centring choices lead to only a 1 per cent change in the total fraction of diffuse intra-group light, f_{IGL}. We find strong correlations of f_{IGL} with the luminosity of the central group galaxy and halo mass. Stacking groups in narrow bins of central galaxy luminosity will therefore make the physical interpretation of the signal more straightforward than combining systems across a wide range of mass.

Ahad, S. L., Bahé, Y. M., Hoekstra, H., 2023, MNRAS, 518, 3685

3.1 Introduction

According to the hierarchical structure formation model from the Λ-cold dark matter (ΛCDM) cosmological paradigm, large-scale structures in the Universe, such as galaxy groups and clusters, assembled via the merging and accretion of smaller systems. During this assembly, the tidal stripping of stars from galaxies and the accretion of smaller systems by the central galaxy produces a diffuse stellar component that surrounds the dominant galaxies in groups and clusters of galaxies. This is most clearly visible around the brightest galaxies in massive clusters (BCGs), where the diffuse low surface brightness light is more commonly referred to as the intracluster light (ICL). The radial extent of ICL around BCGs and the contribution of the ICL in the total light from groups and clusters can provide important constraints for cosmic structure formation. As this diffuse light can extend out to hundreds of kilo-parsecs from the cluster centre and often envelops multiple galaxies in the cluster, it is commonly considered a separate component of the galaxy groups and clusters (for recent reviews, see, e.g. Mihos, 2015; Contini, 2021; Montes, 2022).

In recent years, there have been increasing efforts to study the ICL in clusters, both by using high-quality data for individual clusters (e.g. Mihos et al., 2005; Montes and Trujillo, 2014, 2018; Jiménez-Teja et al., 2018; DeMaio et al., 2018, 2020; Montes et al., 2021), or by stacking a statistical sample of groups/clusters to improve the signal-to-noise-ratio (SNR, e.g. Zibetti et al., 2005; Zhang et al., 2019). Depending on the methods used to separate the ICL from the BCG light, the ICL can comprise more than 30% of the total star light of the host cluster (e.g. Zibetti et al., 2005; Gonzalez et al., 2013; Mihos et al., 2017; Montes and Trujillo, 2018; Zhang et al., 2019; Kluge et al., 2021), although a consensus about the ICL fraction is yet to be reached from both the simulation and observation sides (see, e.g. table 1 from Kluge et al., 2021). Through a large number of simulation studies, the origin and growth of the ICL have been attributed to multiple channels (see e.g. Mihos et al. 2017 and Contini 2021 for more discussion on the origin and growth of the ICL) , including galaxy mergers (Murante et al., 2007), tidal stripping (Gallagher and Ostriker, 1972), galaxy disruption (Guo et al., 2011), and even in-situ star formation in the intracluster medium (Puchwein et al., 2010; Tonnesen and Bryan, 2012). Some recurring findings from recent studies are that the ICL mass distribution follows the global dark matter (DM) distribution, both in observations (e.g. Montes and Trujillo, 2019) and simulations (e.g. Alonso Asensio et al., 2020), and that ICL profiles align more with the underlying cluster halo than with the BCG (Kluge et al., 2021), making the ICL an indirect probe for tracing the

build-up of the structures. These findings collectively confirm that the ICL growth is indeed connected to the evolution of the large elliptical galaxies such as the BCG, the baryon fraction of galaxy clusters, and the build-up of large scale structures like galaxy clusters where the giant galaxies (BCG) reside.

Although most works are based on clusters, because the ICL is more prominent within these most massive haloes and clusters are preferentially targeted by deep surveys such as the Hubble Frontier Fields (HFF) (Lotz et al., 2017) or BUFFALO (Steinhardt et al., 2020), studying the diffuse light in groups, or 'intragroup light' (IGL) is particularly interesting for several reasons. Groups cover the intermediate halo mass regime of cosmic structures between galaxy-mass haloes and galaxy clusters. They are also the main building blocks of clusters. Therefore, understanding the build-up of the diffuse stellar component in groups will improve our understanding of the growth of ICL in clusters. Also, compared to clusters, groups are dynamically less disturbed, have had fewer interactions with other systems, and are more concentrated. As a result, it is more straightforward to connect the growth of the IGL in groups with their dynamical history.

Even though the importance of understanding the buildup of IGL/ICL across a wide range of host halo mass has been recognized for a while, there have only been a few studies on the diffuse light in a large enough sample of group-mass haloes so far (Zibetti et al., 2005; Poliakov et al., 2021). From the observational side, the main reason behind this is the lack of a reliable group catalogue with large enough sample size. Zibetti et al. (2005) studied the diffuse light in 683 SDSS groups and clusters by stacking them to increase the SNR and found that the surface brightness of the diffuse light correlates with BCG luminosity and with cluster richness, but the fraction of the total light in the diffuse component does not vary notably with these properties. However, they only studied these behaviours by dividing their sample in two sub-samples for each property which may not be representative of the full variation of these properties. The dependence of the diffuse light fraction on different group properties (e.g. group halo mass, richness) therefore still remains an open question and needs to be studied with multiple approaches to be well-understood. With high-quality multi-band (u, g, r, i) photometry of the Kilo Degree Survey (KIDS, De Jong et al., 2013) and a group catalogue (Robotham et al., 2011) based on the highly complete spectroscopic Galaxy and Mass Assembly (GAMA, Driver et al., 2009; Driver et al., 2011) survey, it is now possible to push the detection limit of the diffuse light into group-mass haloes and improve the interpretation of the data.

Studying the light distribution of individual groups is useful to understand the

diversity of the IGL signal and their formation channels. However, the low surface brightness of the IGL means that individual systems have a very low SNR, which results in a higher uncertainty in the interpretations. Stacking the light of multiple groups can help to improve the SNR while keeping the key features of the underlying population. However, before simply stacking all the group data, we need to consider a few caveats. In previous group catalogues, the group centres were determined by either taking the centre of the distribution of light, or the brightest galaxy, or the galaxy with the highest stellar mass in the system. Stellar-to-halo-mass-relations (SHMR) have also been used to utilize the halo mass to determine the physical halo centre, but they were mainly assuming a monotonic relation that assigned a fixed halo mass for a fixed galaxy luminosity irrespective of their colour (see e.g. sec. 1.1 of Tinker 2022 for more discussion on this). However, in recent years, it has been shown that the SHMR for central galaxies depends on their colour: a bluer central typically resides in a less massive halo compared to a red central of the same stellar mass (e.g. Bilicki et al., 2021; Mandelbaum et al., 2016). This calls for a re-estimation of the group centres in existing group catalogues, especially the ones that were based on only stellar mass or luminosity. The obvious question is whether this improves our estimates of the group centres. Specifically, how can we determine a spurious central estimation and adjust for any biases that are introduced by such miscentring? And if we are indeed misidentifying an appreciable fraction of group centres, how much does it affect the IGL estimation? Exploring these questions is particularly important to ensure that stacking will actually improve the SNR – not make it worse by adding unwanted signals from miscentred groups and that analysing the stacked profile will provide us with unbiased interpretations regarding the IGL.

Another issue is the dependence of variation in the IGL/ICL distribution on the properties of the central galaxy and the host system. Contini and Gu (2021) reported that the ICL fraction and distance from the centre to where ICL dominates the total galaxy mass vary widely (from 15 kpc to 100 kpc) depending on the morphology (bulge or disk dominated) and dynamical history of the BCG. Kluge et al. (2021) found a positive correlation between BCG+ICL brightness and the host cluster mass, cluster size (radius), and integrated light in the satellites. Therefore, while stacking the group profiles, it is necessary to quantify the effect of galaxy properties and to find the optimal way of scaling and stacking to ensure a robust interpretation of the profiles.

The arguably easiest way to explore this is by using cosmological hydrodynamic simulations. In recent years, their fidelity has improved enough to help us understand

such intricate details as the IGL (see e.g. Oppenheimer et al., 2021, for a recent review). The Hydrangea simulation suite of 24 massive galaxy clusters (Bahé et al., 2017) is an excellent sample to study the IGL around groups because they are specifically made to study galaxy evolution in and around large scale structures. The simulations have also been successful in reproducing the stellar mass distribution of satellite galaxies in both the local Universe (Bahé et al., 2017; Barnes et al., 2017) and intermediate to high redshift ($0.6 < z < 2.0$, Ahad et al., 2021) for galaxy clusters.

In this paper, we explore the impact of miscentring in galaxy groups on the IGL measurements in them with the analysis of simulated data (Hydrangea) that are matched to an observational dataset (GAMA). We also study the extent of the IGL around the group centre to determine the best way of stacking galaxy groups to interpret the IGL signal.

The organization of the paper is as follows. In Sec. 3.2, we describe the Galaxy And Mass Assembly (GAMA) survey data, our group sample selection from the KiDS+GAMA overlap, and test how using a colour-dependent SHMR affects the group centre selection for the GAMA group sample. We describe the Hydrangea simulation suite in Sec. 3.3. Here, we also discuss the group sample selection from the simulations and preparation of the mock photometric data. In Sec. 3.4, we explore the effects of possible miscentring on the IGL measurements by means of the density profiles and the surface brightness profiles of the simulated sample. We discuss the dependence of the measured IGL fraction on different properties of the brightest group galaxy (BGG) and host group properties, and the radial $u-r$ colour profile of the BGG+IGL in Sec. 3.5. Finally, we summarize our conclusions in Sec. 3.6.

3.2 GAMA group data

3.2.1 Galaxy and Mass Assembly survey data

The Galaxy And Mass Assembly (GAMA) galaxy survey (Driver et al., 2009; Driver et al., 2011; Driver et al., 2022) is a unique project with 21-band photometric data and spectroscopic redshifts of $\sim 300,000$ galaxies. It is 98.5% complete for SDSS-selected galaxies with $r < 19.8$ mag. The spectroscopic survey was conducted using the AAOmega multi-object spectrograph on the Anglo-Australian Telescope to measure galaxy spectra in five fields covering a total of ~ 286 deg^2 area, which provided detailed redshift sampling.

In our work, we used the latest GAMA-II Galaxy Group Catalogue (G^{3}CFOFv08,

Robotham et al., 2011), generated using a friends-of-friends (FOF) based grouping algorithm in which galaxies are grouped based on their line-of-sight and projected physical separations, and the accompanying galaxy catalogue G^{3}CGalv09 (Liske et al., 2015). The catalogue consists of 23654 groups across all the GAMA fields and $N_{\rm FOF} \geq 2$ spectroscopically confirmed member galaxies. To ensure the most robust group selection, we only considered groups with $N_{\rm FOF} \geq 5$ here. We also used the stellar mass estimates as well as $u-$ and $r-$band magnitudes of GAMA galaxies from the StellarMassesLambdarv20 catalogue (Taylor et al., 2011; Wright et al., 2016), which includes physical parameters based on stellar population fits to rest-frame $ugrizY$ SEDs, and matched aperture photometry measurements of SDSS and VIKING photometry for all the $z < 0.65$ galaxies from the GAMA Panchromatic Data Release (Driver et al., 2016). This sample contains over 198,000 galaxies, with a median $\log(M_\star/{\rm M}_\odot) \approx 10.5$ assuming $H_0 = 70{\rm km\ s^{-1}Mpc^{-1}}$. Further details on the GAMA stellar mass derivation can be found in Taylor et al. (2011) and Wright et al. (2016).

Four of the GAMA fields (equatorial G09, G12, and G15 of 60 deg^2 each, and southern G23 of 51 deg^2) entirely overlap with the Kilo Degree Survey (KiDS, De Jong et al., 2013) – a large, deep, multi-band optical imaging survey that is designed for measuring cosmological parameters and covers 1350 deg^2 in four broadband filters (u, g, r, i). The GAMA group catalogue, accompanied by the deep KiDS imaging (mean limiting $m_r = 25.02$ at 5σ significance in a $2''$ aperture, mean FWHM of the $r-$band PSF $0\farcs7$, sampling $0\farcs213$/pixel) from data release 4 (DR4, Kuijken et al., 2019) provides us with a unique opportunity to analyse the IGL around the low-mass galaxy groups, which we present in a companion paper (Ahad et al., in prep.). In order to make our results from this work more applicable to the IGL measurement in GAMA groups with KiDS imaging, we considered only GAMA+KiDS cross-matched groups in our sample. With an additional $N_{\rm FOF} \geq 5$ selection cut, we obtained a final sample of 2385 groups which we used in this work.

3.2.2 Challenges in identifying the central galaxy in groups

In the GAMA group catalogue (G^{3}CFOFv08), plausible central galaxy candidates in each group are selected in three ways (Robotham et al., 2011): (i) taking the galaxy at the centre of light (CoL) distribution; (ii) taking the brightest galaxy in the group; and (iii) with an iterative method that starts by taking the group light distribution and then successively discards the galaxy that is the farthest from the CoL. The process is iterated until only two galaxies are left in the group, after which the brighter one

is chosen as the central galaxy. After comparing to a mock galaxy catalogue obtained from populating the Millenium dark-matter simulations (Springel, 2005) with galaxies using the GALFORM (Bower et al., 2006) semi-analytic model, Robotham et al. (2011) concluded that the iterative method provided the most robust selection of the centrals and recommended the selected galaxy with this method as the optimal group centre candidate. Throughout this paper, these iterative centres from the GAMA group catalogue are referred to as the G3C centrals.

Selecting the centre of light or the brightest galaxy in the halo provides a plausible estimate of the halo centre in most cases. This is because the brightest galaxy is typically expected to have more stars (as a result, more mass) than the rest of the group galaxies, and therefore is located at the centre of potential of the halo. But this is not always the case – the mass-to-light ratio is different based on galaxy colours. This means that at a fixed luminosity, a bluer galaxy will have lower stellar mass compared to a redder galaxy (e.g. Van Sande et al., 2015; García-Benito et al., 2019). Moreover, at a fixed stellar mass, the stellar-to-halo-mass ratio is also observed to be different for red and blue galaxies. Using weak lensing measurements for the halo mass of the bright galaxy sample from the KiDS (which include the central galaxies from the KiDS+GAMA overlap), Bilicki et al. (2021) studied the SHMR separately for blue and red galaxies. They reported that for the same stellar mass ($M_\star$), redder galaxies typically reside in a more massive halo compared to the bluer ones (see their fig.9). The difference can be a factor of two at $M_\star < 5 \times 10^{10} h^{-2} \mathrm{M}_\odot$, which is the mass of most of the group centrals in our sample, and even more at higher $M_\star$s. Combined with the colour-dependent mass-to-light ratio, this implies that even if a blue central candidate emits more light, it may have a lower total (baryon + DM) mass than a slightly less massive red central candidate and therefore may not actually sit at the centre of potential of the group halo. This insight calls for a revisit of the GAMA group catalogue to see how robust the G3C central selection is when accounting for a colour-dependent SHMR.

Following the example of fig. 6 of Bilicki et al. (2021), we examined the distribution of GAMA group galaxies (both satellites and centrals) in the rest-frame $(u-r)$ colour vs r-band magnitude parameter space (all magnitudes are obtained from the StellarMassesLambdarv20 catalogue), and separated them into blue and red samples. Figure 3.1 shows the 2D histogram of the GAMA group galaxies in purple. A clear separation in colour is evident from the distribution, divided by a straight line with slope -0.04 and intercept 0.7 (black dashed line) to separate the red galaxies (above) from the blue (bottom) ones. This separating line qualitatively agrees with that from

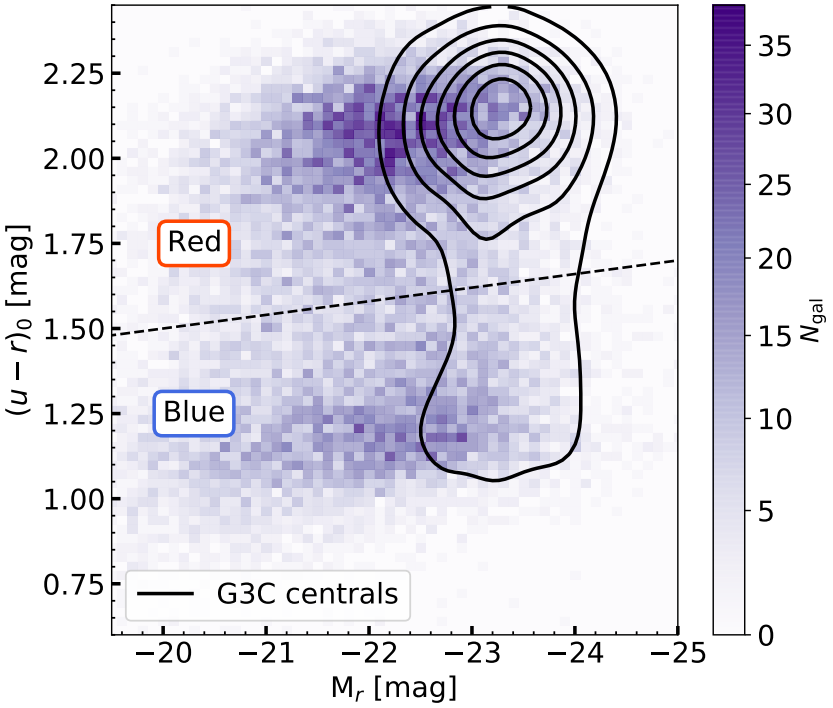

Figure 3.1: The rest frame $(u-r)$ colour of all the GAMA galaxies in our sample (purple). Black contours show the Gaussian kernel density estimation of the rest frame $(u-r)$ colour of the GAMA group centrals in our sample. The black dashed line is used to separate the sample into red (above) and blue (below) galaxies. As expected, the centrals are indeed the brightest galaxies in the entire sample. A non-negligible fraction (28%) of them are blue, which are conceivably misidentified as centrals (see text).

Bilicki et al. (2021), although they used a different colour $(u-g)$ to separate their sample into red and blue galaxies. The distribution of the G3C centrals is shown by the black contours, which are the normalized Gaussian kernel density estimates of the centrals. Unsurprisingly, these are located at the brightest end of the galaxy distribution. More noteworthy, however, is the fact that, although most centrals are "red" according to our definition, a non-negligible minority (28%) lie below our dividing line and are hence classified as "blue".

Using the colour distribution of the GAMA galaxies, we selected the three brightest galaxies (r-band magnitude) from each of the GAMA groups in our sample and assigned a halo mass to each of them by inverting the best-fit SHMR for the appropriate

colour found by Bilicki et al. (2021)(their eqn. 7):

$$M_\star(M_\mathrm{h}) = M_0 \frac{(M_\mathrm{h}/M_1)^{\gamma_1}}{[1+(M_\mathrm{h}/M_1)]^{\gamma_1-\gamma_2}} \tag{3.1}$$

Here, $M_\star$ is the stellar mass, M_h is the corresponding halo mass, and M_0, M_1, γ_1, and γ_2 are constants that are assigned different values depending on whether the galaxy in consideration is blue or red (see table 3 of Bilicki et al. 2021).

Only the brightest three galaxies from each group were considered to remain within the brightness and stellar mass range considered by Bilicki et al. (2021). We picked the galaxy with the highest predicted halo mass as the new central galaxy candidate for the groups because the galaxy with the highest halo mass is likely to have the deepest gravitational potential, and consequently to reside at the centre of potential of the host group. The rest-frame $(u-r)$ colour distribution of the central galaxy candidates from the original GAMA catalogue and our updated sample are shown in Fig. 3.2 in purple and orange histograms, respectively. Out of the 2385 groups in our sample, the fraction of blue centrals has decreased from 28% to 4.4% in our updated central galaxy candidates. Repeating the same procedure but this time selecting the three galaxies with the highest stellar mass from each GAMA group in our sample, resulted in a similar central galaxy re-assignment. However, the validity of these re-assigned central candidates must be checked before drawing any definite conclusion on whether it actually provides a physically more robust group centre in ambiguous cases. We do so in Sec. 3.4.

Another uncertainty in the BGG assignment may come from the aggregation (fragmentation) of low-mass (high-mass) groups in the FOF halo finder algorithm: Jakobs et al. (2018) reported that aggregation of multiple low mass groups into one may cause the halo finder to introduce BGG candidates that are not physical members of the group, and fragmentation of high-mass groups may cause the halo finder to pick up the right BGG but for a halo mass that is too low. They found such effects present in 37% groups/clusters in their sample. Although the fraction of groups where this fragmentation/aggregation effect may occur is unknown for our sample, different small effects can result in a non-negligible accumulated impact during the analysis. We therefore next investigate the miscentering and its impact on diffuse light on simulated galaxy groups.

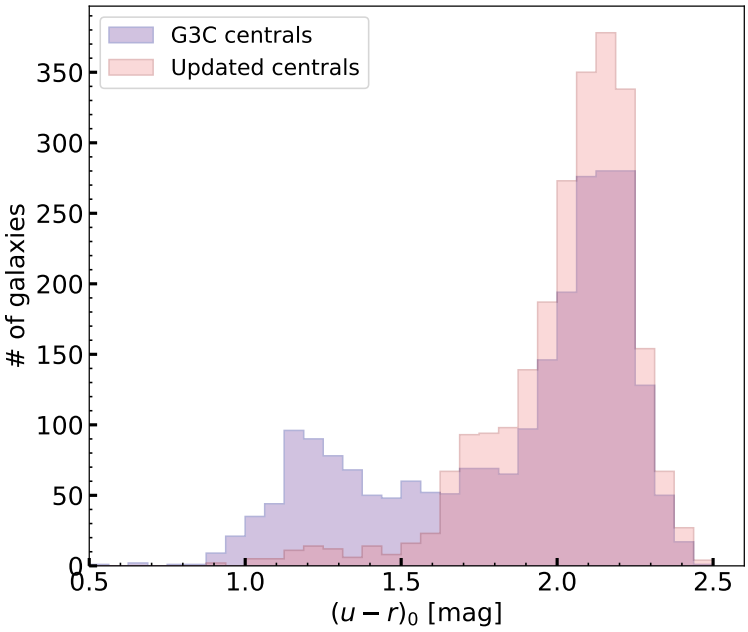

Figure 3.2: Distribution of the rest-frame $(u-r)$ colour of central galaxies from the original GAMA catalogue (purple) and our updated centrals using a colour-dependent SHMR (orange). Compared to the GAMA catalogue, the fraction of blue BGG candidates ($u-r \lesssim 1.6$) is strongly reduced in our updated sample. These groups have been re-assigned with a red central with a higher halo mass.

3.3 Simulated data

3.3.1 The Hydrangea Simulation Suite

The Hydrangea simulations (part of the C-EAGLE project, Bahé et al., 2017; Barnes et al., 2017) are a suite of high-resolution cosmological hydrodynamic zoom-in simulations of 24 massive galaxy clusters. The simulation regions were chosen from a low-resolution dark matter(DM) only parent simulation (Barnes et al., 2017) of a $(3200 \text{ co-moving Mpc})^3$ volume. Each of the high-resolution simulation regions is centred on a massive cluster ($10^{14.0} \leq M_{200c}/\mathrm{M}_\odot \leq 10^{15.4}$ at $z = 0$)*. The particle mass resolutions are $m_{\mathrm{baryon}} = 1.81 \times 10^6\,\mathrm{M}_\odot$ and $m_{\mathrm{DM}} = 9.7 \times 10^6\,\mathrm{M}_\odot$; the gravitational softening length is 0.7 physical kpc (pkpc) at $z < 2.8$. The high-resolution simulation regions include the large scale surroundings of the clusters to ≥ 10 virial radii (r_{200c}) at $z = 0$, and therefore contain many group scale haloes, in addition to the central clusters. The simulations were run using the AGNdT9 calibration of the EAGLE galaxy formation and evolution code (for details about the simulation model, hydrodynamics scheme, and comparison of the model to observed galaxy properties, see Schaye et al. (2015), Schaller et al. (2015), and Crain et al. (2015) and references therein). The subgrid physics models used to simulate astrophysical processes that originate below the resolution scale of the simulation include star formation (following Schaye and Dalla Vecchia 2008, with metallicity-dependent star formation threshold from Schaye 2004), star formation feedback (Dalla Vecchia and Schaye, 2012), radiative cooling and heating (Wiersma et al., 2009), stellar evolution (Wiersma et al., 2009), black hole seeding, growth, and feedback (Rosas-Guevara et al., 2015; Schaye et al., 2015; see also Bahé et al., 2022) A flat ΛCDM cosmology is assumed in the simulations with parameter values $H_0 = 67.77\ \mathrm{kms^{-1}Mpc^{-1}}$, $\Omega_\Lambda = 0.693$, $\Omega_{\mathrm{M}} = 0.307$, and $\Omega_{\mathrm{b}} = 0.04825$ (Planck Collaboration XVI, 2014). We also use the same cosmology throughout any relevant calculations in this paper. Although this slightly differs from the cosmological parameters used for the GAMA catalogue calculations (mentioned in Sec. 3.2.1), our conclusions are not affected.

The primary output of each simulation consists of 30 snapshots between $0 < z < 14$ with a time step of 500 Myr. In each of these snapshots, gravitationally bound structures (and stellar, DM, and gas content of each object) were identified with the SUBFIND code (Springel et al., 2001; Dolag et al., 2009), through a two-step

*M_{200c} refers to the mass enclosed within a sphere centred at the potential minimum of the cluster radius r_{200c}, within which the average density of matter equals 200 times the critical density.

process. In the first step, a friends-of-friends (FOF) algorithm was used to identify spatially disconnected groups of DM particles. Baryon particles were connected to the FOF group (if any) of their nearest DM particle (Dolag et al., 2009) and only FOF groups with more than 32 DM particles were considered. The following step selected gravitationally bound candidate 'subhaloes' within each FOF group as locally over-dense regions. Particles in the FOF group that are not bound to any subhalo, but still gravitationally bound to the group and are self-bound to each other, were considered as the 'background' or 'central' subhalo (see Bahé et al. 2017 and Bahé et al. 2019 for more details). In this paper, we refer to all the subhaloes other than the central subhaloes as the 'satellites'. An important distinction is that in the simulations the central subhalo in the FOF group contains all self-bound particles that are not in a satellite subhalo. Hence, it comprises what would observationally be described as the combination of the central galaxy and the IGL, without any explicit distinction between the two. In Sec. 3.5.2, we discuss different approaches to separate the BGG from the IGL that are directly comparable to observational methods and whether the difference in methods can be quantitatively connected to the detected IGL fraction.

In this work, we have used both the particle data and the FOF groups and subhaloes from SUBFIND outputs at $z = 0.101$. The redshift was chosen to match our group selection from the GAMA group sample described in Sec. 3.2. For the analysis, we prepared mock $r-$band images centred on each of the FOF groups in our sample using projected particle luminosities (Negri et al., 2022) that have been k-corrected to $z = 0$ following Chilingarian et al. (2010) and Chilingarian and Zolotukhin (2012). The size of each of the images is 2 pMpc along both axes. The pixel-to-arcsecond ratio of 0.213 and an appropriate RMS noise (pixel value $\sim 10^{-12}$, in units of flux relative to the flux corresponding to magnitude = 0, this is the same noise level given the zero-point of the AstroWise pipeline that was used to process the KiDS DR4 data) was applied to mimic the KiDS images from DR4 (Kuijken et al., 2019). One major advantage of using simulated data compared to the observational data is that we can also create mock observations of only the central subhalo within each FOF group – recall that this includes the IGL – and analyse its light without the need to mask satellites or line-of-sight projections. We utilized this and prepared another set of mock $r-$band images using only the particles of the central subhalo. All the other specifications of these images remained the same as the projected group images described above.

There are a few points of concern while using the simulated data for our analysis. Biases can be introduced due to the failure of SUBFIND to assign star particles to satellites (Bahé et al., in prep). Uncertainties in the produced IGL fraction and its

radial distribution may arise from the star formation rate model and the resolution limit of the simulations. The EAGLE model matches the observed stellar mass and luminosity functions and their evolution considerably well up to $z = 7$ (Schaye et al., 2015; Furlong et al., 2015; Trayford et al., 2015). The Hydrangea simulations can also reproduce the observed stellar mass functions and mass density profiles in galaxy clusters out to $z = 2$ (Bahé et al., 2017; Ahad et al., 2021). However, an offset in the observed size-mass relation towards more compact passive galaxies in the AGNdT9 variant of the EAGLE model (Schaye et al., 2015) may have been responsible for a lower mass fraction of ICL in the central clusters from the Hydrangea simulations compared to the observed ICL mass fractions as compact galaxies are less prone to stripping (Alonso Asensio et al., 2020). We note that the opposite effect is described in Henden et al. (2020), who found that boosted tidal stripping from artificially large satellite galaxies increases the ICL stellar mass fraction in their simulations. They also noted that uncertainties in galaxy sizes are the principal contributors to the uncertainty in determining the ICL mass fraction in simulations. In this work, we focus on direct observable properties based on mock observations of multi-band photometry. However, discrepancies in the IGL mass fraction measurements caused by the above-mentioned attributes of the simulations may add uncertainties to the optical measurements of the IGL fractions.

3.3.2 Group Selection

We performed a detailed selection procedure to match the simulated groups with the GAMA group sample (described in Sec. 3.2). We considered only the simulated data at $z = 0.101$ and compared this to a matched subsample from our GAMA group sample at $0.09 < z < 0.15$ to minimise any potential redshift evolution within the observations. A detailed analysis of the redshift dependence of the IGL will be discussed in a follow-up paper. We excluded groups near the edge of the simulation zoom-in region to avoid numerical artefacts caused by the artificial gas vacuum and resolution jump outside of the high-resolution region. To match our GAMA sample selection, we only kept groups with at least five member galaxies brighter than an $r-$band magnitude limit of 19.8. For this, we took the absolute magnitudes of the galaxies in $r-$band within 30 kpc aperture, applied the appropriate k-correction to the magnitudes at $z = 0.101$, and applied the distance modulus to obtain the final apparent magnitudes of the group galaxies. The $r-$band absolute magnitude of the central galaxies were also computed from the particle magnitudes within 30 kpc aperture. In our final sample, we have

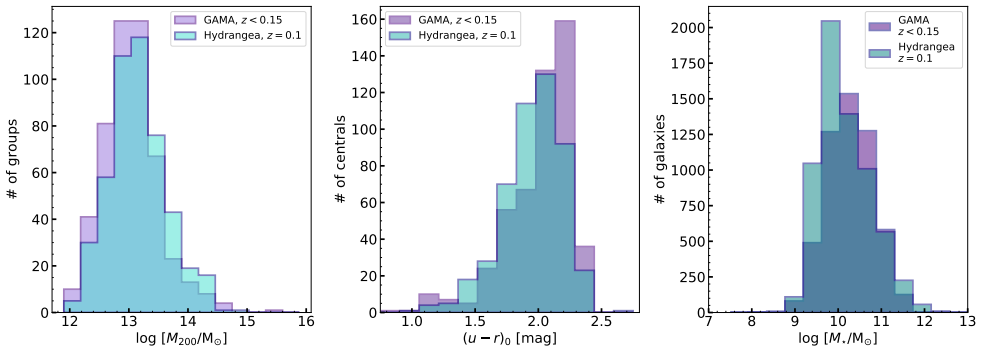

Figure 3.3: Histograms comparing the distribution of different properties of the GAMA (purple) and Hydrangea (turquoise) group samples at comparable redshift ($0.08 < z < 0.15$ for GAMA; $z = 0.1$ for Hydrangea). The left, middle, and right panels show the distributions of halo mass ($\log[M_{200}/\mathrm{M}_\odot]$), dust-corrected rest-frame $(u - r)$ colour of the group BGGs, and total stellar mass of all the group galaxies in the GAMA and Hydrangea samples, respectively. The observed and simulated samples have comparable distributions in these three fundamental properties.

a total of 497 groups, including the 24 central clusters. We prepared a catalogue that contains details (e.g. halo mass, virial radius, BGG ID and location, colour and magnitudes, stellar mass) for these 497 groups to use in our analysis and refer to this as the 'Hydrangea group catalogue' from now on.

Figure 3.3 shows the comparison between the GAMA group sample and the final Hydrangea group sample (excluding the central clusters in each simulation volume). The left, middle, and right panels show the group halo mass ($\log[M_{200}/\mathrm{M}_\odot]$) distribution, the distribution of the rest frame $(u - r)$ colour of the group BGGs, and the stellar mass distribution of all the group galaxies (both centrals and satellites) from the GAMA (purple) and Hydrangea (turquoise) samples, respectively. The $(u - r)$ colour is obtained from dust-corrected magnitudes of Negri et al. (2022). The samples show an excellent agreement in all the panels, especially given that we do not expect perfect agreement between the samples because the Hydrangea sample is not mass-complete. The match suggests that the simulated data can be used to test and predict different properties of the observed group data sample.

3.4 Effect of miscentring on the IGL fraction

We found in Sec. 3.2.2 that 23% of the GAMA groups have a reassigned (redder) central galaxy based on the colour-dependent SHMR of Bilicki et al. (2021) instead of using the iteratively-selected brightest galaxy in the group as the central one. However, it cannot be determined which of these two central galaxy assignments is a more faithful estimate for the potential minimum based on the reassignment only. Selecting the correct centre of potential is important because the IGL is expected to be centred on it. If one selection method for the central galaxies is better than the other, we expect to see a difference in the radial mass and light profiles of the groups around the group centres from these two methods. The mass density profile around the correct centre is expected to be more peaked and the surface brightness (SB) profile around the correct centre is expected to have more flux in the outskirts where the diffuse light dominate the total light profile of the BGG+IGL compared to the corresponding mass and light distributions around the misidentified centre. In this section, we explore whether such a difference is present in the radial surface mass density profiles and the radial surface brightness profiles in our GAMA group sample. To connect whether the presence of such a difference in the radial profiles is significant enough to identify a preferred central galaxy selection method, we used a carefully produced miscentred group sample from the Hydrangea groups to compare with the corresponding GAMA group profiles.

3.4.1 Selection of miscentred groups in Hydrangea sample

In the GAMA group sample, the initial group catalogue considered the brightest galaxy in the group from the iterative method as the halo centre (explained in Sec. 3.2.2). Using SHMR to select the group centres changed the selection criterion from light to associated halo mass of the galaxy in consideration. In the Hydrangea group sample, however, the FOF groups can be centred unambiguously on the true potential minimum of the halo. We considered these as the 'true centres' in our analysis. To mimic the central galaxy selection of the GAMA sample, we picked the brightest galaxy in each group as the 'updated centres'. Similar to the GAMA groups, this different selection method picked a different central galaxy (compared to the true centres) only for a small subsample of the total group sample (a maximum of 18%). We considered this subsample of groups with a different updated centre as our 'miscentred sample'. The detailed selection methods we used is as follows.

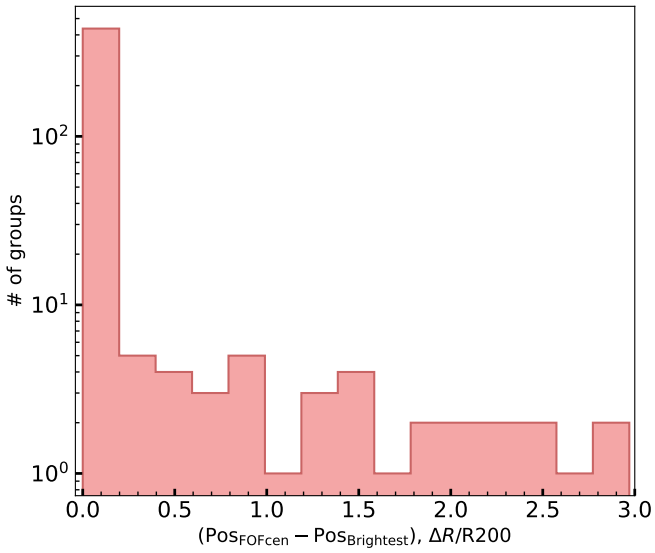

Figure 3.4: The distribution of radial distance of the two central galaxy candidates for each of the Hydrangea groups in our sample. The positions of the FOF halo centres were considered as the initial positions and the positions of the brightest group galaxies from the SUBFIND catalogue were considered as the final positions. The distribution is shown in units of the corresponding group r_{200}. The y-axis is in logarithmic units.

We identified the possible miscentred group candidates using two separate methods. Firstly, we used the projected $r-$band mock images of the groups described in Sec. 3.3.1. The central galaxies in the images are at the corresponding group centre of potentials (true centrals) from the Hydrangea group catalogue (see Sec. 3.3.2). We ran SEXTRACTOR (Bertin and Arnouts, 1996) on each of the images to select the bright extended sources and picked the brightest sources from each group image to mimic the observational BGG selection. After matching the positions of these brightest galaxies to the true centrals, we found that 18% of the groups have a brighter galaxy than its true central within a 1Mpc radial distance from its centre of potential.

Secondly, we directly used the Hydrangea SUBFIND catalogue and picked the brightest galaxy in the $r-$band out of all FOF members as the central galaxy. Here, we considered only the FOF group members as the BGG candidates unlike in the method with the mock images where a projected galaxy can be selected as the brightest galaxy in the group vicinity. After matching the positions with the true centrals, we found that the number of groups having a brighter group galaxy than the true central is

reduced to about 10%. In this second approach, the number of bright galaxies can only go down by eliminating galaxies that only appear to be part of the group in projection, which implies that projections can result in misidentifying the central galaxy. It also suggests that the interlopers can comprise as much as 50% of the misidentified centrals even in our Hydrangea group sample which do not contain uncorrelated fore-/background galaxies.

There is another important issue related to the FOF group finder that can contribute to the miscentring. Due to the nature of the group finder, it can sometimes merge two smaller groups into one large group if they are not very far away, especially if an in-between galaxy serves as a "connecting node" (see appendix A of Jakobs et al., 2018). As a result, such groups can exist in the Hydrangea group catalogue and a galaxy that is brighter than the group central can be simply the central galaxy of the second group that got linked to the first group. To exclude such cases, we applied an additional condition that the updated central cannot be more than 500 kpc away from the true group centre. A radial distance of 500 kpc is about the same as the average r_{200} of the group sample. The distribution of the distance between the FOF halo centres and the brightest group galaxies are shown in units of r_{200} in Fig. 3.4. The distribution of physical distances is similar (not shown). This selection yielded 25 groups (5%, referred as the clean miscentred sample afterwards) from the Hydrangea sample that still have a brighter galaxy than the true central and therefore, can be misidentified as the group centre in a similar sample of observed galaxy groups. Therefore, even with group membership assigned based on perfect spectroscopic redshifts, the line-of-sight projections can lead to a misidentified central galaxy in the observations. This finding provides a fundamental limitation that needs to be accounted for in a stacking analysis.

3.4.2 Mass density profiles of GAMA and Hydrangea groups

If one selection of the central galaxy is physically preferred to the other, then this is expected to be visible through a more peaked density profile around the better-estimated group centres. To test whether the updated central sample for the GAMA groups is more likely to reside in the group centre of potential, we estimated the stacked stellar mass density profile of the groups around the centrals from the original GAMA catalogue and the BGGs from our updated catalogue. The stellar mass was obtained directly from the StellarMassesLambdarv20 catalogue (Taylor et al., 2011; Wright et al., 2016). For the radial distribution of the mass, we calculated the projected distance

of each group galaxy to the corresponding group central and normalized it using the corresponding r_{200}. We took the total stellar mass of the galaxies in each consecutive radial bin from a stack of all the galaxies in the group sample and divided it by the total surface area of the corresponding annulus to obtain the surface mass density profile. The radial bins did not include the central 5% of the r_{200} for each group so that the central galaxy was excluded from the density profile. All the 2385 groups in our GAMA group sample were used to calculate the average surface mass density profile.

We did not see any significant difference in the stacked profiles of all groups before and after the central galaxy reassignment. To focus on the effect on the groups that are affected by updating the centrals, we also considered only those groups that have been assigned with a new redder central galaxy compared to a bluer one in the original catalogue. We prepared the surface mass density profile for this subsample of 498 groups in the same procedure as described above. The left panel of Fig. 3.5 shows the surface density profile of the possibly miscentred groups around the centrals from the GAMA catalogue (blue) and around the centrals from the updated catalogue (red). The error bars on both the blue and red data points show the corresponding 68% uncertainties and are obtained by 100 bootstrap re-samplings from the respective stack of galaxies with replacement. Even in this case, the mass density profiles around the centrals from the original and updated catalogue do not show any visible difference. The density profiles of the same group samples were also measured using the weak lensing signal of the groups instead of the galaxy stellar mass from the StellarMassesLambdarv20 catalogue, which also did not show any visible difference.

A possible reason for this lack of difference can be that both of these selections are equally meaningful. In other words, there is a chance that about half of these updated centrals are correctly updated as the central galaxy, whereas the other half were already correctly identified in the original catalogue. One reason for this is that, even with spectroscopically selected group members, there is a chance of projection effect from foreground groups. This is not possible to test further with only observational data as there is no information about which galaxies are truly residing at the centre of potential of the groups. Therefore, we use the Hydrangea group sample and their mock $r-$band images to look into this issue in more detail. As shown in Sec. 3.4.1, we found that about half of the miscentred groups from Hydrangea sample are indeed coming from the LoS projections. Therefore, we repeated the test of the radial mass density profile with the Hydrangea groups before and after taking out the projected subsample from the Hydrangea miscentred sample described in Sec. 3.4.1.

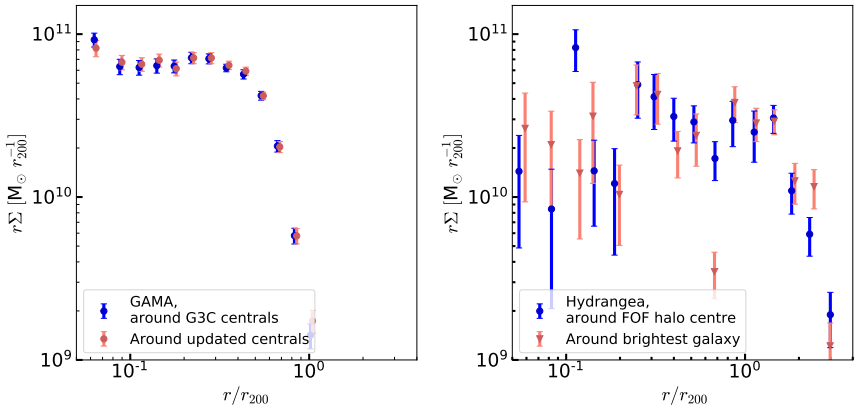

Figure 3.5: The total stellar surface density profiles of the stacked GAMA groups where the central candidate was updated (left), and the stacked Hydrangea groups (right, only those with an ambiguous central) around the true central galaxy from the catalogue (blue), and around the brightest group galaxy within 500 kpc distance from the true central galaxy (red). Error bars indicate the 68% uncertainty from 100 bootstrap re-samplings with replacement. For clarity, the blue and red data points are offset slightly along the x-axis in both panels. For both GAMA and Hydrangea, the profiles are insensitive to the choice of central. The re-assignment of central galaxies from G3C centrals to the galaxies with the highest associated halo mass (in GAMA) is not the exact inverse of the re-assignment of central galaxies from FOF halo centres to the brightest group galaxies (in Hydrangea). However, G3C centrals are broadly analogous to the brightest group galaxies from Hydrangea and galaxies with highest halo mass from GAMA are broadly analogous to the FOF halo centres from Hydrangea.

We prepared the stacked surface mass density profiles around the true centrals and the brightest galaxies (separately) with our clean sample of miscentred groups that were selected as described in Sec. 3.4.1. The right panel of Fig. 3.5 shows the density profile of the Hydrangea group sample (only those with an ambiguous central) around the true central galaxy (blue) and around the brightest galaxy within 500 kpc distance from the true central (red). The error-bars are obtained by 100 bootstrap re-samplings of the galaxies with replacement and show the 68% uncertainties on the data points. A slight offset was added to the red and blue data points along the x-axis in both the panels for an easier distinction between them. The large uncertainties of the density profile from Hydrangea sample resulted from the significantly smaller miscentred sample size (25) compared to the GAMA miscentred sample (498). The halo mass distribution of the miscentred samples are also slightly different – the GAMA sample has a higher average halo mass which is likely due to the presence of miscentred groups from projection effects. This resulted in the difference in the normalization of the density profiles on the panels. However, the red and blue profiles on the right panel look almost identical within the error-bars. This behaviour is the same as the GAMA miscentred groups where we were not sure about the true centres of the groups. Therefore, the mass density profiles do not point to a clear physical preference for either of the two centring methods, based on the SHMR or galaxy brightness.

3.4.3 Surface brightness profiles of Hydrangea groups

The surface brightness (SB) profile around a misidentified centre is expected to be higher in the central region by definition of selecting the brightest galaxy. On the outskirts, the IGL is expected to be suppressed compared to the IGL around the true centre of potential because the true central galaxy will be treated as a satellite galaxy and masked, and the surroundings of the misidentified centre will only have part of the IGL. To test whether our group re-centering based on the colour-dependent SHMR improved the central galaxy selection, we looked into the SB profiles of the miscentred Hydrangea group sample. We took the 25 Hydrangea groups from Sec. 3.4.2 that have a brighter galaxy (which is also located within 500kpc of the group centre of potential) compared to their true central. We prepared mock r-band images of these groups centred around the updated BGGs (brightest galaxies in the corresponding groups in r-band) instead of around their true centrals (centre of potentials) with the same resolution and noise level as we did previously (explained in Sec. 3.3.1). These images also span 1Mpc around the updated centrals.

We computed two stacked radial SB profiles for all the 497 groups: one centred around the true centrals from the catalogue and the other including the updated BGGs for the 25 miscentred groups. For this, we masked out all the sources except for the central galaxies in the group images so that only the central galaxy and the extended IGL around it remains. Similar to our findings from the density profiles, we found no appreciable difference between the two stacked profiles (not shown here). To focus on miscentring, we then prepared the stacked SB profiles of only the 25 miscentred groups around their true and updated centrals. The left panel in Fig. 3.6 shows the stacked surface brightness profile around the true centrals in orange and around the updated centrals in purple.

Two features differentiate the SB profiles around the true FOF centre (orange) and the brightest galaxy as the new group centre (purple). Firstly, the central region of the profile around the updated BGGs (purple) is up to ≈ 1 mag brighter than the profile around the true centrals (orange). This is also demonstrated by the pink data points in the middle panel of Fig. 3.6, where the absolute $r-$band magnitudes of the updated BGGs (y-axis) are brighter by the same amount (the solid blue line shows the position of equal magnitudes for reference) than the true centrals (x-axis) for the 25 miscentred groups. Secondly, even though the profile centred on the brightest galaxy is much brighter at the centre, it is fainter than the profile around the true halo centre beyond 30 kpc (vertical line), where the IGL is dominant. This characteristic agrees with our assumption that around the misidentified central galaxies, the IGL is suppressed. Because the IGL is not evenly distributed around a misidentified BGG, the azimuthally averaged surface brightness around the brightest galaxy is lower than around the actual potential minimum beyond 30 kpc. To check whether this suppression is dependant on the luminosity of the central galaxies, we divided the miscentred groups in two bins based on the $r-$band magnitude of the BGGs, and plotted the SB profiles similar to the left panel of Fig. 3.6 (not shown here). We found that the overall behavior that the extended light is suppressed around the brightest galaxy is present in both of the cases, albeit a bit more pronounced in the bin with brighter BGGs.

We also checked the distribution of different properties for the groups that are likely to have such misidentified central galaxies. The distribution of the groups across two key parameters, the halo mass (M_{200}) and the absolute $r-$band magnitude (M_r) of the centrals are shown in the right panel of Fig. 3.6. The light green circles show the distribution of all the Hydrangea groups, and the orange and purple circles show the distribution of the true and updated centrals of the 25 miscentred groups, respectively. For ease of matching, the FoF halo centre and brightest galaxy from each of the

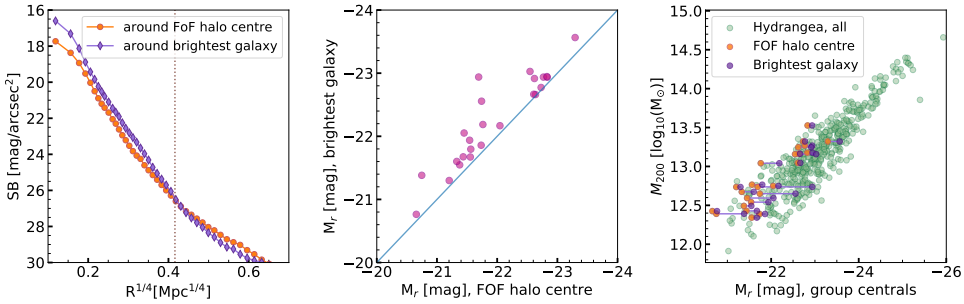

Figure 3.6: *Left:* stacked surface brightness profiles of the Hydrangea groups with ambiguous centres around the potential minimum from the catalogue (orange circles), and around the brightest group galaxy within 500 kpc from the true central galaxy (purple diamonds). The profiles centred on the potential minima have lower central brightness compared to those centred on the brightest galaxy. In contrast, the surface brightness of the diffuse IGL (at $R \gtrsim 30$ kpc; vertical dotted line) is higher when the potential minimum is chosen as the centre. *Middle:* absolute $r-$band magnitude of the brightest galaxy (y-axis) vs the absolute $r-$band magnitude of the galaxy at the potential minimum (x-axis) for the subsample of 25 groups in which they are not coincident (pink circles). The blue solid line here shows the 1-to-1 relation. *Right:* halo mass to absolute r-band magnitude distribution of the entire Hydrangea sample (light green). The orange and purple points show the miscentred subsample in this parameter space with absolute $r-$band magnitudes of the true and updated BGGs, respectively. The FoF halo centre and brightest galaxy from each of the miscentred group are connected with light purple lines. Groups with lower halo mass and a less luminous BGG are more likely to have a misidentified central as they can have brighter galaxies close to the group centre.

miscentred group are connected with light purple lines. The points clearly indicate that the less massive groups ($\leq 10^{13.5}$M$_\odot$, with a majority $\leq 10^{13}$M$_\odot$) in our sample with a less-luminous central galaxy (≤ -23 mag, with a majority ≤ -22 mag) are more likely to have a misidentified central. The points also show that for this work, the majority of our group sample lies above the 10^{13}M$_\odot$ and -22 mag threshold. Although the fraction of groups affected by the miscentring is small (about 5%), to draw any conclusion on the effect of this miscentring on the IGL measurement, we need to quantify the effect. We measure the consequence of this IGL suppression due to the misidentified centrals on the total IGL fraction estimation in Sec. 3.5.2.

The fraction of miscentred groups (i.e. those for which the brightest galaxy is not the one at the potential minimum) compared to the total number of groups in the halo mass range where we see them in the Hydrangea sample ($\leq 10^{13.5}$M$_\odot$) is 7% (and 15% if we include the cases where the BGG was a projected galaxy). The fraction is 23% lower (15% considering the projected ones) compared to the same fraction from Lange et al. (2018, their fig. 10) in the same halo mass range. Working with the GAMA group sample only, Oliva-Altamirano et al. (2014) reported between 10-15% miscentred centrals at $M_h \leq 10^{13.5}$M$_\odot$. An indication to the reason of why the BGGs are not at the halo centre can be found by looking at the magnitude gap (Δm_{12}) between the BGG and the second brightest galaxies in these groups. Oliva-Altamirano et al. (2014) found a lower Δm_{12} (< 1.0 mag) which suggests a recent halo merger for these groups. In our miscentred sample, all the BGGs except one have $\Delta m_{12} < 1.0$ mag, implying a recent halo merger being the most likely reason for the central galaxy to not be the brightest galaxy in the group.

To summarize, we found a noticeable difference in the SB profiles around the true centres and the brightest galaxies in the groups. Therefore, studying the SB profiles can be a way to identify the true central galaxy in groups. In this work, we could only test the SB profiles for the simulated sample, which showed IGL suppression at the outskirts of the SB profiles, and therefore demonstrated that a halo-mass based central galaxy selection is more accurate compared to selecting the brightest galaxy as the central one. We also found that for our sample, the most plausible reason behind the miscentring is interlopers and recent halo mergers.

3.5 Towards a better IGL interpretation

3.5.1 Effect of group and central galaxy properties on the stacking

To study the effect of group and central galaxy properties on the IGL measurement and to test whether there is a quantitatively preferred way to stack multiple groups that makes the physical interpretation of the IGL more straightforward, we computed the azimuthally averaged radial surface brightness profiles for each of the 497 Hydrangea groups (including the central clusters for a wider halo mass range). For this purpose, we took the mock $r-$band images described in Sec. 3.3.1, and ran SExtractor to identify all the bright sources. Starting from the SExtractor segmentation map, we created masks to remove all the sources apart from the central galaxy. To eliminate any residual extended light from the satellites, we extended all the masks by 5 pixels ($\approx 1''$). The mask thus selects only the light from the central galaxy and extended IGL around it in each image. Following a similar method as Zibetti et al. (2005), we fitted the inner region of the surface brightness profiles with a single-component de Vaucouleurs profile (De Vaucouleurs, 1948, SD from now on) to separate the central galaxy from the extended IGL. We fitted the profile out to $0.2 \times r_{200}$ to completely encompass the central in our group sample with a varied halo mass (and hence r_{200}) range. Using the fitted profile as a model for the central, we subtracted it from the masked SB profile to obtain the IGL profile in the outskirts. Also, we obtained the SB profile of the satellite galaxies in the group by subtracting the masked central+IGL profile (azimuthally averaged) from the total group SB profile that was obtained from the unmasked group image. Finally, we integrated these light profiles to obtain the total flux within the central, IGL, and satellites in each group. Thereafter, we calculated the IGL-to-total ($f_{\rm IGL}$), central-to-total ($f_{\rm central}$), and satellite-to-total ($f_{\rm satellite}$) light fractions and examined the distributions of these light fractions with respect to different group properties including the halo mass, central magnitude, richness, and integrated group luminosity.

Figure 3.7 shows the distributions of $f_{\rm satellite}$ (top panels), $f_{\rm central}$ (middle panels), and $f_{\rm IGL}$ (bottom panels) for all the Hydrangea groups against the group halo mass (M_{200}, left panels), $r-$band magnitude of the group BGGs ($M_{\rm r}$, middle panels), and group richness ($N_{\rm FOF}$, right panels), respectively. The group richness was measured considering only the galaxies that have an apparent $r-$band magnitude ≤ 19.8 and stellar mass $\geq 10^9 {\rm M}_\odot$. The red, green, and blue dots represent those groups for which

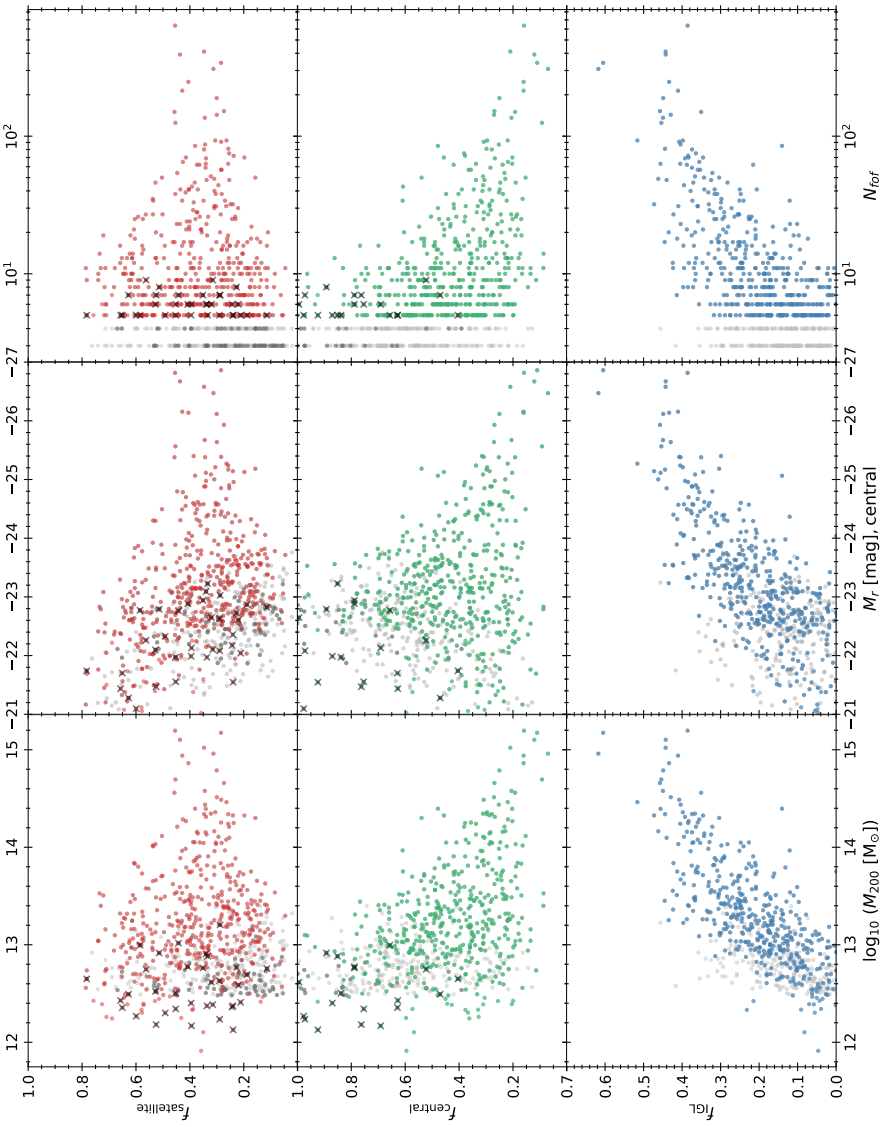

Figure 3.7: Fraction of the total stellar r-band light in satellites (top), the central galaxy (middle), and the IGL (bottom) of Hydrangea groups with respect to, respectively, the group halo mass (left panels), absolute r-band magnitude of the central galaxy(middle panels), and group richness (right panels). Black crosses represent parameters resulting from bad fits (see text). Light grey points represent groups with $N_{\rm FOF} < 5$ but $M_{200} \geq 3 \times 10^{12} {\rm M}_\odot$. The satellite and central fractions do not show any strong correlations with halo mass, $r-$band magnitude, or group richness (but there is some variation in the scatter). However, the IGL fraction correlates strongly with all of these properties.

the single-component de Vaucouleurs fitting procedure resulted in a good fit to the inner 45kpc profile and did not exceed the total central+IGL light profile at larger radii. However, $\sim 6\%$ of the groups did not satisfy these criteria and led to $f_{\rm IGL}$ having a negative value. In Fig. 3.7, the black crosses in the top and middle panels indicate these bad fits. In the bottom panel, the bad fits are not visible as they do not have a positive IGL fraction.

The satellite and central fraction (top and middle row) do not show any strong correlations with M_{200}, $M_{\rm r}$, or $N_{\rm FOF}$. The upper envelope of $f_{\rm central}$ distributions appear as monotonically decreasing functions, whereas the lower envelopes show zero correlation. All the panels showing satellite and central fractions have a high scatter in their distribution, especially at the lower mass, lower central luminosity, and lower richness. The scatter at the highest halo mass, brightest central luminosity, and highest richness ends are smaller and a slight correlation (positive for the satellites and negative for the centrals) is visible there. However, these are the most massive clusters from the Hydrangea sample. The large scatter at the lower mass end indicates that the relative contribution of central and satellite galaxies is highly variable in groups. As groups merge and acquire increasing number of satellites, the satellites may contribute more to the total group light and correspondingly, the central galaxy contributes less to the total group light. Therefore, we conclude that in the group-mass range, the scatter is too high to consider any trend in the top and middle panels.

However, the IGL fraction ($f_{\rm IGL}$) shows a clear trend with all of M_{200}, $M_{\rm r}$, and $N_{\rm FOF}$, as shown in the bottom panel of Fig. 3.7. A similar trend is also visible in other recent cosmological simulation-based IGL/ICL analyses. Pillepich et al. (2018) found a similar $f_{\rm IGL}$ (mass) vs M_{200} relation at $10^{13} \leq m_{200}/{\rm M}_{\odot} \leq 2 \times 10^{14}$ with a radial selection method to separate the central and ICL in the IllustrisTNG simulations. Using a similar ICL separation method as Pillepich et al. (2018), Contini and Gu (2021) also found a positive ICL mass vs host halo mass correlation. By using a phase-space-based galaxy finder algorithm to separate the host galaxies from what they refer to as the 'intra-halo stellar component' (IHSC), Cañas et al. (2020) reported a positive correlation of the fraction of IHSC with the host M_{200} and $N_{\rm FOF}$ for haloes with $10^{11} \leq m_{200}/{\rm M}_{\odot} \leq 10^{13}$ as well. However, Montes (2022) found no significant correlation between the $f_{\rm IGL}$ with the host M_{200} after combining multiple observational studies of the ICL measurements at $z < 0.07$ (see their fig. 3), which also had a large scatter in the $f_{\rm IGL}$ between 5-40%. They speculated that the lack of correlation between the ICL fraction and the halo mass may indicate that both groups and clusters have similarly efficient ICL formation mechanisms. With a contrary argument, a large

scatter in the observational data can be the result of the different systematics in the individual data sets from the different studies.

Before discussing the dependence of IGL fractions in our sample in further detail, it is worth mentioning that we have tested a range of further properties and found no significant correlation with any of the satellite, central, or IGL fractions. These properties include the average rest-frame $u-r$ colour of the centrals, the effective radii (the radius encompassing 50% of the total light of the component) of the central and IGL components, and the integrated $r-$band magnitude of the group.

In all the panels, the grey points show groups with $N_{\rm FOF} < 5$, but within a comparable mass range as the main sample ($M_{200} \geq 3 \times 10^{12} {\rm M}_{\odot}$). In the left and middle columns, these points follow the trend of the coloured points, implying that a halo-mass based group selection gives similar results compared to a richness-based one.

Returning to the bottom panels of Fig. 3.7, the similar correlation of $f_{\rm IGL}$ with M_{200}, $M_{\rm r}$, and $N_{\rm FOF}$ is expected as these are not mutually independent properties. More massive and richer groups have a higher chance of accumulating more mass and light in the central galaxy and the surrounding region. We see, however, a larger scatter in $f_{\rm IGL}$ with respect to $N_{\rm FOF}$, especially for $N_{\rm FOF} \leq 10$ in the bottom right panel of Fig. 3.7, compared to the tighter relations with M_{200} and $M_{\rm r}$. A possible reason for the scatter with $N_{\rm FOF}$ being larger can be the presence of fossil groups, which are defined as the relics of old galaxy groups where the central galaxy grows predominantly by merging with satellite galaxies that are at least as luminous as the characteristic luminosity of the galaxy luminosity function for the system (Ponman et al., 1994). In fossil groups, $N_{\rm FOF}$ is low even though the mass and luminosity of the central galaxy are high enough to be comparable to a rich group or even a cluster with a correspondingly high IGL fraction. An opposite scenario may also occur in fossil groups where the central galaxy has gone through a recent merger, and hence the IGL is not in place yet, which will result in a smaller IGL fraction.

A detailed analysis of whether the groups in our sample are potentially fossil groups is beyond the scope of this paper. However, a quick test of looking into the magnitude gap between the BGG and the second brightest galaxy in the groups with $N_{\rm FOF} \leq 10$ showed that about 18% of these groups have at least a magnitude gap of 2 in $r-$band, and for 8% of these groups, the second brightest galaxy is also located within 0.5 r_{200} distance from the BGG. According to the widely used definition of fossil groups by Jones et al. (2003), a system must have a minimum X-ray luminosity of $10^{42}\ h_{50}^{-2}$ erg s^{-1} and a $r-$band magnitude gap ≥ 2 between the two brightest group

members that are within 0.5 r_{200} distance from each other. The X-ray luminosity limit corresponds to a minimum halo mass of about $10^{13}\mathrm{M}_{\odot}$ (Stanek et al., 2006) which, along with the distance and magnitude criteria, selects about 4% of the low-richness groups in our sample only. Therefore, according to these criteria, about 4% of the groups in our sample with $N_{\mathrm{FOF}} \leq 10$ are likely fossil groups confirming that fossil groups are a minor but non-negligible contributor to the scatter in the IGL fraction at the low-richness end.

Unlike the halo mass, M_{r} of the central galaxy is directly observable. Therefore, its correlation with f_{IGL} is more straightforward to test from the observational data. Because of this, we look into the strong trend of f_{IGL} with M_{r} in Fig. 3.8. The middle panel here is based on the f_{IGL} vs M_{r} plot from Fig. 3.7 and shows f_{IGL} of the Hydrangea groups as the turquoise data points. To identify the average trend of f_{IGL} with respect to M_{r}, we binned the groups along M_{r} from -21 mag to -27 mag and calculated the mean f_{IGL} in each bin. The mean values are obtained from the halo mass-weighted average of the individual data points to account for the fact that more massive groups will have a higher fraction of IGL contribution in the stacked profile. The red circles and solid line in the middle panel show the average f_{IGL} values in each magnitude bin. Each bin is plotted at the average M_{r} of its centrals. The error bars associated with the red points show the statistical 1σ uncertainty on the mean.

To test whether this trend is also present in the SB profiles and is not only an outcome of any bias in the fitting procedure of the individual group profiles, we stacked the surface brightness profiles of the Hydrangea groups in the same M_{r} bins as the red data points. After fitting the average surface brightness profiles of the M_{r} bins and obtaining f_{IGL} following the same procedure as before, we obtained the data points shown by the deep blue squares in the middle panel of Fig. 3.8. The similarity between the stacked and individually measured IGL fractions has two important implications. Firstly, the trend of increasing f_{IGL} with respect to the M_{r} of the group centrals is confirmed. The top panel of Fig. 3.8 shows the correlation between the group halo mass with the M_{r} of the group centrals in turquoise data points. The orange circles show the average halo mass in the equivalent M_{r} bins compared to the middle panel of the figure. The tight correlation of the increasing halo mass with respect to the $M_{\mathrm{r,\,central}}$ indicates why we see an increased f_{IGL} in the middle panel. More massive groups have a brighter central galaxy which also had a chance to accumulate a larger amount of IGL during its growth. Secondly, this similar trend for both the red and deep blue points indicates that the stacking of the surface brightness profiles preserves the underlying IGL fraction distribution in individual groups. Therefore, stacking the

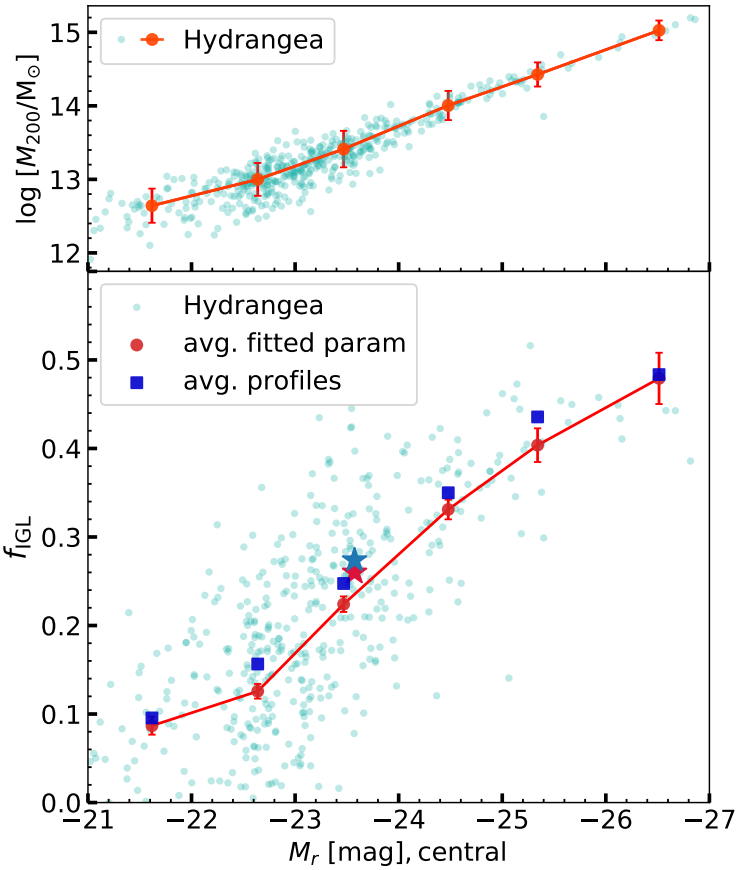

Figure 3.8: Top: halo masses of the Hydrangea group and cluster sample with respect to their absolute $r-$band central galaxy magnitudes (turquoise). The orange circles and error bars indicate the mean values and standard deviations of the distribution in each magnitude bin. Middle: fraction of IGL to the total group light with respect to the absolute $r-$band central galaxy magnitudes of the Hydrangea group sample. The turquoise points indicate the IGL fraction for each individual group obtained by subtracting the central galaxy with a single de Vaucouleurs (SD) fit to the central 40 kpc. Red circles indicate the average values (magnitude-weighted) of individual fits in 1 mag wide bins in central galaxy $M_{\rm r}$. Error bars indicate 1σ uncertainties on the mean. The deep blue squares show the IGL fraction obtained by stacking the individual surface brightness profiles of the group in the same magnitude bins, and then fitting them using an SD profile to subtract the central galaxy. The close agreement between the two methods indicates that stacking the surface brightness profiles of the groups gives a nearly unbiased estimate of the IGL fraction. The red and blue stars indicate the entire ensemble average of the individual $f_{\rm IGL}$, and the $f_{\rm IGL}$ from the stack of all the galaxy profiles considered in this plot, respectively.

profiles to increase the signal-to-noise ratio in observational data is indeed a valuable tool to measure the faint IGL signal.

However, groups with central galaxy in brighter $M_{\rm r}$ bins having larger $f_{\rm IGL}$ means that if all the groups are stacked together to obtain the IGL fraction, this trend is not evident. Ignoring this positive trend of IGL fraction with central galaxy luminosity can bias or limit conclusions that can be drawn from the analysis. The $f_{\rm IGL}$ from the mean SB profile is also likely to be biased towards a slightly higher value because of the higher light contribution from brighter centrals. This is highlighted by the red and blue stars in the middle panel, they indicate the entire ensemble average of the individual $f_{\rm IGL}$, and the $f_{\rm IGL}$ from the stack of all the galaxy profiles considered in this plot against the average galaxy $M_{\rm r}$, respectively. The red and blue stars are located closely, showing again that stacking the profiles (blue star) preserves the behavior of stacking the fitted $f_{\rm IGL}$ (red star). They also show that the values of such broad average (25.6%±0.7%) are slightly higher than the mean trend of the magnitude-based bins (22.4%±0.9%) at the same magnitude, the values in parentheses here are the magnitude weighted average and the standard error to the weighted average of the corresponding samples. Although this is not a large difference, a $M_{\rm r}$-based sub-stacking results in a more accurate estimation of the $f_{\rm IGL}$ while preserving the properties of the underlying central galaxy population. Therefore, instead of stacking a sample of groups with a varied range of central galaxy luminosity, stacking groups in narrow bins of $M_{\rm r}$ will result in a more straightforward interpretation of the measured IGL fraction.

3.5.2 Central-IGL separation

In Sec. 3.5.1, we followed Zibetti et al. (2005) and used a single-component de Vaucouleurs (SD) profile fit to separate the central galaxy from the extended IGL from the satellite-masked group image. This method is also used in other studies of IGL, such as Kluge et al. (2021). Another approach to separate the central and IGL is to fit a double de Vaucouleurs profile to the combined central+IGL light profile, one to fit the inner central galaxy, and another to fit the IGL at the outskirts (e.g. Gonzalez et al., 2005; Kluge et al., 2021, DD method from now on). In this method, the SB profile of the central+IGL light was divided into two regions. The regions were simultaneously fitted with separate de Vaucouleurs profiles such that the sum of the fitted profiles has the minimum χ^2 value compared to the group SB profile. The fitting parameter ranges ensured that the two de Vaucouleurs profiles were in the appropriate radial

zones for the central galaxy ($\leq$ 40 kpc) and IGL ($\geq$ 40 kpc).

While fitting the surface brightness profiles of individual groups, the SD method could successfully separate the central and IGL with a reasonably well-fitted central galaxy profile for $\sim$ 94% of the cases (discussed in more detail in Sec. 3.5.1). The DD method, however, was unsuccessful in more than 80% of the groups for individual group profile fits. Upon visual inspection, the primary reason for the failure was the presence of additional features in the outer regions of the SB profiles of individual groups. These irregularities in the light profile are likely caused by either tidal features of the stars in these regions or by local enhancements in the light profile from recent star formation activity. Such local light enhancement from star formation can be more pronounced in the simulations due to the stellar mass resolution of the simulations, which acts as a lower limit to the added light in such regions. The stellar mass resolution ($\sim 10^6 M_\odot$) in the Hydrangea simulations means that in any region with ongoing star formation, the minimum added stellar mass of young (and bright) stars is of the order of $\sim 10^6 M_\odot$. This feature gets averaged out near the group centre which is already bright. However, in the outskirts, where the distribution of light is sparse, even one young star particle can cause a significant deviation from a regular de Vaucouleurs profile (see also Trayford et al., 2017).

These irregularities in the group light profiles are, however, smoothed out during the stacking procedure. Even in the case of sub-stacking based on luminosity bins as discussed in Sec. 3.5.1 where the number of stacked groups in each bin was not very high ($\leq$ 100), the profiles became smoother, and both the SD and DD fitting procedures worked for all the sub-stacked groups.

Figure 3.9 shows the sub-stacked surface brightness profiles of Hydrangea groups based on their corresponding BGG luminosities. In each of the six panels in Fig. 3.9, cyan circles show the surface brightness profiles of the sub-stacked central+IGL. The average values of the absolute $r-$band magnitudes ($\bar{M}_\mathrm{r}$) of the centrals and the group halo masses ($\bar{M}_\mathrm{h}$) of the groups in the stacks are given in the top-right corner of each panel. The dashed and dotted lines show the profiles from the SD and DD fitting methods, respectively. Red and blue lines show the central galaxy and IGL profiles, respectively, in all panels. The solid purple lines show the combined fitted central+IGL profiles from the DD method. The most prominent feature in this plot is that all the profiles are well-fitted by the SD and DD methods. Also, while the SD and DD fitted lines do not overlap entirely, the red lines indicate similar regions for the centrals, and the IGLs begin to have a higher contribution to the total light compared to the centrals at a similar radial distance in each subplot. However, due to the way the

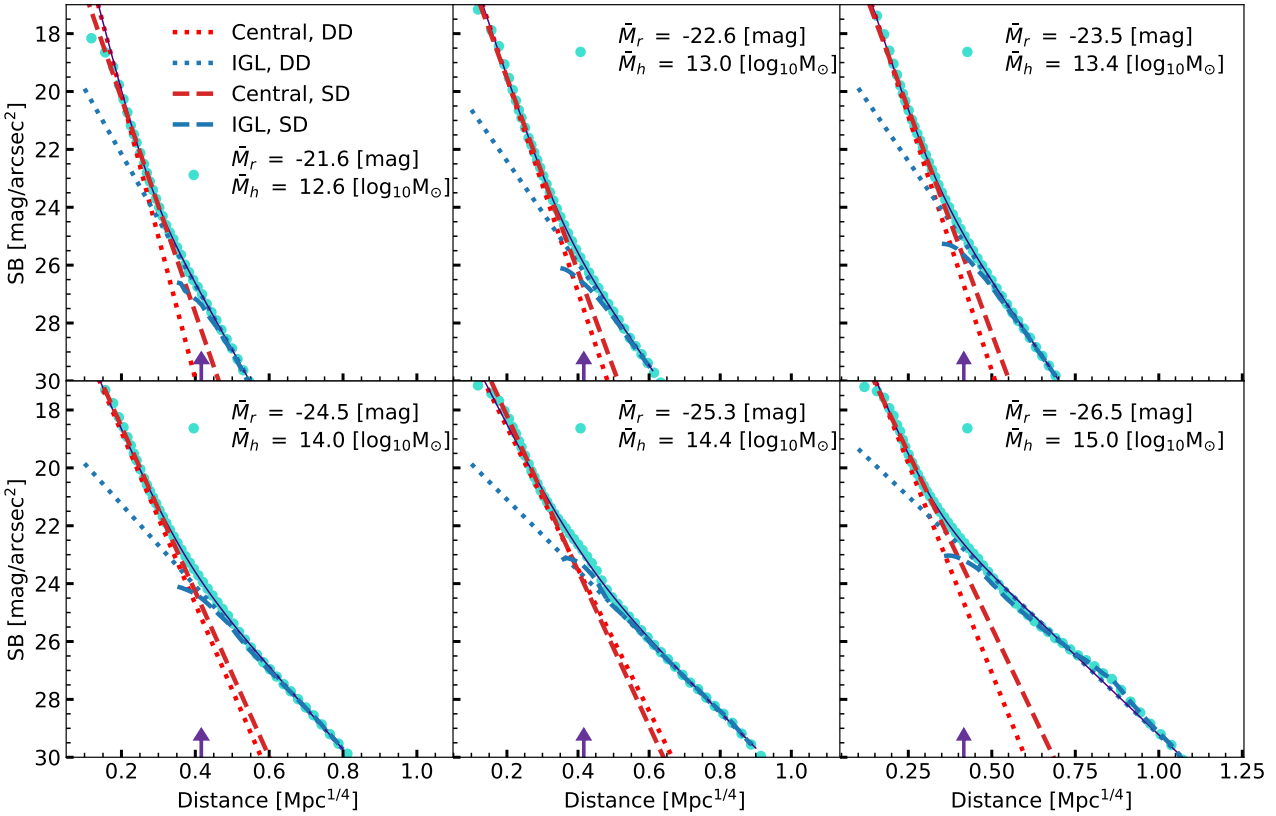

Figure 3.9: The radial surface brightness profiles of Hydrangea groups stacked within narrow magnitude bins. Turquoise circles show the stacked surface brightness profiles of the Hydrangea groups with the average central galaxy magnitude and average halo mass of the groups indicated in the top-right corner of each panel. Dashed lines indicate the best-fit single de Vaucouleurs profile (SD) of the central (red) and the remaining light as the IGL (blue). The dotted lines indicate the best-fit double de Vaucouleurs (DD) profile of the central (red) and the IGL (blue). The solid purple line shows the total central+IGL light from the double de Vaucouleurs fit. In all bins, the single and double de Vaucouleurs profiles provide comparably good fits to the data.

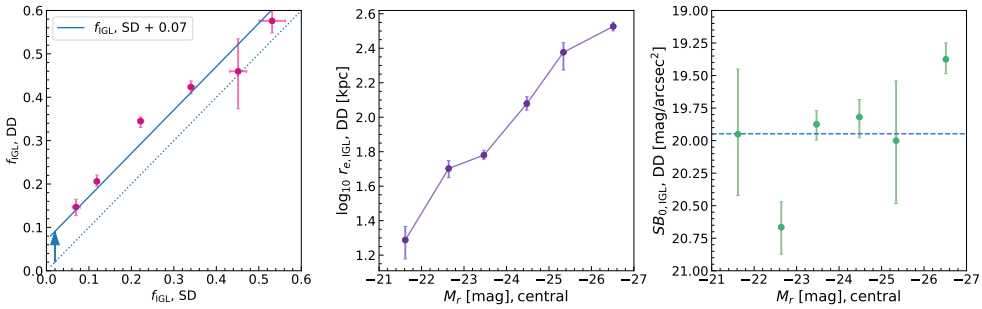

Figure 3.10: Left: comparison of the IGL fractions obtained from fitting the stacked surface brightness profiles with a single de Vaucouleurs profile (SD, x-axis) and a double de Vaucouleurs profile (DD, y-axis). The IGL fraction is systematically higher in the DD fitting. The solid blue line is the best linear fit with slope of unity to the individual points, with an offset of +0.07 (dotted line showing the 1-to-1 relation). Middle: effective radius (r_e) of the IGL profile from the DD fitting (dotted blue lines from Fig. 3.9) with respect to the average M_r bins of the central galaxy. The monotonically higher values of the r_e towards the right indicate that the IGL profile becomes more extended with increasing central galaxy luminosities. Right: central surface brightness of the IGL profiles from the DD fitting with respect to the average $M_{r,\,\mathrm{central}}$ bins. There is no systematic trend, albeit with some scatter. In all the panels, the error bars show the 68% confidence interval for the data points.

IGL is defined in these methods, the SD and DD fitted IGL lines cover different radial ranges in all the subplots. We compare the IGL measurement from these SD and DD methods in more detail in Fig. 3.10.

The left panel of Fig. 3.10 directly compares the IGL fractions obtained from fitting the stacked group surface brightness profiles with the SD and DD methods. In all the three panels in this figure, the error bars show the 68% confidence interval, and they are obtained by 100 bootstrap resampling of the groups in the stack before fitting the profiles. As visible from the left panel, the IGL fractions are consistently and systematically higher when estimated with the DD fit compared to the SD method. The solid blue line here shows the fitted line with unity slope through the points and it is offset by a value of 0.07. This indicates that using a DD fit instead of an SD fit to measure the IGL fraction results in about 7% higher IGL fraction in any of the magnitude-based sub-stacks in a similar group sample. By comparing to the fitted IGL profiles from Fig. 3.9 (dashed and dotted blue lines for the SD and DD fits, respectively), this excess likely comes from the IGL fraction from the inner region in the DD fitting. Because of the methodology we used to measure the central galaxy, IGL, and satellite fractions in these groups (see Sec. 3.5.1), this difference resulted in the central galaxy having a lower light fraction in the DD fits compared to the SD fits.

The satellite light fraction, however, remained unchanged by definition. The $\sim$ 7% difference in the estimated $f_{\rm IGL}$ between the SD and DD methods is similar to what Kluge et al. (2021) reported by using the same two methods to measure the $f_{\rm IGL}$ in their sample of 170 galaxy clusters at $z \leq 0.08$. However, their measured $f_{\rm IGL}$ range (13-18%) is significantly smaller (albeit with a large scatter in the measurement) than what we find (35-50% on the cluster scale). Using stacking analysis on SDSS groups and SD fitting to separate the central galaxy and IGL, Zibetti et al. (2005) also found a smaller $f_{\rm IGL}$ (10.9$\pm$5.0). Based on simulated data and DD fitting, Puchwein et al. (2010) reported a similar $f_{\rm IGL}$ compared to our measurements here. For a more detailed comparison of $f_{\rm IGL}$ measurements among observational and simulation-based studies using different methods, interested readers are referred to table 1 of Kluge et al. (2021). Comparing these existing works to the left panel of Fig. 3.10 demonstrates that although $f_{\rm IGL}$ can vary depending on the data and the method to separate the IGL from the central galaxy, the scatter of $f_{\rm IGL}$ measurements between different methods can be quantified. These systematic differences among other common methods of ICL measurements can be explored and used for a robust comparison between $f_{\rm IGL}$ measurements from different studies.

The middle panel of Fig. 3.10 shows the effective radius (r_e) of the IGL profile from the DD fitting (dotted blue lines from Fig. 3.9) against the average $M_{\rm r,\ central}$ bins. The r_e values have a positive correlation with the increasing central galaxy luminosities, indicating a more extended profile in groups with a brighter central. The right panel shows the central surface brightness of the IGL profiles from the DD fitting with respect to the average $M_{\rm r,\ central}$ bins. They show a small range of the central SB of the IGL profiles regardless of the central galaxy luminosities. Combining with the findings from the middle panel, this indicates that the higher IGL fraction in brighter groups is primarily due to more extended diffuse light rather than a self-similar increase in SB across all radii compared to groups with a fainter central galaxy.

Coming back to the effect of group miscentring from Sec. 3.4.3, we have also explored the effect of the miscentring on the IGL fraction. We took the stacked SB profiles around the true centre of potentials and around the brightest galaxies for the 25 groups where these differ (shown in the left panel of Fig. 3.6). We measured the central, IGL, and satellite light fractions compared to the total group light for both of these stacks following the same procedure as we have used for the analysis in this section. We see a $\sim$ 20% difference in the central and satellite fractions, with the central fraction increasing and the satellite fraction decreasing in the miscentred sample when measured around the brightest galaxies rather than the actual centre-of-

potential. The change in central and satellite fraction is expected as we are swapping the central galaxies in the images with a brighter galaxy. As this is not at the potential minimum of the halo, there are also fewer satellite galaxies within a 1Mpc radius around it in the mock images which can affect the SB profile at larger radii. However, we see almost no change in the IGL fraction (from 14% to 13%). This lack of change is likely because the miscentring occurs only for the less massive groups where the IGL fraction is already small (for majority of such groups, it is <20%). For such small IGL fractions, the difference of the IGL profiles at the outskirts of the blue and red profiles from the left panel of Fig. 3.6 can only measure up to around 1% compared to the total light, which is a much smaller value than the scatter of the IGL fractions from individual groups ($\sim$ 10%). Therefore, the slight difference in the SB profiles does not have any significant impact on the total IGL measurement. This was also reflected by the initial test of the surface brightness profile of all the groups (Sec. 3.4.3) where we did not notice any visible difference in the profiles around the true and updated centrals. Moreover, almost all the ambiguous centrals were found to contain signatures of a recent halo merger, which means that these bright galaxies are most likely central galaxies of another group halo that is falling into the host halo in consideration. In that case, these alternative centrals may well have their own IGL around them that they assembled before the merger. Therefore, we can expect that $\sim$ 5% possibly misidentified centrals will not add any significant bias in the detection and analysis of the IGL in our observed GAMA group sample (to be presented in a companion study, Ahad et al., in prep.).

3.5.3 Radial (u-r) colour profile of central+IGL

Different formation mechanisms of the IGL are expected to leave a distinct imprint in the stellar populations of the IGL, which can be traced by IGL properties such as colour and metallicity. For example, the age, colour, and metallicity profiles of the IGL are very different if the dominant formation channel of IGL is tidal stripping of massive satellites, total disruption of dwarf galaxies, or stellar ejection after major mergers. The gradient of the profiles can indicate which mechanisms were dominant, and the intrinsic values of the properties can point to which type of galaxies contributed to the IGL the most (Montes, 2022; Contini, 2021). Multiple studies based on groups and clusters have found negative gradients in the radial colour profile of the central+IGL which can indicate a gradient in either age or metallicity (more details can be found in Montes, 2022; Contini, 2021, and references therein). However, the age-metallicity

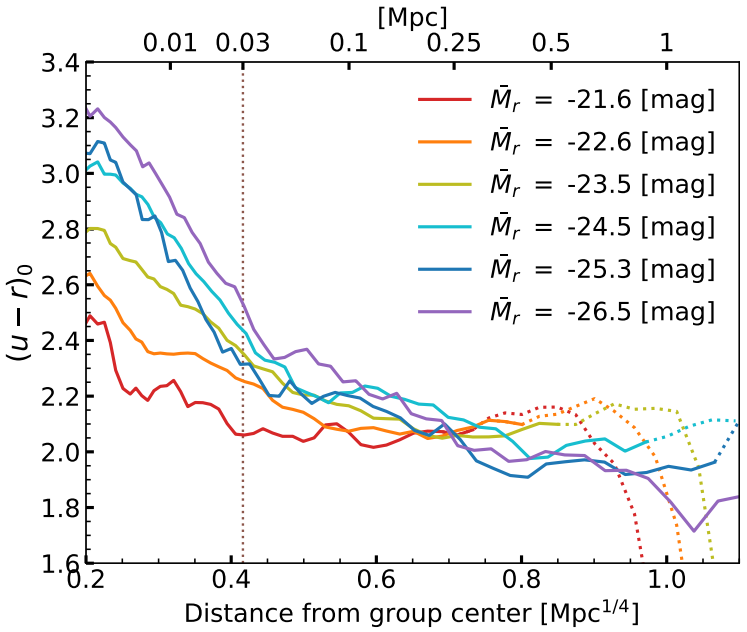

Figure 3.11: The radial profile of the rest frame $u-r$ colour of the central+IGL from Hydrangea groups in different central magnitude bins. Each line represents a different central galaxy magnitude bin as shown in the top right corner. The brown dotted vertical line at 30 kpc from the group centre indicates the typical extent of the central galaxy. All the lines are solid until the average r_{200} within their bin, and dotted beyond.

degeneracy makes disentangling these two quantities from colours alone a challenging endeavour. Having data from a bluer photometric band such as the $u-$band can potentially help with resolving this issue. As we have information about the real age, metallicity, and colour from the simulations, here we studied the radial distribution of these three properties for our group sample.

Figure 3.11 shows the radial $(u-r)_0$ colour profiles of the central+IGL in our central magnitude-based sub-stacks of the groups. We obtained the azimuthally averaged $(u-r)_0$ colour profiles from the mock images of the groups in u and r bands which include only the star particles that are part of the central group galaxy and IGL. The different colours in the figure indicate different magnitude bins (mean magnitudes of the bins are shown in the top right corners). Out to 30 kpc, the approximate extent

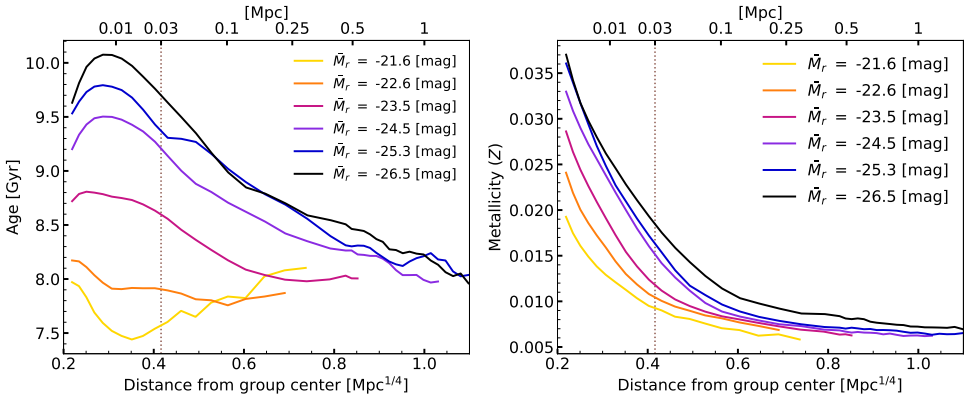

Figure 3.12: The radial age (left) and metallicity (right) profiles of the central+IGL from Hydrangea groups in different central galaxy magnitude bins. In both panels, the brown vertical dotted line shows 30 kpc distance from the group centres. The age profiles show large variation between the groups with faint and bright centrals. The metallicity profiles have similar trends for all the magnitude bins.

of the central galaxy (indicated by the vertical dotted line), all the colour profiles have a negative gradient which is stronger for the brighter centrals. At larger radii, the difference in gradient between the low and high mass groups (with fainter and brighter centrals, respectively) becomes more prominent. The profile of groups with fainter centrals (red and orange) have a shallower or flatter profile compared to the ones with a brighter central (blue and purple) which show a stronger negative gradient out to at least 500 kpc. It may indicate that compared to the lower mass groups, the light in central+IGL of the higher mass groups grew preferably by accretion over mergers. But to confirm any such indication, it is necessary to look into the age and metallicity profiles of the same sample.

We explore the age and metallicity profiles of our sample in Fig. 3.12, computed directly from the simulation outputs. The left and right panels show the azimuthally averaged radial profiles of the age and metallicity of the group central+IGL in the same magnitude bins as Fig. 3.11, respectively. The different colours indicate the different magnitude bins and the mean magnitudes of the bins are shown in the legends. For both the panels, the brown vertical dotted line shows a 30 kpc distance from the group centres. For higher mass groups and clusters (with brighter centrals), the radial age profiles follow a similar negative gradient pattern to the $u - r$ profiles from Fig. 3.11.

The lower mass groups (fainter centrals, yellow, orange, and magenta) have a flatter or irregular age profile which is comparable to the corresponding $u - r$ colour profiles of the corresponding groups. For the metallicity profiles, all the bins have a similar negative gradient in the inner part (<100 kpc) that approaches a flatter profile in the outskirts.

In all three profiles (colour, age, metallicity), the visibly different intrinsic values for different magnitude bins within 30 kpc from the centre indicate that brighter centrals are on average redder, older, and have a higher metallicity which is expected in general for giant elliptical galaxies (e.g. Peletier et al., 1990; Davies et al., 1993; Huang et al., 2018; Santucci et al., 2020). However, the colour profiles here trace the metallicity profile more strongly than the age. The profiles beyond 30 kpc here indicate a different story for different central magnitude bins (or different halo mass ranges). The high mass groups/clusters ($M_r < -24$) have a similar negative age gradient from the centre to the far outskirts. In this case, the colour profiles are more correlated to the age profiles compared to the metallicity profiles. The shallower metallicity profiles in the outskirts are an indication that the IGL was built via the accretion of satellite galaxies. The stellar population of the accreted galaxies then got mixed to produce the flat metallicity distribution (e.g. Montes et al., 2021). The negative gradient of the age profile at the outskirts of the high mass groups, together with the similar colour profile, also supports the scenario of IGL growth via accretion. In contrast, the flatter colour profile at the outskirts of the lower mass groups may indicate ICL formation through expelled stars from a major merger (Krick and Bernstein, 2007; DeMaio et al., 2018). The flat age profile of the low mass groups with a younger average age also supports this hypothesis. However, it is worth mentioning that the intrinsic scatter of these average age profiles for the lower mass groups is rather high ($\sim$ 1 Gyr, not shown here). This is likely resulting from a combination of multiple IGL formation scenario as different groups can have different IGL formation histories which is averaged out in a stacked sample like ours. A smaller intrinsic scatter for the higher mass groups ($\sim$ 0.2 Gyr), on the other hand, indicates that the IGL formation history is more homogeneous for such groups. However, the stacks in narrow magnitude bins still retain some key signatures of the corresponding group ensemble.

To sum up, the negative gradient of the age and colour profiles at the outskirts of the high mass groups indicate the scenario of IGL growth via accretion, whereas the flatter age and colour profiles of the low mass groups support the scenario of IGL formation via major mergers. Therefore, we conclude that in our sample, lower mass groups likely accumulated their IGL predominantly from mergers and the higher mass

groups/clusters likely accumulated their IGL from the accretion of stripped stars from the outskirts of other galaxies.

3.6 Summary and Conclusions

The growth and extent of the diffuse light in galaxy groups (IGL) can provide important insights to improve our understanding of hierarchical cosmic structure formation. However, identifying the centre of a galaxy group in an unambiguous way is observationally nontrivial and may introduce non-negligible bias in the IGL measurements. Central galaxy candidates in galaxy groups have a galaxy colour bimodality in their stellar-to-halo-mass relation (SHMR) that can lead to a misidentification of group centres from only stellar mass (or luminosity) based BGG selection. In this paper, we investigated the effect of misidentifying the group centre on the IGL measurements using data from the Hydrangea cosmological hydrodynamic simulation suite and a comparable group sample from the GAMA survey. We also studied the dependence of the IGL on the properties of the central galaxies in the groups. Our main findings are summarised as follows:

- Using a galaxy colour-based SHMR (Bilicki et al., 2021) to identify the central group galaxies instead of the luminosity-based selection of the Robotham et al. (2011) group catalogue leads to a re-assignment of the group centre in 23 per cent of the GAMA groups in our sample. Applying a similar procedure to mock images of the Hydrangea groups, we found that nearly the same fraction (18 per cent) of them do not have their r-band brightest galaxy at the potential centre of their halo, out of which 49 per cent are due to line of sight projection. The rest are most likely resulting from recent halo mergers.

- Despite the difference in the selected central galaxy, the radial galaxy-mass density profiles remain unchanged when centring on the true halo centre (for Hydrangea) or the updated central galaxy (for GAMA) instead of the brightest group galaxy (BGG). However, the surface brightness (SB) profile of the Hydrangea groups is suppressed by up to 0.5 mag beyond 30 kpc (where IGL dominates) when centred on the BGG rather than the true group centre. Therefore, a similar difference in the SB profile can indicate miscentring in central group galaxy selection. But such miscentring does not significantly affect the measurements of IGL fraction, because even amongst ambiguously centred groups, this suppression only affects the total IGL fraction measurement by $\sim$1 per cent.

- To separate the central galaxy from the IGL, we fitted a single-component de Vaucouleurs (SD) profile to the inner 40 kpc of the satellite-excised SB profile. The excess above the fitted central galaxy light was identified as the IGL. The estimated IGL fraction out of the total group light is positively correlated with the host halo mass, central galaxy magnitude, and richness, albeit with a higher scatter at the low richness end. This correlation indicates that during a stacking analysis to measure the IGL, a sub-stacking based of the central galaxy magnitude will make the interpretation of the measurements more straightforward.

- We also used a double de Vaucouleurs (DD) fit to separate the central and IGL in the SB profile. However, the DD fitting was unsuccessful for 80% of the individual groups, which was primarily due to the presence of additional features in the SB profile beyond 50 kpc from the centres. Such features are smoothed when we stacked the groups in narrow magnitude bins, and both the SD and DD fitting worked well for the stacked profiles. The estimated IGL fractions using an SD fitting compared to a DD fitting to the central+IGL light are consistently about 7% lower for all the magnitude bins. This difference can be used to calibrate IGL measurements from different studies that use either of these methods. Such systematic differences among other common methods can be explored for a robust comparison among different IGL measurement studies.

- The central surface brightness of the IGL from the stacked DD fits is very similar for all the magnitude bins, and the half-light radius of the IGL from the DD fit gets larger from fainter to brighter centrals. This finding indicates that groups with brighter centrals have more extended IGL.

- The rest-frame $u - r$ colour, age, and metallicity profiles of the central+IGL are different for different magnitude bins, with brighter centrals being redder, older, and more metal rich at a given radius. This suggests that the dominant IGL formation channel for the low mass groups is likely major mergers, whereas the dominant IGL formation channel for the high mass groups/clusters is likely stellar stripping from satellite galaxies.

The findings from this work will be used to interpret the IGL component in the GAMA galaxy groups using KiDS imaging data and can be used as crucial predictions to interpret the IGL component from the upcoming next-generation survey data like *Euclid* or LSST.

Acknowledgements

SLA and HH acknowledge support from the Netherlands Organization for Scientific Research (NWO) under Vici grant number 639.043.512. YMB acknowledges support from NWO under Veni grant number 639.041.751. The authors thank Shun-Sheng Li for sharing measurements of the weak lensing signal around the GAMA groups with an ambiguous centre.

The Hydrangea simulations were in part performed on the German federal maximum performance computer "HazelHen" at the maximum performance computing centre Stuttgart (HLRS), under project GCS-HYDA / ID 44067 financed through the large-scale project "Hydrangea" of the Gauss Center for Supercomputing. Further simulations were performed at the Max Planck Computing and Data Facility in Garching, Germany. This work used the DiRAC@Durham facility managed by the Institute for Computational Cosmology on behalf of the STFC DiRAC HPC Facility (www.dirac.ac.uk). The equipment was funded by BEIS capital funding via STFC capital grants ST/K00042X/1, ST/P002293/1, ST/R002371/1 and ST/S002502/1, Durham University and STFC operations grant ST/R000832/1. DiRAC is part of the National e-Infrastructure.

This research made use of data from the Galaxy and Mass Assembly survey (GAMA). GAMA is a joint European-Australasian project based around a spectroscopic campaign using the Anglo-Australian Telescope. The GAMA input catalog is based on data taken from the Sloan Digital Sky Survey and the UKIRT Infrared Deep Sky Survey. Complementary imaging of the GAMA regions is being obtained by a number of independent survey programs including GALEX MIS, VST KiDS, VISTA VIKING, WISE, Herschel-ATLAS, GMRT, and ASKAP providing UV to radio coverage. GAMA is funded by the STFC (UK), the ARC (Australia), the AAO, and the participating institutions. The GAMA website is http://www.gama-survey.org.

The analysis of this work was done using Python (http://www.python.org), and Jupyter notebook (Kluyver et al., 2016), including the Python packages NumPy (Harris et al., 2020), AstroPy (Astropy Collaboration et al., 2013), and SciPy (Jones et al., 2009). Plots have been produced with Matplotlib (Hunter, 2007).

Data Availability

The data presented in the figures are available upon request from the corresponding author. The raw simulation data can be requested from the C-EAGLE team (Bahé

et al., 2017; Barnes et al., 2017).

References

Ahad, S. L., Bahé, Y. M., Hoekstra, H., et al., 2021, MNRAS, 504, 1999
Alonso Asensio, I., Dalla Vecchia, C., Bahé, Y. M., et al., 2020, MNRAS, 494, 1859
Astropy Collaboration, Robitaille, T. P., Tollerud, E. J., et al., 2013, A&A, 558, A33
Bahé, Y. M., Schaye, J., Barnes, D. J., et al., 2019, MNRAS, 485, 2287
Bahé, Y. M., Schaye, J., Schaller, M., et al., 2022, MNRAS, 516, 167
Bahé, Y. M. et al., 2017, MNRAS, 470, 4186
Barnes, D. J., Kay, S. T., Bahé, Y. M., et al., 2017, MNRAS, 471, 1088
Barnes, D. J., Kay, S. T., Henson, M. A., et al., 2017, MNRAS, 465, 213
Bertin, E. and Arnouts, S., 1996, A&AS, 117, 393
Bilicki, M., Dvornik, A., Hoekstra, H., et al., 2021, A&A, 653, A82
Bower, R. G., Benson, A. J., Malbon, R., et al., 2006, MNRAS, 370, 645
Cañas, R., Lagos, C. d. P., Elahi, P. J., et al., 2020, MNRAS, 494, 4314
Chilingarian, I. V., Melchior, A.-L., and Zolotukhin, I. Y., 2010, MNRAS, 405, 1409
Chilingarian, I. V. and Zolotukhin, I. Y., 2012, MNRAS, 419, 1727
Contini, E. and Gu, Q., 2021, ApJ, 915, 106
Contini, E., 2021, Galaxies, 9, 60
Crain, R. A., Schaye, J., Bower, R. G., et al., 2015, MNRAS, 450, 1937
Dalla Vecchia, C. and Schaye, J., 2012, MNRAS, 426, 140
Davies, R. L., Sadler, E. M., and Peletier, R. F., 1993, MNRAS, 262, 650
DeMaio, T., Gonzalez, A. H., Zabludoff, A., et al., 2018, MNRAS, 474, 3009
DeMaio, T., Gonzalez, A. H., Zabludoff, A., et al., 2020, MNRAS, 491, 3751
Dolag, K., Borgani, S., Murante, G., et al., 2009, MNRAS, 399, 497
Driver, S. P., Hill, D. T., Kelvin, L. S., et al., 2011, MNRAS, 413, 971
Driver, S. P., Bellstedt, S., Robotham, A. S. G., et al., 2022, MNRAS, 513, 439
Driver, S. P., Norberg, P., Baldry, I. K., et al., 2009, Astronomy and Geophysics, 50, 5.12
Driver, S. P., Wright, A. H., Andrews, S. K., et al., 2016, MNRAS, 455, 3911
Furlong, M., Bower, R. G., Theuns, T., et al., 2015, MNRAS, 450, 4486
Gallagher John S., I. and Ostriker, J. P., 1972, Astronomical Journal, 77, 288
García-Benito, R., González Delgado, R. M., Pérez, E., et al., 2019, A&A, 621, A120
Gonzalez, A. H., Sivanandam, S., Zabludoff, A. I., et al., 2013, ApJ, 778, 14
Gonzalez, A. H., Zabludoff, A. I., and Zaritsky, D., 2005, ApJ, 618, 195
Guo, Q., White, S., Boylan-Kolchin, M., et al., 2011, MNRAS, 413, 101
Harris, C. R., Jarrod Millman, K., van der Walt, S. J., et al., 2020, arXiv e-prints, arXiv:2006.10256
Henden, N. A., Puchwein, E., and Sijacki, D., 2020, MNRAS, 498, 2114
Huang, S., Leauthaud, A., Greene, J. E., et al., 2018, MNRAS, 475, 3348
Hunter, J. D., 2007, Computing in science & engineering, 9, 90
Jakobs, A., Viola, M., McCarthy, I., et al., 2018, MNRAS, 480, 3338
Jiménez-Teja, Y., Dupke, R., Benítez, N., et al., 2018, ApJ, 857, 79
Jones, D. H., Read, M. A., Saunders, W., et al., 2009, MNRAS, 399, 683
Jones, L. R., Ponman, T. J., Horton, A., et al., 2003, MNRAS, 343, 627
De Jong, J. T. A., Kuijken, K., Applegate, D., et al., 2013, The Messenger, 154, 44
Kluge, M., Bender, R., Riffeser, A., et al., 2021, ApJS, 252, 27
Kluyver, T., Ragan-Kelley, B., Pérez, F., et al. (2016). "Jupyter Notebooks – a publishing format for reproducible computational workflows". *Positioning and Power in Academic Publishing: Players, Agents and Agendas*. Ed. by F. Loizides and B. Schmidt. IOS Press, 87.
Krick, J. E. and Bernstein, R. A., 2007, Astronomical Journal, 134, 466
Kuijken, K., Heymans, C., Dvornik, A., et al., 2019, A&A, 625, A2
Lange, J. U., van den Bosch, F. C., Hearin, A., et al., 2018, MNRAS, 473, 2830

Liske, J., Baldry, I. K., Driver, S. P., et al., 2015, MNRAS, 452, 2087
Lotz, J. M., Koekemoer, A., Coe, D., et al., 2017, ApJ, 837, 97
Mandelbaum, R., Wang, W., Zu, Y., et al., 2016, MNRAS, 457, 3200
Mihos, C. (Aug. 2015). "Intragroup and Intracluster Light". *IAU General Assembly*. Vol. 29, 2247903, 2247903.
Mihos, J. C., Harding, P., Feldmeier, J., et al., 2005, ApJL, 631, L41
Mihos, J. C., Harding, P., Feldmeier, J. J., et al., 2017, ApJ, 834, 16
Montes, M., 2022, Nature Astronomy, 6, 308
Montes, M., Brough, S., Owers, M. S., et al., 2021, ApJ, 910, 45
Montes, M. and Trujillo, I., 2014, ApJ, 794, 137
Montes, M. and Trujillo, I., 2018, MNRAS, 474, 917
Montes, M. and Trujillo, I., 2019, MNRAS, 482, 2838
Murante, G., Giovalli, M., Gerhard, O., et al., 2007, MNRAS, 377, 2
Negri, A., Dalla Vecchia, C., Aguerri, J. A. L., et al., 2022, arXiv e-prints, arXiv:2205.13553
Oliva-Altamirano, P., Brough, S., Lidman, C., et al., 2014, MNRAS, 440, 762
Oppenheimer, B. D., Babul, A., Bahé, Y., et al., 2021, Universe, 7, 209
Peletier, R. F., Davies, R. L., Illingworth, G. D., et al., 1990, Astronomical Journal, 100, 1091
Pillepich, A., Nelson, D., Hernquist, L., et al., 2018, MNRAS, 475, 648
Planck Collaboration XVI, 2014, A&A, 571, A16
Poliakov, D., Mosenkov, A. V., Brosch, N., et al., 2021, MNRAS, 503, 6059
Ponman, T. J., Allan, D. J., Jones, L. R., et al., 1994, Nat., 369, 462
Puchwein, E., Springel, V., Sijacki, D., et al., 2010, MNRAS, 406, 936
Robotham, A. S. G., Norberg, P., Driver, S. P., et al., 2011, MNRAS, 416, 2640
Rosas-Guevara, Y., Bower, R., Schaye, J, et al., 2015, MNRAS, 454, 1038
Van Sande, J., Kriek, M., Franx, M., et al., 2015, ApJ, 799, 125
Santucci, G., Brough, S., Scott, N., et al., 2020, ApJ, 896, 75
Schaller, M., Dalla Vecchia, C., Schaye, J., et al., 2015, MNRAS, 454, 2277
Schaye, J., 2004, ApJ, 609, 667
Schaye, J., Crain, R. A., Bower, R. G., et al., 2015, MNRAS, 446, 521
Schaye, J. and Dalla Vecchia, C., 2008, MNRAS, 383, 1210
Springel, V., 2005, MNRAS, 364, 1105
Springel, V., White, S. D. M., Tormen, G., et al., 2001, MNRAS, 328, 726
Stanek, R., Evrard, A. E., Böhringer, H., et al., 2006, ApJ, 648, 956
Steinhardt, C. L., Jauzac, M., Acebron, A., et al., 2020, ApJS, 247, 64
Taylor, E. N., Hopkins, A. M., Baldry, I. K., et al., 2011, MNRAS, 418, 1587
Tinker, J. L., 2022, Astronomical Journal, 163, 126
Tonnesen, S. and Bryan, G. L., 2012, MNRAS, 422, 1609
Trayford, J. W., Camps, P., Theuns, T., et al., 2017, MNRAS, 470, 771
Trayford, J. W., Theuns, T., Bower, R. G., et al., 2015, MNRAS, 452, 2879
De Vaucouleurs, G., 1948, Annales d'Astrophysique, 11, 247
Wiersma, R. P. C., Schaye, J., Theuns, T., et al., 2009, MNRAS, 399, 574
Wiersma, R. P., Schaye, J., and Smith, B. D., 2009, MNRAS, 393, 99
Wright, A. H., Robotham, A. S. G., Bourne, N., et al., 2016, MNRAS, 460, 765
Zhang, Y., Yanny, B., Palmese, A., et al., 2019, ApJ, 874, 165
Zibetti, S., White, S. D. M., Schneider, D. P., et al., 2005, MNRAS, 358, 949

4

The intragroup light in KiDS+GAMA groups

Abstract

Galaxy groups and clusters assembled through dynamical interactions of smaller systems, resulting in the formation of a diffuse stellar halo known as the intragroup or intracluster light (IGL/ICL). By preserving the records of these interactions, this diffuse light provides valuable insight into the growth history of the halos and their brightest galaxies. Groups are especially interesting in this context because they represent the link between galactic haloes and massive clusters. However, low surface brightness makes it extremely challenging to detect their diffuse light individually. Recent deep wide-field imaging surveys allow us to push such measurements to lower brightness limits by stacking data for large ensembles of groups, which suppresses the noise and biases in the measurements. However, standard data processing pipelines for such surveys are not optimised to retain the diffuse light in IGL/ICL at extended radii. In this work, we present a special-purpose pipeline to reprocess individual KiDS exposures in $r-$band that optimises the IGL detection. Using an initial sample of 2385 groups with at least five spectroscopically-confirmed member galaxies from the Galaxy and Mass Assembly (GAMA) survey at $0.09 \leq z \leq 0.42$ and deep images from the Kilo-Degree Survey (KiDS, reprocessed with our updated pipeline), we present the first robust measurement of IGL from a large group sample down to 31-32 mag/arcsec^2 (varying in different stacked bins). We compare our stacked IGL measurements to predictions from matched mock observations from the Hydrangea cosmological hydrodynamic simulations. We find that systematics in the imaging data can affect IGL measurements even with our special-purpose pipeline. However, with a large sample and carefully optimised analysis, we can place well-constrained upper and lower limits on the IGL fraction for our group ensemble across redshifts $0.09 \leq z \leq 0.27$ and halo-masses $12.5 \leq \log_{10}[M_{200}/\mathrm{M}_\odot] \leq 14.0$ which are comparable to existing measurements of IGL in individual systems at similar redshift and halo mass range. This work explores the potential performance of statistical analysis of diffuse light in large samples of systems from next-generation observational programs like Euclid and LSST.

Ahad, S. L., Hoekstra, H., Bahé, Y. M., 2023, in preparation.

4.1 Introduction

It is well-established that the central galaxies (CG, also commonly referred to as the brightest group/cluster galaxy, BGG/BCG) in groups and clusters of galaxies are surrounded by an extended diffuse distribution of stars, which are often referred to as the intragroup or intracluster light (IGL/ICL, see e.g. Mihos, 2015; Montes, 2022, for recent reviews). Extending out to several hundreds of kilo-parsecs from the centre and often enveloping multiple galaxies in the host system, this diffuse light is generally considered as a separate component of the galaxy groups and clusters they are part of. Over the last few decades, different techniques have been explored to independently measure this diffuse component from their host system, especially to separate this from the CGs they surround. Depending on the measuring technique, the ICL has been found to contain as much as 30 per cent or more of the total starlight of the host system (e.g., Zibetti et al., 2005; Gonzalez et al., 2013; Mihos et al., 2017; Montes and Trujillo, 2018; Zhang et al., 2019; Kluge et al., 2021). However, a unanimous definition of this diffuse component (from simulations and observations) and how much they contribute to the total light of their host systems is still an open discussion (see, e.g. table 1 from Kluge et al., 2021). The origin and growth history of this diffuse light has been explored through multiple simulation-based studies (see, e.g. Mihos et al., 2017; Contini, 2021, for more discussion on the origin and growth of the ICL). These studies found several ways in which the IGL/ICL can build up, including tidal stripping (Gallagher and Ostriker, 1972), galaxy disruption (Guo et al., 2011), galaxy mergers (Murante et al., 2007), and in-situ star formation in the intracluster medium (Puchwein et al., 2010; Tonnesen and Bryan, 2012).

In recent years, studies on this diffuse light in individual clusters by using deep imaging have been increasing (e.g., Mihos et al., 2005; Montes and Trujillo, 2014, 2018; Jiménez-Teja et al., 2018; DeMaio et al., 2018, 2020; Montes et al., 2021), along with a few works where stacking a statistical sample of systems to improve the signal-to-noise-ratio have been performed (e.g., Zibetti et al., 2005; Zhang et al., 2019). Some recurring findings indicate that the ICL mass distribution follows the global dark matter (DM) distribution (e.g., Montes and Trujillo, 2019; Alonso Asensio et al., 2020, from observations and simulations, respectively), and that rather than with the CG, ICL profiles align more with the underlying cluster halo (Kluge et al., 2021). These findings collectively imply that the ICL growth is connected to the evolution of the CG (which are often large elliptical galaxies) in the host system, the baryon fraction of galaxy clusters, and the build-up of large-scale structures like galaxy clusters where

the giant galaxies (BCG) reside.

Although most studies on this diffuse light are based on clusters because the ICL is more prominent and clusters are preferentially targeted by deep surveys such as HFF (Lotz et al., 2017) or BUFFALO (Steinhardt et al., 2020), studying the diffuse light in groups (or IGL) is particularly interesting for several reasons. Firstly, they cover the intermediate halo mass regime of galaxy structures between galaxy-sized haloes and galaxy clusters. Therefore, understanding the build-up of the diffuse light corresponding to the halo mass of the system will not be possible without understanding the growth of IGL. Secondly, groups are interesting and distinct systems compared to the clusters because they are dynamically less disturbed, and have had fewer interactions with other systems. As a result, it is more straightforward to connect the growth of the IGL in groups with their dynamic history. Finally, according to the hierarchical structure formation model, the larger clusters are built by the infall and merging of smaller groups in their already existing larger haloes. In this scenario, a good fraction of the feedback and preprocessing of the member galaxies already happened in the groups before they even became part of a larger halo or a cluster. Detection of IGL at a $z = 1.85$ galaxy group by Coogan et al. (2023) supports this scenario. Recent works on detecting ICL in high-redshift clusters and protoclusters also provide evidence of the growth of this diffuse light for quite a long time over the age of the Universe (e.g. Joo and Jee, 2023; Werner et al., 2023). Therefore, understanding these smaller systems will lead to a better understanding of the physics of the larger systems.

Even though the importance of understanding the fractions and buildup of IGL/ICL across a wide range of host halo mass is clear, there have only been a few studies on IGL, and even fewer that cover a wide range of group-mass haloes so far. The main reason behind this is the lack of data with high enough resolution and signal-to-noise ratio (SNR) to reliably detect and analyze the faint IGL in groups.

Studying the light distribution of individual groups is useful to understand the diversity of the IGL signal and its formation channels. However, the low surface brightness of the IGL means that individual systems have a very low SNR, which makes the systematics in data to have a relatively more prominent effect on the measurements and introduces a higher uncertainty in their interpretations. Stacking the light of multiple groups can help to improve the SNR while keeping the key features of the underlying population. Zibetti et al. (2005) studied the diffuse light in 683 SDSS groups and clusters at $0.2 < z < 0.3$ using g, r, and i band photometry by stacking them to increase the SNR. They reported that, on average, the ICL contributes a small fraction ($\sim 10\%$) of the total visible light in a cluster. They also found that the surface

brightness of the ICL correlates with BCG luminosity and with cluster richness, but the fraction of the total light in the ICL does not vary notably with these properties. However, they only studied these behaviours by dividing their sample into two subsamples for each property (bright BCG - faint BCG, high richness - low richness) which may not be sensitive to a wider variation of these properties. With deep multi-band (u, g, r, i) photometry of the Kilo Degree Survey (KiDS, Kuijken et al., 2019) and the group catalogue based on spectroscopic redshifts by the Galaxy and Mass Assembly (GAMA, Driver et al., 2009; Driver et al., 2011) survey, we can now attempt to push the detection limit of the IGL and explore its co-evolution with the host systems across a wider halo mass range.

However, before simply stacking all the group data, we need to consider a few caveats. One important issue is the diversity of IGL/ICL distribution depending on the properties of the host system (groups/clusters) and its central galaxy (CG). Based on the data from their semi-analytic model, Contini and Gu (2021) reported that the ICL distribution varies widely depending on the dynamical history and morphology of the CG. Another recent work based on 170 low-redshift ($z \leq 0.08$) galaxy clusters in the northern hemisphere by Kluge et al. (2021) reported a positive correlation between CG+ICL brightness and different properties of the host cluster (e.g., mass, size, and integrated light in the satellites). Therefore, it is necessary to quantify the effect of galaxy and host system properties on the IGL measurements in a stacking analysis in order to find the optimal way of stacking for a reliable interpretation of the measurements. We explored this in Ahad et al. (2023), where we used mock observations of a GAMA-like group sample matching the KiDS $u-$ and $r-$band photometry using the Hydrangea cosmological simulations (Bahé et al., 2017). We utilise insights and predictions from Ahad et al. (2023) in this work to design and interpret our analysis.

Another major concern is the suitability of KiDS data for low-surface-brightness (LSB) analysis such as IGL measurement because of this being a cosmology survey with imaging from a wide-field camera. The data processing pipelines for cosmology surveys are usually optimised for measuring shapes and fluxes of small and faint galaxies. This requires a uniform photometric zero-point throughout the large joined pointings, which is often achieved by background-level detection and subtraction on very small scales compared to the total image size. The resulting images can have an uneven background, with the background over-subtracted near bright sources such as the CG of groups and clusters, making them quite unsuitable for IGL measurements. Moreover, in wide-field cameras like the OmegaCAM (Kuijken, 2011), the large aperture can cause internal reflection of light from bright sources, resulting in residual

(radial) patterns in the field image from uneven illumination. A wider field of view also increases the chance of streaks of diffused stray light from bright sources that are nearby, such as the Moon or planets. The stray-light and internal reflection issues are usually taken care of during the data processing phase. However, the standard corrections can leave extremely faint residual patterns in the field-of-view that only surface while stacking many images. This should be accounted for, especially in the case of an LSB analysis. Therefore, we develop a custom-made pipeline to re-process the KiDS data, taking special care of the background subtraction to retain a uniform background as much as possible.

In this paper, we present our custom pipeline to reprocess the multi-band (u, g, r, i) imaging from the KiDS data release 4 to optimise them for LSB analysis, and different checks that were done to ensure a robust measurement of the faint IGL in GAMA groups. We also present IGL measurements in stacked groups of different luminosities and redshift bins and compare them with predictions from the Hydrangea cosmological hydrodynamic simulations.

The organization of the paper is as follows. In Sec. 4.2, we present the GAMA groups and KiDS multi-band data we use for this work along with the selection criteria for our group sample. We also discuss the necessity of a custom pipeline for our analysis and describe the pipeline and its performance in keeping a uniform background level in the data in detail in this section (from Sec. 4.2.3 onward). In Sec. 4.3, we test the performance of the pipeline on retaining the diffuse light in galaxy outskirts and explore how to mask the diffuse light of satellite galaxies from the IGL measurements. In Sec. 4.4, we build an updated PSF model from the re-processed KiDS images and evaluate its impact on simulated IGL measurements. In Sec. 4.5, we present our resulting measurements and discuss how they compare to our predictions from simulations. Finally, in Sec. 4.6, we discuss the performance and expectation from wide-field surveys like KiDS in LSB analysis such as IGL measurement and summarise our findings.

4.2 Data

4.2.1 Galaxy and Mass Assembly survey data

The Galaxy And Mass Assembly (GAMA) project is a unique galaxy survey (Driver et al., 2009; Driver et al., 2011) with 21-band photometric data and spectroscopic redshifts of $\sim 300,000$ galaxies. The high completeness of the survey (98.5% complete

at $r-$band magnitude < 19.8 mag for SDSS-selected galaxies) allows for an excellent group selection (Robotham et al., 2011). The galaxy spectra in the GAMA survey were primarily measured by the AAOmega multi-object spectrograph on the Anglo-Australian Telescope in five fields covering a total of ~ 286 deg^2 area. As well as providing an almost volume-limited selection (of galaxies with $M_{\rm r} < 19.8$) at $z < 0.2$, the GAMA survey includes a large galaxy sample up to $z \sim 0.5$. Four of the GAMA fields (equatorial G09, G12 and G15 of 60 deg^2 each, and Southern G23 of ~ 51 deg^2) entirely overlap with the Kilo Degree Survey (KiDS, De Jong et al., 2013) – a large, deep, multi-band optical imaging survey that has great potential to reveal the faint IGL in GAMA groups (details in the following section).

We used the latest GAMA-II Galaxy Group Catalogue (`G$^3$CFoFv08`, Robotham et al., 2011) in this work. The catalogue was generated using a friends-of-friends (FoF) based grouping algorithm where galaxies are grouped based on their line-of-sight and projected physical separations. Information about the group member galaxies was obtained using an accompanying galaxy catalogue, `G$^3$CGalv09` (Liske et al., 2015).

To ensure the most robust group selection, we only considered groups with 5 or more member galaxies ($N_{\rm FoF} \geq 5$). After applying the $N_{\rm FoF}$ selection cut, we obtained a sample of 2389 groups. The distribution of redshift, CG magnitude, and halo mass of our final GAMA group sample is shown in Fig. 4.1. The halo masses were computed using the 'LumB' parameter of the `G$^3$CFoFv08` catalogue, and eqn. 37 of Viola et al. (2015). We used the stellar mass estimates and r-band magnitudes of GAMA galaxies from the `StellarMassesLambdarv20` catalogue (Taylor et al., 2011; Wright et al., 2016). This catalogue provides physical parameters based on stellar population fits to rest-frame $ugrizY$ spectral energy distributions (SEDs), and matched aperture photometry measurements of SDSS and VIKING photometry for all the $z < 0.65$ galaxies in the GAMA-II equatorial survey regions. This sample contains over 192,000 galaxies, and the stellar mass measurements assume $H_0 = 70$km s^{-1}Mpc^{-1}. Further details on the GAMA stellar mass derivation can be found in Taylor et al. (2011) and Wright et al. (2016).

4.2.2 Kilo Degree Survey

The Kilo-Degree Survey (KiDS, De Jong et al., 2013) is a large, deep, multi-band optical imaging survey that covers 1350 square degrees in four broadband filters (u, g, r, i). This cosmology survey was designed with the primary goal of mapping the large-scale matter distribution in the Universe and constraining the equation-of-state of dark en-

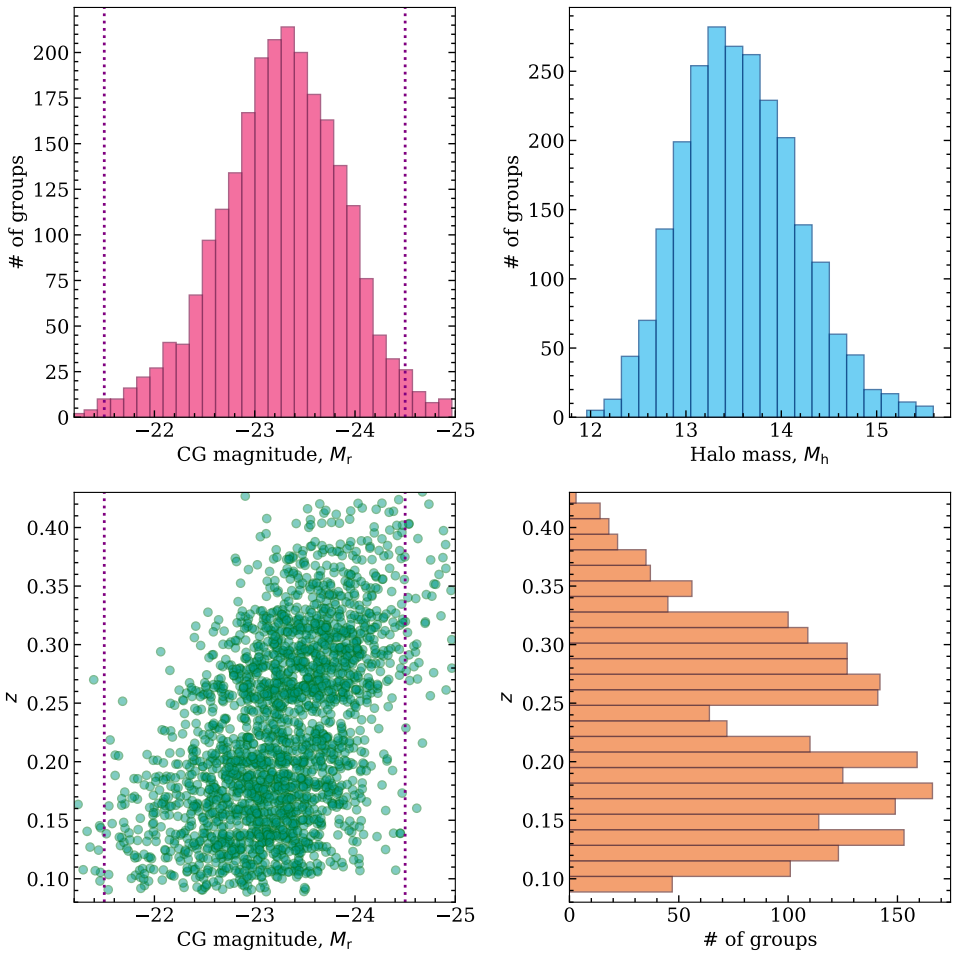

Figure 4.1: Distributions of different properties of the GAMA groups in our sample with $N_{\rm FoF} \geq 5$. The absolute $r-$band magnitudes (M_r) and redshifts (z) of the central galaxies (CG) were directly obtained from the GAMA-II Galaxy Group Catalogue (G^{3}CFoFv08, Robotham et al., 2011). The halo masses were computed from eqn. 37 of Viola et al. (2015). The vertical lines in the left panels indicate the magnitude range of the group CGs used in this work.

ergy (some recent results can be found in, e.g. Giblin et al., 2021; Li et al., 2023; Burger et al., 2023). The cosmological analysis includes measuring the effect of line-of-sight large-scale structures on galaxy shapes due to weak gravitational lensing. KiDS imaging was obtained with the square 268-million pixel CCD mosaic camera OmegaCAM (Kuijken, 2011) that covers a $1.013^\circ \times 1.020^\circ$ area at $0''.213$ pitch at the VLT Survey Telescope (VST; Capaccioli and Schipani, 2011; Capaccioli et al., 2012). The best seeing conditions (FWHM $< 0''.8$) were used for exposures in the $r-$band filter in order to take deep images (mean limiting $m_r = 25.02$ within 5σ in a $2''$ aperture) for the measurement of galaxy shapes. The GAMA group catalogue with spectroscopically confirmed member galaxies, accompanied by the deep KiDS imaging, provides us with a unique opportunity to analyze the IGL around the low-mass galaxy groups.

The optical imaging of the survey included in the public data release was produced by two dedicated pipelines. The AstroWISE information system (McFarland et al., 2013) was used for producing the co-added images in the *ugri* bands, and the THELI (Erben et al., 2005; Schirmer, 2013) pipeline was used to separately reduce the $r-$band images for providing a suitable source catalogue for the core weak lensing science case. These pipelines were optimized to have a uniform photometric zero-point throughout the full mosaic, which is essential for measuring shapes and photometry of small faint galaxies. However, the sky background is defined locally (by interpolating a 3×3 median-filtered map of background estimates in 128×128 pixel blocks), and can be over-estimated around bright sources (like central group/cluster galaxies) in the resulting images. Such background over-subtraction does not impact the galaxy shape measurements, however, it strongly affects the faint diffuse light around bright galaxies. The final outputs from the standard KiDS pipeline are therefore unsuitable for low-surface-brightness (LSB) analyses such as a measurement of the IGL, and require a re-processing of the raw images to retain the faint light. We explain the reasoning more in Sec. 4.2.3, and introduce our updated pipeline to reprocess the KiDS data for IGL analysis in Sec. 4.2.3 (also see Fig. 4.5 for the impact of the standard and updated pipeline on PSF profile). For further details on the latest (fourth) public data release of the KiDS survey, and the image reduction procedure, we refer the interested reader to Kuijken et al. (2019).

4.2.3 Customized data processing

Large cosmological imaging surveys, such as KiDS, aim to detect small, faint galaxies and measure their positions, fluxes, and shapes. Commonly, multiple exposures

(typically five in the case of KiDS) are combined to obtain a deeper image, which in turn is used for object detection. As the exposures are offset in position, and the background varies between them, an estimate for the background is subtracted before combining the data. This avoids imprinting the pattern of the individual chips in the final combined images used for object detection and photometry.

As the background also varies spatially, subtracting a constant value does not suffice. The standard KiDS pipeline uses SWARP (Bertin et al., 2002), which estimates the background on a mesh grid. The resulting values are clipped to remove outliers that may arise from the presence of bright stars. The mesh size sets the scale on which background variations can be captured, and it is typically chosen to be significantly smaller than the size of the chip, such that the spatial variations can be captured. A cubic spline is then fit through the remaining samples and this background model is subtracted. As cosmological applications focus on galaxies that are much smaller than the mesh size, this approach is adequate.

However, the presence of bright objects can bias the background estimate locally, thus leading to overestimating the background near those locations. As discussed in more detail in Sec. 4.4.1, this leads to a region of negative flux around bright stars. Similarly, we find that the surface brightness profiles of the group central galaxies are also affected. It may be possible to, at least partially, alleviate this problem by post-processing the survey images, as was done in Furnell et al., 2021. We take a different approach and reprocess the KiDS imaging data, attempting to take care to avoid this issue altogether.

For robust IGL measurements, we need to ensure that the background estimation is not correlated with the objects of interest. Provided the fact that we are averaging a large number of profiles, the impact of residual flux is to increase the uncertainty in the measurements. The residuals, which may be artefacts, scattered light from stars or galaxies below the detection limit, introduce excess variation in addition to the sky noise in the images. This is a major advantage of stacking the profiles of CGs, compared to analysing individual objects. In the latter, residuals may be difficult to distinguish from the signal of interest, whereas in a stacking analysis, residuals only contribute to a uniform background, albeit with increased noise. The only remaining concern is the contribution from satellite galaxies associated with the CGs, something we will explore in Sec. 4.3.2. We found that varying scattered light, in the end, is a limiting factor in these data.

Although we expect a stacking approach to be more robust, we nonetheless wish to reduce the contribution from residuals as much as possible, to ensure that they

are a subdominant contributor to the uncertainty in the measurements of the surface brightness profile. To this end, we developed an independent pipeline for the sole purpose of measuring the low surface brightness around bright galaxies in KiDS. In Sec. 4.2.3 we describe the various steps in the analysis and test the performance in Sec. 4.2.3. We demonstrate the value of our dedicated pipeline by measuring the average surface brightness profile around bright stars in Sec. 4.4.1.

Description of the pipeline

For our purpose, it is not necessary to combine the exposures of a pointing before measuring the profiles. Instead, we measure the profiles around the galaxies in each exposure and average these at a later stage. In principle, creating a catalogue with object detection from a stack would allow us to identify and mask fainter galaxies, but as the images are sky-background limited, we expect this to lead to a negligible improvement, while complicating the pipeline. We therefore process individual exposures in the various filters.

We start with the bias-subtracted and flat-fielded images ('reduced science frames') from the AstroWISE archive*. This ensures that the pixel response non-uniformities are accounted for. We want to ensure that we start with images with a minimal spatial variation in the sky level and with a minimum of coherent background features. To this end, we created a new flatfield from these science exposures. To do so, we first identified objects using SExtractor (Bertin and Arnouts, 1996) and masked those. The unmasked pixels were used to create the new flatfield that should, ideally, result in images with a constant background. However, this was unfortunately not the case.

The resulting flatfield for the r-band is shown in Fig. 4.2. The top image shows the full mosaic. We observe a clear radial pattern, which is caused by the illumination correction that is applied in the AstroWISE pipeline. The jumps between the chips arise because we normalise the individual chips to have a mean of unity. Unlike lensing studies that use these data to determine photometric redshifts, ensuring a consistent zero-point across the field-of-view is not essential for our aim: our objective is a smooth sky on average. To achieve this, we apply a zero-point correction to the background subtracted images, which is discussed in Sec. 4.2.3.

The bottom row in Fig. 4.2 shows the bottom-left chip, as well as a zoom-in of the top-left corner (red square). Although we started with already flat-fielded images, some structure is visible. This is likely caused by the variations in the illumination,

*http://www.astroWISE.org

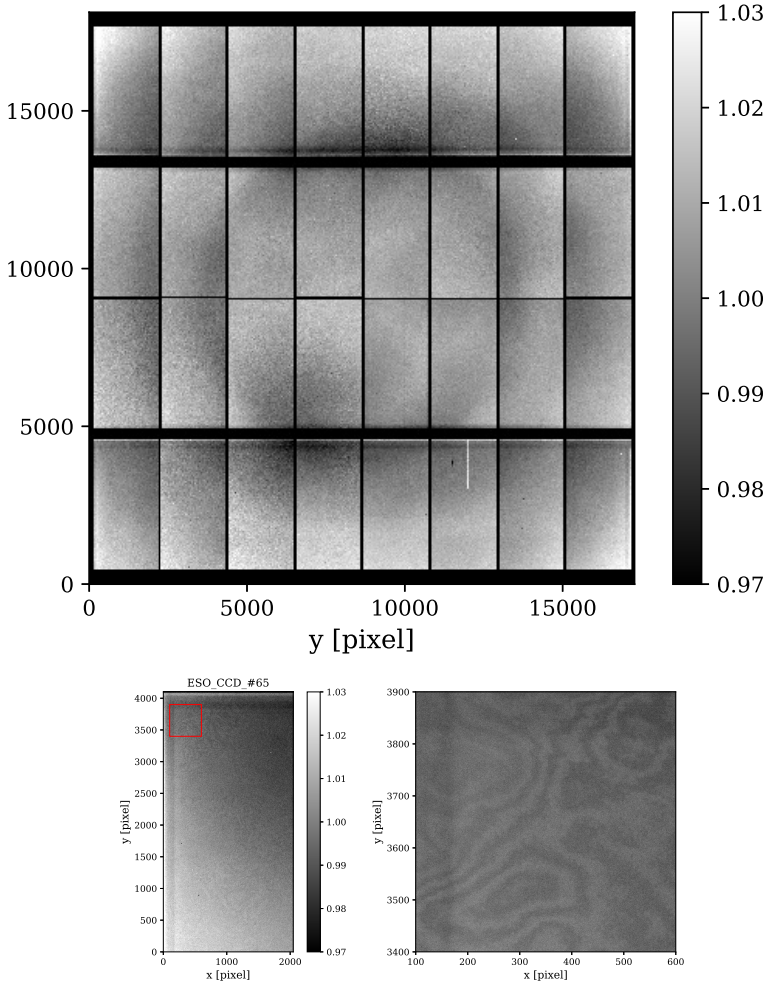

Figure 4.2: Flatfield in the r-band obtained by averaging the science observations that were already flatfielded using the standard AstroWISE pipeline. The top panel shows the full mosaic. The bottom figures show the bottom-left chip with a zoom-in of the top-left corner of that chip (red square). Some structure is visible, likely due to variations in the illumination, as well as some low-level fringing.

as well as some low-level fringing. Moreover, after we apply this additional flatfield to the data we find that the background also shows features. In particular, gradients in the background persist. The data we used in this paper were obtained early in the survey, as fields overlapping with GAMA were prioritized. At that time, the baffling of the telescope was not optimal (this was corrected later). This is the likely cause for the remaining variation, caused by changes in the illumination. We decided not to attempt further improvements and accepted that this will limit our IGL measurements in the end. To make the images more homogeneous for the masking step, we subtract a constant background from each chip using the median of the pixels that are unmasked in the SExtractor segmentation image.

Although the 'reduced science frames' contained an initial astrometric solution, it needed to be refined (in the standard KiDS pipeline, they were astrometrically calibrated at this stage as well). We used Scamp (Bertin, 2006) using the Gaia DR2 (Gaia Collaboration et al., 2018) as reference. To map the distortion of the camera we used a second-order polynomial because the overall distortion of the camera was found to be small. We found that with this setup the residuals in the astrometric solution are negligible (about $0\farcs01$ dispersion). We use Swarp without background subtraction to map the individual chips to a single image that is used for the measurements of the surface brightness profiles.

Internal reflections result in ghost haloes (for details on this feature and how they were masked, see de Jong et al. 2015). These are very apparent near bright stars, but are in fact always present. We chose to mask the reflection ghosts for very bright stars, for which the excess flux is clearly visible. This ensures that the most significant contributions are removed, while the remaining ghosts increase the uncertainty in our measurements somewhat. We determined the locations of the reflection ghosts as a function of position in the focal plane. We used the *Gaia* third Early Data Release (EDR3; Gaia Collaboration et al. 2021) to estimate the fluxes of bright stars in the images, and masked the affected regions if the predicted magnitude is brighter than $m = 10.5$ in the filter of interest. Although the ghosts are shaped like a doughnut, we also masked the inner regions. We also masked all stars brighter than $m = 16.5$ using the *Gaia* photometry with an aperture of radius $r_{\rm ap} = 175 - 20 \times (m - 10)$ pixels, which ensures that most of the starlight is masked.

We also masked bad columns. Finally, some of the images suffer from erratic gain variations caused by a problem with one of the video boards[†]. We identified those images and masked these from our analysis.

[†]http://www.eso.org/observing/dfo/quality/OMEGACAM/qc/problems.html

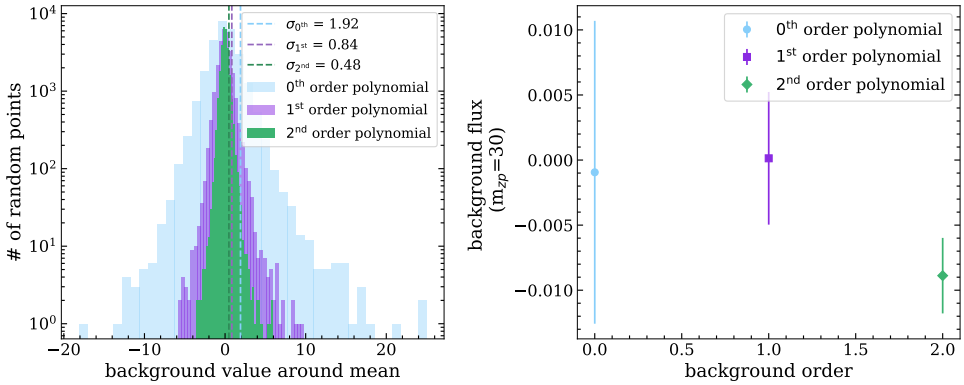

Figure 4.3: Left: histogram of the background values in randomly placed annuli on the field images with polynomial sky subtractions of order 0 (blue), 1 (purple), and 2 (green). The vertical lines denote the corresponding 1 σ values, as shown in the upper right corner. The scatter to the background values is smaller for higher-order polynomial estimation of the background. It is clear that higher-order polynomials remove spatial variation in the background more efficiently. Right: mean and scatter of the mean background values for the different polynomial background estimations (indicated in the upper right corner). This again demonstrates how the scatter is gradually reduced for higher-order polynomial estimation to the background values.

The contributions of remaining objects, stars, and galaxies were masked using the SExtractor segmentation images. We extend the marked regions in the segmentation image and explore the best setting in Sec. 4.3.2. The resulting masked images should only contain background, but occasionally objects are missed by SExtractor. These are readily removed by masking pixel values $|f| > 50$ counts (we adopt a zero-point where 1 count corresponds to $m = 30$). When measuring the surface brightness profiles around BGGs, we unmask the pixels that correspond to the segmentation image of the galaxy of interest.

Illumination and zero-point Correction

The non-uniform illumination due to the presence of additional stray light in the joined field images was corrected for all the photometric bands (for more details on the stray light issue, see de Jong et al. 2017 and Kuijken et al. 2019). For this, we selected SExtractor magnitudes (AUTO_MAG) of the stars with $m \geq 16$ in our field images and measured the residual systematic magnitude differences compared to the KiDS DR4 source catalogue (Kuijken et al., 2019), which was corrected for all these systematics. The spatial variations of these differences were then fitted with a second-

order, two-dimensional polynomial for a subset of the field images. As the distribution of the non-uniform illumination is expected to be the same for all the images in a particular filter for the same instrument, we took the average fitted coefficients for the two-dimensional polynomial and created a 'correction' image with the same pixel size of the field images. Each of the field images was then divided by the correction image on a pixel level to obtain the illumination-corrected images. As the background was already subtracted beforehand, this division does not affect the overall background level of the image, but makes the zero point of the sources spatially uniform. Using a second-order polynomial may leave some small-scale features in the photometric calibration, but this effect is mostly suppressed after stacking.

The zero-point shifts of all the illumination-corrected images were finally measured by comparing the magnitudes of the stars in each field to the KiDS DR4 source catalogue. These shifts were accounted for while converting counts to surface brightness of the CG radial profiles.

Performance of the sky subtraction

The masked images have a low background (we subtracted a constant value from each chip before combining them using SWARP), but now that most sources are masked, we need to improve the sky subtraction as there are still remaining gradients in the background. In this section, we explore the impact of subtracting a low-order polynomial from each chip.

To quantify the performance, we measured the scatter in the background estimates in randomly placed annuli with inner and outer radii of 100 and 150 arcseconds, respectively. We measured the mean and scatter in the values. Especially the latter is of interest, as a lower scatter implies we can measure the surface brightness profiles to larger radii. However, even though the images have been masked rather aggressively, the main concern is that the diffuse light around the CG may still impact the estimate. This will be more relevant for higher-order polynomial fits to the background. We therefore explore the impact on the galaxy profiles in Sect 4.3.1 as well because, in that case, the data are weighted differently. Nonetheless, focusing on the background estimates alone will provide a first indication of the performance of our pipeline.

Figure 4.3 shows the scatter of the background values in the randomly placed annuli described above for three different polynomial background estimations: zeroth order (blue), first order (purple), and second order (green) in the left panel. The right panel shows the mean values of the background with the standard error to the mean for each of the polynomial background estimations as indicated in the top right corner.

For each of the background estimations, 30 random annuli were placed in every field image and exposure. As all the SExtractor-detected sources, bad pixels containing too high or low values, and bright foreground stars were masked in the image before placing the random annuli (as described in sec. 4.2.3), some of the annuli had a large fraction of the possible pixels masked. Especially if the location of the annulus was near any of the bright stars, up to 90 per cent of the possible pixels in the annulus were masked in some cases. This gave rise to a higher noise and scatter to the mean background value for such annuli. To avoid such cases, we selected only those random annuli where at least 40 per cent of the total possible pixels in the annulus were unmasked for the background value estimation.

As is clearly visible from Fig. 4.3 (values of σ specified in the legend of the left panel and the error bars in the right panel), there is about a factor of two improvement in the scatter of the background values for each increased order of polynomial to subtract the background. This means that the precision of the background value estimation increases with increased order of the polynomial as structures in the background are removed, and for the cases we considered, a second-order polynomial results in the lowest scatter to the estimated value. However, to select the most efficient background estimation for our purpose, we also need to consider the accuracy of the background estimation. We explore this in Sec. 4.3.1.

4.3 Galaxy profiles

4.3.1 Impact of background subtraction on extended galaxy profiles

An over-subtracted sky background will particularly affect the outer edges of galaxy light profiles. If a model over-subtracts the background light, then the faint and diffuse light at the outer edge of a galaxy will be removed as background light. As a result, a galaxy's surface brightness (SB) profile will reach zero at a lower radial distance from the galactic centre, and the profile will have more negative values towards the outskirts. The background subtraction that preserves the most flux in the outermost radii of an extended source will therefore be the most accurate estimation of the global sky background. To test the accuracy of the background subtraction models, we checked the extended profiles of the bright sources with each of the background estimation cases (0^{th}, 1^{st}, and 2^{nd} order polynomials).

For this test, we selected GAMA groups at $0.09 < z < 0.15$ with a bright central

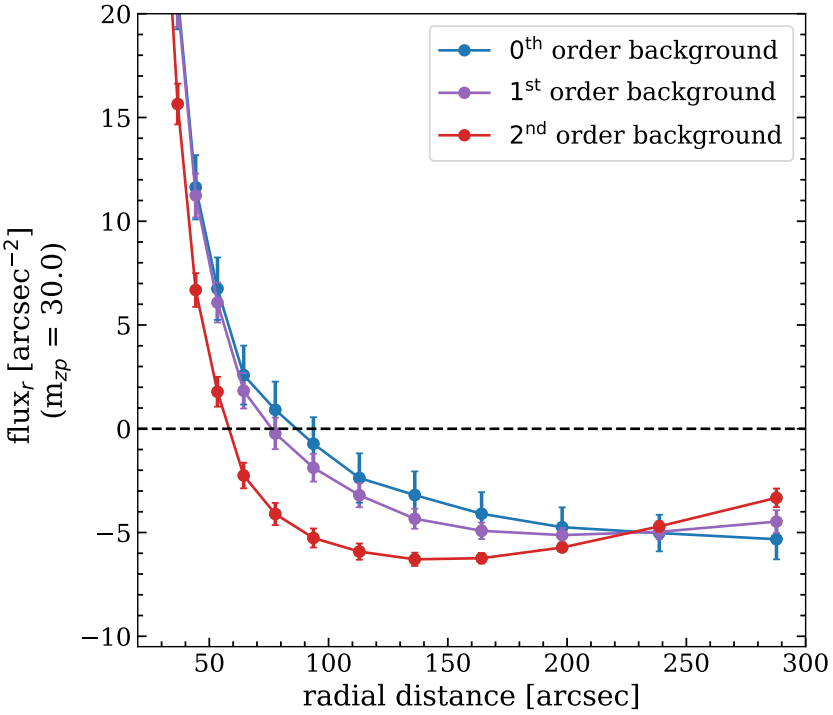

Figure 4.4: Surface brightness profiles of the group central galaxies beyond 20 arcseconds radial distance from the centre for 0^{th} (blue), 1^{st} (purple), and 2^{nd} (red) order polynomial background estimations, respectively. In all the profiles, error bars indicate 1σ uncertainties on the mean. All three profiles are the same within 20 arcseconds (not shown). Beyond that, however, higher-order background estimations over-subtract the background compared to the lower-order ones. This is the most prominent for the 2^{nd}-order polynomial estimation of the background.

galaxy ($M_r \leq -23$) and constructed their stacked SB profiles for each of our background models. The extended part of the resulting SB profiles is shown in Fig. 4.4. As visible from the figure, the 0^{th} order polynomial fit to the background retains the most light at the outer edge of the galaxies, with higher order polynomial fits retaining consecutively less light, and 2^{th} order fit having the worst case of light retention at the outskirts. Considering the tests demonstrated here and in Fig. 4.3, the 1^{st} order background subtraction seems to have a reasonable performance in both cases. However, none of the background subtraction models is unambiguously preferred above the rest. In our following analyses and tests, we therefore use all three background-subtracted images and compare their performances.

4.3.2 Masking the satellites

Along with the central galaxies, large satellite galaxies in galaxy groups and clusters can also have extended light, albeit a smaller amount. In a stacking analysis, such residual satellite light can result in a systematically higher diffuse light estimation than the actual amount. While measuring the IGL, it is therefore essential to ensure that light from satellite galaxies is completely masked out. We obtain the initial masking to the satellite galaxies and other sources in the image from the segmentation map of the SExtractor output. However, such masks can fail to include the fainter light distribution around the sources, which is more visible for the satellite galaxies and projected nearby galaxies along the line of sight. To address this, we extended the source masks obtained from the segmentation map. An increased mask size is expected to cover possible faint light surrounding the sources, but it also has a potential risk of masking the faint IGL signal and reducing the total light fraction in the IGL. We explored different levels of mask extension to identify an optimum extension for our analysis, and found that a radial extension of the mask of at least 10 pixels is needed to lower the contribution of extended light from satellites in the CG+IGL content. We therefore used this 10-pixel mask extension throughout this work where any masking was used. More details on this test are provided in Appendix 4.6.1.

4.4 Prediction from simulations

In Ahad et al. (2023), we prepared mock observations from the Hydrangea simulations (Bahé et al., 2017; Barnes et al., 2017), a suite of cosmological hydrodynamic zoom-in simulations of 24 massive galaxy clusters with virial mass between $10^{14.0}$ and $10^{15.4}$ $M_\odot$

at $z = 0$. Each of the zoom-in regions includes the large-scale surroundings of the clusters to ≥ 10 virial radii (r_{200c}) at $z = 0$, containing many group-mass haloes in addition to the central clusters. The simulations were run using the AGNdT9 calibration of the EAGLE galaxy formation and evolution code (Schaye et al., 2015). Different subgrid physics models were used to simulate astrophysical processes that originate below the resolution scale of the simulation, including star formation, star formation feedback, radiative cooling and heating, stellar evolution, black hole seeding, growth, and feedback. For details about the simulation model, hydrodynamics scheme, and comparison of the model to observed galaxy properties, see Schaye et al. (2015), Schaller et al. (2015), Crain et al. (2015), and Bahé et al. (2017) and references therein.

The group sample in Ahad et al. (2023) was chosen to be comparable to our baseline KiDS+GAMA group sample with $0.09 \leq z \leq 0.15$. The $u-$ and $r-$band mock observations were also made with comparable noise levels to the KiDS data. However, to make a better comparison to the KiDS+GAMA group analysis, we still need to account for the smearing by the point spread function (PSF) of the KiDS images (with updated background models) on the stacked SB profiles from Hydrangea groups because light from the central part is detected at large radii.

4.4.1 Point spread function

The PSF of updated KiDS images was constructed following a similar method as Montes et al. (2021) and Zhang et al. (2019)[‡]: we constructed the PSF by stitching profiles of bright and faint stars in different sections because very bright stars are saturated in the central region and light from the fainter stars at larger radii are not detectable with a high signal-to-noise ratio.

We started by running SExtractor (Bertin and Arnouts, 1996) on each of our updated KiDS field images to obtain the source catalogues. To determine which stars are suitable for which parts of the PSF we used the half-light radius ('FLUX_RADIUS') and the magnitude ('MAG_AUTO') parameters of the detected sources. We also used the stellarity index ('CLASS_STAR') provided by SExtractor to classify if an object is a star (1) or a galaxy (0). To select the unsaturated stars, we used all objects with CLASS STAR larger than 0.65 (arbitrarily chosen to maximise selected stars in the flux vs. half-light radius parameter space). The saturated stars were chosen only from their magnitude and size.

[‡]This part of the analysis was carried out by Stefan van der Jagt as a part of his second-year MSc research project, which was partially supervised by me.

Estimating core, intermediate, and outer parts

We divided the PSF into 4 sections: core, intermediate, outer 1, and outer 2. The half-light radius and the aperture magnitude were used carefully to select which stars construct which part of the PSF. The core section is constructed from the SB profile of bright unsaturated stars between magnitudes 16.5 and 18. Slightly brighter stars with saturated central regions but extended profiles out to larger radii were used for the intermediate part of the PSF. These stars for the intermediate profile had magnitudes between 14 and 15.5. The outer 1 and outer 2 sections consist of the brightest stars in the fields of view, with magnitudes between 12 and 14. We chose to divide the brightest stars into two samples to make a better transition from the outer 1 part to the intermediate part.

Stacking and Stitching different parts of the PSF

To estimate the PSF, we made cutout stamps of stars, stacked the images, and from the stacked images, calculated their radial SB profiles. The sizes of these stamps vary based on the part of the PSF the stars were used for. For the core part, we did not need a profile that extends to the full range of the PSF, and made 100×100 pixel stamps centred on the stars. For the intermediate stars, we made 500×500 pixel stamps; for the stars in the outer 1 region, we made 1000×1000 pixel stamps, and for the outer 2 region stars, these were 2000×2000 pixel stamps.

We used the segmentation map from SExtractor to exclude all other sources except for the central star in each stamp. To exclude light that is not masked away by the segmentation map, we also applied a $3-\sigma$ clipping method (excluding any pixel that has a value above or below $3-\sigma$ from the median pixel value in the masked image, where the masks also included the central stars). We also excluded all the stars from the sample that have a brighter star in the field of view. Another influence on the background of the KiDS field images is the large reflection ghost caused by large saturated stars. These ghosts cause the surface brightness to be elevated in certain parts of the PSF. This effect was tested, and all the fields with such ghosts were removed from the stack in the final PSF estimation.

The selected stamps were stacked, and the radial SB profiles of the stacked images were measured. Finally, the four partial profiles were stitched together. The stitching was done by selecting part of the profile before it drops discontinuously from the continuum and replacing it with the next region from there. The final stitched PSF profile is normalised by the total flux in the PSF. The final PSF profile is shown in

Fig. 4.5. Figure 4.5 also shows the PSF from the original KiDS DR4 field images. Comparing these two PSF profiles, it is clear that the updated background-subtracted images can detect PSF flux at larger distances compared to the images from the standard pipeline.

Effect of PSF on the outskirts of the galaxy profiles

The PSF of the instrument distributes the bright light at the core of stars and galaxies to the outer region. As a result, the diffuse light at the outskirts of bright group CGs may get excess contribution from the smearing of the central light. We tested the effect of PSF on the IGL measurement in two ways. First, we measured whether the fraction of light in IGL changes due to the PSF. Second, we tested whether the radial range of IGL detection is affected by the PSF.

To measure the effect of the PSF on the IGL fraction measurement, we took stacked SB profiles of Hydrangea groups at relevant bins of their $r-$band magnitudes from Ahad et al. (2023) and fitted a single de Vaucouleurs profile to the CG to separate the IGL. The fitting was done for both unconvolved and PSF-convolved SB profiles. The fraction of light in IGL ($f_{\rm IGL}$) from the PSF-convolved profiles were measured using the corresponding PSF-convolved total group light profiles. The $f_{\rm IGL}$ measurements are shown in Fig. 4.6 for both convolved (blue) and unconvolved (grey) cases, with errorbars showing the uncertainty to the measurements given the sample size. As is visible from Fig. 4.6, the values do not change much considering the error bars. However, for groups with a brighter CG, $f_{\rm IGL}$ seems to be slightly underestimated due to the effect of PSF.

The measurement of $f_{\rm IGL}$ was done until an SB limit of 32 mag/arcsec^2. Along with measuring $f_{\rm IGL}$, we also checked how the radial range of IGL is affected by the PSF convolution within the SB limit. For this, we measured the radial distance from the group centre within which 90 per cent of the IGL is enclosed (r_{90}). For the three magnitude bins we considered, r_{90} increased with CG magnitude. Compared to the unconvolved profiles, values for r_{90} were about 100kpc larger in the PSF-convolved profiles. For the convolved profiles, r_{90} for the three considered magnitude bins were about 260, 380, and 470 kpc. We used these radial distances as the predicted distance limit to which the fraction of light in IGL was measured in GAMA groups.

The key conclusion from this test is that the PSF does increase the radial IGL detection range. However, it does not increase the measured $f_{\rm IGL}$ because the same PSF effect is also present in the total group light. As a result, the impact of the PSF is not large for the CG magnitude range we consider, but we consider this effect in

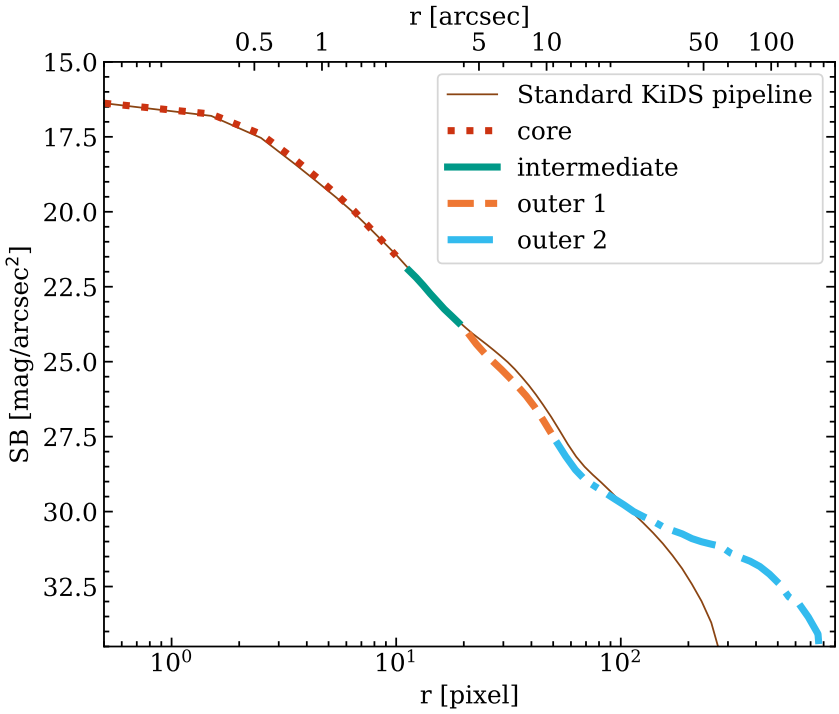

Figure 4.5: Stitched point spread function (PSF) from combining stars within different magnitude ranges (see text) from all fields with updated background-subtracted images. This PSF was re-normalized before convolving with the SB profiles of stacked Hydrangea groups. The colours and line styles indicate the radial range where different groups of stars (core, intermediate, outer 1, and outer 2) contributed to constructing the total PSF. The brown solid line shows the PSF constructed in the same way as above from standard KiDS data-release 4 images. The excess of faint light beyond 200 pixels in the PSF from the updated pipeline indicates the missing light in the standard KiDS pipeline.

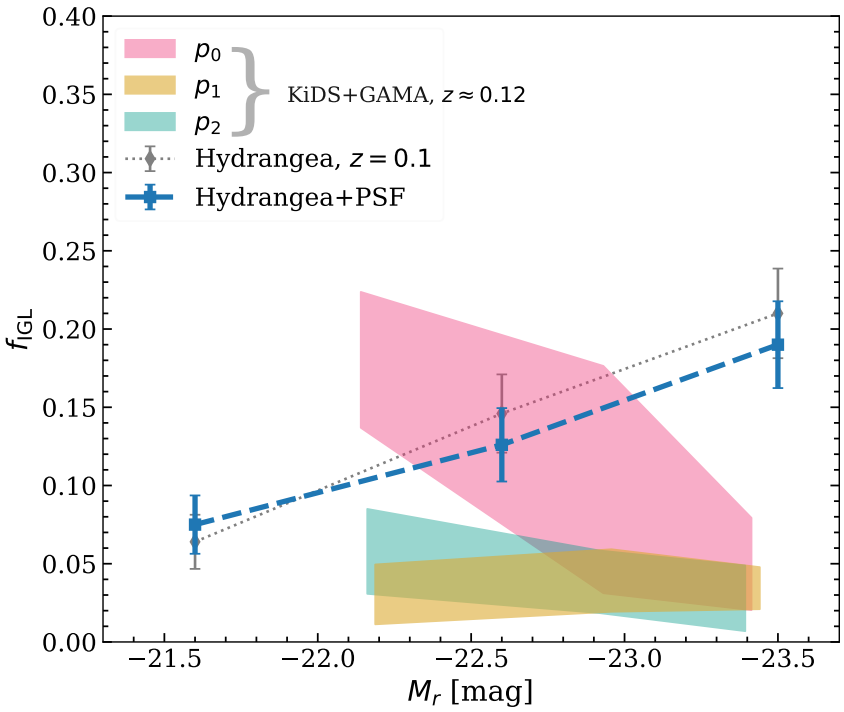

Figure 4.6: Fraction of light in IGL compared to the total group light ($f_{\rm IGL}$) of our KiDS+GAMA group sample at $0.09 < z < 0.15$ in the $M_{\rm r}$ bins they were stacked. The values along the x-axis indicate the mean $M_{\rm r}$ of the corresponding bins. Pink, yellow, and cyan shaded regions show the upper and lower limit of $f_{\rm IGL}$ for the 0^{th} (p_0), 1^{st} (p_1), and 2^{nd} (p_2) order background-subtracted images, respectively. Here, p_0 measurement is the upper limit of $f_{\rm IGL}$ for each magnitude bin at this redshift bin, while p_1 and p_2 measurements provide a lower limit. Details on how we define the upper and lower limits for each of the measurements are discussed in the text.

our comparison nevertheless.

4.5 The intragroup light in GAMA+KiDS groups

To quantify the intragroup light (IGL) in our group sample, we first measured the radial surface brightness (SB) profiles of each group from the reprocessed KiDS field images. The profiles were then checked visually to flag any profile that could potentially introduce bias in our measurements. Only the unflagged profiles were grouped in redshift and central galaxy (CG) magnitude bins before stacking and measuring the IGL in stacked profiles. Details of this process are given below.

4.5.1 Radial surface brightness profiles

For each of the KiDS pointings, we have five exposures in g, r, and $i-$bands and four exposures in $u-$band. Our results are based on the $r-$ band data because these are the deepest among the four bands. We did not create a mosaic of the pointings, but analysed each exposure separately. For each group, we created a 2×2 Mpc cutout (at the appropriate redshift) centred on the group CG.After applying the bright star and bad column masks, two different SB profiles were made from each cutout: (i) the CG+IGL SB profile that had all the sources masked except for the CG; and (ii) the total group SB profile that had all the sources masked, except for the group member galaxies (including the CG). The zero-point correction discussed in Sec. 4.2.3 was accounted for during the SB profile measurement.

During the total group light measurement, we applied an additional distance selection for the satellite galaxies considered for the total group light. This selection was made to account for the uncertainty in the group member assignment that comes from the aggregation of low-mass groups in the FoF halo finder algorithm. Jakobs et al. (2018) found that aggregation of multiple low-mass groups into one was present in 37 per cent of groups/clusters in their sample. To limit the inclusion of such wrongly-included satellite galaxies, we use the Rad_{50} and Rad_{100} parameters of the GAMA group catalogue, which indicate the distance from the group CG within which 50 and 100 per cent of the group members are located. Looking at the distribution of the $\mathrm{Rad}_{100}/\mathrm{Rad}_{50}$ ratio, we found that, in about 20 per cent of our group sample, there is at least one satellite galaxy that is more than $3\times\mathrm{Rad}_{50}$ away from the CG. We decided that these distant satellites are potentially wrongly-assigned group members due to the effect of aggregation and only considered satellites within $3\times\mathrm{Rad}_{50}$ distances from

the group CG in our total group light profiles.

4.5.2 Profile selection to lower measurement bias in stacking

During the stacking analysis, significant outliers can bias the overall measurement. Therefore, to ensure the robustness of our measurement, a representative subset of the SB profiles was visually inspected to identify possible causes for having an outlier and a 'flag' value was given to each of the SB profiles. A flag value of 0 indicates no issue and a good profile. A positive integer value of the flag was assigned based on the type of irregularity in the SB profiles. The most frequent reason to flag was the fraction of masked pixels in a cutout. If a group cutout or its central 25 per cent area had at least half of the total pixels in that area masked (bad pixels, stars, or other galaxies), it was flagged. If the masked fraction was low in a group, but the mask overlapped with part or entirety of the CG and resulted in a non-existent segmentation map at its CG location, it was also masked. If a CG SB profile had its brightest point shifted from the centre or had too low (≤ 200, compared to more than ~ 1000 for a standard profile) central flux count, it was also flagged. These particular cases happened mostly due to a partially masked CG, which was checked and confirmed for all the group cutouts that were assigned with the corresponding flag value. All of these flagging reasons are connected to our conservative masking procedure. In addition, SB profiles that had empty values (defined as 'not a number' or 'NaN', mainly in cutouts where masked areas covered a ring-like pattern around the CG for presence of many bright sources around) for multiple radial distances and CG+IGL SB profiles that had high scatter (larger than the median variation of flux count beyond 400 kpc for each considered group sample, usually ~ 1.0 flux count variation) in the far outskirts were also flagged. Finally, if any CG+IGL SB profile was flagged in ≥ 3 of the five available exposures, the rest were flagged for lack of reliability. After flagging, we were left with about 55 per cent of the initial SB profiles in each redshift bin we considered.

Another selection criterion we applied was removing GAMA groups that potentially have an ambiguous CG in the GAMA catalogue. In Ahad et al. (2023), we demonstrated that if the group CGs were selected based on the galaxy halo mass instead of selecting the brightest galaxy at the centre of light distribution, about 20 per cent of the GAMA groups in our sample gets assigned with a different CG (predominantly a red one instead of a blue one). We also showed in Ahad et al. (2023), based on our mock observations from Hydrangea simulations, that such miscentring can slightly suppress the IGL measurements. However, the small suppression is inferred from a

simulated sample-based work, in which case, we had information about the 'true' halo centre, which is not the case for observational data. Therefore, we chose only the GAMA groups in our sample that did not have a re-assignment of their CG based on the galaxy halo mass. This selection lowered our sample size by a further 10 per cent.

4.5.3 Sub-stacking based on BGG luminosity

In Ahad et al. (2023), we have found that, based on mock images of groups in the Hydrangea simulations, the IGL content has a positive correlation with the luminosity of the group CG. We also found that while stacking multiple group CGs, binning them along the absolute magnitude of the CGs preserved the underlying IGL fraction trend (fig. 8 of Ahad et al., 2023). We utilised this result in this work and stacked group CGs of similar absolute magnitudes.

To keep a uniform range of absolute $r-$band magnitude ($M_{\rm r}$) in our different redshift samples, groups with CG $M_{\rm r}$ between -21.5 and -23.5 were divided into three bins. The bin widths were selected to have a similar number of groups in each bin. The SB profiles of the groups in each redshift and magnitude bin were first normalised to have appropriate flux values at the mean redshift of the sample. Also, the radii in each bin were converted to physical kpc at their corresponding redshifts. Finally, the profiles were stacked to obtain the mean profile in each redshift and magnitude bin for the CG+IGL and total group light.

4.5.4 Residual background subtraction

Instead of a local background-subtraction in the standard AstroWISE pipeline, our approach of a chip-by-chip global background subtraction minimizes any remaining flux pattern in the background (e.g. as shown in Fig. 4.2). However, as Fig. 4.2 shows, there are also some small-scale patterns at the chip edges that are difficult to remove even with our updated background subtraction model. Besides, due to the presence of stray light (e.g., from the reflected light of planets), there are some global remaining patterns in the joined field image. These patterns result in a non-flat background in the field image, which is likely comparable in all the field images. We accounted for this residual background by measuring a background SB profile and subtracting this from the stacked SB profiles of groups.

To do so, we measured the residual background profile at a random location for each of the group profiles. The random locations were obtained by taking the pixel location of a group CG in one pointing and measuring SB profiles at the same pixel location and

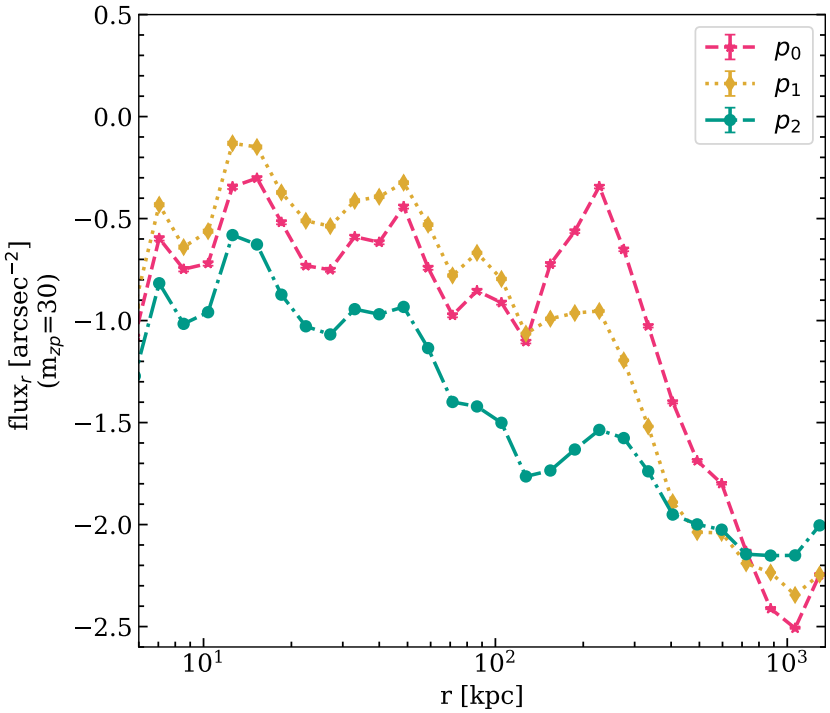

Figure 4.7: Surface brightness profile of the mean residual background at random points for the three background-subtracted field images used in this work. From the central region out to 100 kpc, their variation is similar. However, beyond 200 kpc, the 0^{th} order background-subtracted images (p_0) have a steeper downturn than the other two.

cutout size in a different pointing. While preparing these profiles, all the SExtractor detected sources were masked with extended segmentation maps, and the masking was similar to how the group profiles were made. No pointing-and-exposure combination was used more than once to create the background profiles. Because we use the pixel location and cutout size of a group to create the background SB profiles, any global background pattern that may be included in the group SB profile due to its location (e.g., the centre of the image or edge of a chip), is accounted for in the residual background profile. Finally, the background profile fluxes were adjusted for the zero-point correction, and the radial range was adjusted to the appropriate physical kpc units before stacking and subtracting them from the group SB profiles.

Figure 4.7 shows the mean residual background profiles in the field images for the three different background-subtraction models. Beyond 200 kpc, all the profiles shown have a downturn towards the end, especially for the 0^{th} (p_0) and 1^{st} (p_1) order background-subtracted images. This bias towards lower values in the outskirts is not as prominent for p_2 images. However, there is an overall trend of smaller values in the outskirts for the p_2 background profile. After subtracting this residual background profile, we could reach 32 mag/arcsec^2 SB limit for some of the stacked group profiles. In other cases, it was between 30 and 31 mag/arcsec^2.

4.5.5 Fraction of light in IGL

The fraction of light in IGL compared to the total group light ($f_{\rm IGL}$) in each redshift and magnitude bin was measured in a similar process as done in Ahad et al. (2023) using a single de Vaucouleurs (SD) profile fitting to keep the comparison consistent. We used the following steps:

1. Any residual flat background light at the far outskirts (beyond 500 kpc from the group centre) was removed by fitting a constant background to the outer profile.

2. The CG profile was fitted using a single de Vaucouleurs (SD) profile out to 40kpc from the CG centre. During this fitting procedure, the central 2.5 kpc region was not included to avoid any saturated pixels.

3. The fitted CG profile was subtracted from the CG+IGL profile to obtain the IGL profile. Any remaining light in the central region due to fitting beyond 2.5 kpc was excluded.

4. The total flux in the IGL was computed by integrating the IGL profile out to r_{90} for each magnitude bin based on the Hydrangea stacked profiles (see Sec. 4.4.1).

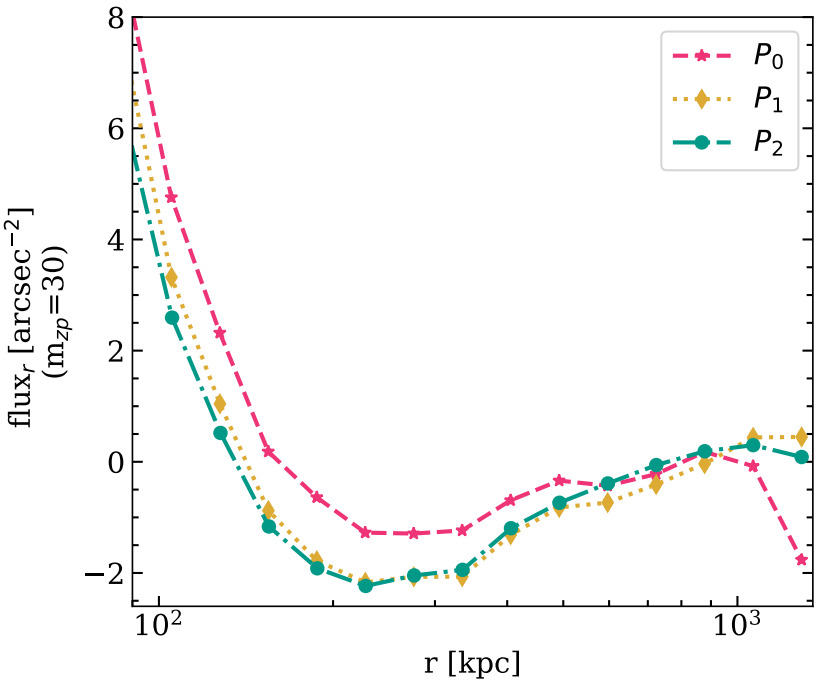

Figure 4.8: Surface brightness profile of the mean residual background at random points for the three background-subtracted field images used in this work. From the central region out to 100 kpc (not shown here), their variation is similar. However, beyond 200 kpc, the 0^{th} order background-subtracted images (p_0) have a steeper downturn than the other two.

Similarly, the total group light was measured by integrating the total group profile out to the same radial distance. Their ratio was taken as the fraction of total light in IGL, or $f_{\rm IGL}$.

The measured $f_{\rm IGL}$ in the redshift range $0.09 \leq z \leq 0.15$ with respect to the $M_{\rm r}$ bins in our three different background (p_0, p_1, p_2) subtracted images are shown in Fig. 4.6. The shaded regions in pink, yellow, and cyan are showing the upper and lower limits of $f_{\rm IGL}$ measurements for p_0, p_1, and p_2 cases, respectively. The blue dashed line here shows prediction from the Hydrangea simulations (details in Sec. 4.4). While our measurements for p_1 and p_2 background subtraction models are lower than the simulation predictions, $f_{\rm IGL}$ for the p_0 case is comparable to the predictions.

To define the upper and lower limit of $f_{\rm IGL}$ measurement for each background subtraction case for a specific redshift and magnitude bin (i.e. each of the shaded

regions), we considered the outer regions ($\leq$ 200 kpc) of the SB profiles. Figure 4.8 shows the outer regions for all three background subtraction cases at $0.09 \leq z \leq 0.15$ for the brightest magnitude bin we considered (mean $M_{\rm r} \approx -23.4$). We expect that the overall sky background dominates only beyond 500kpc from the group centres because most of the groups have a virial radius below this limit, and we see that the average flux count beyond this limit is consistent with 0 for all p_0, p_1, and p_2 cases. However, between 150 and 500 kpc distances from the group centres, all three profiles show a 'U' shaped down and up turn in the profile, which indicates a ring-like over-subtracted region in the image. This over-subtraction is similar for p_1 and p_2, which show a stronger over-subtraction compared to p_0. As there is no reliable way to recover this missing light, it poses a limiting factor in our measurements. For each of the p_0, p_1, and p_2 cases, we fitted a horizontal line to the data points beyond 500 kpc in Fig. 4.8 and considering it as the sky background, subtracted this value from these profiles before fitting the CG to separate the IGL. Given the over-subtracted region in the profiles, this background subtraction brings the extent of the SB profiles down to $\approx$ 190 kpc for p_0, and $\approx$ 150 kpc for p_1 and P_2. The IGL measurement from this background definition provided our lower limit to $f_{\rm IGL}$, which is shown in the lower bound of the shaded regions in Fig. 4.6 and Fig. 4.9. The upper limit to the measurements came from taking the minimum value of the profiles as the background value and subtracting that before the IGL measurement. In this case, all the profiles could be measured until the r_{90} limits defined in Sec. 4.4.1. This measurement and its scatter define the upper bounds of the shaded regions in Fig. 4.6 (and also Fig. 4.9 below).

Measurements with different background-subtraction models

Considering how we already showed in Sec. 4.3.1 that the p_0 model has the best retention of faint light at the outskirts of the galaxy SB profiles, we conclude that our measured $f_{\rm IGL}$ for p_0 (pink shaded region) is the upper bound of this measurement in all the background subtraction models we considered in this work. One point of concern here is that the p_0 model only subtracts a constant background, and therefore can leave the most amount of residual background pattern out of the three models we used. This can especially impact the $f_{\rm IGL}$ measurement for the fainter $M_{\rm r}$ bin, causing a potential overestimation. On a different note, the $f_{\rm IGL}$ measurement for the brightest $M_{\rm r}$ bin is likely the best estimate out of the three background subtraction models, although even p_0 shows signs of some over-subtraction at the edge of the SB profile of the brightest CGs (Fig. 4.8). Unlike p_0, both p_1 and p_2 profiles have

comparably high over-subtraction at the edge of the SB profiles (Fig. 4.8) and similar $f_{\rm IGL}$ measurements (Fig. 4.6). Considering all the above points, we decided to use only the p_0 background subtracted images to measure $f_{\rm IGL}$ in GAMA groups at different redshift ranges.

Impact of redshift on background and measurements

Groups with the same physical size have a smaller angular size at higher redshifts. Also, for the same apparent magnitude limit of the GAMA galaxy measurements, groups with intrinsically brighter CG are more numerous at higher redshifts. Compared to the groups with similarly luminous CGs at lower redshifts, these high redshift groups have different systematics in the data due to their different angular sizes on the sky. We check the impact of these different systematics on the $f_{\rm IGL}$ measurements in three different redshift bins. The first is our nearest redshift bin, $0.09 \leq z \leq 0.15$ (with and average $z \approx 0.12$), for which the $f_{\rm IGL}$ is shown in Fig. 4.6. The other two consecutive redshift ranges are $0.16 \leq z \leq 0.21$ (with an average $z \approx 0.18$) and $0.21 \leq z \leq 0.27$ (with an average $z \approx 0.24$). The $f_{\rm IGL}$ in these redshift ranges for the 0^{th} order background subtracted images (p_0) are shown in Fig. 4.9. The shaded regions show the upper and lower limits of $f_{\rm IGL}$ at different redshift ranges as indicated in the labels (how we define these limits is discussed previously in this section). Blue and purple lines indicate our predictions from Hydrangea simulations at comparable redshifts. The mean halo mass of the stacked groups in each bin is shown along the x-axis.

As is visible from Fig. 4.9, there is no strong redshift-evolution in the $f_{\rm IGL}$ measurements in either simulations or observations. Especially the measurements for the lowest-mass bins have similar values throughout. The measurements for the highest-mass bins slightly increase at higher redshifts, and their scatter gets smaller (as indicated by the vertical span of the shaded region). However, these increased $f_{\rm IGL}$ values are likely not an indication of increased IGL at these slightly higher redshifts, but an improvement of the profile over-subtraction issue at extended radial distances. Because our measurements are done on cutouts extending to 1 Mpc distance from the group centres, and this distance corresponds to less than half of the angular size at $z \approx 0.24$ compared to $z \approx 0.12$, the residual background patterns have a smaller impact on the group SB profiles. For example, a 1 Mpc cutout can span up to 6 CCD chips in the joined field of view at $z \approx 0.12$, including the uneven background at the chip edges. Compared to that, at $z \approx 0.24$, a 1 Mpc cutout can span only two chips, avoiding the large-scale residual patterns. Also, CGs with the same luminosity are

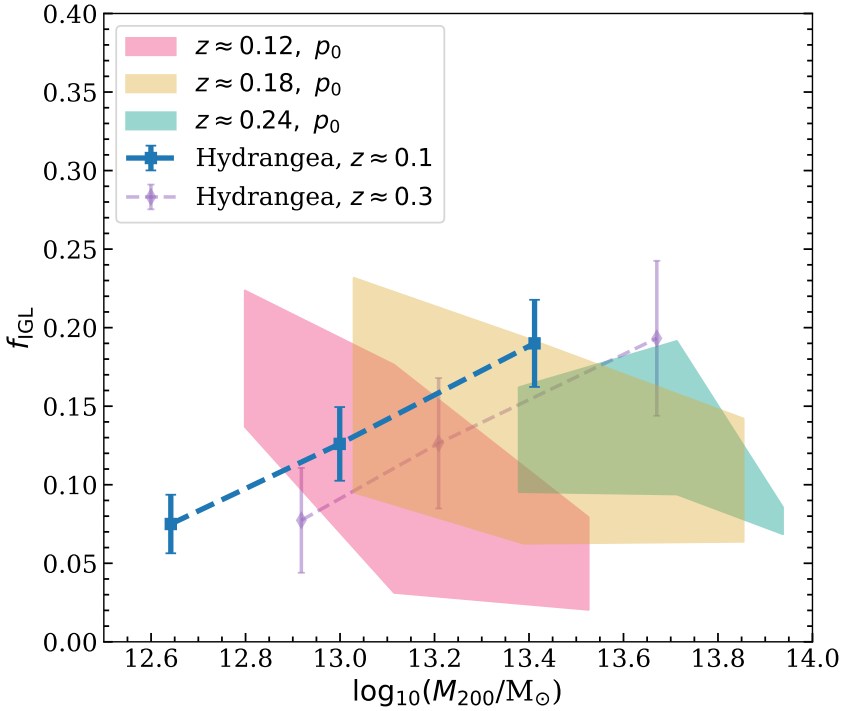

Figure 4.9: Fraction of light in IGL compared to the total group light ($f_{\rm IGL}$) of our KiDS+GAMA group sample at different redshifts from the 0^{th} order (p_0) background-subtracted images. The values along the x-axis indicate the mean halo mass M_h of the corresponding bins. Pink, yellow, and cyan shaded regions show the upper and lower limit of $f_{\rm IGL}$ for the redshift ranges $0.09 < z < 0.15$, $0.16 < z < 0.21$, and $0.21, z < 0.27$, respectively. Details on how we define the upper and lower limits for each of the measurements are discussed in the text. Blue and purple lines show the prediction of $f_{\rm IGL}$ measurement from Hydrangea simulations at comparable redshifts (mentioned in labels). The range of $f_{\rm IGL}$ is comparable between simulations and observations.

fainter at higher redshifts. As a result, we see a reduced over-subtraction compared to what we see in Fig. 4.8. As we measure faint and diffuse IGL, a naive initial assumption can be that the lower the redshift, the best measurement of the faint light we can get. However, after considering this background pattern issue, considering a slightly higher redshift bin can instead improve the robustness of the IGL measurement.

Comparison to other works

Our measurement of the IGL fraction is comparable to other existing IGL/ICL measurements. Given the halo mass range of our group sample, the strength of our measurements comes from stacking many groups, which reduced the scatter in our measurements compared to existing works, especially ones that are computed in individual systems. Martínez-Lombilla et al. (2023) measured the IGL fraction in a GAMA group with ID 4001389 (RA 35.834163 deg, DEC -5.454157; J2000) from the GAMA group catalogue G^3Cv10 (Robotham et al., 2011) using multi-band data from the Hyper Suprime-Cam Subaru Strategic Program Public Data Release 2 (Aihara et al., 2019). Their measurement of $f_{\rm IGL}$ using different surface brightness cuts and a 2D composite model spans 0.035 - 0.305 (among different methods) in the $r-$band. Although our method of separating CG from IGL is not the same one as they used, at the redshift ($z \approx 0.2$) and halo mass ($M_{\rm dyn} = 1.3 \times 10^{13} {\rm M}_{\odot}$) of their measured group, our measurements indicate $\sim 0.1 - 0.2$ for the p_0 images. In another recent work, Ragusa et al. (2023) measured IGL/ICL fractions for VST Early-type GAlaxy Survey (VEGAS, Iodice et al. 2021) data at $z \leq 0.05$, and their $f_{\rm IGL}$ measurements for individual groups at $M_{\rm vir} < 10^{14} {\rm M}_{\odot}$ ranges between ∼0.2 - 0.4 (from their fig. 2). Although their measurements are from the local Universe, unlike our slightly higher redshifts, we do not expect a lot of evolution on the IGL component over this time. Our measurements are also similar to the IGL fraction of individual groups at different redshifts from fig. 2 of Montes (2022), groups of different halo masses (using N-body simulations) from Rudick et al. (2011), and stacked measurements of 687 SDSS groups at $0.2 \leq z \leq 0.3$ from Zibetti et al. (2005). We found in Ahad et al. (2023) that the IGL fraction increases with the host halo mass and luminosity of the group CG. We do not see that trend in our KiDS+GAMA IGL measurements (as shown in Fig. 4.9). However, the range of values is comparable, and given the strong systematics in the background of our data, it is not possible to comment on the overall trend with certainty.

4.6 Discussion and Summary

Due to the small and large-scale background pattern in the KiDS data, even after our re-processing, it is quite challenging to obtain a clean measurement of the IGL. Nevertheless, using our custom background estimation and subtraction pipeline, careful selection and binning of sample groups, and stacking many groups to improve the SNR has allowed us to obtain a good constraint on the IGL measurement. This is the first well-constrained stacked measurement based on such a large sample of groups in the halo mass range we considered ($12.5 \leq \log_{10}[M_{200}/\mathrm{M}_{\odot}] \leq 14.0$). Moreover, this analysis highlights the potential of wide-field surveys for LSB analyses, such as the IGL measurement.

A crucial factor for robust IGL (or any LSB) measurement is a uniform and flat sky background with the minimum possible residual background pattern. Wide-field cameras, by construction, pick up light from a wide area of the sky in each field-of-view, and therefore particularly susceptible to stray light from passing objects outside of the field-of-view which cause internal reflection in the camera and non-uniform illumination patterns in the joined image. There can also be image regions that contain scattered light shadows from bond wire baffles. These issues need to be carefully resolved from pointings during the data processing stages. Along with these, there is one added layer of complexity that came with using KiDS data that overlap the GAMA fields-of-view. Because the GAMA overlapping regions were prioritized during the KiDS survey design, the data we used were taken in the early stages of the survey. These early data from KiDS suffered from a problem with the baffling, resulting in more stray light. The later data releases have these issues resolved, but the KiDS+GAMA fields were already in place by then. Therefore, instead of the GAMA overlapping fields, images from the later KiDS data production may be more suitable for LSB measurements once reprocessed by our custom pipeline with updated background subtraction. However, we lack a reliable group catalogue (like the GAMA catalogue we use here) in those regions.

Despite the challenging image data, with our carefully designed and tested analysis we present IGL measurement from the largest group sample so far, demonstrating the strength of a stacking analysis. Our complete pipeline (from data processing to sample selection and analysis steps) will be a useful tool for statistical analysis of the IGL across a wide halo-mass and redshift range for the next generation of wide-field surveys such as *Euclid* (Troja et al., 2023) and LSST (Ivezić et al., 2019).

4.6.1 Summary

Our main findings from this work are listed below.

- To optimize cosmology survey data for low-surface-brightness (LSB) analysis, the most important adjustment is to ensure a flat sky background. A non-uniform background can be caused by non-uniform illumination from reflections of stray light into the wide-field camera. On the data processing side, background patterns from over-subtraction of faint light around bright sources can be caused by local sky detection and subtraction based on small units of area on the large image. The issues caused by the instrument can be mostly modelled and corrected, and a new pipeline is needed to resolve the background subtraction issue. We perform these before our analysis.

- We tested the performance of different background estimation models in this work based on their effect on the scatter of mean background value at random points in the field-of-view (Fig. 4.3), and the retention of faint light in the extended galaxy profiles (Fig. 4.4). Based on these two criteria, we initially concluded that a first-order polynomial (p_1) for the background model had the most reasonable performance. However, the other two models (zeroth order, p_0, and second order, p_2) had their advantages too. Further analysis with images from all three cases showed that p_0 performs best in retaining the extended faint light for our brightest CG bins.

- We used our IGL measurement predictions based on cosmological simulations from Ahad et al. (2023), adjusted for the updated KiDS PSF, to compare with our results in this work. A comparison of the standard KiDS PSF and our updated image PSF shows improvement of faint light retention at the extended profile (Fig. 4.5). The effect of PSF convolution on the IGL fraction ($f_{\rm IGL}$) measurement is small, but non-negligible.

- Even after the updated background subtraction, there are residual large- and small-scale patterns in the background that affect the extended galaxy profiles where IGL dominates. Therefore it is necessary to compute and account for the residual background pattern at large radii for all the updated background-subtracted images.

- Not all the SB profiles of group central galaxies (CG) were usable for the stacked analysis due to the presence of significant irregularities which could potentially

bias the measurements. These irregularities were primarily caused by the presence of nearby bright sources or bad pixels due to random noise. All SB profiles were visually inspected and flagged for such irregularities. This conservative selection resulted in leaving about half of our initial group samples in the final measurement, but it made the measurement more reliable. Because of starting with a large sample, even after such a strict selection process, we had at least $\sim 250(\times 5$ exposures) groups in each redshift bin we considered.

- We obtained upper and lower limits for $f_{\rm IGL}$ for our group sample in the lowest redshift bin ($0.09 \leq z \leq 0.15$) from the three background-subtraction methods we used (Fig. 4.6). Due to over-subtraction of faint light at large radii, p_1 and p_2 models provide a lower limit to $f_{\rm IGL}$, while p_0 model provides an upper limit. Although the trend of $f_{\rm IGL}$ against the luminosity of group CGs from the KiDS+GAMA sample is not the same as predictions from simulations, the values are comparable.

- We repeated our analysis for two more consecutively higher redshift bins, with average group redshifts being $z \approx 0.18$ and $z \approx 0.24$ using the p_0 images to check for any redshift evolution in the measurement. The predictions from the simulations at $z = 0.3$ show a small sign of evolution. However, $f_{\rm IGL}$ from GAMA groups does not show a clear trend with redshift (Fig. 4.9). Overall, our measurements are consistent with existing works on systems with comparable halo mass and redshifts, and have a smaller scatter in the measurements because of stacking many groups.

- One interesting finding from analysis at higher redshifts is that stacked SB profiles at higher redshifts have reduced over-subtraction than at the lowest redshift bin, and therefore have a more reliable measurement. This is because the same physical size of groups corresponds to a smaller angular size at higher redshift. As a result, group cutouts with 1 Mpc side length span across fewer chips at higher redshifts, consequently avoiding large-scale residual background patterns in the image mosaic. This is especially prominent for the brightest CG bin (i.e. the most massive groups) at each redshift. Therefore, in this work, at the same average halo mass (or CG luminosity) of the stacked groups, measurements from a slightly higher redshift bin are more reliable than those at a lower redshift.

Acknowledgements

The authors acknowledge support from the Netherlands Organization for Scientific Research (NWO) under Vici grant number 639.043.512 (SLA, HH), and Veni grant number 639.041.751 (YMB). YMB also gratefully acknowledges financial support from the Swiss National Science Foundation (SNSF) under funding reference 200021_213076. The Hydrangea simulations were in part performed on the German federal maximum performance computer "HazelHen" at the maximum performance computing centre Stuttgart (HLRS), under project GCS-HYDA / ID 44067 financed through the large-scale project "Hydrangea" of the Gauss Center for Supercomputing. Further simulations were performed at the Max Planck Computing and Data Facility in Garching, Germany. This work used the DiRAC@Durham facility managed by the Institute for Computational Cosmology on behalf of the STFC DiRAC HPC Facility (www.dirac.ac.uk). The equipment was funded by BEIS capital funding via STFC capital grants ST/K00042X/1, ST/P002293/1, ST/R002371/1 and ST/S002502/1, Durham University and STFC operations grant ST/R000832/1. DiRAC is part of the National e-Infrastructure.

This research made use of data from the Galaxy and Mass Assembly survey (GAMA). GAMA is a joint European-Australasian project based around a spectroscopic campaign using the Anglo-Australian Telescope. The GAMA input catalogue is based on data taken from the Sloan Digital Sky Survey and the UKIRT Infrared Deep Sky Survey. Complementary imaging of the GAMA regions is being obtained by a number of independent survey programs including GALEX MIS, VST KiDS, VISTA VIKING, WISE, Herschel-ATLAS, GMRT, and ASKAP providing UV to radio coverage. GAMA is funded by the STFC (UK), the ARC (Australia), the AAO, and the participating institutions. The GAMA website is http://www.gama-survey.org.

The KiDS imaging data is based on observations made with ESO Telescopes at the La Silla Paranal Observatory under programme IDs 177.A-3016, 177.A-3017, 177.A-3018 and 179.A-2004, and on data products produced by the KiDS consortium. The KiDS production team acknowledges support from: Deutsche Forschungsgemeinschaft, ERC, NOVA and NWO-M grants; Target; the University of Padova, and the University Federico II (Naples).

The analysis of this work was done using Python (http://www.python.org), including the packages NumPy (Harris et al., 2020), AstroPy (Astropy Collaboration et al., 2013), and SciPy (Jones et al., 2009). Plots have been produced with Matplotlib (Hunter, 2007).

Data Availability

The data presented in the figures are available upon request from the corresponding author. The Hydrangea data are available at https://ftp.strw.leidenuniv.nl/bahe/Hydrangea/. The KiDS DR4 data are available at https://kids.strw.leidenuniv.nl/DR4/access.php, and the GAMA catalogues can be accessed from http://www.gama-survey.org/dr3/schema/.

References

Ahad, S. L., Bahé, Y. M., and Hoekstra, H., 2023, MNRAS, 518, 3685

Aihara, H., AlSayyad, Y., Ando, M., et al., 2019, Publications of the Astronomical Society of Japan, 71, 114

Alonso Asensio, I., Dalla Vecchia, C., Bahé, Y. M., et al., 2020, MNRAS, 494, 1859

Astropy Collaboration, Robitaille, T. P., Tollerud, E. J., et al., 2013, A&A, 558, A33

Bahé, Y. M. et al., 2017, MNRAS, 470, 4186

Barnes, D. J., Kay, S. T., Bahé, Y. M., et al., 2017, MNRAS, 471, 1088

Bertin, E. (July 2006). "Automatic Astrometric and Photometric Calibration with SCAMP". *Astronomical Data Analysis Software and Systems XV*. Ed. by C. Gabriel, C. Arviset, D. Ponz, et al. Vol. 351. Astronomical Society of the Pacific Conference Series, 112.

Bertin, E. and Arnouts, S., 1996, A&AS, 117, 393

Bertin, E., Mellier, Y., Radovich, M., et al. (Jan. 2002). "The TERAPIX Pipeline". *Astronomical Data Analysis Software and Systems XI*. Ed. by D. A. Bohlender, D. Durand, and T. H. Handley. Vol. 281. Astronomical Society of the Pacific Conference Series, 228.

Burger, P. A., Friedrich, O., Harnois-Déraps, J., et al., 2023, A&A, 669, A69

Capaccioli, M. and Schipani, P., 2011, The Messenger, 146, 2

Capaccioli, M, Schipani, P, De Paris, G, et al. (2012). *Science from the Next Generation Imaging and Spectroscopic Surveys*.

Contini, E. and Gu, Q., 2021, ApJ, 915, 106

Contini, E., 2021, Galaxies, 9, 60

Coogan, R. T., Daddi, E., Le Bail, A., et al., 2023, arXiv e-prints, arXiv:2302.08960

Crain, R. A., Schaye, J., Bower, R. G., et al., 2015, MNRAS, 450, 1937

de Jong, J. T. A., Verdoes Kleijn, G. A., Boxhoorn, D. R., et al., 2015, A&A, 582, A62

de Jong, J. T. A., Verdoes Kleijn, G. A., Erben, T., et al., 2017, A&A, 604, A134

DeMaio, T., Gonzalez, A. H., Zabludoff, A., et al., 2018, MNRAS, 474, 3009

DeMaio, T., Gonzalez, A. H., Zabludoff, A., et al., 2020, MNRAS, 491, 3751

Driver, S. P., Hill, D. T., Kelvin, L. S., et al., 2011, MNRAS, 413, 971

Driver, S. P., Norberg, P., Baldry, I. K., et al., 2009, Astronomy and Geophysics, 50, 5.12

Erben, T., Schirmer, M., Dietrich, J. P., et al., 2005, Astronomische Nachrichten, 326, 432

Furnell, K. E., Collins, C. A., Kelvin, L. S., et al., 2021, MNRAS, 502, 2419

Gaia Collaboration, Brown, A. G. A., Vallenari, A., et al., 2018, A&A, 616, A1

Gaia Collaboration, Brown, A. G. A., Vallenari, A., et al., 2021, A&A, 649, A1

Gallagher John S., I. and Ostriker, J. P., 1972, Astronomical Journal, 77, 288

Giblin, B., Heymans, C., Asgari, M., et al., 2021, A&A, 645, A105

Gonzalez, A. H., Sivanandam, S., Zabludoff, A. I., et al., 2013, ApJ, 778, 14

Guo, Q., White, S., Boylan-Kolchin, M., et al., 2011, MNRAS, 413, 101

Harris, C. R., Jarrod Millman, K., van der Walt, S. J., et al., 2020, arXiv e-prints, arXiv:2006.10256

Hunter, J. D., 2007, Computing in science & engineering, 9, 90

Iodice, E., Spavone, M., Capaccioli, M., et al., 2021, The Messenger, 183, 25

Ivezić, Ž., Kahn, S. M., Tyson, J. A., et al., 2019, ApJ, 873, 111

Jakobs, A., Viola, M., McCarthy, I., et al., 2018, MNRAS, 480, 3338
Jiménez-Teja, Y., Dupke, R., Benítez, N., et al., 2018, ApJ, 857, 79
Jones, D. H., Read, M. A., Saunders, W., et al., 2009, MNRAS, 399, 683
De Jong, J. T. A., Kuijken, K., Applegate, D., et al., 2013, The Messenger, 154, 44
Joo, H. and Jee, M. J., 2023, Nat., 613, 37
Kluge, M., Bender, R., Riffeser, A., et al., 2021, ApJS, 252, 27
Kuijken, K., 2011, The Messenger, 146, 8
Kuijken, K., Heymans, C., Dvornik, A., et al., 2019, A&A, 625, A2
Li, S.-S., Hoekstra, H., Kuijken, K., et al., 2023, arXiv e-prints, arXiv:2306.11124
Liske, J., Baldry, I. K., Driver, S. P., et al., 2015, MNRAS, 452, 2087
Lotz, J. M., Koekemoer, A., Coe, D., et al., 2017, ApJ, 837, 97
Martínez-Lombilla, C., Brough, S., Montes, M., et al., 2023, MNRAS, 518, 1195
McFarland, J. P., Verdoes-Kleijn, G., Sikkema, G., et al., 2013, Experimental Astronomy, 35, 45
Mihos, C. (Aug. 2015). "Intragroup and Intracluster Light". *IAU General Assembly*. Vol. 29, 2247903, 2247903.
Mihos, J. C., Harding, P., Feldmeier, J., et al., 2005, ApJL, 631, L41
Mihos, J. C., Harding, P., Feldmeier, J. J., et al., 2017, ApJ, 834, 16
Montes, M., 2022, Nature Astronomy, 6, 308
Montes, M., Brough, S., Owers, M. S., et al., 2021, ApJ, 910, 45
Montes, M. and Trujillo, I., 2014, ApJ, 794, 137
Montes, M. and Trujillo, I., 2018, MNRAS, 474, 917
Montes, M. and Trujillo, I., 2019, MNRAS, 482, 2838
Murante, G., Giovalli, M., Gerhard, O., et al., 2007, MNRAS, 377, 2
Puchwein, E., Springel, V., Sijacki, D., et al., 2010, MNRAS, 406, 936
Ragusa, R., Iodice, E., Spavone, M., et al., 2023, A&A, 670, L20
Robotham, A. S. G., Norberg, P., Driver, S. P., et al., 2011, MNRAS, 416, 2640
Rudick, C. S., Mihos, J. C., and McBride, C. K., 2011, ApJ, 732, 48
Schaller, M., Dalla Vecchia, C., Schaye, J., et al., 2015, MNRAS, 454, 2277
Schaye, J., Crain, R. A., Bower, R. G., et al., 2015, MNRAS, 446, 521
Schirmer, M., 2013, ApJS, 209, 21
Steinhardt, C. L., Jauzac, M., Acebron, A., et al., 2020, ApJS, 247, 64
Taylor, E. N., Hopkins, A. M., Baldry, I. K., et al., 2011, MNRAS, 418, 1587
Tonnesen, S. and Bryan, G. L., 2012, MNRAS, 422, 1609
Troja, A., Tutusaus, I., Sorce, J., et al. (June 2023). "Euclid in a nutshell". *41st International Conference on High Energy physics*, 94, 94. DOI: 10.48550/arXiv.2211.09668. arXiv: 2211.09668 [astro-ph.IM].
Viola, M., Cacciato, M., Brouwer, M., et al., 2015, MNRAS, 452, 3529
Werner, S. V., Hatch, N. A., Matharu, J., et al., 2023, MNRAS, 523, 91
Wright, A. H., Robotham, A. S. G., Bourne, N., et al., 2016, MNRAS, 460, 765
Zhang, Y., Yanny, B., Palmese, A., et al., 2019, ApJ, 874, 165
Zibetti, S., White, S. D. M., Schneider, D. P., et al., 2005, MNRAS, 358, 949

Appendix A

Test with different mask extensions

The fraction of unmasked diffuse light around sources other than the CG is expected to decrease with increasing redshift, because at higher redshifts the faint signals are likely to be comparable to the background noise level. Therefore, we tested the effect of an extended masking on removing the diffuse light from satellites for the subsample

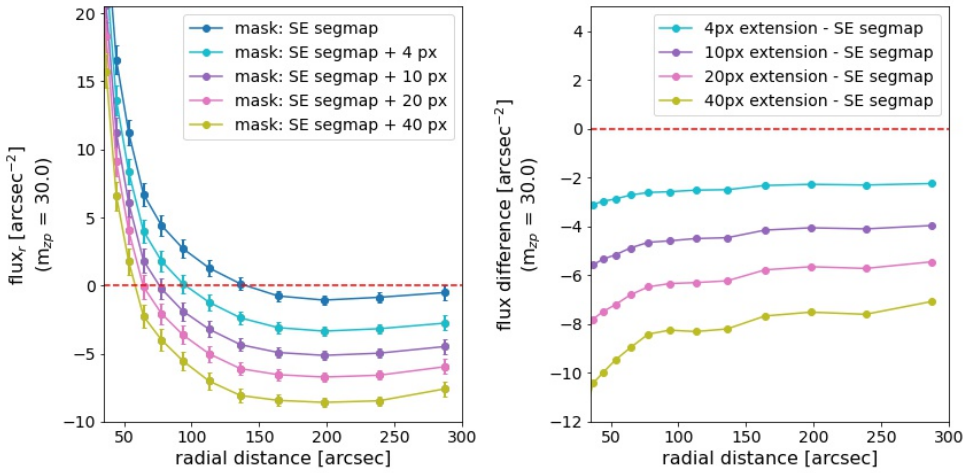

Figure 4.A.1: Left: surface brightness (SB) profiles of group central galaxies (CG) beyond 50" with different levels of mask-extension (as shown in the top-right corner). Compared to the original segmentation map (blue), the 4, 10, 20, and 40-pixel extended masks to sources other than CG produce monotonically lower flux profiles. Error bars show the 1 σ error to the corresponding mean values. Right: change of measured SB profiles of the stacked BGGs. Different lines here show the difference between different levels of mask extension (as shown in the top-right corner) compared to the initial mask obtained from the segmentation map of SExtractor . The main noticeable feature from both the panels is that, even with a 4-pixel (about 1.3 kpc) extension to the segmentation map, the outer profile is lowered by about 3 ADU compared to the original mask from the segmentation map.

of GAMA groups at the lowest redshift bin, which is at $0.09 < z < 0.15$. We picked the groups with the brightest BGGs ($M_r < -23$) in this lowest z bin for this test to have comparable light profiles for the stacking. The masks for the sources obtained from the segmentation map were extended by 4, 10, 20, and 40 pixels by convolving them with a two-dimensional box kernel of the corresponding pixel size, and these extended masks were added to the already existing masks of the bright stars and bad columns as explained in Sec. 4.2.3. The fluxes from the unmasked pixels were then used to estimate radial surface brightness (SB) profiles of individual group images and then stacked together to obtain the final SB profiles for the different mask extension levels, including the original mask without any extension.

A comparison of the SB profiles with the original mask from the segmentation maps and different extended masks is shown in Fig. 4.A.1. The left panel shows a zoomed-in plot of the SB profiles at larger radii for all the mask levels. The expected noticeable point is that compared to the original segmentation map (blue), the 4 (cyan), 10

(purple), 20 (pink), and 40 (olive) pixels extended masks produced monotonically lower flux profiles. This implies that an extended mask indeed results in retaining a lower SB profile. The right panel of Fig. 4.A.1 shows the change of measured radial surface brightness profiles of the stacked BGGs. The different lines show the difference of the CG SB profile for different levels of mask extension (as shown in the labels) compared to the initial mask obtained from the segmentation map of SExtractor (labelled as 'SE segmap'). From the group centre out to 20 arcseconds, the difference is negligible because the CG is unmasked (not shown here). Beyond 20", the increasing mask extension resulted in increasingly lower flux values.

An interesting feature from the right panel is that beyond 100", the profile differences are slightly different from each other. The original segmentation map and 4 pixels-extended masks produced similar SB profiles, resulting in a smooth outer profile for the difference in these cases (cyan line in the right panel). However, the 10, 20, and 40 pixels-extended masks produced slightly different outer SB profiles, resulting in a slightly uneven pattern in the outer profiles in the right panel. This is likely because there is still some extended light from satellites left in the original segmentation map and with 4-pixel mask extensions, which is covered for 10-pixel and larger mask extensions. It implies that a minimum of 10 pixels mask extension is needed to remove the extended light from the satellite galaxies contributing to the uneven light profile. The similar profiles between 10, 20, and 40-pixel extension implies that the removal of uneven light does not improve between these extension levels. Moreover, in the left panel, it is visible that with increased mask extensions, there is increased over-subtraction of faint light, resulting in negative values in the SB profiles beyond 50 kpcs.

To sum up, we found that masks from the original segmentation map and the 4-pixel extension are too small to exclude residual extended light from satellites. At the same time, a larger (20 or 40 pixels) extension of the segmentation map over-subtracts the extended light. Considering both issues, we decided to use a 10-pixel extension to the original segmentation map as our default mask size.

5

An environment-dependent halo mass function as a driver for the early quenching of $z \geq 1.5$ cluster galaxies

Abstract

Many $z = 1.5$ galaxies with a stellar mass ($M_\star$) $\geq 10^{10}\,\mathrm{M}_\odot$ are already quenched in both galaxy clusters (> 50 per cent) and the field (> 20 per cent), with clusters having a higher quenched fraction at all stellar masses compared to the field. A puzzling issue is that these massive quenched galaxies have stellar populations of similar age in both clusters and the field. This suggests that, despite the higher quenched fraction in clusters, the dominant quenching mechanism for massive galaxies is similar in both environments. In this work, we use data from the cosmological hydrodynamic simulations Hydrangea and EAGLE to test whether the excess quenched fraction of massive galaxies in $z = 1.5$ clusters results from fundamental differences in their halo properties compared to the field. We find that (i) at $10^{10} \leq M_\star/\,\mathrm{M}_\odot \leq 10^{11}$, quenched fractions in the redshift range $1.5 < z < 3.5$ are consistently higher for galaxies with higher peak maximum circular velocity of the dark matter halo ($v_{\mathrm{max,peak}}$), and (ii) the distribution of $v_{\mathrm{max,peak}}$ is strongly biased towards higher values for cluster satellites compared to the field centrals. Due to this difference in the halo properties of cluster and field galaxies, secular processes alone may account for (most of) the environmental excess of massive quenched galaxies in high-redshift (proto) clusters. Taken at face value, our results challenge a fundamental assumption of popular quenching models, namely that clusters are assembled from an unbiased subset of infalling field galaxies. If confirmed, this would imply that such models must necessarily fail at high redshift, as indicated by recent observations.

Ahad, S. L., Muzzin, A., Bahé, Y. M., Hoekstra, H., 2023, *Submitted to MNRAS*

5.1 Introduction

Understanding the quenching of star formation in galaxies as a function of mass and environment is a key unsolved question of contemporary astrophysics. A widely used model in the literature is the quenching model introduced by Peng et al. (2010) ("Peng model" hereafter). Its key feature, motivated directly by $z < 1$ observations, is that mass and environment affect the quenched fraction of galaxies in separable ways. This suggests the existence of two distinct quenching channels that are commonly referred to as mass- or self-quenching on the one hand, and environmental quenching on the other (Peng et al., 2010, 2012). Self-quenching depends on the galaxy stellar mass, plausibly through its connection with feedback from active galactic nuclei (AGN), which is likely to drive the quenching (e.g. Tremonti et al., 2007; Silk and Mamon, 2012; Fabian, 2012; Bower et al., 2017). Environmental quenching, on the other hand, arises only in denser environments such as massive clusters of galaxies, where the interaction with other galaxies, including the brightest cluster galaxy (BCG), and with the hot gas in the host halo stop the star-formation process by stripping the galaxy of cold gas e.g. Gunn and Gott, 1972; Larson et al., 1980; Moore et al., 1998; Boselli et al., 2022.

The Peng model has the strength of using real observables such as the star formation rate (SFR) and stellar mass function (SMF) at $z \approx 1$ to model the shape of the SMF of star-forming (SF) and quenched galaxies as a function of the environment in the local Universe, matching the Sloan Digital Sky Survey (SDSS) data. It also correctly describes the quenched fraction as a function of mass and environment. However, some recent studies have challenged the separability of mass and environment on quenched galaxy fractions at both low and high redshifts ($0.3 < z < 3$; e.g. Darvish et al., 2016; Pintos-Castro et al., 2019; Taylor et al., 2023).

Also, several studies have shown that this simple model fails to explain observations at high-redshift ($z > 1$) dense environments (e.g. van der Burg et al., 2013; van der Burg et al., 2020). In particular, van der Burg et al. (2020) studied a set of 11 massive clusters at $1 < z < 1.5$ from the Gemini Observations of Galaxies in Rich Early Environments (GOGREEN) project (Balogh et al., 2017, 2021) and found that the SMF of quenched galaxies has almost the same shape as in the (non-cluster) UltraVISTA field (Muzzin et al., 2013) at the same redshift. The Peng et al. (2010) model would predict them to look different, because the SMF of quenched galaxies in clusters is a product of both self-quenched and environmentally quenched galaxies, whereas field galaxies are only self-quenched. As long as there is any excess environ-

mental quenching—which is clearly the case for the GOGREEN clusters—the shapes of quenched SMFs of cluster and field galaxies should therefore at no redshift look the same.

Moreover, Webb et al. (2020) showed that the mean stellar ages of these quenched massive galaxies from the GOGREEN clusters are slightly older ($0.31^{+0.51}_{-0.33}$ Gyr at stellar mass range 10^{10} – $10^{11.8}\mathrm{M}_{\odot}$) than field galaxies (from UltraVISTA) at the same redshift, with an inferred quenching epoch at $z \gg 2$. This is firmly during the proto-cluster era, when the intracluster medium (ICM) was still very diffuse and is not expected to give rise to efficient ram-pressure stripping (RPS). If environmental quenching were significant for these massive cluster galaxies, one would therefore instead expect them to have been quenched later than the field, and hence have younger stellar populations, contrary to what is observed.

The small stellar age difference between quenched cluster and field galaxies observed by Webb et al. (2020), and the similar SMF of SF and quenched galaxies in cluster and field observed by e.g. van der Burg et al. (2013) and van der Burg et al. (2020) hint at the necessity of an updated quenching model at high redshift that can explain both of the findings. One possibility is that galaxy quenching at high redshift is not only connected to the stellar mass but also the halo mass, similar to what is observed at lower redshift ($z \approx 0.4$) by Mandelbaum et al. (2016). If, at the same stellar mass, galaxies surrounded by a more massive halo are more likely to quench* *and* these galaxies are proportionally more common in clusters, then massive quenched galaxies in both clusters and the field could quench purely as a result of their massive haloes. This would be independent of environmental quenching physics and could therefore happen even before they became cluster members, consistent with the observed ages (Webb et al., 2020). A crucial prerequisite for this scenario is that clusters and the field at high-z have different shapes of their halo mass functions (HMF). A similar suggestion was also made by Werner et al. (2022) based on a higher satellite number density around massive quenched galaxies in the cluster infall region (for GOGREEN clusters, defined as the area within $1 < r/r_{200} < 3$ radial distance from the cluster centre) compared to quenched galaxies of similar stellar mass in the field at $z \approx 1$. Their findings suggest that the infall region has a higher density of high-mass halos than the field, and this excess of massive haloes in the infall region can possibly enhance the galaxy quenching rate.

One caveat to our above hypothesis is that at low redshift the shapes of the (sub-

*The galaxy halo, or the halo surrounding a galaxy, is commonly referred to as the galaxy 'subhalo' in simulations, unlike the group/cluster 'halo' where the galaxy/subhalo resides.

)halo mass function (HMF) in clusters and the field are identical (e.g. Gao et al., 2012; Bahé et al., 2017), although clusters have an (expected) normalisation offset in the HMF compared to the field due to the higher galaxy density. Based on these similar HMFs, the Peng model assumes that high density regions such as galaxy groups and clusters are simply accumulations of field galaxies. If cluster and field HMFs remain the same at high redshifts ($z > 1$), this would imply that even in their formation epoch, galaxy clusters were just accumulations of field galaxies and that the increased number of quenched galaxies in clusters must be due to environmental quenching. However, if the shapes of the HMFs differ at $z \gtrsim 1$, then the excess quenched fraction in clusters can possibly be explained without any environmental quenching. Therefore, the HMFs at higher redshifts and in different environments need to be checked along with the quenched fractions for the stellar mass range of our interest.

Such an investigation using only observational data is not possible, because it is not the current halo mass that matters (it is strongly affected by tidal stripping; see e.g. Bahé et al. 2017), but the unobservable pre-infall (peak) halo mass. Therefore, the best approach to test this hypothesis is to use data from cosmological hydrodynamic simulations. In recent years, state-of-the-art cosmological simulations have been able to successfully reproduce many fundamental observable properties of different galaxy populations along with their DM halo masses, stellar mass functions (SMF), and density profiles across a significant fraction of the age of the Universe (e.g. Dubois et al., 2014; Schaye et al., 2015; Pillepich et al., 2018; Davé et al., 2019).

We use the Hydrangea suite of 24 zoom-in simulations of massive clusters (Bahé et al., 2017) and the corresponding EAGLE 50 cMpc^3 volume (Schaye et al., 2015) to test our hypothesis in this work. Both simulations were run using the exact same physics models, eliminating systematic offsets between the field and cluster galaxies for our analysis. The Hydrangea simulations successfully reproduce the observed galaxy SMF in clusters out to redshift 1.5 (Ahad et al., 2021), and the EAGLE simulations reproduce observed field SMFs out to even higher redshifts considerably well (Furlong et al., 2015). Although the simulations fail to reproduce the quenched fraction of cluster galaxies at $z \sim 1.5$, especially over-quenching the satellites at the low-mass end (Kukstas et al., 2023), the most relevant parts for our analysis are the halo and stellar masses, which they do reproduce well. Furthermore, considering the use of the same galaxy formation model and a large enough galaxy sample size from both environments, EAGLE and Hydrangea are the most suitable companion simulations to test our hypothesis.

The organization of the paper is as follows. In Sec. 5.2.1, we briefly introduce

the simulations used in this work. We describe our sample selection and analysis in Sec. 5.2.2. In Sec. 5.3 we present our results, and discuss our interpretations in Sec. 5.4. Finally, we summarize our findings in Sec. 5.5.

5.2 Data

5.2.1 Simulations

We used data from the Hydrangea simulation suite (Bahé et al., 2017; Barnes et al., 2017) for the clusters and data from the 50 Mpc^3 volume box of the EAGLE simulations (Schaye et al. 2015, see also Crain et al. 2015) for the field environment. The 50 Mpc^3 EAGLE simulations box used here was run with the 'S15-AGNdT9' model (Schaye et al., 2015), which is the largest volume EAGLE box run with the exact same model as Hydrangea, ensuring a consistent comparison between clusters and field in our analysis.

The Hydrangea simulations (Bahé et al., 2017; Barnes et al., 2017), part of the Cluster-EAGLE or 'C-EAGLE' project, consist of high-resolution cosmological hydrodynamic zoom-in simulations of 24 massive galaxy clusters. Each simulation region is centred on a massive cluster with M_{200c} in the range $10^{14.0}$–$10^{15.4}\,\mathrm{M}_\odot$ at $z = 0$[†]. The high-resolution simulation boxes encompass ≥ 10 virial radii (r_{200c}) of the cluster surroundings, making them also suitable to study the large-scale environmental influence on galaxies within and around clusters.

The resolution in both Hydrangea and the 'S15-AGNdT9' EAGLE box are the same, with particle mass $m_{\mathrm{baryon}} = 1.81 \times 10^6\,\mathrm{M}_\odot$ for baryons and $m_{\mathrm{DM}} = 9.7 \times 10^6\,\mathrm{M}_\odot$ for dark matter, respectively. The gravitational softening length is $\epsilon = 0.7$ physical kpc (pkpc) at $z < 2.8$. In both simulations, structures (galaxies and clusters) were identified in post-processing using the SUBFIND code (Dolag et al. 2009, see also Springel et al. 2001), using a friends-of-friends (FoF) algorithm and subsequent identification of bound substructures.

A flat ΛCDM cosmology is assumed in both Hydrangea and EAGLE, with parameters taken from the *Planck* 2013 results, combined with baryonic acoustic oscillations, polarization data from WMAP, and high multipole moment experiments (Planck Collaboration XVI, 2014): Hubble parameter $H_0 = 67.77$ km s^{-1} Mpc^{-1}, dark energy density parameter $\Omega_\Lambda = 0.693$, matter density parameter $\Omega_{\mathrm{M}} = 0.307$, and baryon

[†] M_{200c} refers to the mass within a sphere centred at the potential minimum of the cluster, and radius r_{200c}, within which the average density of matter is equal to 200 times the critical density.

density parameter $\Omega_{\rm b} = 0.04825$.

5.2.2 Sample selection

At all redshifts, our galaxy sample was selected from two distinct environments: massive clusters and the field. The cluster galaxies were chosen from the central clusters of each of the 24 Hydrangea zoom-in regions. All the subhaloes (or member galaxies) of the cluster from the FoF halo finder with a stellar mass of at least $10^9\,{\rm M}_\odot$ and within the virial radius (r_{200}) of the corresponding cluster were included. To isolate the effects of environmental influence versus self-quenching, we also selected a subsample of the cluster galaxies by excluding the massive central galaxies and only keeping the satellites. This subsample is referred to as 'cluster satellites' throughout this paper.

For our field galaxy sample, we selected all galaxies with $M_* \geq 10^9{\rm M}_\odot$ from the EAGLE 50 Mpc^3 S15-AGNdT9 simulation. To separate the impact of environmental effects from self-quenching, we also selected the subset of centrals from this field sample. This sub-sample is referred to as 'field centrals' throughout this paper.

5.2.3 Galaxy properties

For the selected galaxies within each environment, we defined different galaxy properties based on the data from the simulation outputs. We selected the integrated mass of star particles within 30 physical kpc (pkpc) radius from the galaxy centre of potential as the galaxy stellar mass. In Ahad et al. (2021), we tested and verified that this definition of stellar mass is comparable to those obtained from running SExtractor (Bertin and Arnouts, 1996) on the 2-dimensional projected stellar mass maps of the cluster galaxies.

The galaxy halo mass was calculated from summing up the total mass of stars, dark matter, gas, and black hole particles that are connected to each subhalo. As the maximum circular velocity of the stars or gas is commonly used as an observational proxy to estimate the galaxy halo mass (e.g. Nagai and Kravtsov, 2005), we also calculated the maximum circular velocity $v_{\rm max}$ for each galaxy, which we define as the maximum of $v = \sqrt{GM(<r)/r}$ where r is the radial distance from the centre of potential of each galaxy and $M(<r)$ the total mass enclosed within a sphere of radius r. At each redshift snapshot from the simulations, we also identified $v_{\rm max,peak}$, the maximum value of $v_{\rm max}$ for an individual galaxy across all previous snapshots including the current one. This is motivated by the findings of Reddick et al. (2013), who show that $v_{\rm max,peak}$ of a dark matter halo correlates tightly with the properties

of its galaxy. At each redshift, along with the $v_{\rm max,peak}$ for each galaxy, we selected the value of their stellar mass when $v_{\rm max,peak}$ occurred ($M_\star, v_{\rm max,peak}$ or $M_{\star,\,\rm peak}$), which can help with identifying the stellar mass growth at any redshift after $v_{\rm max,peak}$ occurred through comparison with the stellar mass at that epoch. As an independent component from the $v_{\rm max,peak}$, we also measured the peak halo mass, which is the maximum halo mass of an individual galaxy halo across all the redshifts from when the galaxy emerged until the redshift of interest.

We also use the spatially integrated star formation rate (SFR) for each galaxy in every snapshot, which we divide by $M_\star$ at the same redshift to obtain the specific SFR (sSFR). We consider galaxies with sSFR $\geq 10^{-10}$ yr^{-1} as star-forming and those with lower sSFR as quenched. However, at $z \geq 1$, the sSFR threshold separating star-forming galaxies from quenched ones is expected to evolve due to the evolution of their star-forming activity and stellar mass over cosmic time (e.g. Furlong et al., 2015). We followed a similar principle as Furlong et al. (2015) and Furlong et al. (2017) and applied an sSFR cut approximately one order of magnitude below the observed main sequence of star formation at each redshift of our concern. Our results in the following section are shown based on the fixed sSFR cut throughout this work because this threshold corresponds approximately to the separation between quenched and star-forming galaxies in Kukstas et al. (2023) for $z = 1$.

5.3 Results

5.3.1 Halo mass function in cluster and field

In this work, we test whether the quenching of massive galaxies in both cluster and field environments can be attributed to the distribution of their halo masses, rather than their stellar masses or environments. In the local Universe, the shape of the halo mass function of cluster galaxies is comparable to that in the field environment (e.g. Bahé et al., 2017). At higher redshifts however, when the galaxy clusters are still forming, the halo mass distribution may well be different between (proto-)clusters and the field. We therefore start by looking at the distribution of halo mass, or the halo mass function (HMF) in cluster and field at several redshifts between 1.5 and 3.5. We used the peak maximum circular velocity ($v_{\rm max,peak}$, see Sec. 5.2.3 for details) of the galaxies to construct the HMF.

The HMF[‡] at $z \approx 1.5$ is shown in the left panel of Fig. 5.1. The HMFs here

[‡]We acknowledge that the distribution of $v_{\rm max,peak}$ is not exactly the distribution of the halo

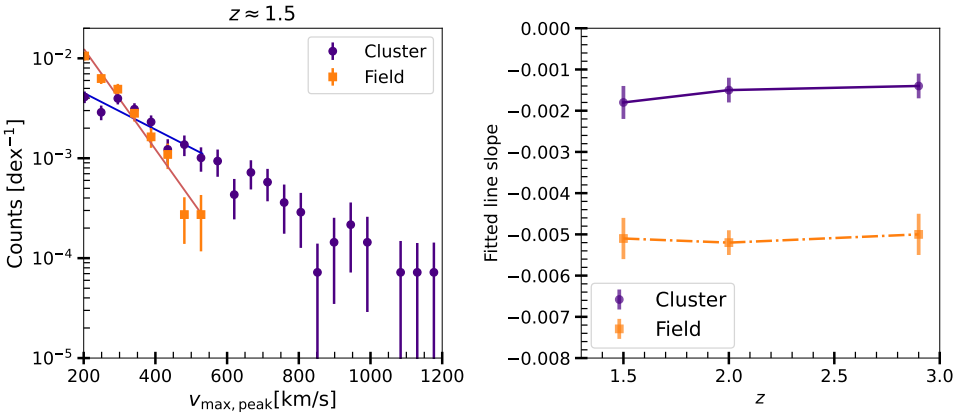

Figure 5.1: $v_{\mathrm{max,peak}}$ distribution in clusters (purple), and the field (orange) at $z = 1.5$, normalized by the total number of galaxies in each of the environments. At the lower $v_{\mathrm{max,peak}}$ end, they are similar but they evolve differently from low to high $v_{\mathrm{max,peak}}$ in field and clusters, with clusters having a larger number of galaxies with high $v_{\mathrm{max,peak}}$ values. To demonstrate their different slopes, a log-linear function is fitted to the data points (shown by straight lines in left panel) and the slopes of the fitted lines are plotted in the right panel at different redshifts.

are normalised by the integrated values of the corresponding distributions and, consequently, represent the halo mass distribution if the field and cluster environments had the same number of galaxies. As the figure shows, compared to the field galaxies (orange points), galaxies in clusters (purple points) reach a much higher $v_{\mathrm{max,peak}}$. The highest values of $v_{\mathrm{max,peak}}$ in clusters are expected because clusters host, by definition, the most massive haloes. However, even at $v_{\mathrm{max,peak}}$ values where both cluster and field galaxies exist, clusters have more galaxies than the field does. This is more clearly demonstrated by the fitted lines in the distributions, as shown in Fig. 5.1 with the same colour as the data points. The slope of the field HMF is steeper than the slope of the cluster HMF. The same behaviour is visible at all the redshifts of our consideration, shown in the right panel of Fig. 5.1. This panel shows that the slope of the field HMF is always steeper than the cluster HMF across our considered redshifts. Therefore, the HMFs in field and cluster environments are clearly different at all the redshifts we considered.

mass, i.e., the HMF, as we mention here. However, for their comparability and for simplifying the terms to compare with similar works, we use 'HMF'.

5.3.2 Stellar-to-halo-mass relation and galaxy quenching

To explore whether or how the different HMFs in different environments affect galaxy quenching, we study the stellar-to-halo-mass-relation (SHMR)[§] of galaxies in our samples of clusters and field galaxies. For this part onward, we only select the 'cluster satellite' and 'field central' subsamples as described in Sec. 5.2.2. This selection ensures that the field galaxies in consideration are not subject to any environmental quenching process and the cluster galaxies in our sample are exposed to the environmental quenching processes that are relevant at the corresponding redshifts. Similar to the HMF, we used the maximum circular velocity ($v_{\rm max,peak}$) of each galaxy halo in our sample at each environment to construct the SHMR.

Figure 5.2 shows the SHMR in clusters (left) and the field (right) at $z = 1.5$, respectively. In both panels, red points represent quenched (sSFR $\leq 10^{-10}$ yr^{-1}) galaxies and blue points represent star-forming ones (sSFR $> 10^{-10}$ yr^{-1}). The black lines indicate the running medians of the cluster (dashed) and field (dotted) samples. The dotted black line is also plotted in the left panel to allow a comparison of the running median values of both samples: at $M_* < 10^{10}\,{\rm M}_\odot$, the median $v_{\rm max,peak}$ values are similar in clusters and the field whereas above $10^{10}\,{\rm M}_\odot$, the median $v_{\rm max,peak}$ values are higher in clusters. The same figure was constructed at the other redshifts considered (2.0 and 3.5); they show a similar characteristic as at $z = 1.5$, albeit with a smaller fraction of quenched galaxies overall because they had less time to go through the quenching process.

The smaller fraction of quenched galaxies at higher redshifts could also be partially due to our choice of a fixed sSFR to separate the quenched and star-forming galaxies at our redshifts of concern. Therefore, we reproduced the same figures with an evolving sSFR cut with redshift (as explained in Sec. 5.2.3). The exact number of quenched galaxies changed slightly with the evolving sSFR cut. However, our primary conclusions from this test with a fixed sSFR cut remained unchanged.

Three main features are visible in the panels of Fig. 5.2. First, there are more galaxies in clusters with higher stellar masses and $v_{\rm max,peak}$ than in the field, even when we only consider cluster satellites and field centrals. Second, for both environments, above $10^{10}\,{\rm M}_\odot$ stellar mass, quenched galaxies (red) tend to have a higher $v_{\rm max,peak}$ (or halo mass) than star-forming galaxies (blue) at the the same stellar mass. Third, there are quite a few quenched galaxies below $10^{10}\,{\rm M}_\odot$ stellar mass in clusters, whereas

[§]Similar to our use of the term 'HMF' instead of 'distribution of $v_{\rm max,peak}$', we use 'SHMR' instead of 'distribution of $v_{\rm max,peak}$ vs M_*' for their comparability and for simplifying the terms to compare with similar works.

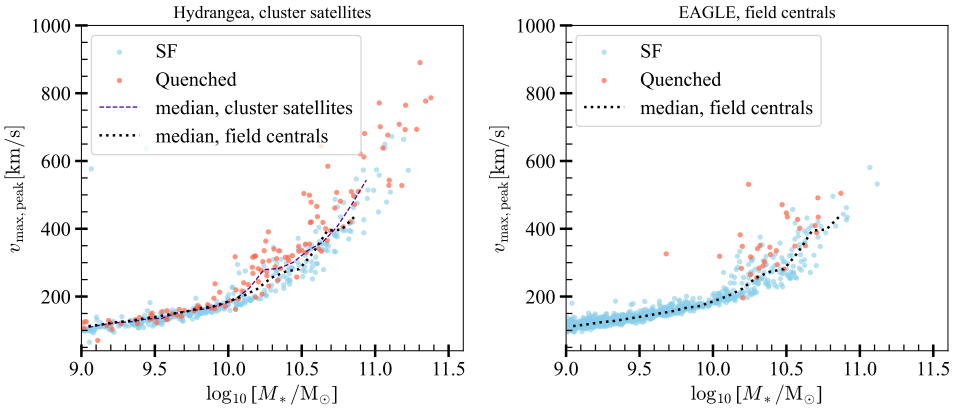

Figure 5.2: $v_{\rm max,peak}$ vs. stellar mass (analogous to stellar-to-halo-mass) relations in clusters (left) and the field (right) at $z = 1.5$. In both panels, red points represent galaxies that are quenched (sSFR≤-10) while star-forming galaxies are shown in blue. The dashed (dotted) black lines indicate the running median distribution of the $v_{\rm max,peak}$ in cluster satellites (field centrals).

there are almost none in the field. All of these are interesting features to understand galaxy assembly and quenching, and require further investigation. However, before doing so, it is crucial to ensure that the second feature in Fig. 5.2 is real and that the increased $v_{\rm max,peak}$ of the quenched galaxies does not occur after the quenching, rather than driving it.

There are two possible explanations for this feature: (i) There could be an upward shift in $v_{\rm max,peak}$ between the quenched and star-forming galaxies at fixed stellar mass, which would imply that the quenched galaxies indeed have higher $v_{\rm max,peak}$ (or higher halo-mass). Alternatively (ii), there could be a shift to the left in stellar mass (i.e. to lower masses) of quenched galaxies at a fixed $v_{\rm max,peak}$, which implies that the quenched galaxies with the same $v_{\rm max,peak}$ did not grow as much in stellar mass compared to the star-forming ones. The upward-shift scenario occurs when $v_{\rm max,peak}$ rises either before or after the galaxy quenches. The left-shift scenario, on the other hand, can occur either due to significant stellar mass stripping of quenched galaxies, or because stellar mass growth stops for quenched galaxies while star-forming galaxies continue to grow and hence move to the right in Fig. 5.2).

To identify which of these two scenarios is the dominant reason for the separation

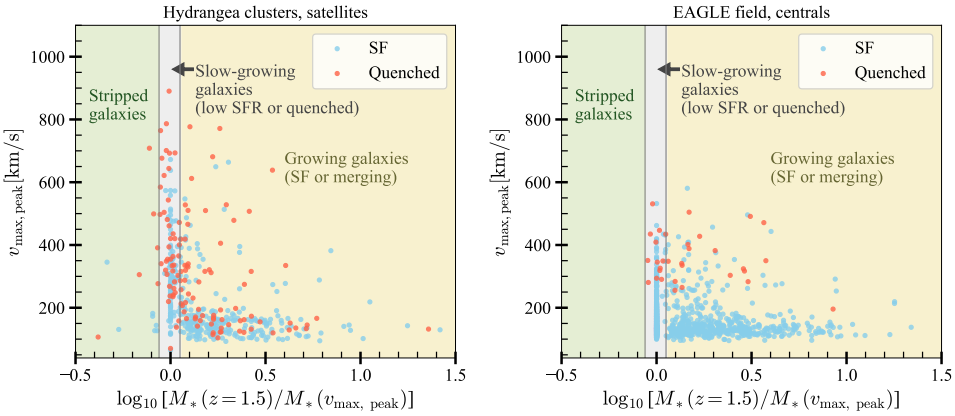

Figure 5.3: $v_{\rm max,peak}$ vs stellar mass ratio in clusters (left) and the field (right). The stellar mass ratio is obtained from the ratio of the galaxy stellar mass at $z = 1.5$ and the galaxy stellar mass at the epoch when $v_{\rm max,peak}$ occurs. In both panels, the colours of the data points indicate whether they are quenched (sSFR≤-10, red) or star-forming (blue). The ratio of stellar mass at $z = 1.5$ and stellar mass where $v_{\rm max,peak}$ occurs indicates what happened to the galaxy since $v_{\rm max,peak}$ occurred. If the galaxy went through stripping of stars since $v_{\rm max,peak}$ occurred, it will have a negative log mass ratio, as indicated by the light green area in both panels. If galaxies kept on growing since $v_{\rm max,peak}$ occurred (primarily by star formation or merging), they would have a positive log mass ratio, indicated by the yellow area. If a galaxy stopped forming stars and did not grow in stellar mass since $v_{\rm max,peak}$, it will be at or near the 0 log mass ratio location, shown by the grey area. This last case can also occur if $v_{\rm max,peak}$ happened at or close to $z = 1.5$.

of the star-forming and quenched galaxies in Fig. 5.2, we took the stellar masses of each galaxy at the redshift when its $v_{\rm max,peak}$ occurs ($M_{\star,\,\rm peak}$), and plotted the $v_{\rm max,peak}$ vs $M_\star(atz = 1.5)/M_{\star,\,\rm peak}$ relation in Fig. 5.3. This ratio of stellar mass at $z1.5$ to the stellar mass at $v_{\rm max,peak}$ is an indication of how the stellar mass of the galaxy has changed since the epoch of $v_{\rm max,peak}$. There are three possible areas where galaxies can be in this plot (shown by shaded regions in Fig. 5.3), and each location implies a possible scenario about why they are there. (i) If significant stellar stripping were responsible for the left-shift of quenched galaxies in Fig. 5.2, then $M_\star(z = 1.5) < M_{\star,\,\rm peak}$ and hence $\log(M_\star(z = 1.5)/M_{\star,\,\rm peak}) < 0$. (ii) If quenched galaxies have $M_\star(z = 1.5) \approx M_{\star,\,\rm peak}$ whereas star-forming galaxies have $M_\star(z = 1.5) \gg M_{\star,\,\rm peak}$, it would imply that a strong right-shift of star-forming galaxies (and lack thereof for quenched galaxies) created the trend visible in Fig. 5.2. If $M_\star(z = 1.5) \approx M_{\star,\,\rm peak}$ for both star-forming and quenched galaxies, it could also imply that $v_{\rm max,peak}$ occurred recently in both environments. And finally, (iii) if there is no substantial difference in the distribution of $\log(M_\star(z = 1.5)/M_{\star,\,\rm peak})$ values between star-forming and quenched galaxies, and both span a broad range in the positive $x-$axis, it would imply that the primary cause of the separation of the star-forming and quenched galaxies in Fig. 5.2 is not a horizontal shift of the galaxies along the stellar mass axis.

Figure 5.3 shows that at redshift 1.5, only a handful of cluster satellites are in the area that shows stripped galaxies (light green shaded region), i.e., only a few show any sign of strong stellar stripping. In addition, not all of these galaxies with $M_\star(z = 1.5) < M_{\star,\,\rm peak}$ are quenched. Therefore, this scenario can be ruled out as the primary reason for the star-forming and quenched galaxy separation in Fig. 5.2. Figure 5.3 also shows that in both environments, a good fraction of both star-forming and quenched galaxies have $M_\star(z = 1.5) \approx M_{\star,\,\rm peak}$ (i.e. close to 0 along the x-axis), whereas the rest of them – especially galaxies with $v_{\rm max,peak} < 200$ km s^{-1} – scatter up to $\log(M_\star(z = 1.5)/M_{\star,\,\rm peak}) \approx 1$, with no clear separation between star-forming and quenched galaxies. This implies that a right-shift of star-forming galaxies alone cannot explain the separation of star-forming and quenched galaxies in Fig. 5.2. Although we only show $z = 1.5$ in Fig. 5.3, we have verified that the same conclusion holds at the other redshifts between 1.5 and 3.5. In short, the best explanation for the offset of quenched galaxies to higher $v_{\rm max,peak}$ values at fixed $M_\star > 10^{10}\,{\rm M}_\odot$ as seen in Fig. 5.2 is that these galaxies have intrinsically deeper potential wells and that this is connected to their quenching mechanism, e.g., AGN feedback.

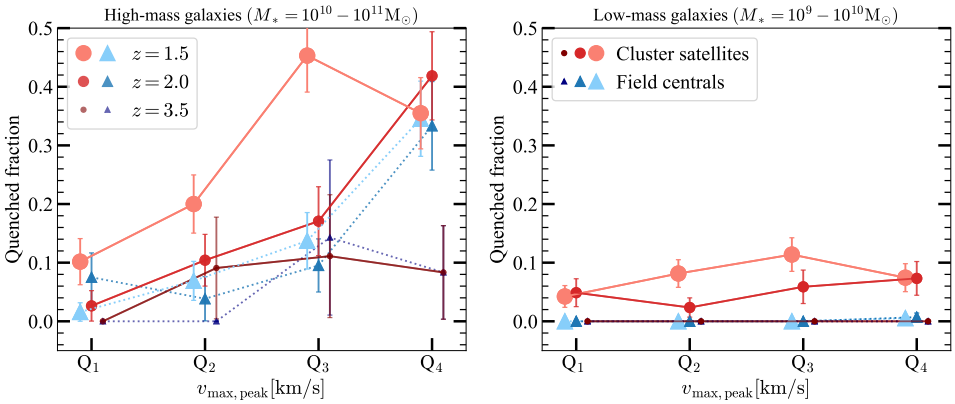

Figure 5.4: Fraction of quenched galaxies vs. the $v_{\rm max,peak}$ quartile in clusters (red shades) and field (blue shades) at different redshifts. The evolution is shown for two different galaxy mass ranges, $10^{10} - 10^{11}$M$_\odot$ (left-hand panel) and $10^{9} - 10^{10}$M$_\odot$ (right-hand panel). Higher redshift data points are respectively smaller and in darker tones or the same colours. There is no variation of quenched fractions with $v_{\rm max,peak}$ quartile for low-mass galaxies. However, for the high-mass galaxies, a higher $v_{\rm max,peak}$ corresponds to a higher quenched fraction at $z \leq 2$. This trend is visible both in cluster satellites and field centrals.

5.3.3 Quenched fraction and halo mass

To demonstrate the correlation between quenching and $v_{\rm max,peak}$ more clearly, we show in Fig. 5.4 the fraction of quenched cluster and field galaxies in running quartiles of $v_{\rm max,peak}$. The quenched fraction here is measured in running $v_{\rm max,peak}$ quartiles[¶]. The relation for clusters is shown by circles in red shades and for the field by blue shaded upward triangles. In each case, we show three different redshifts, with higher redshifts represented by smaller markers and darker shades. For clarity, the trends are shown separately for two broad stellar mass bins, low-mass galaxies with $M_\star$ between 10^9 and 10^{10} M$_\odot$ in the right-hand panel, and high-mass galaxies ($M_\star$ between 10^{10} and 10^{11} M$_\odot$) on the left.

A number of key features are worth pointing out in Fig. 5.4. Starting with the low-mass field galaxies (blue triangles in the right-hand panel), we see that there are almost no quenched galaxies at any redshift or $v_{\rm max,peak}$. For low-mass galaxies in

[¶]One of the $v_{\rm max,peak}$ bin separators, the running median, is shown by the black dashed (clusters) and dotted (field) lines in Fig. 5.2. The other two are the running 25th and 75th percentiles.

clusters (red circles in the right-hand panel), the same is true at the highest redshift in this figure, $z = 3.5$. At $z \approx 2.0$, however, we see that about 5 per cent of low-mass galaxies are already quenched in all four $v_{\rm max,peak}$ quartiles. At $z = 1.5$, the fraction of quenched low-mass galaxies increases to approximately 9 per cent in the 2$^{\rm nd}$ and 3$^{\rm rd}$ $v_{\rm max,peak}$ quartiles, while remaining unchanged in the 1$^{\rm st}$ and 4$^{\rm th}$ quartiles. In other words, there is no dependency of quenched fraction on $v_{\rm max,peak}$ for low-mass galaxies in clusters or the field, but low-mass cluster galaxies are beginning to quench due to environmental mechanisms[‖] unrelated to $v_{\rm max,peak}$ by $z = 2$.

Considering instead the high-mass galaxies (left-hand panel in Fig. 5.4), we see that, in both clusters and the field, the quenched galaxy fraction correlates almost always with $v_{\rm max,peak}$. This behaviour is consistent with our hypothesis that, at fixed stellar mass, halo properties (such as a higher halo mass) can make galaxies more likely to be quenched irrespective of the environment they reside in.

5.4 Discussion

5.4.1 Quenched fraction in clusters and the field

To understand the effects of environmental and self-quenching in our high-mass galaxy samples from Fig. 5.4, we need to compare the quenched fractions in clusters (red shades) and the field (blue shades) at the same redshifts (similar marker size as indicated in the labels) in the left panel of Fig. 5.4. At $z = 3.5$, the quenched fractions of cluster and field galaxies are similar for both the high- and low-mass galaxy samples, implying that environmental quenching was negligible at very high redshift, regardless of galaxy mass. At $z = 2$, the quenched fraction of high-mass cluster satellites is still relatively comparable (with a slight increase) to the high-mass field centrals (medium dark red and blue symbols in Fig. 5.4, left-hand panel). The environmental effect is similarly low for the low-mass galaxies, hinting that at $z = 2$, the environmental effect in clusters is already present, albeit weakly. At $z = 1.5$, the difference in the quenched fraction is prominent for high-mass galaxies. Especially in the lowest three $v_{\rm max,peak}$ quartiles, the quenched fractions in clusters are almost a factor of two higher at the same $v_{\rm max,peak}$ compared to the field, which is likely due to environmental effects.

[‖] Instead of a constant sSFR threshold across redshifts, we repeated this analysis using an evolving sSFR threshold with redshift, e.g. a fixed offset from the star-forming main sequence to define quenched galaxies. There is a slight hint that the first signs of environmental quenching appear even earlier than shown in Fig. 5.4, but this change of the sSFR threshold did not affect our primary conclusions.

Interestingly, at the highest $v_{\rm max,peak}$ bin, the quenched fraction is almost the same in clusters and the field. The high-mass quenched fractions in the field increase only marginally between $z = 2$ and 1.5, by < 0.05.

The most plausible explanation is that, for massive galaxies, self-quenching is directly correlated to $v_{\rm max,peak}$ while environmental quenching is either inversely correlated or uncorrelated with $v_{\rm max,peak}$. At the same high stellar mass range, if a galaxy has a higher $v_{\rm max,peak}$, it is similarly likely to be quenched in both clusters and the field, but for lower $v_{\rm max,peak}$ ranges, it is more likely to be quenched as a satellite in a massive cluster compared to being an isolated or central galaxy in the field. This is likely because, if a galaxy in a dense environment has a higher halo mass, it will retain its cold gas more efficiently than a galaxy with the same stellar mass but a smaller halo mass, resulting in slower or less efficient quenching. Therefore, at this stellar mass range ($10^{10} - 10^{11}$M$_\odot$), in redshift 1.5 clusters, along with galaxies that quenched after becoming a satellite, there can also be satellites that were already quenched in the field before being accreted onto the cluster. In this scenario, the age of the stellar population in quenched cluster galaxies would be comparable to that of similarly massive quenched field galaxies, consistent with the results from the GOGREEN survey (Webb et al., 2020).

5.4.2 Do $v_{\rm max,peak}$ and halo mass have the same effect on quenching?

In our analysis, we have chosen $v_{\rm max,\,peak}$ as proxy for the halo mass of a galaxy, motivated by its similarity to observational methods. However, the simulated halo catalogue also provides (galaxy) halo masses directly, as well as their peak values across cosmic time. We used the peak halo mass of our galaxy sample across the considered redshifts, and repeated the same analysis with the HMF, SHMR, and quenched fraction of galaxies in halo mass quartiles. We found somewhat similar results for the halo mass (more details in Appendix 5.5). However, compared to the $v_{\rm max,peak}$, the findings in terms of the peak halo mass have more scatter. The most likely reason for this is that quenching is actually controlled by a third property that correlates with both halo mass and $v_{\rm max,\,peak}$, the latter correlation being stronger.

One promising candidate that drives the quenching more directly is the mass of the central supermassive black hole (SMBH, $M_{\rm SMBH}$). A high $M_{\rm SMBH}$ indicates high past accretion and AGN feedback activity of the SMBH, which can drive the quenching, as shown by multiple simulation- and observation-based works (see e.g. Bower et al.,

2017; Piotrowska et al., 2022). Besides, the size (half-mass radius, $r_{1/2,\mathrm{mass}}$) of the galaxies is a likely parameter that adds to the scatter between halo mass and $v_{\mathrm{max,\,peak}}$. Due to the definition of $v_{\mathrm{max,peak}}$ (see Sec. 5.2.3), a low $r_{1/2,\mathrm{mass}}$ can increase the value of $v_{\mathrm{max,peak}}$ since it indicates a higher concentration of mass near the galactic centre. Furthermore, if a galaxy came too close to the cluster centre not long before reaching its $v_{\mathrm{max,peak}}$, the quenching is more likely to be environmental, irrespective of the $v_{\mathrm{max,peak}}$ value. Therefore, along with $r_{1/2,\mathrm{mass}}$ and M_{SMBH}, we also tested the correlation of the minimum distance from the cluster centre reached by each galaxy before they attained their $v_{\mathrm{max,peak}}$ to the quenched galaxies in our high-mass galaxy sample.

Only 27 per cent of the quenched cluster satellites showed a close proximity (within 20 percent of their instantaneous virial radius) to the cluster centre before reaching their $v_{\mathrm{max,peak}}$, excluding the majority of these early-quenched galaxies (more details in Appendix 5.5). Therefore, most of the cluster satellites in our sample were not close enough to the cluster centre to experience environmental quenching via strong tidal or hydrodynamic forces before reaching their $v_{\mathrm{max,peak}}$.

In field centrals, where self-quenching must be the dominant mechanism, 85 per cent of quenched galaxies have central black hole masses above $10^{7.5}$ $\mathrm{M}_{\odot}$**. Similarly, 41 per cent of quenched cluster satellites have a high black hole mass (above $10^{7.5}$ $\mathrm{M}_{\odot}$), which indicates that at least for 41 per cent of the quenched cluster galaxies, AGN feedback can be the dominant quenching mechanism. As far as their sizes are concerned, approximately 70 per cent of quenched galaxies have a small half-mass radius ($\leq$ 1 kpc) in both clusters and the field. More details on this test are provided in Appendix 5.5.

5

Although most of the quenched galaxies have either a massive central black hole or a small size (or both, for a few), none of these properties can completely explain the scatter between the effects of halo mass and $v_{\mathrm{max,peak}}$ on galaxy quenching. Previous studies have found that, instead of the galaxy mass, smaller galaxy size ($<$ 1 kpc) and higher central density can also be connected to inducing galaxy quenching, and these properties are connected to the central baryonic properties of the galaxy (e.g. Yano et al., 2016; Whitaker et al., 2017). These findings hint that the central baryonic properties of a galaxy could be responsible for the scatter that we find between how halo mass or $v_{\mathrm{max,peak}}$ affect quenching. Instead of halo mass, $v_{\mathrm{max,peak}}$ better captures this connection between the central baryonic properties of a galaxy and the quenching

**This mass limit was arbitrarily chosen to keep all the quenched field centrals with a massive black hole above the threshold. See top right panel of Fig. 5.B.1.

of its star formation. Models of galaxy quenching at high redshifts should therefore consider their halo mass and $v_{\rm max,peak}$, along with their stellar mass and environment.

5.5 Summary and Conclusions

In recent works based on the GOGREEN cluster survey, a similar shape of the stellar mass function of quenched galaxies in clusters and the field (van der Burg et al., 2020), and similar ages of massive quenched galaxies in both environments (Webb et al., 2020), have been observed. These findings cannot be explained using the widely-accepted model for separable mass- and environmental quenching proposed by Peng et al. (2010), and therefore necessitate a review of existing galaxy quenching models, especially at high redshifts. In this work, we tested whether a difference in the halo mass function between cluster and field environments above redshift 1.5, along with a halo-mass dependant quenching efficiency, can explain the observed discrepancies by using data from the cosmological hydrodynamic simulations Hydrangea and EAGLE. Our findings are as follows:

(i) The normalized distribution of $v_{\rm max,peak}$ has a different shape in cluster and field environments at $z \geq 1.5$. The shape of the distributions, quantified by the slope of a fitted line, was consistently different between clusters and the field out to redshift 3 (Fig. 5.1).

(ii) The stellar mass to $v_{\rm max,peak}$ relations of cluster satellites and field centrals show that most quenched galaxies have a $v_{\rm max,peak}$ value higher than the median $v_{\rm max,peak}$ at any given stellar mass, which is more prominent for higher mass galaxies (Fig. 5.2). This behaviour suggests that a higher $v_{\rm max,peak}$ (which is similar to observational proxies of halo mass) may be correlated with the quenching of high-mass galaxies above redshift 1.5.

(iii) We see almost no quenched galaxies among $z = 3.5$ low mass galaxies ($9 < \log(M_*)/\mathrm{M}_\odot < 10$) in both field and clusters, which remains the same in low-mass field centrals even at $z = 1.5$. Low-mass cluster satellites however, show an increase in their quenched fraction over time, independent of $v_{\rm max,peak}$, which grows to 10 per cent by redshift 1.5. This increase demonstrates that environmental quenching becomes significant between $2 < z < 3.5$ in these low-mass galaxies (Fig. 5.4). The absence of quenched galaxies in this stellar mass range for field centrals also indicates that environmental quenching is the primary mechanism for quenching these low-mass galaxies.

(iv) High-mass galaxies ($10 < \log(M_*)/\mathrm{M}_\odot < 11$) in both clusters and the field have a clear correlation of their quenched fractions with $v_{\mathrm{max,peak}}$ at all redshifts considered in this work ($1.5 \leq z \leq 3.5$). This suggests that the same mechanism(s) quenched high-mass field centrals and cluster satellites, at least until redshift 2.

(v) For high-mass galaxies, the enhancement of quenched fraction is higher in cluster satellites compared to the field centrals between $z = 2$ and 1.5, indicating a contribution from environmental quenching in high-mass cluster satellites. However, for the highest $v_{\mathrm{max,peak}}$ quartile, the quenched galaxy fraction is comparable in field and clusters at all the considered redshifts, suggesting that at fixed stellar mass, galaxies with the highest halo mass are the least affected by the environmental quenching compared to galaxies with a lower halo mass.

Our finding is qualitatively consistent with the discussions of van der Burg et al. (2020), that the stellar mass functions of quenched galaxies in clusters and field at $z = 1.5$ have a similar shape because their primary quenching mechanisms were similar. Summary point (v) is also qualitatively consistent with the findings of Webb et al. (2020), explaining that at $z = 1.5$, high-mass cluster satellites can be both environmentally quenched or self-quenched before they enter into the clusters and, therefore, can have a comparable age of the stellar population to the quenched field galaxies.

Compared to the existing simple quenching models that separate mass and environmental quenching based on low-redshift observations, this work using cosmological simulations better reconciles the high quenched fraction in clusters with the lack of an age dependence of quiescent galaxies on the environment. If true, it also implies that the majority of high-mass galaxies in (proto-)clusters are quenched by secular processes, not by their environment.

Finally, the differing halo mass functions imply that (proto-) clusters do not grow simply from the infall of field halos. Therefore, galaxy quenching models at high redshifts need careful revision, especially with improved observations and insights in the *JWST* era. Considering the effect of the underlying halo-mass distributions and central baryonic concentrations will be a valuable starting point in this direction.

Acknowledgements

The authors acknowledge support from the Netherlands Organization for Scientific Research (NWO) under Vici grant number 639.043.512 (SLA, HH), and Veni grant

number 639.041.751 (YMB). YMB also gratefully acknowledges financial support from the Swiss National Science Foundation (SNSF) under project 200021_213076. The Hydrangea simulations were in part performed on the German federal maximum performance computer "HazelHen" at the maximum performance computing centre Stuttgart (HLRS), under project GCS-HYDA / ID 44067 financed through the large-scale project "Hydrangea" of the Gauss Center for Supercomputing. Further simulations were performed at the Max Planck Computing and Data Facility in Garching, Germany. This work used the DiRAC@Durham facility managed by the Institute for Computational Cosmology on behalf of the STFC DiRAC HPC Facility (www.dirac.ac.uk). The equipment was funded by BEIS capital funding via STFC capital grants ST/K00042X/1, ST/P002293/1, ST/R002371/1 and ST/S002502/1, Durham University and STFC operations grant ST/R000832/1. DiRAC is part of the National e-Infrastructure.

The analysis of this work was done using Python (http://www.python.org), including the packages NumPy (Harris et al., 2020), AstroPy (Astropy Collaboration et al., 2013), and SciPy (Jones et al., 2009). Plots have been produced with Matplotlib (Hunter, 2007).

Data Availability

The data presented in the figures are available upon request from the corresponding author. The Hydrangea data are available at https://ftp.strw.leidenuniv.nl/bahe/Hydrangea/. The Eagle simulations are publicly available; see McAlpine et al. (2016) and The EAGLE team (2017) for how to access EAGLE data.

5

References

Ahad, S. L., Bahé, Y. M., Hoekstra, H., et al., 2021, MNRAS, 504, 1999
Astropy Collaboration, Robitaille, T. P., Tollerud, E. J., et al., 2013, A&A, 558, A33
Bahé, Y. M. et al., 2017, MNRAS, 470, 4186
Balogh, M. L., Gilbank, D. G., Muzzin, A., et al., 2017, MNRAS, 470, 4168
Balogh, M. L., van der Burg, R. F. J., Muzzin, A., et al., 2021, MNRAS, 500, 358
Barnes, D. J., Kay, S. T., Bahé, Y. M., et al., 2017, MNRAS, 471, 1088
Bertin, E. and Arnouts, S., 1996, A&AS, 117, 393
Boselli, A., Fossati, M., and Sun, M., 2022, A&AR, 30, 3
Bower, R. G., Schaye, J., Frenk, C. S., et al., 2017, Monthly Notices of the Royal Astronomical Society, 465, 32
van der Burg, R. F. J., Muzzin, A., Hoekstra, H., et al., 2013, A&A, 557, A15
Crain, R. A., Schaye, J., Bower, R. G., et al., 2015, MNRAS, 450, 1937
Darvish, B., Mobasher, B., Sobral, D., et al., 2016, ApJ, 825, 113

Davé, R., Anglés-Alcázar, D., Narayanan, D., et al., 2019, MNRAS, 486, 2827
Dolag, K., Borgani, S., Murante, G., et al., 2009, MNRAS, 399, 497
Dubois, Y., Pichon, C., Welker, C., et al., 2014, MNRAS, 444, 1453
Fabian, A. C., 2012, ARA&A, 50, 455
Furlong, M., Bower, R. G., Crain, R. A., et al., 2017, MNRAS, 465, 722
Furlong, M., Bower, R. G., Theuns, T., et al., 2015, MNRAS, 450, 4486
Gao, L., Navarro, J. F., Frenk, C. S., et al., 2012, MNRAS, 425, 2169
Gunn, J. E. and Gott J. Richard, I., 1972, ApJ, 176, 1
Harris, C. R., Jarrod Millman, K., van der Walt, S. J., et al., 2020, arXiv e-prints, arXiv:2006.10256
Hunter, J. D., 2007, Computing in science & engineering, 9, 90
Jones, D. H., Read, M. A., Saunders, W., et al., 2009, MNRAS, 399, 683
Kukstas, E., Balogh, M. L., McCarthy, I. G., et al., 2023, MNRAS, 518, 4782
Larson, R. B., Tinsley, B. M., and Caldwell, C. N., 1980, ApJ, 237, 692
Mandelbaum, R., Wang, W., Zu, Y., et al., 2016, MNRAS, 457, 3200
McAlpine, S., Helly, J. C., Schaller, M., et al., 2016, Astronomy and Computing, 15, 72
Moore, B., Lake, G., and Katz, N., 1998, ApJ, 495, 139
Muzzin, A., Marchesini, D., Stefanon, M., et al., 2013, ApJS, 206, 8
Nagai, D. and Kravtsov, A. V., 2005, ApJ, 618, 557
Peng, Y.-j., Lilly, S. J., Kovač, K., et al., 2010, ApJ, 721, 193
Peng, Y.-j., Lilly, S. J., Renzini, A., et al., 2012, ApJ, 757, 4
Pillepich, A., Nelson, D., Hernquist, L., et al., 2018, MNRAS, 475, 648
Pintos-Castro, I., Yee, H. K. C., Muzzin, A., et al., 2019, ApJ, 876, 40
Piotrowska, J. M., Bluck, A. F. L., Maiolino, R., et al., 2022, MNRAS, 512, 1052
Planck Collaboration XVI, 2014, A&A, 571, A16
Reddick, R. M., Wechsler, R. H., Tinker, J. L., et al., 2013, Astrophysical Journal, 771,
Schaye, J., Crain, R. A., Bower, R. G., et al., 2015, MNRAS, 446, 521
Silk, J. and Mamon, G. A., 2012, Research in Astronomy and Astrophysics, 12, 917
Springel, V., White, S. D. M., Tormen, G., et al., 2001, MNRAS, 328, 726
Taylor, E., Almaini, O., Merrifield, M., et al., 2023, MNRAS, 522, 2297
The EAGLE team, 2017, arXiv e-prints, arXiv:1706.09899
Tremonti, C. A., Moustakas, J., and Diamond-Stanic, A. M., 2007, ApJL, 663, L77
van der Burg, R. F. J., Rudnick, G., Balogh, M. L., et al., 2020, A&A, 638, A112
Webb, K., Balogh, M. L., Leja, J., et al., 2020, MNRAS, 498, 5317
Werner, S. V., Hatch, N. A., Muzzin, A., et al., 2022, MNRAS, 510, 674
Whitaker, K. E., Bezanson, R., van Dokkum, P. G., et al., 2017, ApJ, 838, 19
Yano, M., Kriek, M., van der Wel, A., et al., 2016, ApJL, 817, L21

Appendix A

Quenched fraction vs. halo mass quartile

Instead of the $v_{\rm max,peak}$, here we checked the quenched fraction of cluster satellites and field centrals in $M_{\rm h,peak}$ quartiles. Figure 5.A.1 shows this for the high-mass ($M_\star$ within $10^{10} - 10^{11}{\rm M}_\odot$) galaxy sample in clusters and the field. This is analogous to the left panel of Fig. 5.4, excluding the data points at $z = 2$ to demonstrate the most trend between our highest and lowest redshifts of concern.

Similar to the left panel of Fig. 5.4, at $z = 3.5$, cluster satellites and field centrals have a comparable quenched fraction against the $M_{\rm h,peak}$ quartiles, which again sup-

ports the notion that at this redshift, cluster and field galaxies likely quenched through similar mechanisms. At $z = 1.5$, field centrals have a similar trend as in Fig. 5.4 – having a higher quenched fraction in higher halo mass quartiles. Cluster satellites, however, differ strongly at the lowest halo mass quartile. At the other three points, the trend is comparable to Fig. 5.4, especially at the highest quartile, where their quenched fraction is the same as the field centrals. Overall, Fig. 5.A.1 is consistent with our main conclusions about the high-mass galaxies: at this stellar mass range, if a galaxy has a higher halo mass (Q_4), it is similarly likely to be quenched in both clusters and the field, but for lower halo masses, it is more likely to be quenched as a satellite in a massive cluster than an isolated galaxy in the field.

Appendix B

Black hole mass, half mass radius, and cluster-centric distance

We studied the distribution of $M_{\rm SMBH}$ and $r_{1/2,\rm mass}$ with M_* of our high-mass galaxy samples for field centrals and cluster satellites and compared these trends with those as a function of $v_{\rm max,peak}$ as used in the main text. This is shown in Fig. 5.B.1. For all the panels here, star-forming (blue) and quenched (red) galaxies have the same selection criteria as is throughout the paper. For both cluster satellites and field centrals, most of the quenched galaxies have a high $v_{\rm max,peak}$, which we discussed in detail in Sec. 5.3. However, we see different distributions of quenched cluster and field galaxies in terms of the $M_{\rm SMBH}$ and $r_{1/2,\rm mass}$.

Quenched cluster satellites have a smaller $r_{1/2,\rm mass}$ ($\leq$1kpc) for 74 per cent of the sample galaxies, and 90 per cent of the quenched cluster satellites have their $r_{1/2,\rm mass}$ value $\leq$ 1.5kpc. In terms of their $M_{\rm SMBH}$, there is a larger scatter – 41 per cent of them have a high SMBH mass ($\geq 10^{7.5}$M$_\odot$), but the rest have a wide range of values, with some as low as 10^5M$_\odot$. On the other hand, 85 per cent of the quenched field centrals have a high $M_{\rm SMBH}$ value ($\geq 10^{7.5}$M$_\odot$), with a few having mass $\sim 10^6$M$_\odot$. In terms of their $r_{1/2,\rm mass}$, they have a large scatter with 67 per cent having $r_{1/2,\rm mass}$ $\leq$1 kpc.

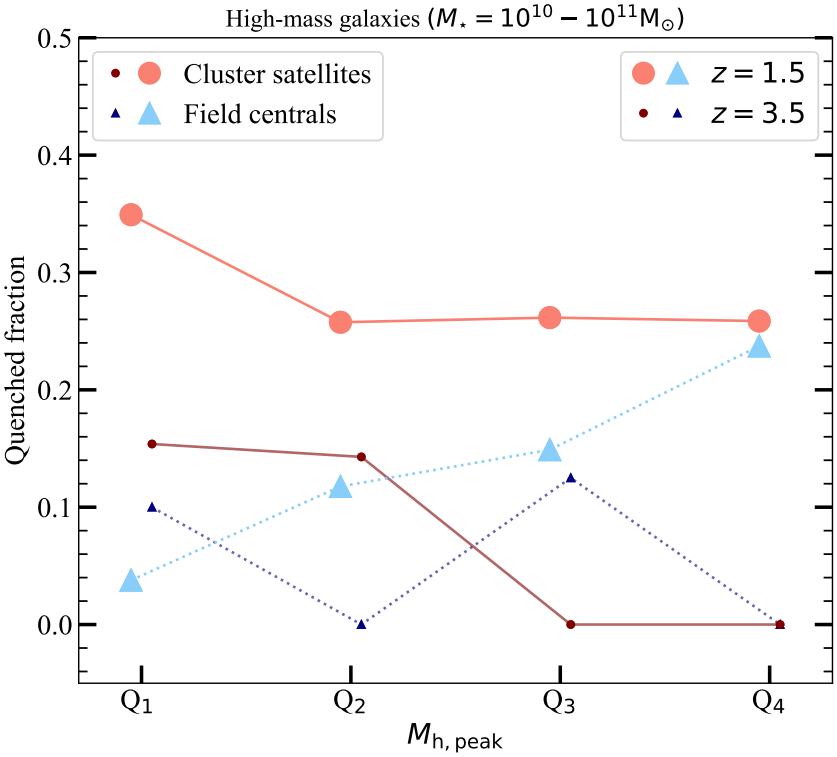

Figure 5.A.1: Fraction of quenched galaxies vs. the $M_{\mathrm{h,peak}}$ quartile in clusters (red shades) and field (blue shades) at different redshifts. The evolution is shown for high-mass galaxies, with $10^{10} - 10^{11}\mathrm{M}_\odot$. Higher redshift data points are respectively smaller and in darker tones of the same colours. Similar to the left panel of Fig. 5.4, at $z = 3.5$, field centrals and cluster satellites have a comparable trend of quenched galaxy fraction. Also, for the high-mass field centrals, a higher $M_{\mathrm{h,peak}}$ corresponds to a higher quenched fraction at $z = 1.5$, as observed in Fig. 5.4. At the highest quartile, the field centrals and cluster satellites have comparable quenched fraction as well. However, the enhancement of quenched fraction is stronger at lower halo-mass quartiles, compared to lower $v_{\mathrm{max,peak}}$ quartiles.

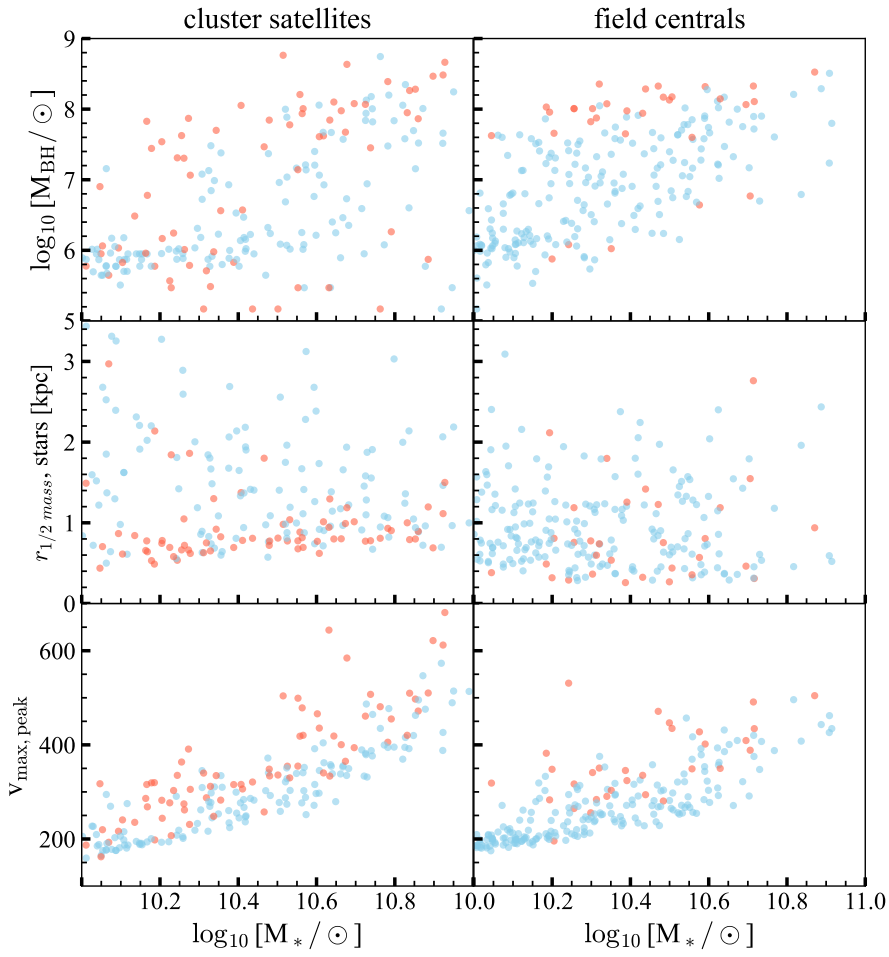

Figure 5.B.1: Central SMBH mass (top), half mass radius (middle), and $v_{\rm max,peak}$ (bottom) vs the stellar mass of cluster satellites (left panels) and field centrals (right panels) in galaxy stellar mass range $10^{10} - 10^{11}$M$_\odot$. Quenched (sSFR≤-10) and star-forming galaxies are in red and blue, respectively. Quenched cluster satellites have a higher $v_{\rm max,peak}$, smaller (< 1 kpc) half-mass radii, and a high scatter in SMBH mass range compared to the star-forming ones. Quenched field centrals also have a higher $v_{\rm max,peak}$ value, however, unlike the cluster satellites, their half-mass radii have a higher scatter whereas the SMBH masses have a consistent higher value ($\geq 10^{10}$ M$_\odot$).

The high fraction of quenched field centrals with a high SMBH mass is consistent with the scenario that they are self-quenched and the process is primarily AGN feedback, which can get stronger for more massive black holes.

With cluster satellites, however, both the smaller size and more massive SMBH of the cluster satellites could be connected to their previous proximity to the cluster halo centre. In that case, their quenching that followed their proximity to the cluster centre has a high chance of being environment-driven. To further test the effect of environment on cluster satellites, we measured the distance of these satellites from the cluster centre between $z = 14$ and the epoch when $v_{\rm max,peak}$ occurs, in units of r_{200}. If a satellite came too close to the central galaxy before $v_{\rm max,peak}$ occurred, and therefore, was subjected to hydrodynamical and/or tidal forces, then it could possibly be stripped of its cold gas, and consequently quench its star formation.

Instead of the standard 500 Myr time-steps of the simulation outputs, we used a smaller 10 Myr time-step to reduce the chance of missing a short-lived phase where a satellite may be the closest to the central galaxy. We plotted the minimum distance between the satellite and central over the considered redshift range vs the stellar mass of the galaxies (similar to Fig. 5.B.1 but not shown here). We found that only 27 per cent of the quenched satellites have come as close as $0.2 \times r_{200}$ of the cluster at some point before attaining their $v_{\rm max,peak}$. Therefore, stripping in the cluster environment cannot be the primary reason for quenching the cluster satellites.

Moreover, half of the quenched satellites were never within r_{200} distance from the cluster centres before $v_{\rm max,peak}$ occurred. These satellites were likely already self-quenched before being a part of the cluster. A similar suggestion was made by Werner et al. (2022), where they considered the area within $1 < r/r_{200} < 3$ distances of GOGREEN clusters as the cluster infall region. Because of the excess quenching in the infall region, they suggested that some massive quenched galaxies in the infall region quenched before they became part of the clusters. In Hydrangea, galaxies in $1 < r/r_{200} < 3$ distances can also be part of the cluster halo if they satisfy the FoF membership criteria. In our sample, most of the massive quenched cluster satellites with $M_{\rm SMBH} \geq 10^{7.5}\,{\rm M}_{\odot}$, have a minimum distance from the cluster centre (before attaining $v_{\rm max,peak}$) above their corresponding r_{200}. They are, therefore, in the 'infall region' defined by Werner et al. (2022). This can also indicate that these quenched cluster galaxies with a massive black hole are central galaxies of infalling groups.

In total, 97 per cent of the quenched field centrals have either $r_{1/2,\rm mass} \leq$1 kpc or $M_{\rm SMBH} \geq 10^{7.5}{\rm M}_{\odot}$, whereas, 87 per cent of the quenched cluster satellites satisfy the same conditions or have been at a distance of less than 20% of the r_{200} from the cluster

centre at some point before $v_{\rm max,peak}$ occurred. Therefore, the majority of quenched galaxies in our samples are consistent with having a high $v_{\rm max,peak}$, which is connected to the halo mass, with a combination to the SMBH mass, galaxy size, and proximity to the cluster centre (only for the satellites). Dynamical interactions can be another important factor for the quenched galaxies, especially for the remaining 13 per cent cluster satellites and 3 per cent field centrals that do not correlate with any of our tested parameters.

Nederlandse samenvatting

Het huidige standaardmodel van de kosmologie, het 'Lambda Cold Dark Matter' (ΛCDM) model met koude donkere materie en een kosmologische constante (Λ) als belangrijkste ingrediënten, is één van de indrukwekkendste prestaties van de moderne wetenschap. De theorie wordt ondersteund door een reeks aan verschillende kosmische metingen. Volgens de oerknaltheorie in het ΛCDM-paradigma is het universum grofweg 13,8 miljard jaar geleden ontstaan. Vlak na de oerknal had het universum een enorm hoge dichtheid, het was heet, en alle atomen waren geïoniseerd en opmerkelijk homogeen verdeeld, wat heeft geleid to de bijna isotrope temperatuur van de kosmische achtergrondstraling die we waarnemen. De dichtheidsverdeling had echter zeer kleine oneffenheden, die in de loop van de tijd onder de invloed van zwaartekracht zijn gegroeid en uiteindelijk donkere materiehalo's (dm-halo's) vormden. Naarmate het universum voldoende was afgekoeld, klonterden de atomen samen in deze dm-halo's. Ongeveer 100 miljoen jaar na de oerknal ontstonden de eerste sterren waaruit vervolgens de eerste sterrenstelsels zijn gevormd.

Vandaag de dag zijn de sterrenstelsels in het heelal verdeeld in een complexe structuur die bekend staat als het kosmische web. De grootschalige verdeling van materie lijkt op een web, met grote leegtes, draden en knooppunten op de kruisingen van deze draden. Van de kleine dm-halo's tot de kosmische webstructuur is het hele heelal in de loop van de kosmische tijd hiërarchisch gegroeid doordat individuele dm-halo's fuseerden tot steeds grotere objecten. Sterrenstelsels vormden zich in deze dm-halo's en groeiden mee langs de reeds bestaande kosmische filamenten, wat uiteindelijk resulteerde in vorming van de grootste door zwaartekracht gebonden structuren in het heelal, namelijk gigantische clusters van sterrenstelsels, op de kruispunten van de draden van het kosmische web. Omdat dit de grootste gevormde structuren zijn binnen het hiërarchische vormingsmodel kan hun hoeveelheid en hun massaverdeling gebruikt worden om de theorie van structuurvorming in de loop van de kosmische tijd te testen.

Clusters van sterrenstelsels en hun kleinere tegenhangers, groepen van sterrens-

telsels, bestaan uit tientallen tot duizenden sterrenstelsels in een relatief klein volume in vergelijking met andere gebieden in het heelal. Door de hoge dichtheid van sterrenstelsels zijn groepen en clusters van sterrenstelsels unieke kosmische laboratoria om de invloed van de interacties tussen sterrenstelsels en hun omgeving en de impact hiervan op de evolutie van sterrenstelsels te bestuderen. Hoewel ons begrip van de processen die de evolutie van deze sterrenstelsels bepalen in de laatste decennia is gegroeid, zijn er nog veel open vragen.

Een van deze open vragen is waarom de sterrenstelsels in deze drukke omgeving stoppen met het vormen van sterren. In het lokale heelal begrijpen we de groei van sterrenstelsels in groepen en clusters redelijk goed met behulp van vereenvoudigde modellen die het stoppen van stervorming beschrijven. Op hogere roodverschuivingen ($z > 1$) kunnen deze theorieën echter een aantal recente waarnemingen, zoals dat zware sterrenstelsels in clusters en protoclusters al eerder stoppen met het vormen van sterren, niet verklaren.

Verder krijgt de verdeling van licht binnen deze groepen en clusters, zoals de diffuse halo van sterren rond de centrale sterrenstelsels in groepen/clusters van sterrenstelsels recent meer aandacht. De diffuse stellaire halo is een overblijfsel van de wisselwerking tussen sterrenstelsels tijdens de vorming van de grootschalige structuren. Bovendien is er waargenomen dat de massaverdeling van deze sterren de universele dm-verdeling volgt, waardoor het een potentiële tracer is van de onzichtbare dm-halo waarin het sterrenstelsel verblijft. Door de diffuse aard vallen deze studies in het regime van lage oppervlaktehelderheden ($27 \geq \mathrm{mag/arcsec^2}$), waardoor ze bemoeilijkt worden door de limitaties van de optische observationele sterrenkunde. Ondanks recente vooruitgang blijft de bijdrage van de diffuse sterren aan de totale baryonische massa van de sterrenstelsels en de invloed van vormingsmechanismen op het ontstaan en de groei van sterrenstelselclusters en hun centrale sterrenstelsels nog steeds onduidelijk.

Het verklaren van de rijke diversiteit binnen de sterrenstelselpopulatie in verschillende omgevingen met een uitgebreide theorie over sterrenstelselvorming is een ingewikkelde uitdaging. Het ontstaan en de groei van dm-halo's en de vorming van sterrenstelsels daarin kan numeriek gesimuleerd worden. Vooral hydrodynamische simulaties zijn een succesvol hulpmiddel geweest om de individuele bestandsdelen van het universum, namelijk donkere materie en gewone (baryonische) materie bestaande uit gas, stof en sterren, te verbinden in de context van sterrenstelselvorming.

Omdat deze simulaties een extreem groot bereik van dynamische schalen, van stervorming via koud moleculair gas tot grootschalige structuren, moeten bestrijken, is het numeriek onmogelijk om de simulaties volledig vanuit eerste principes op te bouwen.

Een oplossing is om onder de resolutieschaal zogenaamde subgrid natuurkundige modellen te gebruiken voor processen die op kleinere schalen plaatsvinden. Voorbeelden van deze processen zijn het afkoelen van gas, stervorming en de energie- en impulsinjectie die wordt veroorzaakt door extreem zware zwarte gaten en supernova's. De parameters die de subgrid modellen beschrijven hebben onbekende en onmeetbare waardes en worden meestal afgeschat zodat geselecteerde relaties in de simulatie overeenkomen met metingen in het lokale heelal, zoals bijvoorbeeld de massa functie van sterrenstelsel of de sterren-over-halo-massafunctie. De relaties tussen de parameters van het subgrid model en de gesimuleerde eigenschappen van sterrenstelsels zijn echter niet-lineair en het grofweg reproduceren van één waarneembare sterrenstelseleigenschap garandeert geen overeenkomst tussen andere eigenschappen. Het vermogen van simulaties om realistische waarneembaarheden te voorspellen moet daarom worden getoetst met zorgvuldig ontworpen controletests.

In dit proefschrift heb ik gebruik gemaakt van de EAGLE en Hydrangea simulaties. Hydrangea is een suite van 24 hoge-resolutie zoomin simulaties van zware sterrenstelselclusters en hun directe omgeving. De Hydrangea-simulaties en het EAGLE-project gebruiken dezelfde versie en afstelling van de EAGLE-code. Tot op heden zijn de Hydrangea simulaties de grootste set van zware sterrenclusters met een vergelijkbare hoge resolutie. De simulaties zijn over het algemeen succesvol in het reproduceren van waargenomen eigenschappen van sterrenstelsels in omgevingen met een hoge dichtheid.

Het is cruciaal om de accuraatheid van de simulaties op hogere roodverschuivingen te testen voordat conclusies kunnen worden getrokken, omdat deze simulaties, net als alle moderne simulaties, zijn geijkt op $z = 0$. Vanwege de grove behandeling van de onderliggende fysisca met de subgrid modellen betekent het feit dat de simulaties een waarneembare functie reproduceren niet dat ze de daadwerkelijke natuurkundige processen in het echte heelal nauwkeurig reproduceren. Bovendien kunnen subtiele details bij het vergelijken van de simulaties en waarnemingen de conclusie sterk beïnvloeden. Een zorgvuldige vergelijking tussen de simulaties en waarnemingen die rekening houdt met hun fysische aard en mogelijk geïntroduceerde fouten van beide kanten overweegt is daarom van cruciaal belang.

Met de enorme recente vooruitgang in zowel theorie als waarnemingen zal de meetfout klein genoeg worden dat de tekortkomingen in de methodologie de beperkende factor zijn in de interpretatie van de data. Daarom is dit het uitgelezen moment om de hulpmiddelen te bouwen die de kwaliteit van de interpretatie bevorderen.

In dit proefschrift

In dit proefschrift hebben we verschillende eigenschappen van sterrenstelsels in groepen en clusters uit de Hydrangea en EAGLE-simulaties vergeleken met recente waarnemingen op $z < 3,5$. We zijn begonnen met algemene eigenschappen, zoals de totale massa in sterren in groepen en clusters, waarna we verder gingen met meer gedetailleerde eigenschappen, zoals de ruimtelijke verdeling van massa in sterrenstelsels binnen de clusters. We hebben de waarnemingen nagebootst in simulaties, zodanig dat dat ze overeenkomen met echte data van de Kilo-Degree Survey, waarna we andere eigenschappen met elkaar vergeleken. Door een breed scala aan eigenschappen van sterrenstelsels uit kosmologische hydrodynamische simulaties te vergelijken met recente waarnemingen van hoge kwaliteit, hebben we de betrouwbaarheid van de simulaties bij hogere roodverschuivingen getest en laten we zien hoe deze vergelijkingen nieuwe tests motiveren en nieuwe inzichten opleveren over de evolutie van sterrenstelsels in omgevingen met hoge dichtheden.

In **Hoofdstuk 2** hebben we verschillende eigenschappen van massieve sterrenclusters uit de Hydrangea-simulaties vergeleken met recente waarnemingen van clusters tot een roodverschuiving z=2. We hebben bevestigd dat de totale massa in sterren in de Hydrangea-clusters bij een vaste halomassa en roodverschuiving vergelijkbaar is met waargenomen sterrenstelselclusters. Daarna ontdekten we dat bij een vaste roodverschuiving de normalisatie van de massafunctie in sterrenstelsels van clusters sterk correleert met de halo-massa van de cluster. Ook voorspelden de simulaties, met een halo-massaverdeling die overeenkomt met een waargenomen cluster dataset, de waargenomen stellaire massa functie correct tot een roodverschuiving z=1,5. Vervolgens bestudeerden we de dichtheidsprofielen van clusters op $z < 2$, voor zowel de donkere materie als de sterren. Door de concentratie-parameters van de Navarro-Frenk-White (NFW) model profielen te vergelijken met eerder onderzoek, hebben we geverifieerd dat de tegenovergestelde evolutie van de donkere materie en sterren concentratie in clusters over de kosmische tijd niet in strijd is met de ΛCDM-kosmologie.

In **Hoofdstuk 3** bestudeerden we het licht in groepen en clusters, met als doel de kloof te overbruggen tussen simulatie-gebaseerd werk (waar de massaverdeling bepaald wordt) en observationeel werk (waard de lichtverdeling bepaald wordt). We hebben waarnemingen van meerdere filters gesimuleerd voor 500 sterrenstelselgroepen en -clusters uit de Hydrangea-simulaties. We hebben deze beelden vergeleken met de gegevens van de Kilo Degree Survey (KiDS) en Galaxy and Mass Assembly (GAMA) survey. Dit werk loste een cruciaal probleem op in de analyse, namelijk door het

selecteren van de beste plaats voor het centrum van de groep. We ontdekten dat in plaats van het helderste sterrenstelsel, het stelsel met de hoogste geassocieerde halomassa een betere kandidaat is voor centraal sterrenstelsel. Bovendien konden we de sterrenstelsels beter begrijpen door ze te groeperen op basis van de helderheid van het centrale sterrenstelsel. Ten slotte gaven de kleur-, massa- en metaalprofielen van het diffuse sterlicht van Hydrangea aan dat in groepen met een lage massa het diffuse sterlicht voornamelijk groeit door grote fusies, terwijl in zwaardere clusters de groei van het diffuse sterlicht voornamelijk verloopt via de aangroei van sterren uit satelliet sterrenstelsels.

In **Hoofdstuk 4** hebben we de fractie van het diffuse sterlicht in sterrengroepen gemeten op basis van de gegevens van het KiDS+GAMA-onderzoek en deze resultaten vergeleken met de bevindingen van **Hoofdstuk 3**. De standaard dataverwerkingspijplijn voor KiDS is geoptimaliseerd om kleine, zwakke sterrenstelsels te detecteren en niet om diffuus licht te meten. We ontwikkelden een speciale pipeline om de afbeeldingen van KiDS te gebruiken voor de meting van diffuus licht. Hiermee verkregen we de eerste robuuste meting van het diffuse licht voor 850 groepen. We ontdekten dat beperkingen in de gegevens de metingen kunnen beïnvloeden, zelfs met onze speciale pipeline. Door een grote dataset en zorgvuldig geoptimaliseerde analyse te combineren, kunnen we echter robuuste boven- en ondergrenzen stellen aan de fractie van diffuus licht voor ons groepsensemble over roodverschuivingen van $0{,}09 \leq z \leq 0,27$. Onze metingen zijn compatibel met bestaande metingen in individuele systemen op vergelijkbare roodverschuiving en met overeenkomende halo-massa's, echter met grotere precisie. Dit werk demonstreert de potentie van statistische analyse van diffuus licht in grote groepen en clusters van de volgende generatie observatieprogramma's zoals Euclid en LSST. Bovendien kan de ontwikkelde pipeline met minimale aanpassingen worden toegepast op de toekomstige gegevens van deze studies.

Recent onderzoek heeft uitgewezen dat een fractie van de zware sterrenstelsels in clusters van melkwegstelsels al gestopt is met de vorming van sterren op een roodverschuiving van $z = 1,5$. De aanleiding hiervoor is onbekend omdat de clusters nog niet volledig gevormd zijn en de bekende mechanismen voor het stoppen van stervorming in clusters niet sterk genoeg kunnen zijn. Bovendien hebben deze zware sterrenstelsels sterren populaties van vergelijkbare leeftijd in zowel clusters als het veld, wat suggereert dat het dominante mechanisme voor zware sterrenstelsels vergelijkbaar is in beide omgevingen. In **Hoofdstuk 5** hebben we gegevens van de Hydrangea en EAGLE-simulaties gebruikt om te testen of deze vroege uitdoving van zware sterrenstelsels in $z \geq 1,5$ clusters het gevolg is van fundamentele verschillen in

hun halo-eigenschappen. We vonden dat de fracties van zulke zware sterrenstelsels in $1,5 < z < 3,5$ consequent hoger zijn voor sterrenstelsels met een hogere maximale rotatiesnelheid van de donkere materiehalo. De bevindingen suggereren dat seculiere processen alleen al verantwoordelijk kunnen zijn voor de waargenomen eigenschappen van zware sterrenstelsels in (proto)clusters op hoge roodverschuiving. Onze resultaten stellen een fundamentele aanname van populaire modellen ter discussie, namelijk dat clusters worden samengesteld uit een representatieve subgroep van invallende sterrenstelsels uit het veld. Als dit wordt bevestigd, zou dit impliceren dat dergelijke modellen noodzakelijkerwijs moeten falen bij een hoge roodverschuiving, zoals blijkt uit recente waarnemingen.

Publications

Refereed publications

1. *How to Interpret Measurements of Diffuse Light in Stacked Observations of Groups and Clusters of Galaxies*
   Ahad, S. L., Bahé, Y. M., Hoekstra, H., 2023, MNRAS, 518, 3685.

2. *Ultra-Diffuse galaxies in the MATLAS low-to-moderate density fields*
   Marleau, F. R., Habas, R., Poulain, M., Duc, P.-A., Müller, O., Lim, S., Durrell, Durrell, P. R., Sánchez-Janssen, R., Paudel, S., **Ahad, S. L.**, Chougule, A., Bílek, Bílek, M., Fensch, J., 2021, A&A, 654, A105.

3. *Structure and morphology of the MATLAS dwarf galaxies and their central nuclei*
   Poulain, M., Marleau, F. R., Habas, R., Duc, P.-A., Sánchez-Janssen, R., Durrell, P. R., Paudel, S., **Ahad, S. L.**, Chougule, A., Müller, O., Lim, S., Bílek, M., Fensch, J., 2021, MNRAS, 506, 5494.

4. *The stellar mass function and evolution of the density profile of galaxy clusters from the Hydrangea simulations at* $0 < z < 1.5$
   Ahad, S. L., Bahé, Y. M., Hoekstra, H., van der Burg, R. F. J., Muzzin, A., 2021, MNRAS, 504, 1999.

Submitted/To be submitted

1. *An environment-dependent halo mass function as a driver for the early quenching of* $z \geq 1.5$ *cluster galaxies*
   Ahad, S. L., Muzzin, A., Bahé, Y. M., Hoekstra, H., 2023, submitted to MNRAS

2. *Preparing for low surface brightness science with the Vera C. Rubin Observatory: A Comparison of Observable and Simulated Quantities*
   Brough, S., **Ahad, S. L.**, Bahé, Y. M., Ellien, A., Gonzalez, A. H., Jiménez-Teja, Y., Kimmig, L. C., Martin, G., Martínez-Lombilla, C., Montes, M., Pillepich, A., Ragusa, R., Remus, R.-S., Collins, C. A., Knapen, J. H., Mihos, J. C., 2023, submitted to MNRAS

3. *The Intragroup Light in KiDS+GAMA Groups*
   Ahad, S. L., Hoekstra, H., Bahé, Y. M., 2023, in preparation

Curriculum Vitae

I was born in Madaripur, a small town near Dhaka, Bangladesh, in 1992. Like most children, I loved listening to stories, especially stories of adventure, fairy tales, and discoveries. This, paired with the inspiration from my mother, who was a high school teacher of Chemistry and told me stories of all the fun things science can do, made me decide what I wanted to do when I grew up - travel the world and be a scientist! I suppose I never grew out of this wish, although my fascination for astronomy only became strong enough for me to pursue it much later.

I was always curious about how and why things happen, making my academic journey quite a fun experience. After finishing middle school in Madaripur, I moved to Dhaka for a better high school experience than what my hometown could offer. Right before starting high school, I got interested in astronomy after reading a book about how our understanding of the Universe changed with the last few centuries of work in physics and cosmology. Around the same time, I saw a newspaper advertisement for the National Astronomy Olympiad that was going to happen in a few months. I collected the few available books back then in Bengali on introductory astronomy and stargazing to prepare for the Olympiad. I surprisingly became the regional champion that year, and, not so surprisingly, did quite poorly in the national one. This experience made me excited to learn more about physics and astronomy.

However, there was no scope for studying astronomy in Bangladesh. Going abroad right after high school was not an option for me, especially to study astronomy, because it also had no future as a career option back home. So, after finishing high school, I sat for the university admission tests in Bangladesh and got selected for all the best options in the country. While my family wanted me to pursue medical school like most of my cousins, I opted for Electrical and Electronic Engineering, thinking that learning about electronics and robotics would be fun. But with the ulterior motive that I may be able to switch to astronomy in graduate school. Meanwhile, between finishing high school and starting my undergraduate, I again participated in the Astronomy Olympiad, became the national runner-up, and participated in the

10th International Olympiad of Astronomy and Astrophysics in Beijing, China as the first female participant from Bangladesh. Exploring problems in astronomy with participants from around the world in those ten or so days was the best experience of my life back then, and this experience made it clear that what I wanted to do in the long run was astronomy indeed.

My undergraduate thesis was in optoelectronics, on designing and simulating performances of optoelectronic biosensors with Prof. dr. Md. Zahurul Islam. I learned about the research process during this time and greatly enjoyed the experience. After graduation, I applied for astronomy master programs and was thrilled to get accepted for the two-year Erasmus Mundus Joint Master Degree program (AstroMundus) with a scholarship. Throughout the program, I studied at the University of Innsbruck in Austria, the University of Padova in Italy, and the University of Belgrade in Serbia. Apart from the mandatory and additional (optional) courses, I worked on short projects on different topics of interest, from asteroseismology and stellar evolution to studying the active galactic nuclei from SDSS archival data. During the second semester, I attended the MPIA summer school in Heidelberg on compact objects and gravitational waves. During these explorations, I realized that I enjoyed studying the multi-scale and big-picture aspect of extragalactic astronomy the most, and decided to work on characterising the nucleated dwarf galaxies from the MATLAS survey at the University of Innsbruck with Prof. dr. Francine Marleau for my master's thesis.

I started my PhD at Leiden Observatory under the supervision of Prof. dr. Henk Hoekstra and Dr. Yannick Bahé in October 2018. My research was at the interface of simulations and observations, where I studied different aspects of galaxy evolution in galaxy groups and clusters. My work primarily focused on developing systems to carefully compare simulations and observations to facilitate improved insights from the next generations of simulations and observations. Despite the pause during the pandemic, I was fortunate to attend summer and winter schools and present my work in different workshops and conferences. The interactions from these experiences have been very inspiring and stimulating in shaping my research direction.

During my PhD, I worked as a Teaching Assistant for the Numerical Recipes course (Master) and the Galaxies and Cosmology course (Bachelor). I also had the pleasure to co-supervise two master students in their research projects. I was also a part of the EDI and Sustainability committees of the observatory from 2021 until 2023. Apart from research, astronomy and science outreach is something I deeply care about. In the absence of academic astronomy, outreach programs gave me the opportunity to pursue this fascinating field as a career, and I have been actively

connected to astronomy outreach for over a decade. During my undergraduate years, I co-authored an introductory astronomy book for high school students in my native language, Bengali. In Leiden, I helped organise Astronomy on Tap from 2019 to 2022. I have also given many in-person and remote talks on introductory astronomy and galaxy evolution for Bangladeshi audiences ranging from middle school to university graduates.

I will join the Waterloo Centre for Astrophysics (WCA) in December 2023 as a WCA Postdoctoral Fellow. In the next three years, I am excited to study galaxy quenching in high redshift clusters and protoclusters, and perform statistical analysis of intragroup and intracluster light from Euclid and LSST data.

Acknowledgements

My PhD journey has been challenging and transformational in many ways, and approaching the finish line has been possible thanks to the remarkable and kind people who helped along the way.

First, I want to express my deepest gratitude to my supervisors, Henk Hoekstra and Yannick Bahé. Thank you for giving me the opportunity and freedom to follow my curiosity through the PhD projects. I am very grateful for sharing your insights that helped me improve my understanding of astronomy, academia, science, outreach, and more. I look up to your passion for science and pursuit of excellence, and how you guided me with kindness and patience throughout difficult times is what I want to internalize the most in my future career. I hope our paths will cross again in future and allow me to further learn from your wisdom. Also, I am grateful for the kind guidance of Adam Muzzin through several of my PhD projects. I have learned a lot from you and thoroughly enjoyed our discussions about exciting science. I look forward to more opportunities to work together in future!

I want to thank the past and current admin and support staff of the Observatory - Evelijn, Marjan, Monica, Alexandra, Robin, Nancy, Somayeh, Châtelaine, Alina, Hafize, and others for their constant support from the beginning till the end of my PhD experience. I am incredibly grateful for the support from the SCIS team with the residence permit, and the IT Helpdesk team, especially during the 'work from home' era. Also, I want to thank the Graduate School Office staff for their support throughout. All of your efforts not only kept things going smoothly but also helped me stay sane whenever things went wrong.

I would also like to thank the observatory social committee for keeping up the social and fun energy at the institute. The yearly social events are some of the best memories I have of my time here. Also, I highly appreciate the information and support the Observatory Wellbeing committee provided through the difficult pandemic and post-pandemic era.

I extend my thanks to the past and present members of the weak lensing and cos-

mology group, for all the nice interactions and engaging science discussions these past years. I have learnt a lot from all of you about science and collaboration. Stefan and Cas, being your daily supervisor have been a pleasure and a great learning opportunity that only comes through mentoring. Thank you for your dedication and enthusiasm during the projects. I am also thankful to other staff members of the Observatory with whom I had interactions on different occasions. Koen, Matthieu, Jackie, Marcel, Leonard, Violette, Aurora, Xander - thank you very much for the pleasant interactions and your support and care for the students.

My thanks to the Astronomy on Tap Leiden organising team for the welcoming and fun work environment. Francisca, Wendy, Alex, Alex, Anniek, Aida, Stella, Marta, Andrés, Zuzanna, Michelle, and everyone else - it was a great pleasure to be a part of the team. I also thank the members of the EDI and Sustainability committees of the observatory. I surely learned way more than I could contribute as a part of these two committees, and I owe every one of the committee members for my personal journey towards promoting more inclusive and sustainable practices in the scientific community and the broader society in general.

I want to thank my collaborators from the LSST low-surface-brightness working group and the ISSI protocluster research group for the opportunity to be a part of such engaging and supportive teams. I hope to continue our collaboration in future.

A big part of my PhD went in a fast-forward mode because of the pandemic and some additional personal challenges. However, I have been lucky to meet many incredible people in the PhD cohort and made great friends. Our first-year PhD retreat at Duinrell is a very dear memory (thanks to the observatory for organizing the introductory event!), and so was the end-of-first-year trip around the Hoge Veluwe park (Thanks a lot to Marina and Lýdia for organizing this!). My thanks to the PhD candidates who started before our 2018 cohort for being incredibly kind and welcoming. Kim, thank you for all the nice lunch times, and for listening to my venting when I was overwhelmed. Kim, Pedro, Yapeng, Niccolò, Amy, and Christian - it was a pleasure sharing the office with you at different times. Marina, one of the few good things that happened to me during the pandemic was your friendship! Your courage and kindness always inspire me. Thank you and Folkert for all the long conversations (including ranting about work of course), fun tours, art sessions, board game bonanzas, and wonderful meals we had together. Lýdia, I greatly admire your resilience. Thank you for always reaching out, for the honest conversations, and for being a great friend. Sanjana, thank you for all the nice memories - especially for letting me play with Akupara. I always enjoyed our conversations about travelling, food, and whatnot.

Anna and Mantas - it was a joy having you two as office neighbours! Nastasha, thank you very much for your help during my job application time! Thanks to all the PhDs, postdocs, and master students of the Observatory who made the past five years in Leiden an engaging, and enjoyable experience - Maria Cristina, Christos, Andrej, Jit, Gabriella, Omar, Danna, Valeriya, Tomasso, Eleonora, Santiago, Olivier, Martijn, Martijn, Stijn, Turgay, Shun-Sheng, Jeger, Dirk, Xiaoyuan, Sander, Shravya, Jeroen, Rens, Naadiyah, Sarah, Ashley, Willeke, Dora, Zephyr, Luna, Dario, Alessandro, MJ, Pooneh, Roland, Chloe, Erik, Evgenii, Roi, Zorry, Andrés, Joey, Fraser, Dilovan, Bas, Kirsty, Hiddo, Pranjal, Morgan, Katie, Brian, Wil, Xuechen, Zhenlin, Patrick, Danial, Alex, and everyone else I had the pleasure to interact with.

My biggest thanks to my husband Ruslan, my family in Bangladesh and my family-in-law from Ukraine for being constant sources of support and strength during my PhD journey, even when they themselves were going through very challenging times. Ruslan, I can never express my gratitude enough for all your support throughout these years, all on top of working on your PhD yourself. Thank you for all the packed lunches, the discussions about work whenever I needed to think out loud, and for restoring my belief in my capacity to finish the work whenever I felt lost. I am grateful for all the ups and downs we have been through together across Europe, and I am excited to see what awaits us in Canada!

I want to thank my undergraduate besties — Manira, Maitraye, Sunandita, who are more like sisters and have been the best work-from-home buddies and support system whenever I needed. It was curious how the pandemic made our PhD journeys way more connected than it would have been otherwise. I cannot wait to finally live closer to you girls and hopefully meet more than once every five years!

Last but not least, I want to thank my mentors from Bangladesh. As there is still no way to pursue astronomy as a career there, the path I walked is a rarely chosen one. I am grateful to Mrityunjoy Saha, Asrafuzzaman Akhunji, Farseem Mannan Mohammedy, Md. Zahurul Islam, Arshad Momen, and Munir Hasan, who supported and encouraged me on my journey to pursue astronomy. Also, my thanks to the astronomers from Bangladesh who showed that this is possible and shared their experiences whenever I asked for direction - Sultana N. Nahar, Khan Md. Bin Asad, and Syed Ashraf Uddin.